UTILISING GALACTIC ARCHAEOLOGY SURVEYS FOR EXOPLANETARY SCIENCE

A Thesis Submitted by

Jake T. Clark,
M.Sc.Comm.Outreach, B.Sc(Hons), B.Sc(SSAP)

For the Award of

Doctor of Philosophy

2021

ABSTRACT

During the last decade, a wealth of new large-scale surveys have come online across the world. These huge spectral, astrometric and photometric surveys are providing astronomers with the richest datasets to date, to better characterise stars contained within the Milky Way like never before. Not only are these resources used to better understand the formation and evolution of our Galaxy and the stars contained within it, but these surveys can also be used to better understand the exoplanets found within the Milky Way. More planets are now being discovered in our galaxy, thanks largely to NASA's new exoplanetary mission, the *Transiting Exoplanet Survey Satellite* (*TESS*). *TESS* has been operating since 2018, with an unprecedented number of stars being observed to monitor transit signals of exoplanets around nearby stars.

My thesis firstly cross-matched spectroscopic, photometric, and astrometric data from GALAH Data Release 2, the *TESS* Input Catalog and *Gaia* Data Release 2, to create a curated, self-consistent catalog of physical and chemical properties for 47,285 stars, known as the GALAH-*TESS* catalog. Using these data, this thesis has derived isochrone masses and radii that are precise to within 5%. These masses and radii have then helped redetermine the physical properties of known and candidate exoplanets, casting doubt on the exoplanetary nature of at least three candidate systems discovered by TESS.

The GALAH-*TESS* catalog contains abundances for up to 23 elements that specifically contains the abundance ratios for C/O, Mg/Si, Fe/Si and Fe/Mg, to assist in determining the composition and structure of planets with $R_p < 4R_\oplus$. From these ratios, 36 % fall within 2 sigma of the Sun/Earth values, suggesting that these stars may

host rocky exoplanets with geological compositions similar to planets found within our own Solar system.

With GALAH releasing DR3, to include the K2 fields and the Southern TESS continuous viewing zone, and *Gaia* releasing EDR3, my thesis then focused on improving the characteristics of known and candidate exoplanets and their host stars. This thesis not only revises the physical properties for hundreds of confirmed and candidate exoplanets, but it has also decreased the uncertainties for some of these derived properties too. It was able to improve the parameters for five ultra-short period exoplanets, in particular, refining the radius and mass of three to their most precise values yet, to less than 2.3% and 8.5% uncertainty respectively. The radius estimate for CoRoT-7 b further suggests that it is large enough for an atmosphere to contribute to its overall radius. It also uncovered that Ultra-Hot Neptunes are more likely to be found around thick-disc stars rather than their thin-disc counterparts.

Finally, my thesis presents the discovery of a hot-Jupiter orbiting a rapidly rotating ($v \sin(i) = 28$ km s^{-1}) early F dwarf HD 115447 (TOI-778). Combining the transit signal taken from Sector 10 of *TESS*'s initial detection of the exoplanet, this thesis also uses ground-based photometry, along with radial velocity measurements taken from Minerva-Australis, TRES, CORALIE and CHIRON to confirm and characterise TOI-778 b. A spectroscopic transit of TOI-778 b was taking to derive its spin-orbit angle of 19.1 ± 9.6 degrees, consistent with an aligned planetary system.

CERTIFICATION OF THESIS

This Thesis is the work of Jake Thomas Clark except where otherwise acknowledged, with the majority of the authorship of the papers presented as a Thesis by Publication undertaken by the Student. The work is original and has not previously been submitted for any other award, except where acknowledged.

Student and supervisors signatures of endorsement are held at the University.

Professor Robert Wittenmyer
Principal Supervisor

Professor Jonathan Horner
Associate Supervisor

Doctor Natalie Hinkel
Associate Supervisor

A/Professor Duncan Wright
Associate Supervisor

Professor Bradley Carter
Associate Supervisor

LIST OF CONTRIBUTIONS FROM PUBLICATION CO-AUTHORS

This section details contributions by the various authors for each of the papers presented in this thesis by publication.

Chapter 2, Clark et al. (2021): Clark, J. T., Clerté, M., Hinkel, N. R., Unterborn, C. T., Wittenmyer, R. A., Horner, J., Wright, D. J., Carter, B., Morton, T. D., Spina, L., Asplund, M., Buder, S., Bland-Hawthorn, J., Casey, A., De Silva, G., D'Orazi, V., Duong, L., Hayden, M., Freeman, K., Kos, J., Lewis, G., Lin, J., Lind, K., Martell, S., Sharma, S., Simpson, J., Zucker, D., Zwitter, T., Tinney, C. G., Ting (丁源森), Y.-S., Nordlander, T., & Amarsi, A. M. (2021). The GALAH Survey: using galactic archaeology to refine our knowledge of TESS target stars. *Monthly Notices of the Royal Astronomical Society*, 504(4), 4968–4989

Author	Percent Contribution	Tasks Performed
Jake T Clark	85	Designed and implemented the methodology to create the GALAH-TESS catalouge. Lead the interpretation of the catalouge's data, created all of the plots in the paper except one, wrote all drafts of paper and lead the conception of project.
Mathieu Clerté Natalie R Hinkel Cayman T Unterborn Robert A Wittenmyer Jonathan Horner Duncan J Wright Brad Carter Timothy D Morton Lorenzo Spina Martin Asplund Sven Buder Joss Bland-Hawthorn Andy Casey Gayandhi De Silva Valentina D' Orazi Ly Duong Michael Hayden Ken Freeman Janez Kos Geraint Lewis Jane Lin Karin Lind Sarah Martell Sanjib Sharma Jeffrey Simpson Dan Zucker Tomaz Zwitter Christopher G Tinney Yuan-Sen Ting (丁源森) Thomas Nordlander Anish M Amarsi	15	Supervision of paper, assisted in the interpretation of molar abundances, debugging software, implementation of software onto the HPC, Conception of GALAH project, steering committee of GALAH collaboration and suggested edits to the manuscript.

Chapter 3, Clark et al. (2021): Clark, J. T., Wright, D. J., Wittenmyer, R. A., Horner, J., Hinkel, N. R., Clerté, M., Carter, B. D., Buder, S., Hayden, M. R., Bland-Hawthorn, J., Casey, A. R., De Silva, G. M., D' Orazi, V., Freeman, K. C., Kos, J., Lewis, G. F., Lin, J., Lind, K., Martell, S. L., Schlesinger, K. J., Sharma, S., Simpson, J. D., Stello, D., Zucker, D. B., Zwitter, T., Munari, U., & Nordlander, T. (2021). The GALAH Survey: improving our understanding of confirmed and candidate planetary systems with large stellar surveys. *Monthly Notices of the Royal Astronomical Society*, 510(2), 2041–2060

Author	Percent Contribution	Tasks Performed
Jake T Clark	90	Designed and implemented the methodology, lead the interpretation of the data, created all of the plots in the paper, wrote all drafts of paper and lead the conception of project.
Duncan J Wright Robert A Wittenmyer Jonathan Horner Natalie R Hinkel Mathieu Clerté Brad Carter Sven Buder Michael Hayden Joss Bland-Hawthorn Andy Casey Gayandhi De Silva Valentina D' Orazi Ken Freeman Janez Kos Geraint Lewis Jane Lin Karin Lind Sarah Martell Katharine J Schlesinger Sanjib Sharma Dennis Stello Jeffrey Simpson Dan Zucker Tomaz Zwitter Ulisse Munari Thomas Nordlander	10	Supervision of paper, assisted in the interpretation of chemo-kinematic data, Conception of GALAH project, steering committee of GALAH collaboration and suggested edits to the manuscript.

Chapter 4, Clark et al. (2022): Clark, J. T., Vach, S., Heitzmann, A., Rodriguez, J. E., Addison, B. C., Wright, D. J., Clerté, M., Brown, C. J., Fetherolf, T., Wittenmyer, R. A., Plavchan, P., Kane, S. R., Horner, J., Kielkopf, J. F., Shporer, A., Tinney, C. G., Hui-Gen, L., Ballard, S., Bedding, T., Bowler, B. P., Mengel, M. W., Zhou, G., Lee, A. S., David, A., Heim, J., Lee, M. E., Sevilla, V., Zafar, N. E., Hinkel, N. R., Allen, B. E., Berberyan, A., Berlind, P., Bieryla, A., Bouchy, F., Brahm, R., Bryant, E. M., Christiansen, J. L., Ciardi, D. R., Ciardi, K. N., Collins, K. A., Dallant, J., Davis, A. B., Díaz, M. R., Dressing, C. D., Esquerdo, G. A., Harre, J.-V., Howell, S. B., Jenkins, J. M., Jensen, E. L. N., Jones, M. I., Jordán, A., Latham, D. W., Lund, M. B., McCormac, J., Nielsen, L. D., Otegi, J., Quinn, S. N., Radford, D. J., Ricker, G. R., Schwarz, R. P., Seager, S., Smith, A. M. S., Stockdale, C., Tan, T.-G., Udry, S., Vanderspek, R., Wang, S., Wingham, G., & Winn, J. N. (2022). Spinning up a Daze: *TESS* Uncovers a Hot Jupiter orbiting the Rapid-Rotator TOI-778. *Astronomical Journal, Submitted*

The papers to which co-author contributions were made by J. T. Clark during the period of Candidacy, but not germane to the main thesis and narrative are presented in Appendix A and B.

Author	Percent Contribution	Tasks Performed
Jake T Clark	60	Derived stellar parameters for TOI-778 from spectra, organised and collated data from various sources for the paper's analysis, ran software and interpreted results to write in the paper, created all plots and wrote the majority of paper.
Jack Okumura Sydney Vach Alexis Heitzmann Joseph E. Rodriguez Brett C. Addison Duncan J. Wright Mathieu Clerté Carolyn J. Brown Tara Fetherolf Robert A. Wittenmyer Peter Plavchan Stephen R. Kane Jonathan Horner John F. Kielkopf Avi Shporer C.G. Tinney Liu Hui-Gen Sarah Ballard Timothy Bedding Brendan P. Bowler Matthew W. Mengel George Zhou Annette S. Lee Avelyn David Jessica Heim Michele E. Lee Verónica Sevilla Naqsh E. Zafar Natalie R. Hinkel Bridgette E. Allen Arthur Berberyan ...	40	Collection of data from various observatories and facilities, processed data to be used for analysis, supervision on project, verified results, assisted in the writing of paper (specifically the specifics of instruments and observatories used other than Minerva-Australis, Conception and steering committees of various telescope facilities and suggested edits to the manuscript.

Author	Percent Contribution	Tasks Performed
Perry Berlind Allyson Bieryla François Bouchy Rafael Brahm Edward M. Bryant Jessie L. Christiansen David R. Ciardi Krystina N. Ciardi Karen A. Collins Jules Dallant Allen B. Davis Matías R. Díaz Courtney D. Dressing Gilbert A. Esquerdo Jan-Vincent Harre Steve B. Howell Jon M. Jenkins Eric L. N. Jensen Matías I. Jones Andrés Jordán David W. Latham Michael B. Lund James McCormac Louise D. Nielsen Jon Otegi Samuel N. Quinn Don J. Radford George R. Ricker Richard P. Schwarz Sara Seager Alexis M. S. Smith Chris Stockdale Thiam-Guan Tan Stéphane Udry Roland Vanderspek Songhu Wang Geof Wingham Joshua N. Winn	40	Collection of data from various observatories and facilities, processed data to be used for analysis, supervision on project, verified results, assisted in the writing of paper (specifically the specifics of instruments and observatories used other than Minerva-Australis, Conception and steering committees of various telescope facilities and suggested edits to the manuscript.

ACKNOWLEDGEMENTS

Don't have to face this on my own
(No) I got my squad with me everywhere I go
(Yeah) you're never ever on your own
(No) no matter where you're at you got fam, never alone.
– Deez Nuts

Never in my wildest dreams would I say that I would be typing these words, wrapping up a PhD in Astrophysics. It seems like I've been climbing this mountain for years, ever since I fell in love with astronomy, waving to Andy Thomas and the rest of the International Space Station within my backyard in the 5108. Growing up in the 5108, I never knew anyone that had even finished high school, let alone complete a PhD; but, here we are! I could not be more grateful for each and every one of you who have not only helped me get to achieve this incredible feat, but have also shaped me into the person that I am today. This has been such a long and fulfilling journey and it would have not been possible without the love and support from the people below.

Firstly, I would like to thank my direct family unit; Mum, Dad, Andrew, Cherie, Nich and Monica for all your love and support. A massive shout-out to Mum and Dad assisting in the 4,400 kilometre journey of driving back to Adelaide from Toowoomba during the pandemic. That trip alone is a memory that I will treasure forever. To my number one lady, Nan, thank you for all of your support and love not only during this PhD but throughout my life. To my little man Björn, your unconditional love got me through the toughest period of my life. Covid world in isolation was incredibly tough, and some don't know just how hard it was. But it was your love and energy that got me through it all. I wish I could tell you this, but belly rubs, "roo" sticks and adventures to the dog park is my way of showing this to you.

Thank you to the Kobs, Williams' and Radcliffe families for taking me under your wings during the last decade and more; including Pete, Cath, Al, Josh, Manf, Tracey, David, Krissie, Madison, Amelia, Alex, John, Loz, Vernice, Kerry and Sam. Thank you Tracy for being my second mum and placing me under your roof during my late-teen years. In particular, thank you to David for giving me a job during my undergraduate, for driving me half way across the country and making sure I was settled in Canberra. You have taught and shown me that persistence and determination alone can push a human through the most intense of life challenges.

To all my fellow students, my academic family that I have learnt off from across multiple institutes... what a journey! A massive thanks to my Adelaide crew including Andrew Malouf, Andrew Spargo, Luke Bowman, Valerie Peters, Rebekah Little, Elyse Purkis, Alex Wallace, Stephanie Pointon, Jason Oliver and Alex Kyriacou. You made undergrad and our honours' year some of the most enjoyable years of my life. A big shout out to Dr. Commendable himself, Nathanial Wilson, for the dark homour and emo beats that got me through this PhD. Thank you to my Questacon Circus and Canberra Crew (Shoutouts to Tyrone, Nate, Nicole, Carly and my FOOTY FOOTY FOOTY crew xo) I miss you all and I hope we can share some #classicclark moments sooner, rather than later. Finally, thank you so much to all the USQ students that I've been immersed around during this journey including Vanessa Crouch, Mathew Mengel, Fraser Border, 裴维, Danny Johns, Alexis Heitzmann, Mathieu Clerté, Nataliea Lowson, Dag Evensberget, Chris Johnson, Dan Peluso, Tim Holt, Belinda Nicholson and James O'Connnor. There is a missing name here. Jack, mate, you're a bloody legend and I am so incredibly grateful for your friendship. Again, through the tough times, it was you who pulled me out of the office, taking me for a walk through the Japanese Gardens or grabbing a feed in town to get me away from it all. I definitely owe you a cocktail or two!

In the same vein, I would like to thank my unofficial PhD supervisor Dr. Carolyn Brown. There is so much I could say here. I had no idea how to use a telescope before living in Toowoomba, let alone write a grant or redesign an entire astronomy course. You are one of my idols, and the way you carry yourself as a lecturer, scientist and more importantly as a human being, is something I will continue to strive towards. You've taught me my self-worth and that it's okay to ask friends for help when you're in need of a hand. I will forever be in

your debt and I can't wait to share a Milton Mango with you and Hippy when I'm back. Speaking of, thanks Hippy for all your support too mate. I've loved our yarns and can't wait to see how the HQ is looking upon my return!

Speaking of supervisors, I am completely indebted to my PhD supervisors for their patience, guidance and allowing me to grow into the scientist I am today. Thank you to my principal supervisor Rob, you've shown me the strength of developing collaborations and the sense of community in our research field. I'll miss you making coffee for me and all the Simpson's references we sling across to one another. Hopefully with some newly found spare time, we'll catch up in the Northern Territory for that Kakadu hike!

Jonti, thank you so much for showing me that all great journeys start off with a single step, and that no mountain can't be climbed without a little bit of planning. I really appreciate the sense of community you bring and can not thank you and Ness enough for all the gaming nights, puppy play-dates and making me feel like Toowoomba was home, right from day one.

Duncan, your patience and guidance to help, no matter the time or day was immensely appreciated during this entire journey. Your calmness and proactiveness in problem solving is something I have learnt from you and will carry with me beyond this PhD.

Brad, your leadership, sense of community and seeing the value and strengths of others around you, has made this journey infinitely better. Thank you for making my PhD journey as smooth as possible. Every time I have Richie Blackmore's Rainbow blaring in the background, I'll be thinking of you!

Finally, Natalie. You are the scientist and human being that I want to become. I can not thank you enough for helping me become a better person and scientist, through my PhD and right now during my Fulbright experience. You've not only brought me into your home, you've taught me how to sell myself as a researcher, how to be a more organised person (... that's still a WIP) and taught me the power of paying it forward. I can't wait to supervise my own students because of you and show them all the tools and lessons you've shown me during this journey! This research has been supported by an Australian Government Research Training Program Scholarship and the University of Southern Queensland's ReD-Train scholarship.

My gratitude also goes out to George and Brett, I've enjoyed our office chats immensely and the guidance you two have given me has been greatly appreciative, thanks legends! I

would also like to thank the GALAH collaboration in allowing me to be a part of their incredible team. I have loved every moment of it and I hope to continue working with the GALAH team and data long after my PhD.

To the numerous friends outside of academia that have helped me along the way, thank you. From my University Cougars Australian Football Club team mates, a big shout out to Kodes, Rhyno, Nige, BT, JT, Mayes, Ev, Linch, Whitey and my Toowomba mum and dad Mike and Rhonda. My Toowoomba and Brisbane fam; Kaitlin, Amanda, Bronte, Josh and Danielle, thank you for all your positive vibes!

Heading back home, Patrick, Scott, Evan and Chey, Thank you for being such incredible friends and keeping me sane throughout this journey. To Mr. MOSH himself, Nicholas, thank you my man for always being a motivator. I can't wait to get back into creating some BRILLIANT radio shows with your beautiful face in the near future. My favourite ginger-bearded man, Boyd, thank you so much for your words, friendship and getting me through all of this with rad tunes and excellent array of fresh memes *chef kisses*. Aaron, my brother from another mother, what can I say. You've had my back since high school and have always supported me no matter where I wanted to go. You're someone who I can always depend upon when things get rough, and I can't thank you enough for keeping me going through some of the toughest moments through all this. And Ben. MATE! I could not be the person I am today without your friendship. Again, you got me through the toughest parts of this. I won't forget the countless hours we played No Man's Sky, and had an avenue to chat about my concerns and woes about my PhD and life in general. You are an amazing friend and I can't wait to see you on the big screen brother!

From the start of this journey, being taken in by Phil and Claire (thank you!) to now writing these words in Knoxville, Tennessee (thanks Marissa and Andrew), I have been super grateful to have an entire army of supporters behind me, waving my flag. None bigger right now than you, Kaitlyn. Thank you for showing me that beauty, kindness and love is within us all.

Finally, I dedicate this thesis to everyone who have lost their battle with their own mental health. You are never alone. SK Forever!

TABLE OF CONTENTS

LIST OF FIGURES

(Excluding publications included in Chapters 2-4)

I can see the light at the end of the road
We're just stardust, and I'm going home.

– Behind Crimson Eyes

1

INTRODUCTION

Since the dawn of humankind, we have scaled treacherous mountains, trekked through rolling plains and sailed across boundless oceans to answer one simple question; are we alone? All of these activities were conducted on just one blue marble, known as planet Earth. In the late 19th Century, Italian astronomer Giovanni Schiaparelli drew humankind's attention to one of our nearest neighbours, Mars, showcasing to the world one of the first ever maps of the Martian surface. This map showed off "seas" and "continents" across the red planet, postulating the possible existence of life, thus were born the Martians. We now know the Martian surface is barren, where permanent liquid water can not exist, as water ice will sublimate to water vapour on its dusty surface due to its surface pressure and temperature.

Life might exist within our own Solar system, with Jovian and Saturnian moons

harbouring oceans that may contain microbial life, to the detection of potential biomarkers within the atmosphere of Venus (Shapiro & Schulze-Makuch, 2009; Greaves et al., 2021). In the last thirty years, focus for life elsewhere has been centred around discovering and charcterising planets beyond our Solar system, objects known as exoplanets. The first detected planets orbiting other stars came in the late 1980s, with the disccovery of planet-mass objects orbiting the stars Gamma Cephei A (Lawton & Wright, 1989) and HD 114762 (Latham et al., 1989). However both objects had to wait years before having their planetary status either confirmed, or in the case of HD 114762 b, being promoted to a red dwarf (Kiefer, 2019). The first confirmed discovery of a planetary system came from the pulsar PSR B1257+12 (Wolszczan, 1994). By measuring slight variations in its pulses, three exoplanets were uncovered orbiting a neutron star, and thus starting the "Exoplanet Era" of astronomical sciences.

In 2019, astronomers Michel Mayor and Didier Queloz were jointly awarded the Nobel Prize in Physics for "the discovery of an exoplanet orbiting a solar-type star", this being 51-Pegasi b (Mayor & Queloz, 1995). The first exoplanets being discovered were typically Jupiter-massed planets with orbital periods of a few days, as these planets induced large radial velocity signals (which is discussed in more detail in Section 1.1) upon their stars, making them the easiest planets to detect at the time. Into the 21st century, the exoplanet community continued to discover a vast number of Jupiter-sized planets orbiting incredibly close to their host stars, known as hot Jupiters (e.g. Fischer et al., 2008; Vogt et al., 2010; Lovis et al., 2011; Wittenmyer et al., 2014; Endl et al., 2016). To this day the origin and evolution of such unconventional and mysterious worlds is still an active field of exoplanetary research (Hands & Helled, 2022; Addison et al., 2021). However, as instruments and methodologies improved surrounding the radial velocity technique, our sensitivity towards detecting planets with smaller masses and planets with longer orbital periods also increased.

In parallel to the advances in the radial velocity technique, came along a new and novel method to finding exoplanets, known as transit photometry. This method (ex-

plained in greater detail in Section 1.1) detects exoplanets by the shadows they cast whilst passing between us and their host, decreasing the amount of stellar flux, as seen in our line-of-sight. Currently, this is by far the most successful method in detecting outside worlds, with 76% of all known exoplanets being found with transit photometry [1]. This second great revolution shifted the exoplanetary paradigm thanks largely to NASA's *Kepler* and K2 missions (Borucki et al., 2010; Koch et al., 2010). The *Kepler* space telescope was one of the first space-based missions dedicated to the discovery of exoplanets, peering into a 115 square degree patch of the sky between the Cygnus and Lyra constellations. Launched in 2009, this single mission successfully uncovered 53% of all known exoplanets at the time of writing. But, due to the malfunction of two reactor wheels in 2013, the mission had to deviate from a single patch of sky, to several campaigns across the ecliptic, known as Kepler's "Second Light". Due to the better sensitivity of both space-based missions and ground-based technology, our understanding about planetary systems and architectures also changed. This is illustrated by diverse discoveries like multi-planet systems (Gillon et al., 2017; Shallue & Vanderburg, 2018), planets in extremely eccentric orbits (Naef, D. et al., 2001; Wittenmyer et al., 2017) and carbon-rich worlds (Hebb et al., 2009; Madhusudhan et al., 2012) to name a few.

The statistics of known planetary systems also changed during this era, with discoveries from the *Kepler* and K2 missions showcasing a new class of planets dominating our galaxy. Not seen within our own Solar system, exoplanets significantly larger than Earth, $> 1R_{\oplus}$, yet smaller than Neptune, $< 4R_{\oplus}$, are now thought to be one of the most common types of planets within our galaxy (Batalha et al., 2013). This planetary realm is divided into two sub-categories; rocky, terrestrial Super-Earths, and gassy, icy Sub-Neptunes. Since there are no planets of this type within the Solar system, fundamental questions arise; What fraction of super-Earths are scaled up terrestrial worlds? What fraction are scaled down ice giants worlds? What fraction of these planets are

[1] As of December 31 2021, the exoplanetary community has discovered 4,858 planets in 3,660 planetary systems as per NASA's Exoplanet Archive

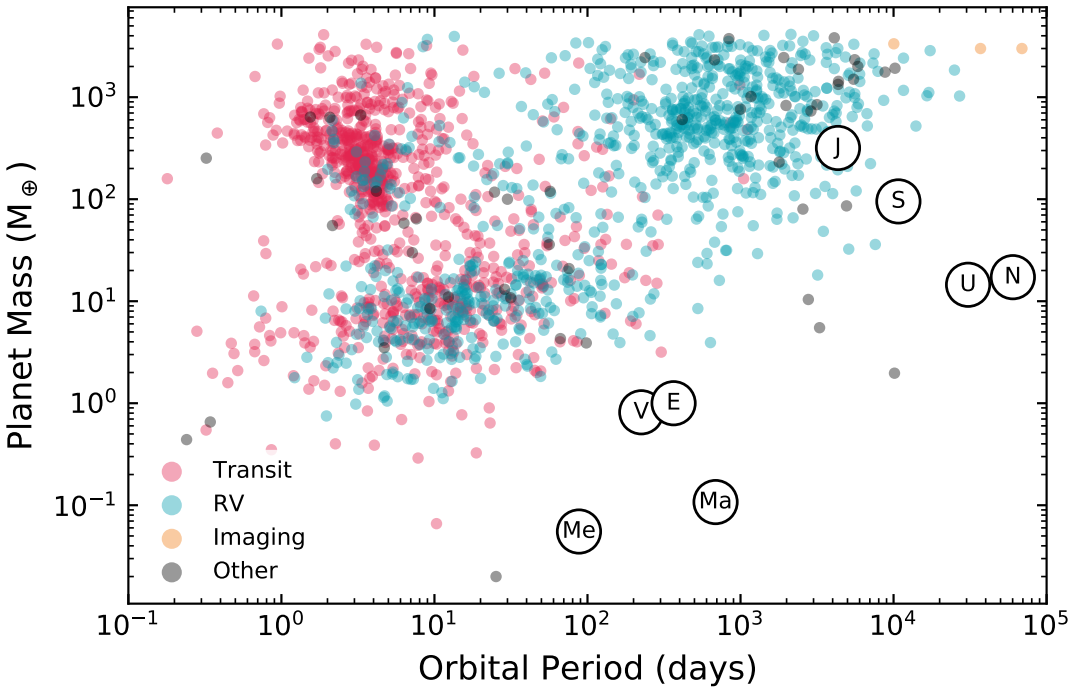

Figure 1.1: All exoplanets with known mass measurements are plotted in this figure, coloured by the detection method used to discover them. The eight planets found within the Solar system are shown in this figure for comparison. Data was collected from NASA's Exoplanet Archive.

evaporated cores of larger, gassier worlds? Or are these planets made from something else entirely? These questions are motivating astronomers to better probe the geological and chemical compositions of exoplanets within this size regime.

1.1 Exoplanetary Detection

Even though the first exoplanets discovered were through the pulsar timing variations, only seven of the 4,800+ planets found thus far have been found through this technique. There are five main methods to detect exoplanets, these being transit photometry, Doppler spectroscopy, direct imaging, microlensing and astrometry. As this thesis focuses on both transit photometry and Doppler spectroscopy, also known as the radial velocity technique, these methods will be covered in greater detail below. How-

ever, the avid reader is encouraged to read more about the fore mentioned detection methods (astrometry, microlensing & direct imaging; Perryman et al., 2014; Tsapras, 2018; Brooks et al., 2015).

1.1.1 Transit Photometry Method

To date, almost 80% of all exoplanets have been detected using the transit photometry technique, making it the most successful exoplanetary detection method thus far. Planets detected by the transit photometry method are discovered by periodic decreases in the relative host star brightness, as the exoplanet transits across the stellar disk from our observational perspective. To confirm an exoplanetary signal detection, especially in multi-planet systems, a minimum of three transit events are needed - neglecting noise and false-positives (although candidates can be confirmed using false-positive probabilities Morton et al., 2016).

An exoplanet's radius, R_p, can be extracted from the stellar flux decrease, ΔF, as:

$$R_p = R_* \sqrt{\frac{\Delta F}{F}} \tag{1.1}$$

where F is the stellar flux and R_* is the stellar radius. As shown by Equation 1.1, an exoplanet's radius is proportional to the change of stellar flux observed in the light curve. Thus, a larger planet will result in a larger change in stellar flux and visa versa. In the same context, it is much easier to find smaller exoplanets around smaller stars. For example, an Earth-sized planet would change the flux of a typical M dwarf star ($\sim$ $R_* = 0.4$ $R_\odot$) by 520 ppm. In contrast to this, the same sized exoplanet will only change an A star host's flux ($\sim$ $R_* = 2.5$ $R_\odot$) by 13 ppm. To put that into perspective, there is only one exoplanet candidate discovered with a transit depth less than 13 ppm, that being Kepler-37 b with a transit depth of 12 ppm (Barclay et al., 2013).

Not only can a light curve provide information that allows the determination of

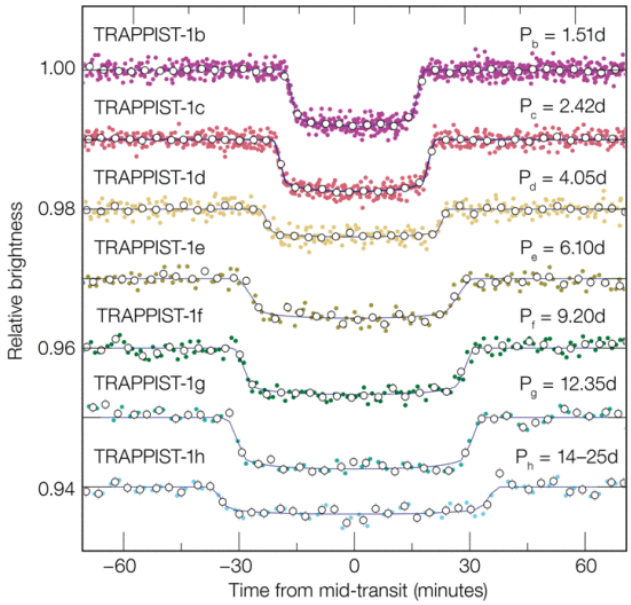

Figure 1.2: Period-folded transit photometry measurements of TRAPPIST-1, currently known to host at least seven terrestrial worlds, reproduced from (Gillon et al., 2017). The total transit duration t_T, for TRAPPIST-1h (aqua line) is around 80 minutes (time duration when the stellar flux is below the normalised value), compared with the transit duration between ingress and egress t_F, of around 60 minutes (length of the flat bottom).

an exoplanet's radius, they can also provide information about the planet's orbital period, semi-major axis and orbital inclination. Transit photometry can also potentially measure the mass of exoplanets through transit timing variations. As mentioned previously, the *Kepler* spacecraft shifted the paradigm of detecting exoplanets, with its wealth of discoveries using the transit photometry method. However, as it now spirals uncontrollably behind planet Earth, its successor has continued its legacy, uncovering more planet candidates than ever before.

1.1.2 *TESS* - NASA's *Transiting Exoplanet Survey Satellite*

On April 18 2018, Space X's Falcon 9 rocket launched from Cape Canaveral Florida, carrying a payload that is predicted to revolutionise exoplanetary research, the *Transiting Exoplanet Survey Satellite TESS* (Ricker et al., 2014). *TESS* is a NASA Astrophysics Explorer mission and is the first, space-based, all-sky planet hunter. *TESS* has been monitoring roughly 200,000 target stars with spectral types from F5 to M5,

monitored across both ecliptic hemispheres for its primary two-year mission (a year-long survey for each hemisphere) (Ricker et al., 2014). Each ecliptic hemisphere is divided into 13 observational sectors, spanning a 24° by 96° field-of-view, spanning a declination range of ±6° to ±90° (positive for Northern hemisphere and negative for southern hemisphere). There is then a significant overlap across the ecliptic poles, giving continuous coverage to search for long-period planets, this is known as the continuous viewing zone. Each observational sector is monitored for 27.4 days, watching over the pre-selected stars, which have all been designated catalogue identifiers created by the *TESS* Input Catalogue (TIC) (Stassun et al., 2018). There were then hand-selected stars using algorithms based upon the *TESS* mission's primary science requirements and were observed with 2-minute cadence, catalogued within a subsection of the TIC known as the Candidate Target List. Stars not found within the Candidate Target List were observed with a 30-minute cadence, yielding results on over two million background stars. *TESS* completed its primary mission on 11th August 2020 and has now commenced a secondary mission to revisit both hemispheres as well as the ecliptic plane.

In each sector, potential candidates, known as *TESS* Objects of Interest (TOIs) are found through two pipelines, the Quick-Look Pipeline (Huang et al., 2020) and the *TESS* Science Processing Operations Center pipeline (Jenkins et al., 2016). These two independent teams feed TOIs into the community to be followed up by space and ground-based facilities. There are five separate science working groups who get notified of potential candidates, these being named from Science Group 1 – 5. SG1 through to SG5 follow up potential exoplanets by seeing-limited photometry (SG1), reconnaissance spectroscopy to rule out false positives in spectra and bad stellar hosts to follow up (i.e rapidly rotating stars) (SG2), high-resolution imaging with adaptive optics to rule out nearby stars (SG3), precise radial velocity groups to derive the planetary properties of the exoplanet (SG4) and space-based photometry to confirm and/or improve the photometric ephemerides provided by TESS[2] (SG5). These teams set the

[2]https://tess.mit.edu/followup/

dynamical disposition of *TESS* candidates from a confirmed exoplanet all the way to being a false positive, aiming to fulfil the scientific requirements of the *TESS* mission.

The three primary scientific mission requirements for *TESS* are:

1. Searching over 200,000 stars to discover planets with periods <10 days and radii <2.5 Earth radii orbiting the brightest stars in the solar neighbourhood, and discovering planets with radii smaller than 2.5 Earth radii distributed across the celestial sphere.

2. Search for transiting planets with periods up to 120 days among the 10,000 stars in regions surrounding the ecliptic poles.

3. Determine the masses for at least 50 planets with radii <4 Earth radii.

Several simulations of the exoplanetary yield outcomes of *TESS* have been produced including Sullivan et al. (2015) and Barclay et al. (2018). Sullivan et al. (2015) proposed *TESS* will discover 20,000 planets over the entirety of its lifetime (1,700 from CTLs and the rest from full-frame images), with over 900 and 4,000 being super-Earths and sub-Neptunes respectively. The peak orbital-period and planetary radii for Sullivan's simulations nears 7 days and 2.5 radii. Barclay et al. (2018) simulated yield suggested a more conservative total, with 1,300 planets discovered around TICs and 4,500 discovered around the full frame stars. At the time of writing, the *TESS* mission has confirmed 77 exoplanets with 4,708 TOIs and 1,695 Community TOIS (CTOIs) awaiting confirmation. These numbers are more favourable to those predicted by Barclay et al. (2018) but far outweigh the number of candidates the *Kepler* mission sought out within its nine year lifetime. Regardless of the final tally of exoplanets simulated or confirmed to be discovered by the *TESS* mission, there will be plenty of candidates to be confirmed by both transit photometry from *TESS* and radial velocity measurements from the ground.

1.1.3 Radial Velocity / Doppler Spectroscopy Technique

Radial velocity (RV) or Doppler spectroscopy method is a robust technique used in detecting exoplanets. The radial velocity describes the projected motion, along Earth's line-of-sight, of the star as it orbits the planetary system's barycentre, due to the presence of an exoplanet. This periodical velocity shift is obtained by viewing a wavelength shift in a star's spectral lines. This shift $\Delta\lambda$ from the resting spectral line wavelength λ_0 can be translated to a velocity, v, by $v = c\frac{\Delta\lambda}{\lambda_0}$ where c is the speed of light in a vacuum. Celestial mechanics can show the modelled RV of a star orbiting around its barycentre, along our line-of-sight to be:

$$\nu_{rv}(t) = K\big[\cos(\omega + \nu) + e\cos(\omega)\big] + \gamma \tag{1.2}$$

where K is the semi amplitude, ω is the argument of periapsis, ν is the orbit's true anomaly, i is the orbital inclination, e is the eccentricity of the orbit, and γ incorporates offsets, linear trends, and noise terms (Perryman, 2018). The time of pericenter passage, t_p, is a parameter within ν that is usually solved for in RV exoplanetary detections. The RV's semi-amplitude can be defined by:

$$K = \left(\frac{2\pi G}{P}\right)^{-\frac{1}{3}} \frac{M_p \sin i}{(M_* + M_p)^{\frac{2}{3}}} \frac{1}{\sqrt{1-e^2}} \tag{1.3}$$

where G is the gravitational constant, P is the orbital period, M_p is the exoplanetary mass, M_* is the stellar mass and e is the orbital eccentricity. M_p and M_* can be converted to Earth masses, $M_\oplus$, and Sol masses, $M_\odot$ respectively. Assuming $M_p \ll M_*$ Fischer et al. (2014) equation 1.3 can be rearranged to discover $M_p \sin i$:

$$\frac{M_p \sin i}{M_\oplus} = \frac{\sqrt{1-e^2}}{K \cdot 0.0895 ms^{-1}} \left(\frac{M_*}{M_\odot}\right)^{\frac{2}{3}} \left(\frac{P}{\text{Years}}\right)^{\frac{1}{3}} \tag{1.4}$$

noting that, $M_p \sin(i)$ is the minimum mass of the exoplanet as the orbital inclination, i, can not be determined through RV measurements. However, the orbital inclination can be determined through transit photometry. Dedicated observatories, such

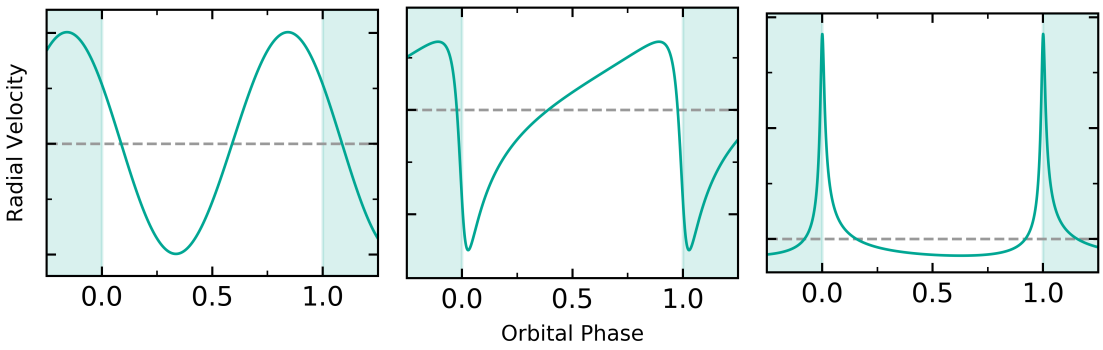

Figure 1.3: Radial velocity curves can vary quite dramatically in shape and size. From left to right, the orbital phase of the radial velocity curves for Pegasi 51b ($e = 0.013$, $\omega = 58°$ (Mayor & Queloz, 1995)), HD 17156b ($e = 0.67$, $\omega = 122°$ (Fischer et al., 2007)) and HD 76920b ($e = 0.86$, $\omega = 353°$ (Wittenmyer et al., 2017)).

as Minerva-Australis, are assisting in the *TESS* mission, confirming the planetary nature of exoplanetary candidates discovered by the telescope.

Minerva-Australis is the only telescope array in the southern hemisphere solely dedicated to RV follow-up of *TESS* candidates. Minerva-Australis is the southern counterpart to the MINERVA-North telescope array on Mount Hopkins, Arizona (Swift et al., 2015) and is a robotic facility based at the Mount Kent Observatory (-27.80°, 151.86°), 25 Km SSW of Toowoomba, Queensland (Addison et al., 2019). Minerva-Australis has four 0.7 m corrected Dall-Kirkham PlaneWave CDK-700s, with an effective aperture of 1.4 m. At the time of writing, Minerva-Australis has assisted in the discovery of over 20 planetary systems with the *TESS* mission, ranging from planets from young systems to planets around evolved stars. One particular discovery assisted by Minerva-Australis was the three exoplanet, planetary system known as HR 858 (Vanderburg et al., 2019). What's interesting about this particular system is that all three exoplanets have radii that's consistent with being either super-Earths or sub-Neptunes. The combined masses of all three was constrained to being about 45 $M_\oplus$, with a wide range of possible masses and compositions for the planet's within this system. Thus it is important to better understand the mass, radius and compositions of planets around this regime.

1.2 Current Types of Exoplanets under 4 Earth Radii

Aside from Jupiter and Saturn, every planet within the Solar system is below $4R_{\oplus}$. The Solar system, however, contains no known planets with radii above $1R_{\oplus}$ and less than $3.8R_{\oplus}$, with Earth being the largest terrestrial planet in the Solar system and Neptune being the smallest gaseous planet. Mass-radius relationships for exoplanets have been developed for planets below this regime (Weiss & Marcy, 2014), but as Figure 1.4 depicts, these relationships fail to account for the extreme diversity of exoplanets with a sweeping range of densities, especially above $4M_{\oplus}$, demonstrating the stochastic nature of planet formation (Seager, 2013).

1.2.1 Terrestrial "Super-Earths"

In August 2004, 55 Cancri was announced to have a planet with a minimum mass of $8.6M_{\oplus}$ orbiting around the carbon-rich star (McArthur et al., 2004). This discovery unearthed a new class of planet, the super-Earth. The super-Earth definition is under contention, but the most accepted definition being a planet within the mass range of $1.25 \leq M_{\oplus} \leq 10$ (Borucki et al., 2011) composed predominately of Si, Mg, Fe and O. If the host-star's C/O molar ratio (explained in more detail in Section 1.4) is greater than 0.8, planetary simulations suggest carbon-dominated terrestrial worlds (Carter-Bond et al., 2012) including 55 Cancri e (Dawson & Fabrycky, 2010). Above 10 Earth masses, theories suggest solid protoplanetary cores are expected to retain a gaseous atmosphere (Duffy et al., 2015). Terrestrial "mega-Earths", worlds above $10M_{\oplus}$ have been discovered (Espinoza et al., 2016), challenging the mass constraint on the super-Earth definition. Several studies suggest terrestrial worlds gain a significant atmospheric envelope near 1.5 - 1.75 Earth radii (Rogers, 2015; Fulton et al., 2018) setting an upper-limit for the transition from super-Earth to sub-Neptune worlds. Commonly, exoplanets with planetary radii dominated by their solid layers are referred to as super-Earths. As in situ observations are limited with current technology, theoretical models are needed to determine if the planet's radius is dominated by a solid rocky layer (super-Earth) or by a gaseous envelope (sub-Neptune).

Most super-Earths have been discovered around low-mass stars, currently due to observational biases, as shown in equation 1.2. Some of these super-Earths orbiting around M-dwarfs might even be tidally locked, and as a consequence, their atmospheres may undergo atmospheric collapse, if no mechanism exists for the atmosphere to circulate the heat (Tasker et al., 2017). The day-time surfaces of most close-in super-Earths reach well into the melting point of silicate rock, promoting surface magma oceans (Dorn et al., 2018a). These magma worlds could display extensive degassing of the planet's interior, including stagnant-lid super-Earths (Dorn et al., 2018b), producing theorised silicon atmospheres (Schaefer & Fegley, 2009; Duffy et al., 2015; Kislyakova et al., 2017), with greenhouse gasses. Interestingly, an Earth-like atmosphere would be easier to detect than that of a Venusian atmosphere (Barstow et al., 2016). Atmospheric outgassing, plate tectonics and capacity to generate an internal magnetic field is influenced by the interior mineralogy (Duffy et al., 2015) and are important factors whilst considering the habitability of super-Earths (Horner & Jones, 2010; Seager, 2013; Noack et al., 2014). Planetary diversity of super-Earths is varied beyond magma worlds (Valencia et al., 2007), including theorised worlds harbouring global oceans (Léger et al., 2004) and dense leftover cores of giant planets (Mocquet et al., 2014).

1.2.2 sub-Neptunes and Ice Giants

Sub-Neptunes (also known as mini-Neptunes) seem to be the most populous planet within our galaxy (Batalha et al., 2013) and are super-Earths with their planetary radii dominated by volatile layers. This transition occurs near 1.5-1.75 Earth radii (Lopez & Fortney, 2014; Rogers, 2015; Fulton et al., 2018) with the planets theorised to have ice-giant like compositions similar to Uranus (14.5 $M_{\oplus}$,4.0 $R_{\oplus}$) and Neptune (17.1 $M_{\oplus}$,3.9 $R_{\oplus}$). Ice-giants like Uranus and Neptune are modelled as a three layer planet consisting of; a rocky core, an "icy" shell (H_2O,CH_4 etc.) and a gaseous envelope of molecular hydrogen, helium and highly enriched heavier elements (Helled & Guillot, 2018). Scientific data on ice-giant interiors is scarce, with NASA's Voy-

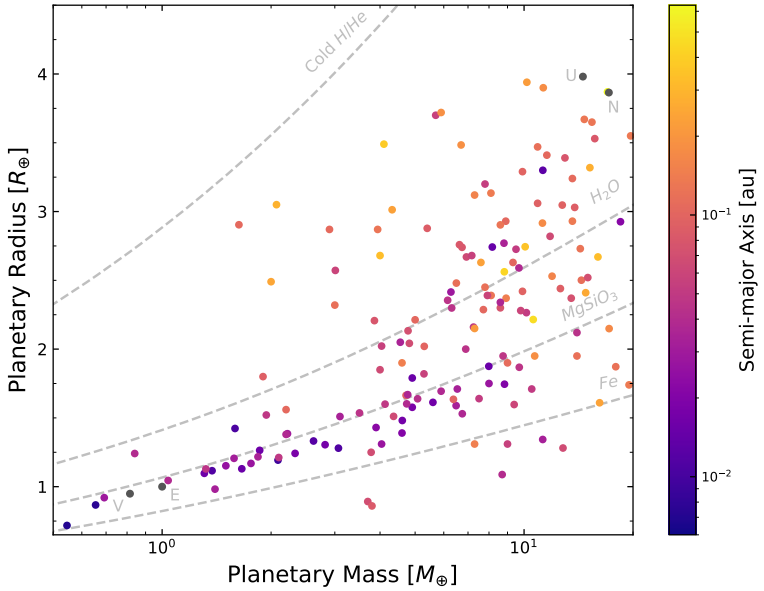

Figure 1.4: Mass-Radius relationship for all known exoplanets with mass and radius measurements below 4 Earth radii. Venus, Earth, Uranus and Neptune are shown for reference. Error bars have been suppressed for clarity. Dashed lines represent planets consisting of solid iron (*Fe*), rock ($MgSiO_3$), water (H_20) and cold Helium/Hydrogen (Cold H/He). Most super-Earths discovered have semi-major axes much less than 1 AU. (Zeng et al., 2016)

ager 2 spacecraft being the only probe to flyby both planets in the late 80s. However, what is known, is the internal structure of Neptune and Uranus are quite different and could demonstrate the diversity of ice-giant and sub-Neptune exoplanets (Spiegel et al., 2014).

Mass–radius relationships show the mass ratio of an ice-giant's envelope to its bulk mass, will be under 30% for planets under $4R_\oplus$ (Venturini & Helled, 2017), with most simulations demonstrating the planetary mass will be dominated by a deep fluid ionic ocean (Spiegel et al., 2014; Helled et al., 2011). Empirical models of Uranus and Neptune suggest a gradual increase in interior density towards the planetary centre (Helled & Guillot, 2018). This is strikingly different to terrestrial worlds that have sharp internal boundaries. These non-adiabatic interior structures can also retard the internal convection and transport of heat inside these worlds (Helled & Guillot, 2018). Such an interior could explain Uranus' heat flux being 90% smaller than that of Neptune.

1.3 Modelling and Categorising a Super-Earth Interior

The characterisation of exoplanetary interiors is crucial to understanding the planetary diversity within our galaxy, assisting in planet formation models and further determining how unique Earth is. As previously mentioned, there's a distribution of planet masses for a given planetary radius (Rogers, 2015), and hence interiors of exoplanets under four Earth radii will also be richly diverse.

The interior structure is obtained by solving a set of coupled differential equations for mass, pressure and density using equations for hydrostatic equilibrium and equations of sate for different planetary material. To a first-order approximation, scaling laws from Mass-Radius relationships (Valencia et al., 2006; Grasset et al., 2009) and Preliminary Reference Earth Models (Zeng et al., 2016; Zeng & Jacobsen, 2017) plotted on a Mass-Radius diagram give reasonable characteristics of a super-Earth, as shown in Figure 1.4. Simulated thermal and rigidity models for discovered super-Earths have also been produced (Wagner et al., 2012; Barr et al., 2018; Kellermann et al., 2018) to constrain the core, mantle and volatile layers within. Ternary diagrams, example of which in Figure 1.5, have also been used with stellar abundances to constrain super-Earth interiors (Brugger et al., 2017).

Rogers & Seager (2010) introduced the concept of equipping grid-based Bayesian techniques to quantify the degenerices of super-Earth interiors, through quaternary diagrams (a three dimensional ternary diagram similar to that in 1.5). The grid search method however uses strong priori assumptions on structure and composition to significantly reduce the composition parameter space.

A fundamental problem with inferring planetary compositions through mass-radius or ternary/quaternary diagrams is that they cannot uniquely predict the interior composition of a given planet. A variety of different interior compositions can lead to identical mass and radius values. This gives rise to the inherent density degeneracy

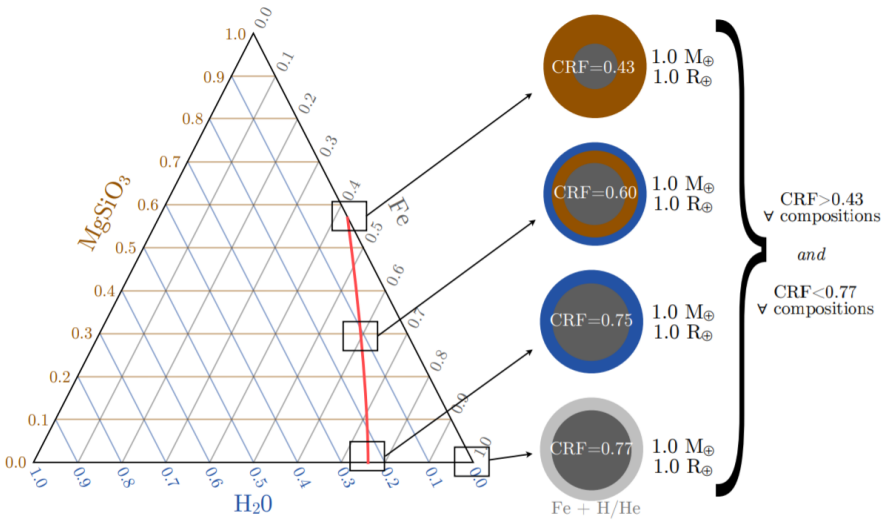

Figure 1.5: A ternary diagram of a three-layer interior structure model for a solid planet. All points along the red line lead to an Earth sized and mass planet. Reproduced from (Suissa et al., 2018).

problem. There's a wide variety of planetary compositions allowed, especially if the models used have three or more layers. This is typical for most that assume a three (core, mantle, ocean) or four layered planet (core, mantle, ocean, atmosphere). Models such as Dorn et al. (2015, 2017); Unterborn et al. (2018) break down this degeneracy, using stellar abundances to infer exoplanetary compositions.

Bond et al. (2010b) demonstrated the relative elemental abundances for Fe, Mg and Si are similar among the Sun, Earth, Mars, Moon and meteorites and also discovered through planet formation models that the planetary bulk and stellar ratios of Fe/Si and Mg/Si are very similar as Fe, Mg and Si all condense at similar temperatures. The elemental ratios for Fe/Si and Mg/Si are similar in exoplanets and the stars that host them (Thiabaud et al., 2015). Thus we then equate the stellar abundance ratio of planet-hosting stars of these elements to their planets, to better model the planet's interior structure.

Parameters derived from models such as Dorn et al. (2017) and Unterborn et al. (2018) include the mantle composition, core size and ocean layers through using the

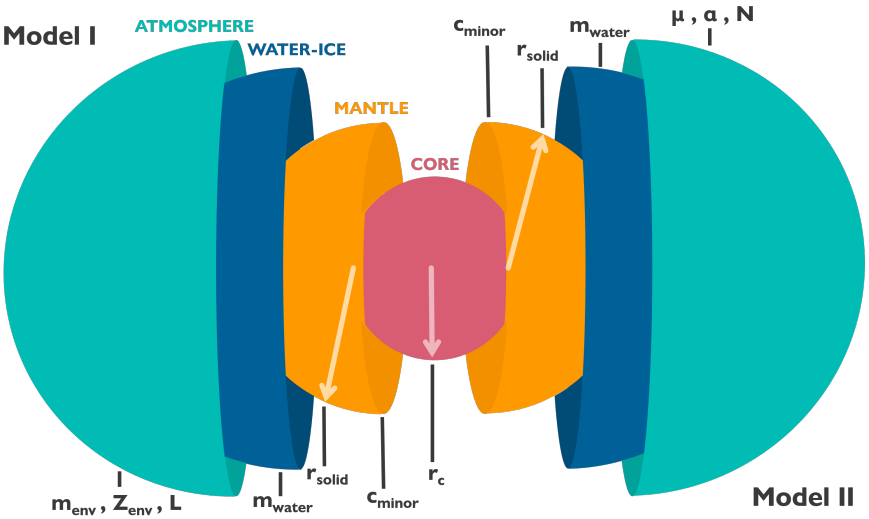

Figure 1.6: Dorn's generalised exoplanetary model for super-Earth and sub-Neptune interiors (Dorn et al., 2017) incorporating a four layer model. These four layers consist of an iron core, rocky mantle, water-ice and an atmospheric layer. Each layer consists of unique model parameters.

stellar abundance ratios, also known as molar ratios, of certain refractory elements. Refractory elements, elements with high melting and condensation temperatures, used within this models are iron, silicon, magnesium, sodium, calcium, aluminium among others. The three commonly used elements within these models are iron, magnesium and silicon. The Fe/Si ratio will dictate the core size of a rocky world, with the Mg/Si elemental ratio controlling the relative abundance of major silicates such as pyroxenes (Mg/Si=1) and olivine (Mg/Si=2) (Duffy et al., 2015) within an exoplanet's mantle. A second order approximation of a planet's mantle composition can be derived with knowledge about the host star's calcium and aluminium stellar abundances (Dorn et al., 2017). In addition to all this, the magnesium number, $Mg_{\#}$, determines the iron content of in the silicate material, where the Mg# is determined by:

$$Mg_{\#} = \left(\frac{Mg}{Mg+Fe} \right)_{silicates} \tag{1.5}$$

With known values of Earth's and Mars' magnesium number to be 0.9 and 0.7 respectively (Sotin et al., 2007; Grasset et al., 2009). However, all this information above,

including the stellar abundances, planetary mass, radius etc. are all derived by the properties of the host stars. Thus to know thy planet, we need to know thy star.

1.4 How do we characterise stars?

It is often said in the field of exoplanetary science that 'know thy star, know thy planet'. Meaning in order to better understand and characterise the exoplanets across the Galaxy, we also need to better understand the fundamental characteristics of the stars that host them.

Stars can be classified in various ways, with the most straightforward classification coming from placing a star upon a Hertzsprung-Russell diagram. One can potentially infer the properties of a star upon this diagram, but more sophisticated methodologies are needed to derive the astrophysical parameters of a star. Fundamental properties of a stellar atmosphere, including its effective temperature (T_{eff}) surface gravity ($\log g$) and overall metallicity ([M/H]) are typically determined through the star's spectrum. Absorption features of different elements are imprinted on a star's spectrum, with the shape, width and depth of these lines being effected by a star's T_{eff}, $\log g$ and abundance of different elements (Smalley, 2005; Catanzaro, 2014). Once these parameters are determined, stellar models such as isochrone modelling and spectral energy distributions can then be employed to then determine the stellar mass, radius and age of the star. Isochrones are curves on the Hertzsprung-Russell diagram that represent a population of stars of the same metallicity and age, but with different masses. Where a star lies on a Hertzsprung-Russell diagram will then place constraints on its mass, radius, age etc. which can be modelled with different isochrones (Demarque et al., 2004; Choi et al., 2016).

Abundances of elements can also be modelled through a stellar spectrum and are typically normalised to 10^{12} atoms of hydrogen. The abundance in the element X is given by:

$$[X] \equiv \left[\frac{X}{H}\right] = \log\left(\frac{n_X}{n_H}\right)_* - \log\left(\frac{n_X}{n_H}\right)_\odot \tag{1.6}$$

where n_X and n_H are the number of nuclei of element X and hydrogen respectively, per unit volume in the stellar photosphere. The elemental abundance ratio, of element X to element Y in a star * is defined to be:

$$\left(\frac{X}{Y}\right)_* = 10^{([X]+X_\odot)-([Y]+Y_\odot)} \tag{1.7}$$

where $X_\odot$ and $Y_\odot$ are the Solar normalisation values for elements X and Y. There are numerous solar normalisations to use, with the most popular within planetary science being Lodders et al. (2009).

Since the first discoveries of exoplanets in the late 20th century, astronomers have been trying to determine if there is a link between planetary architectures and/or demographics and the physical and/or chemical properties of the exoplanet's host star. The first such link between planet types and chemical abundances was the discovery of hot Jupiters tending to favour iron-rich host stars (Santos et al., 2001; Fischer & Valenti, 2005; Gonzalez, 1997; Bond et al., 2006). This trend has, however, weakened in more recent studies (Osborn & Bayliss, 2020; Teske et al., 2019) showing a more tenuous link than once predicted. Similarly, the relationship between a star's iron abundance and the number of planets it hosts remains the subject of significant debate (e.g. Petigura et al., 2018; Adibekyan et al., 2017; Bond et al., 2008; Bond et al., 2010a) with no clear consensus within the astronomical community.

Other such trends have also been discovered, with Adibekyan et al. (2012, 2015) showing that there is an overabundance of alpha-elements in short-period exoplanet hosts, in particular Neptune and super-Earth sized exoplanets, compared to stars hosting larger planets. Winn et al. (2017) has also showed through iron abundances of planet hosts, that there was a population difference between hot Jupiter's and their ultra short period counterparts, concluding that ultra-short period, rocky planets might

not necessarily be remnants of hot Jovian cores. Further, Dai et al. (2019) also argued that short-period rocky worlds are more than likely exposed rocky cores of sub-Neptunes, rather than hot Jupiters. Per the discovery of the short-period planet TOI-1444b, Dai et al. (2021) showed that hot Neptunes tended to favour iron-rich stars, compared to their rockier counterparts. All of the above shows that the link between the chemical abundance of a stellar host, and the types of exoplanets they host, is a complex one, and will still be a very active area of astronomical research for many years to come.

1.5 Large Stellar Surveys

Huge space and ground-based surveys are now scouring the entire sky, mapping out stellar abundances, alongside of the physical and astrometric properties for millions of stars across the Milky Way. The history of modern stellar surveys started in the late 19th Century with the Henry Draper Catalogue. Pioneered by the Harvard Computers, this catalogue was the first to classify stars by their spectra, in particular cataloguing the stars by the strength of their hydrogen absorption lines. Fast forward a hundred years and the advancement of stellar surveys have extended from ground-based surveys into space, characterising stars within the Milky Way like never before.

The European Space Agency's *Gaia* telescope has been the most ambitious stellar survey to date, collecting astrometric data for over 1.8 billion stars since its science operations started back in 2014 (Gaia Collaboration et al., 2018, 2021). It has been collecting information on the parallax, distance, space velocities, magnitudes and other physical quantities (including effective temperature and stellar radius) to better determine the fundamental properties of stars within the Galaxy. In parallel to the *Gaia* mission, large ground-based surveys have been collecting the physical and chemical properties for millions of stars. These surveys include LAMOST (Cui et al., 2012), RAVE (Steinmetz et al., 2006), APOGEE (Majewski et al., 2017) and GALAH (Martell et al., 2016; Buder et al., 2018, 2021) to name a few.

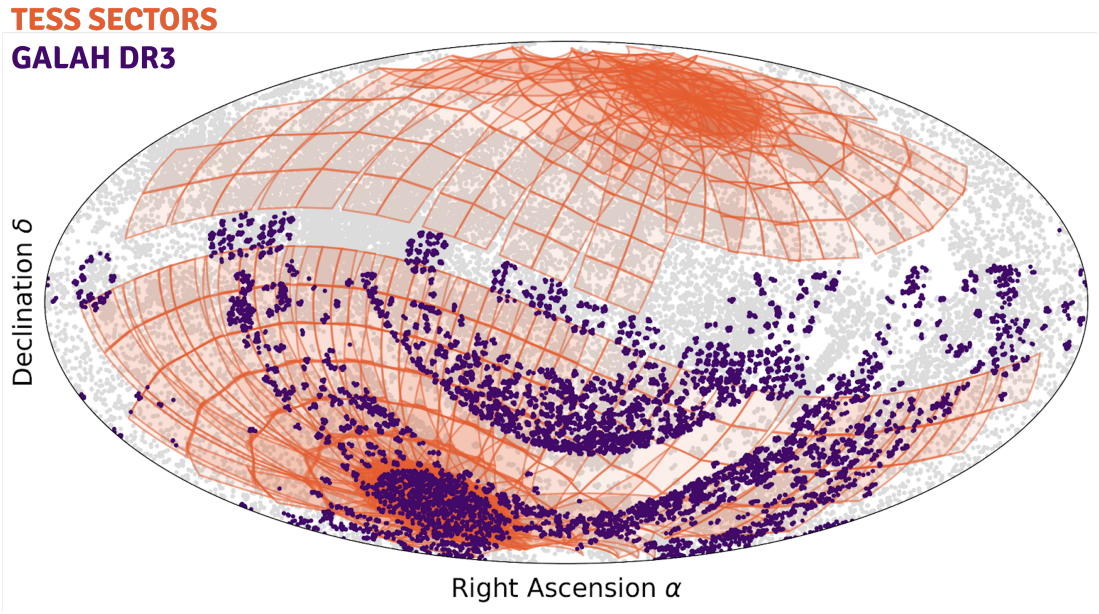

Figure 1.7: The overlap between the third data release of GALAH (stars in purple dots) with the *TESS* sectors (in orange). Each grey dot in the background is a star that's been observed by other large-stellar surveys including LAMOST, RAVE and APOGEE.

Just like most of the mentioned stellar surveys, the southern hemisphere's largest spectroscopic stellar abundance survey – the Galactic Archaeology with HERMES (GALAH) survey – was formulated and designed to investigate the stellar formation and chemical enrichment history of the Milky Way galaxy (De Silva et al., 2015; Martell et al., 2016; Buder et al., 2018). The GALAH survey has collected high-resolution spectra for more than 600,000 stars, from which the abundances of up to 23 elements can be determined for each individual star. However, GALAH's main focus is looking at the overall picture of our galaxy and the stars contained within it. What if you could use the information from large scale surveys such as GALAH and *Gaia* to not only better understand the stars contained within the Milky Way, but also the exoplanets these stars host? What could we learn with such rich data sets and what could we infer about the potential compositions of planets missions such as *TESS* are likely to find? This is what this thesis aims to investigate.

1.6 Research Questions

In this thesis, two broad questions are being addressed.

1.6.1 What can we learn about the types of planets *TESS* will discover around GALAH stars?

Chapter 2 investigates how we can use GALAH, along with the *Gaia* survey to better characterise stars being observed by the *TESS* mission. This chapter, which is also Clark et al. (2021), determines the physical parameters for over 47,000 stars, including the stellar radii, masses, ages and luminosities. These fundamental stellar parameters are crucial in better characterising the planets these stars are likely to host. Molar abundance ratios were also calculated in this chapter, assisting exogeologists in determining the potential origins of rocky exoplanets discovered by *TESS*. It then uses these molar ratios to forward predict the likely geological compositions of potentially discovered worlds, discussing the implications of said work in both Clark et al. (2021) and Chapter 4.

1.6.2 What can we learn about current exoplanetary systems orbiting GALAH stars?

In Chapter 3 the paper Clark et al. (2021) then uses new data from GALAH and *Gaia* to recharacterise confirmed and candidate planet hosts. Most of these candidates have now come from to the *TESS* mission. This chapter characterises 105 confirmed exoplanets and 293 exoplanet candidates, using a weighted mean approach of the planetary observables (i.e radial velocity semi-amplitude and transit depths) along with the newly derived stellar parameters to better estimate the planet's mass and radius. Chemical abundance trends between different planetary populations are explored, along with determining the stellar populations of planet hosting stars through chemokinematics.

This chapter also highlights the importance of measuring stellar rotation velocities

which are used to determine what exoplanet candidates are better to follow-up from the ground than others. With that motivation from Chapter 4, Clark et al. (2022) confirms and characterises the planet TOI-778 b orbiting around a rapidly rotating F star. Finally, the conclusions of this thesis are then presented in Chapter 5.

Let's leave no words unspoken and save regrets for the broken
Will you even look back when you think of me?
All I want is a place to call my own
To mend the hearts of everyone who feels alone
Whoa, you know to keep your hopes up high, and your head down low.

– A Day To Remember

2

THE GALAH-*TESS* CATALOGUE

The published paper Clark et al. (2021), "The GALAH Survey: using galactic archaeology to refine our knowledge of *TESS* target stars" follows.

Monthly Notices of the ROYAL ASTRONOMICAL SOCIETY

MNRAS **504,** 4968–4989 (2021) doi:10.1093/mnras/stab1052
Advance Access publication 2021 April 16

The GALAH Survey: using galactic archaeology to refine our knowledge of *TESS* target stars

Jake T. Clark [1]★ Mathieu Clerté,[1] Natalie R. Hinkel,[2] Cayman T. Unterborn,[3] Robert A. Wittenmyer,[1] Jonathan Horner,[1] Duncan J. Wright,[1] Brad Carter [1] Timothy D. Morton,[4] Lorenzo Spina [5] Martin Asplund,[6] Sven Buder [6,7] Joss Bland-Hawthorn [7,8] Andy Casey [5] Gayandhi De Silva,[5] Valentina D'Orazi,[9] Ly Duong,[6] Michael Hayden,[7,8] Ken Freeman,[6] Janez Kos,[7,10] Geraint Lewis [8] Jane Lin,[6] Karin Lind,[11] Sarah Martell [7,12] Sanjib Sharma [8] Jeffrey Simpson [7,8] Dan Zucker,[13,14] Tomaz Zwitter [10] Christopher G. Tinney,[15,16] Yuan-Sen Ting (丁源森),[6,17,18,19] Thomas Nordlander [6,7] and Anish M. Amarsi [7,11]

[1]*Centre for Astrophysics, University of Southern Queensland, West Street, Toowoomba, QLD 4350, Australia*
[2]*Space Science and Engineering Division, Southwest Research Institute, San Antonio, TX 78238, USA*
[3]*School of Earth and Space Exploration, Arizona State University, Tempe, AZ 85287, USA*
[4]*Department of Physics and Astronomy, University of Southern California, Los Angeles, CA 90089, USA*
[5]*Monash Centre for Astrophysics, School of Physics and Astronomy, Monash University, VIC 3800, Australia*
[6]*Research School of Astronomy & Astrophysics, Australian National University, ACT 2611, Australia*
[7]*Center of Excellence for Astrophysics in Three Dimensions (ASTRO-3D), ACT 2611, Australia*
[8]*Sydney Institute for Astronomy, School of Physics, University of Sydney, NSW 2006, Australia*
[9]*INAF Osservatorio Astronomico di Padova, vicolo dell'Osservatorio 5, I-35122, Padova, Italy*
[10]*Faculty of Mathematics and Physics, University of Ljubljana, Jadranska 19, 1000 Ljubljana, Slovenia*
[11]*Max Planck Institute for Astronomy (MPIA), Koenigstuhl 17, D-69117 Heidelberg, Germany*
[12]*School of Physics, University of New South Wales – Sydney, Sydney 2052, Australia*
[13]*Department of Physics & Astronomy, Macquarie University, Sydney, NSW 2109, Australia*
[14]*Research Centre in Astronomy, Astrophysics & Astrophotonics, Macquarie University, Sydney, NSW 2109, Australia*
[15]*Exoplanetary Science at UNSW, University of New South Wales, Sydney, NSW 2052, Australia*
[16]*Australian Centre for Astrobiology,University of New South Wales, Sydney, NSW 2052, Australia*
[17]*Institute for Advanced Study, Princeton, NJ 08540, USA*
[18]*Department of Astrophysical Sciences, Princeton University, Princeton, NJ 08544, USA*
[19]*Observatories of the Carnegie Institution of Washington, 813 Santa Barbara Street, Pasadena, CA 91101, USA*

Accepted 2021 March 17. Received 2021 March 17; in original form 2020 August 12

ABSTRACT

An unprecedented number of exoplanets are being discovered by the Transiting Exoplanet Survey Satellite (*TESS*). Determining the orbital parameters of these exoplanets, and especially their mass and radius, will depend heavily upon the measured physical characteristics of their host stars. We have cross-matched spectroscopic, photometric, and astrometric data from GALAH Data Release 2, the *TESS* Input Catalog and *Gaia* Data Release 2, to create a curated, self-consistent catalogue of physical and chemical properties for 47 285 stars. Using these data, we have derived isochrone masses and radii that are precise to within 5 per cent. We have revised the parameters of three confirmed, and twelve candidate, *TESS* planetary systems. These results cast doubt on whether CTOI-20125677 is indeed a planetary system, since the revised planetary radii are now comparable to stellar sizes. Our GALAH–*TESS* catalogue contains abundances for up to 23 elements. We have specifically analysed the molar ratios for C/O, Mg/Si, Fe/Si, and Fe/Mg, to assist in determining the composition and structure of planets with $R_p < 4R_\oplus$. From these ratios, 36 per cent fall within 2σ sigma of the Sun/Earth values, suggesting that these stars may host rocky exoplanets with geological compositions similar to planets found within our own Solar system.

Key words: methods: observational – catalogues – planets and satellites: interiors – stars: fundamental parameters – stars: abundances.

★ E-mail: jake.clark@usq.edu.au

1 INTRODUCTION

Exoplanets (planets that exist beyond the Solar system) moved beyond science fiction and into the realm of hard science late in the 20th century (Latham et al. 1989; Lawton & Wright 1989; Wolszczan & Frail 1992; Mayor & Queloz 1995). From the first discoveries until the launch of the *Kepler* spacecraft, exoplanets were largely detected by radial velocity techniques, leading to a wealth of massive planet discoveries around largely Sun-like stars (e.g. Fischer et al. 2008; Vogt et al. 2010; Lovis et al. 2011; Wittenmyer et al. 2014; Endl et al. 2016).

Towards the end of the first decade of the 2000s, the transit technique became the numerically dominant method for making new exoplanet discoveries, and revealed an abundance of planets moving on very short period orbits (e.g. Noyes et al. 2008; Hellier et al. 2012; Muirhead et al. 2012; Rowe et al. 2014; Coughlin et al. 2016). The great advantage of transit observations over those using the radial velocity technique is that they permit surveys to target large numbers of stars simultaneously. The ultimate expression, to date, of the transit method as a tool for exoplanetary science came with the *Kepler* space telescope, launched in 2009 (Borucki et al. 2010).

At the time of writing, *Kepler* has been by far the most successful exoplanet detection program, discovering 65.5 per cent of currently known exoplanets.[1] These planetary discoveries have showcased the vast richness and diversity of exoplanets across our galaxy. The great diversity of exoplanets and exoplanetary systems is illustrated by the discovery of large numbers of multiplanet systems (e.g. Gillon et al. 2017; Shallue & Vanderburg 2018), planets in extremely eccentric orbits (e.g. Naef et al. 2001; Santerne et al. 2014; Wittenmyer et al. 2017), and planets that some have argued might resemble the Earth (e.g. Barclay et al. 2013; Torres et al. 2015).

The *Kepler* and K2 missions also revealed that planets larger than Earth, $>1R_\oplus$, yet smaller than Neptune, $<4R_\oplus$, are remarkably common – despite there being no such planets in the Solar system. Indeed, of those planets that we can readily detect, these 'super-Earths' and 'mini-Neptunes' seem to be by far the most common (Batalha et al. 2013). On 30 October 2018, the *Kepler* spacecraft depleted all of its on-board fuel, immediately retiring the mission and leaving behind a legacy that is unmatched in exoplanetary science. Fortunately, NASA's Transiting Exoplanet Survey Satellite (*TESS*) mission, launched in April 2018, has picked up where the K2 mission left off.

The *TESS* mission (Ricker et al. 2014) is a space-based photometric survey that will cover the entire sky, except for the region within ±6 deg of the ecliptic plane. The mission is designed to find small planets ($R_p < 2.5R_\oplus$) around nearby, bright, main-sequence stars. As of 2020 August, there have been 66 confirmed planetary discoveries made as a result of *TESS*' ongoing survey (e.g. Huang et al. 2018; Nielsen et al. 2019b; Vanderspek et al. 2019; Addison et al. 2020; Gilbert et al. 2020; Jordán et al. 2020). In addition to the 66 confirmed *TESS* exoplanets, there are more than two thousand *TESS* Targets of Interest (TOI) and Community Targets of Interest (CTOI)[2] waiting for their exoplanetary status to be confirmed by ground-based teams (e.g Addison et al. 2019; Davis et al. 2019; Nielsen et al. 2019b; Wang et al. 2019a; Dalba et al. 2020; Eisner et al. 2020).

Once potential planets have been identified by *TESS*, the *TESS* Input Catalog (TIC) (Stassun et al. 2018; Stassun et al. 2019) and Candidate Target List (CTL) are the key catalogues that enable follow-up teams to characterize – for both stars and planets – the members of *TESS* candidate systems. In particular, radial velocity data are needed to measure the planetary mass, and spectroscopic observations are needed to refine mass and radius of the host star. These measurements, in combination with the transit radius measurement from *TESS*, allow the bulk density of the planet in question, ρ_p,[3] to be determined, and thereby provide constraints on that planet's overall composition (Valencia, O'Connell & Sasselov 2006; Seager et al. 2007; Unterborn, Dismukes & Panero 2016).

Whilst the bulk density of a planet does provide clues to its potential bulk composition, it does not provide enough information for us to determine the geological structure of a potentially rocky planet, or to precisely determine its true composition. This is clearly illustrated by the work of Suissa, Chen & Kipping (2018), who demonstrate that a newly discovered 'Earth-like' planet (a planet observed to be both the same mass and the same size as the Earth; i.e. $1M_\oplus$, $1R_\oplus$) could have a wide variety of internal compositions. Distinguishing between the many possible compositions and structures of such a planet will be of great interest in the years to come, particularly in the context of the search for potentially habitable planets, and the selection of the most promising such planets for further study (e.g. Horner & Jones 2010).

Recent studies, however, have demonstrated that planetary scientists could potentially unlock the viscera of distant rocky worlds by combining our knowledge of the planets themselves with detailed information on the chemical abundances of their host stars (e.g. Bond, Lauretta & O'Brien 2010a; Bond, O'Brien & Lauretta 2010b; Dorn et al. 2015; Unterborn et al. 2016; Dorn et al. 2017a; Unterborn & Panero 2017; Hinkel & Unterborn 2018; Unterborn et al. 2018a; Dorn et al. 2019; Unterborn & Panero 2019). In particular, knowledge of the chemical abundances of refractory elements (such as Mg, Al, Si, Ca, and Fe) and volatile elements (such as C and O) can help us to determine the likely structure and composition of exoplanets smaller than $4R_\oplus$ (Dorn et al. 2019; Putirka & Rarick 2019).

The most crucial elements for such an analysis are C, O, Mg, Si, and Fe, as these elements will determine the core to mantle fraction (in particular Fe/Mg[4]) and the composition of a rocky exoplanet's mantle (e.g. Mg/Si and C/O, as per Bond et al. 2010b; Madhusudhan, Lee & Mousis 2012; Unterborn et al. 2014; Dorn et al. 2015; 2017a). Such models have recently proven vital in inferring the geological and chemical composition of the planets in the TRAPPIST-1 (Unterborn et al. 2018a), 55 Cnc (Dorn, Hinkel & Venturini 2017b), HD 219134 (Ligi et al. 2019), and other planetary systems.

As the catalogue of known exoplanets has grown, it has becoming increasingly obvious that our understanding of the planets we find is often limited by the precision with which we can characterize their host stars. In particular, measurements of the elemental abundances of exoplanet host stars are becoming increasingly important in developing our understanding of the fundamental synergies between stars and the planets they host. As a result, there is an increasing amount of research within exoplanetary science that aims to understand the relationship between a star's chemical abundances and the types of planets and planetary systems that they can form (e.g. Fischer &

[1] https://exoplanetarchive.ipac.caltech.edu/; accessed 2020 August 6 , counting discoveries from both *Kepler*'s primary mission, and the K2 survey.
[2] https://exofop.ipac.caltech.edu/tess/; accessed 2020 August 6.

[3] $\rho_p = M_p \left(\frac{4}{3}\pi R_p^3\right)^{-1}$; where M_p and R_p are the planet's mass and radius, respectively.
[4] Stellar abundance ratios are calculated by $\left(\frac{X}{Y}\right)_\star = 10^{\left(\left[\frac{X}{H}\right]_\star + A(X)_\odot\right) - \left(\left[\frac{Y}{H}\right]_\star + A(Y)_\odot\right)}$.

Valenti 2005; Adibekyan et al. 2012; Buchhave et al. 2014; Buchhave & Latham 2015; Teske et al. 2019).

The relationship between planetary demographics and a star's measured photospheric iron abundance is a complex one. Over twenty years ago, studies showed that stars hosting hot-Jupiters (giant planets in very short period orbits) are typically iron-enriched compared to the Sun (Gonzalez 1997; Santos, Israelian & Mayor 2001; Fischer & Valenti 2005). This trend has, however, weakened in more recent studies (Osborn & Bayliss 2019; Teske et al. 2019). Similarly, the relationship between a star's iron abundance and the number of planets it hosts remains the subject of significant debate (e.g. Petigura et al. 2018; Adibekyan et al. 2017). Recent machine-learning work by Hinkel et al. (2019) has indicated that elemental abundances, including those of C, O, and Fe, can be used as a means to identify potential planet-hosting stars amongst the wider stellar population.

In addition to potentially helping us to understand the interior structure and composition of newly discovered exoplanets, recent work has also suggested that measurements of the elemental abundances of stellar photospheres and planetary atmospheres could also aid our investigation of the formation and migration history of the exoplanets we study. For example, Brewer, Fischer & Madhusudhan (2017) describe how measurements of an enhanced C/O ratio and [O/H] abundance in the atmospheres of ten hot Jupiters, compared to the equivalent abundances in their stellar hosts, serve as evidence that those planets must have formed beyond the water ice line, and that they must have then migrated inwards to reach their current location. In a similar fashion, studies of the composition and isotopic abundances of the planets and small bodies have long been used to attempt to disentangle their formation locations and migration histories (see e.g. Horner et al. 2020, and references therein). In summary, this recent work reveals that, if we are to fully characterize the exoplanets we discover, it is vital that we consider the elemental abundances of their host stars.

The Southern hemisphere's largest spectroscopic stellar abundance survey – the Galactic Archaeology with HERMES (GALAH) survey – is designed to investigate the stellar formation and chemical enrichment history of the Milky Way galaxy (De Silva et al. 2015; Martell et al. 2016; Buder et al. 2018). To do this, GALAH has collected high-resolution spectra for more than 600 000 stars, from which the abundances of up to 23 elements can be determined for each star. GALAH's latest public release, GALAH DR2 (Buder et al. 2018), contains the details of 342 682 stars for which both physical and chemical properties have been observed and derived.

In this work, we make use of the data in GALAH DR2 to calculate revised values for the mass and radius of 47 285 stars that have been cross-matched between GALAH DR2 and the TIC. We then calculate the C/O, Fe/Mg, and Mg/Si abundance ratios for those stars, providing a database of stellar abundances for potential planet hosting stars to facilitate future studies of the composition, structure, habitability, and migration history of exoplanets discovered by *TESS*.

In Section 2, we describe how GALAH DR2 is cross-matched with the *TESS* and *Gaia* catalogues (Section 2.1), before describing how we derive the characteristics for our stars through isochrone modelling (Section 2.2). We then go on to discuss the derivation of elemental abundances and abundance ratios for GALAH–*TESS* stars using GALAH DR2 (Section 2.3). The resulting physical and elemental parameters are then validated by comparison with other catalogs in Sections 3.1 and 3.2. In our discussion section, we examine our refined stellar and planetary parameters for confirmed and candidate exoplanet host stars (Section 4.1) and the abundance ratio trends in our stellar sample (Section 4.2). Finally, we summarize our findings and draw our conclusions in Section 5.

2 METHODOLOGY AND DATA ANALYSIS

In this methodology section, we describe how we cross-matched the GALAH–*TESS* catalogue (Section 2.1), derived our physical stellar parameters including isochronic masses and radii from GALAH DR2 (Section 2.2), and calculated our [X/H] and X/Y abundance ratios using GALAH DR2 data (Section 2.3).

2.1 Cross-matching the CTL and GALAH catalogues

The *TESS* Input Catalog (TIC; Stassun et al. 2018; Stassun et al. 2019) presents the physical characteristics of stars that are likely to be observed during the primary *TESS* mission. Built before the launch of the spacecraft, the TIC uses photometric relationships to derive the physical properties of over 470 million point sources. Due to the large number of stars being observed by *TESS*, there is a selection process that gives a higher priority to stars that better suit the *TESS* mission goals, which are primarily to discover planets around bright, cool dwarfs (Ricker et al. 2014; Stassun et al. 2018). Stars within this subset of the TIC are a large component of the Candidate Target List (CTL), and are observed by *TESS* at a 2-min cadence, whilst the remaining targets are recorded at a 30-min cadence in the full-frame images (FFIs).

Several simulations of the exoplanetary outcomes of *TESS* have been produced, including Sullivan et al. (2015) and Barclay, Pepper & Quintana (2018). Sullivan et al. (2015) predicted that *TESS* will discover 20 000 planets over the next 2 yr (1700 from CTLs and the rest from full-frame images). A more conservative yield prediction by Barclay et al. (2018) estimates that 1250 exoplanets will be discovered orbiting CTL stars, with an additional 3100 being found orbiting stars within the full-frame images. Both sets of simulations suggest that a large number of planets will discovered by *TESS*, from both the CTL and full TIC samples.

The most recent data release from GALAH (DR2; Buder et al. 2018) contains data derived from high resolution spectra for a total of 342 682 southern stars. Stars in the GALAH DR2 were first cross-matched with *Gaia*'s second data release (DR2; Gaia Collaboration et al. 2018), using the TOPCAT (Taylor 2005) tool to match GALAH and *Gaia* sources with a position tolerance of ± 1 arcsec, providing *Gaia*-band magnitudes and parallaxes for our isochronic models. The returned stars were then cross-matched against release 8.0 of the TIC[5] using 2MASS (Skrutskie et al. 2006) identifiers from the GALAH catalogue, accessed through the Mikulski Archive for Space Telescopes `astroquery`'s API (Ginsburg et al. 2019).

For our catalogue, we selected GALAH DR2 stars with a high signal-to-noise ratio (S/N) across all four of HERMES's CCDs, only accepting stars that had a S/N ratio value of 50 or higher in each wavelength band. We also omit stars with a `flag_cannon` greater than zero, which indicates some problem in the data analysis, from our data set. The flagging scheme utilized in GALAH DR2 is described in greater detail in Buder et al. (2018).

For completeness, we compared the *Gaia* G-band magnitude from the TOPCAT cross-match to the same value found in the CTL catalogue. These values should be identical to one another, and hence

[5] https://filtergraph.com/tess_ctl; accessed 2020 August 6.

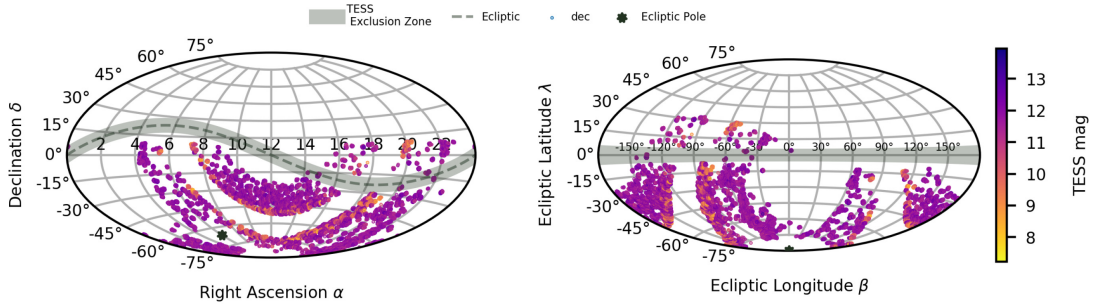

Figure 1. Aitoff projection of GALAH–*TESS* stars in both equatorial (right ascension and declination) and ecliptic (latitude and longitude) co-ordinates. The ecliptic plane, southern ecliptic pole, and *TESS* exclusion zone are shown in each (except for the ecliptic from the ecliptic co-ordinate plot as it corresponds to $\lambda = 0°$). Stars that are observed with HERMES within *TESS*'s Continuous Viewing Zone are a part of the TESS-HERMES survey, and thus not observed with GALAH. Stars within the *TESS* exclusion zone have been left within the GALAH–*TESS* catalogue, as these stars may be observed in the future with *TESS*.

serve as confirmation that we have the correct stars cross-matched within our catalogue. We considered a match to be confirmed if the difference in a star's celestial coordinates was less than 0.0001 deg and the difference in 2MASS J–H colour magnitudes (J–H) was also below 0.0001 mag for the exoplanet hosts.

We also wanted to include in our GALAH–*TESS* sample any stars that may have slightly lower S/N spectra in GALAH, but which are known to host either a confirmed exoplanet, a *TESS* TOI, or a CTOI. We accessed the *TESS* Follow-up Observing Program and NASA's EXOFOP-TESS data bases, and cross-matched them with GALAH DR2 and *Gaia* DR2. Our cross-match approach was simpler for these targets, as we merely needed to match them by their TIC IDs. There was only one star cross-matched within the CTOI list that had its S/N less than 50, this being UCAC4 306-282520. This star's green and blue channels have S/N values of 32 and 42, respectively.

Taking all of the above into consideration, our newly formed GALAH–*TESS* catalogue boasts 47 285 stars across the southern night sky, as shown in Fig. 1. Of these 47 285 stars, 2260 are prioritized sufficiently highly by the *TESS* mission that they are included in the TIC's CTL catalogue, being observed with a higher cadence relative to other stars in the general TIC. Fig. 2 shows the distributions of our GALAH–*TESS* stars as a function of their *TESS* and *V*-band magnitudes. The median *TESS* magnitudes for our CTL and TIC stars are 11.4 and 12.5, respectively, whilst the median V-band magnitudes for our CTL and TIC stars are 10.7 and 11.9, respectively. The slightly lower median values for stars on the CTL compared to those for the general TIC reflect *TESS*'s primary mission objectives, prioritizing brighter stars.

Due to flexible constraints by which we cross-matched the catalogues, there are GALAH–*TESS* stars that are located within the ecliptic, with a *TESS* priority of zero, that will not be observed within the initial 2 yr *TESS* primary mission. We have left those stars in our GALAH–*TESS* catalogue, as they might be explored during the *TESS* extended mission, following the conclusion of the primary survey. There is a large, deliberate absence of stars surrounding the *TESS* Continuous Viewing Zone, with no star within our catalogue being found at ecliptic latitudes south of $-78°$, in order to avoid any crossover of stars being observed and analysed by the TESS-HERMES Survey (Sharma et al. 2018). There are also no stars in our catalogue which overlap fields observed as part of the K2 survey, in order to avoid any potential crossover with the K2-HERMES survey (Wittenmyer et al. 2018; Sharma et al. 2019).

2.2 Deriving stellar radii and masses from GALAH stellar parameters

Details on the observation strategy and data pipeline for GALAH DR2 can be found in Kos et al. (2017), Martell et al. (2016), and Buder et al. (2018). Briefly, all GALAH DR2 observations are acquired with the 3.9 m Anglo-Australian Telescope situated at the Siding Spring Observatory, Australia. The two degree-field prime focus top-end (2dF; Lewis et al. 2002) with 392 science fibres is used to feed the High Efficiency and Resolution Multi Element Spectrograph (HERMES; Sheinis et al. 2015), delivering high resolution ($R \approx 28\,000$) spectra in four wavelength arms covering 471.3–490.3, 564.8–587.3, 647.8–673.7, and 758.5–788.7 nm.

The spectra for each star are corrected for systematic and atmospheric effects and then continuum normalized. Detailed physical parameters, including effective temperature ($T_{\rm eff}$), surface gravity ($\log g$), global metallicity ([M/H]), and individual abundances ([X/Fe]), have been determined for 10 605 selected stars using 1D stellar atmospheric models via the Spectroscopy Made Easy (Valenti & Piskunov 1996) package. Both the spectroscopic information and stellar parameters for these 10 605 stars then form a training set for the machine-learning algorithm *The Cannon* (Ness et al. 2015), which is used to train a data-driven spectrum model algorithm on the entire GALAH DR2 survey. Flags are produced by *The Cannon*'s processing for the 'quality' of the derived physical parameters in each star. For our analysis, we only include stars in the GALAH–*TESS* catalogue if they have a '0' `flag_cannon` in the GALAH DR2 release.

To derive the mass, radius, and ages of our GALAH–*TESS* stars, we used the PYTHON package `isochrones` (Morton 2015). The `isochrones` code uses MESA Isochrones & Stellar Tracks (MIST; Choi et al. 2016) stellar evolution grids to infer the physical characteristics of stars. For this analysis, we used as input observables: the star's effective temperature ($T_{\rm eff}$), surface gravity ($\log g$), 2MASS (J, H, K_s), and *Gaia* (G, $G_{\rm RP}$, $G_{\rm BP}$) photometric magnitudes, along with parallax values obtained by *Gaia* DR2 (Gaia Collaboration et al. 2018) where available.

Isochrone models rely on knowledge of a star's global metallicity, [M/H]. The assumption that the iron abundance [Fe/H] can be a proxy (or even equal) to [M/H] breaks down for metal-poor stars (e.g. Fuhrmann 1998; Reddy, Lambert & Allende Prieto 2006; Adibekyan et al. 2012, 2013a; Recio-Blanco et al. 2014). The radiative opacity of metal poor stars can be heavily affected by Mg, Si, Ca, and Ti

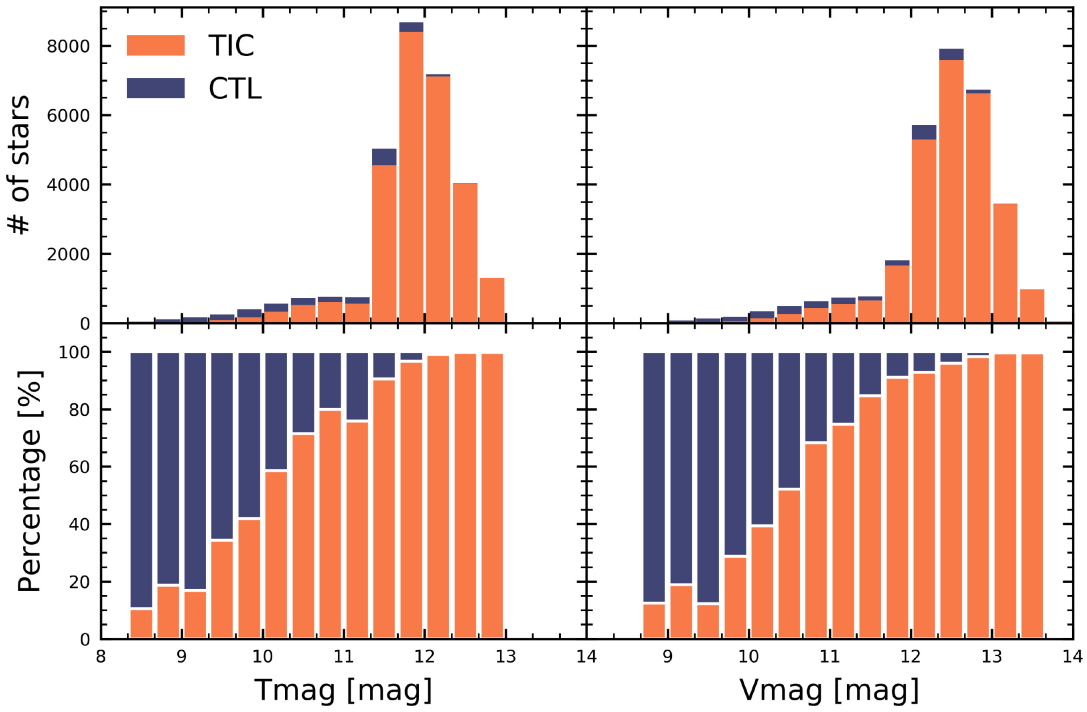

Figure 2. Of the 47 285 stars that are included in both the GALAH DR2 catalogue and the *TESS* input catalogue (TIC), 2260 are members of the Candidate Target List (CTL; shown here in purple), and are scheduled to be observed with a higher cadence relative to stars within the general TIC (orange). Left: Of the 2260 CTL stars, 650 stars are brighter than a *TESS* magnitude ($T_{\rm mag}$) of 10, 1527 lie between $T_{\rm mag}$ 10 and 12, and 83 with a $T_{\rm mag}$ between 12–14. The median *TESS* magnitudes for our CTL and TIC stars are 11.4 and 12.5, respectively. The top plot shows the number of TIC and CTL members in each bin whilst the bottom plot shows the percentage of stars in each magnitude bin that belong to the TIC and CTL, respectively. Right: Of the 2260 CTL stars, 299 stars are brighter than a *V* magnitude of 10, 1099 lie between *V* magnitudes of 10–12, and 862 have a *V* magnitude between 12 and 14. The median *V* magnitudes for our CTL and TIC stars are 10.7 and 11.9, respectively. The slightly lower median values for CTL values compared to the TIC reflect *TESS*'s primary mission objectives, prioritizing brighter stars. The significant increase in the number of stars between *V*mag 12.0–13.7 and $T_{\rm mag}$ 11.3–13.0 reflects GALAH's observing strategy.

(i.e. by α-elements). Including these α-elements in our calculations of global metallicity better predicts the physical parameters derived with `isochrones`. GALAH DR2 calculates an [α/Fe] value for each star using equation (1):

$$[\alpha/\mathrm{Fe}] = \frac{\sum \frac{[\mathrm{X/Fe}]}{(\mathrm{e\_[X/Fe]})^2}}{\sum (\mathrm{e\_[X/Fe]})^{-2}}, \quad (1)$$

where X = Mg, Si, Ca, and Ti and e_[X/Fe] is the abundance's associated uncertainty. [α/Fe] will be calculated even if one or more of these elements are missing. From our iron abundance, [Fe/H], and [α/Fe], we can then calculate [M/H] using Salaris, Chieffi & Straniero (1993):

$$[\mathrm{M/H}] = [\mathrm{Fe/H}] + \log_{10}\left(0.638 f_\alpha + 0.362\right), \quad (2)$$

where f_α is the α-element enhancement factor given by $f_\alpha = 10^{[\frac{\alpha}{\mathrm{Fe}}]}$. Our calculated [M/H] value is then used in the isochrone modelling of each star.

When using `isochrones`, if a star failed to converge, it was omitted from our catalogue. Of our original 47 993 stars, 708 stars failed to converge, leaving the 47 285 stars that comprise the GALAH–*TESS* catalogue. When the model reached convergence, the median output values of the stellar mass, radius, density, age, and equivalent evolution phase, as well as their corresponding 1σ uncertainties are calculated from the posterior distributions. We calculate stellar luminosity through the Stefan–Boltzmann relationship, and use those luminosities to derive the five habitable zone distances for each star, as formulated by Kopparapu et al. (2013). GALAH DR2 rotational, radial, and microturbulence velocities have been included in the GALAH–*TESS* catalogue to assist ground-based radial velocity teams to better prioritize follow-up targets.

2.3 Deriving stellar abundances and ratios for GALAH–*TESS* stars

In addition to providing the physical parameters for over 47 000 stars, our catalogue also contains the chemical parameters that could prove vital in determining the composition of rocky planets potentially hosted by these stars. Stellar elemental abundances for 23 elements, as well as quality flags, are derived from *The Cannon*, with the details of the derivation of these abundances their associated systematics discussed in detail in Buder et al. (2018). To ensure that we deliver to the community a usable catalogue, we have removed values with [X/Fe] flags not equal to zero.

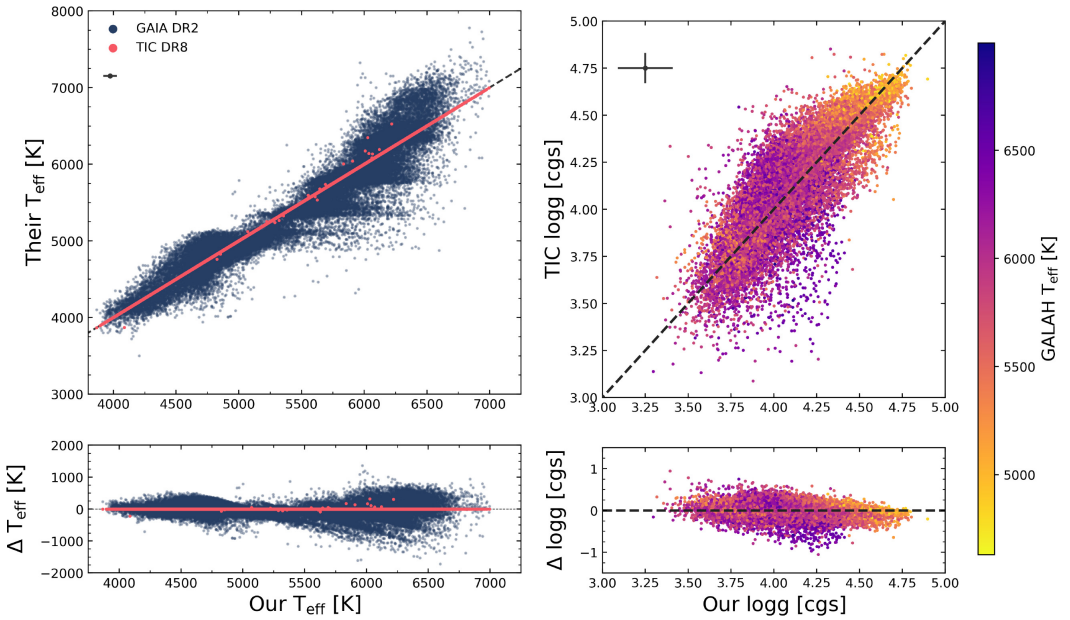

Figure 3. Left: Comparing the GALAH derived effective temperatures, with those published by *Gaia* DR2 (blue) and TIC DR8 (pink) for our GALAH-*TESS* sample of 47.974 stars. The GALAH DR2 effective temperatures have been included within the TIC, indicated by scatter points lining up on top of the equality line (black dashed line). With our cross-matching methodology, *Gaia* DR2's data set does not contain $T_{\rm eff}$ errors, and hence not visible within the plot. Right: Comparing the GALAH and TIC derived surface gravities with each star colour coded by its effective temperature. Only ∼60 per cent of CTL stars within our GALAH–*TESS* sample have measured surface gravity measurements. Error bars for both figures have been suppressed due to clarity; however, a median error bar is shown in the figures' top-left corner.

Whilst GALAH DR2 has its own internal Solar normalization, we have converted our elemental abundances from a GALAH normalized scale to Lodders, Palme & Gail (2009), and moved the abundances from being normalized by iron to hydrogen [X/H], since such values are more widely used within the current exoplanetary community. The derived Mg/Si, Fe/Mg, and C/O ratios were all calculated using our [X/H] stellar abundances and Lodders et al. (2009) Solar normalizations, where available.

3 RESULTS

Our results section is split into two separate parts, which detail the in-depth results of both the physical (Section 3.1) and chemical (Section 3.2) characteristics of stars within our GALAH–*TESS* catalogue, and provide comparisons of those results to other surveys and catalogues.

3.1 Atmospheric and physical characteristics of GALAH–*TESS* stars

The current TIC incorporates data from large, ground-based spectral surveys including LAMOST (Cui et al. 2012), RAVE (Steinmetz et al. 2006), TESS-HERMES (Sharma et al. 2018), and GALAH. For the vast majority of stars in our sample, the TIC has incorporated GALAH DR2 effective temperatures, which can be see as a line of equality in Fig. 3. Our GALAH–*TESS* temperatures, which have a median error of 54 K, seem to be in reasonable agreement with *Gaia*'s, with a larger scatter for hotter stars than for cooler stars.

There tends to be a slightly better agreement with *Gaia*'s $T_{\rm eff}$ for stars slightly cooler than the Sun ($4750 \leq$ GALAH–*TESS* $T_{\rm eff} \leq 5500$) with an rms of 146 K and median bias of 50 K, compared to the hotter stars ($T_{\rm eff} > 5500$), and cooler stars ($T_{\rm eff} < 4750$), with rms values of 168 and 253 K and median bias values of 34 and 25 K, respectively. The high scatter in results for the hotter stars is to be expected, with (Buder et al. 2018) noting an underestimate of GALAH $T_{\rm eff}$ values for hotter *Gaia* benchmark stars, which might be due to GALAH's input training set preferentially favouring cooler temperatures. There are horizontal structures between 5250 and 5750 K for *Gaia* $T_{\rm eff}$ values compared to those obtained using GALAH data. Similar structures were found by Hardegree-Ullman et al. (2020) when comparing *Gaia* $T_{\rm eff}$ values with spectral values obtained with LAMOST. These structures suggest that the *Gaia* temperature calculations in this range tend to certain preferred temperatures, which may be the result of *Gaia*'s input training set.

Because the TIC prioritizes stars being observed with a 2-min cadence (the CTL), surface gravities are only presented within the TIC for stars with a $\log g > 3$. In addition, the TIC does not include derived $\log g$ values from other surveys, opting instead for a homogeneous data set to ensure internal consistency with their mass and radius values. In our cross-matched sample, we include both dwarfs and giants, since giant stars are also known to be planet hosts (Johnson et al. 2011; Jones et al. 2016; Huber et al. 2019; Wittenmyer et al. 2020). As a result, Fig. 3 only shows the comparison for GALAH–*TESS* stars that have both measured $\log g$ values in both catalogues. For our sample of main-sequence stars that have TIC $\log g$ values, the agreement between their $\log g$ values

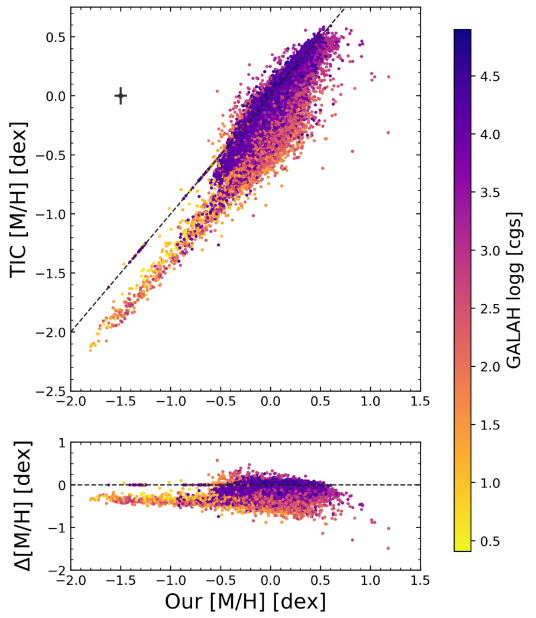

Figure 4. Comparing GALAH's global metallicity [M/H] to that of the TIC, with the colour of each star colour denoting its surface gravity, as derived by GALAH. The median error bar is given by the grey point to the figure's top-left corner, with an equality line given by the dark grey dashed line. The TIC directly uses GALAH DR2's [Fe/H] as [M/H], which this equality holds for thin-disc and alpha-poor stars. However, for thick-disc and alpha-rich stars, this equality does not hold true. From this figure, the median difference between [M/H] and [Fe/H] for alpha-rich stars is ∼0.3 dex. Since isochronic evolutionary tracks depend on [M/H], this assumption of [M/H] = [Fe/H] would have given less accurate mass, radius, and age results for our alpha-rich stars. For a small portion of our stars, there was no [α/Fe] abundance, and hence, we use [Fe/H] as [M/H] in our isochrone models for these specific stars.

and ours appears reasonable, with an rms and median bias of 0.14 and −0.03 dex, respectively, compared to the median GALAH log g error of 0.16 dex. In comparsion, the TIC's median error bar is only 0.08 dex.

The TIC's global metallicity values, [M/H], have mostly been acquired from the large, ground-based surveys such as LAMOST, RAVE, etc. (Cui et al. 2012; Steinmetz et al. 2006). For those stars for which the TIC used GALAH DR2 parameters, they directly incorporated GALAH's [Fe/H] as the TIC's [M/H]. This equality does hold for metal-rich stars. However, there is a large discrepancy between [M/H] and [Fe/H] for thick-disc and metal-poor stars that are enriched in α-elements. These α-elements affect the radiative opacity of iron-poor stellar surfaces, with the overall metallicity and iron abundance equality breaking down within this regime. If the overall metallicity does not take into account the α-abundance, [α/Fe], for iron-poor stars, this could drastically alter the star's derived isochrone track. This in turn would alter the final stellar parameters that are produced with this model.

If we wish to better characterize stars observed with *TESS*, we therefore need to take [α/Fe] into consideration, as we did in Section 2.2. Fig. 4 shows the comparison between the overall metallicities taken from the TIC, and those calculated using GALAH data. There are 317 stars that do not have a [α/Fe] measurement, and for those stars, we simply equated their iron abundance to the overall stellar metallicity. The rms and bias between the TIC and GALAH's overall metallicity is 0.18 and 0.08 dex, respectively. As we expected, however, the rms between the two data sets is significantly lower for alpha-poor stars ([α/Fe] < 0.1), with an rms and bias values being 0.08 and 0.05 dex, respectively. There is a much larger difference in [M/H] for iron-poor/alpha-rich stars, which is to be expected, with an rms and bias of 0.32 and 0.27 dex, respectively. For comparison, the median error in the derived [M/H] values is 0.07 dex.

GALAH's $T_{\rm eff}$, log g and [M/H] values together with the astrometric and photometric observables are fed into the ISOCHRONES code, producing the radius and mass values which are depicted in Fig. 5. Our radii show good overall agreement with both *Gaia* DR2 and TIC. However, at large radii (giant stars), our calculated radii tend to be smaller than those taken from the TIC and *Gaia*. The median relative error for our stellar radii is 2.7 per cent, with the relative RMS between our results and those of *Gaia* DR2 and TIC found to be 10 per cent and 14 per cent, respectively. Our median stellar radius value is 1.89 $R_\odot$, which is comparable to the median values of the *Gaia* and TIC data of 1.84 $R_\odot$ and 1.92 $R_\odot$, respectively.

The general agreement between our results and the radii derived by *Gaia* and the TIC is not unexpected, since our ISOCHRONES models rely on *Gaia* DR2's photometric magnitudes and parallax values. The TIC's methodology is similar in that it also relies on data from *Gaia* to derive its stellar radii values. These stellar radii values will prove fundamental in calculating planetary radii for exoplanet host stars discovered by *TESS* within our sample.

Ground-based follow-up teams mostly rely upon the radial velocity method to confirm TOIs (e.g Addison et al. 2019; Davis et al. 2019; Nielsen et al. 2019b; Wang et al. 2019a; Dalba et al. 2020; Eisner et al. 2020). From this methodology, it is possible to infer the planetary mass through the radial–velocity semi-amplitude. However, the planetary mass is inferred based on our knowledge of the mass of the host star. It is therefore important to not only determine and refine the stellar radii of GALAH–*TESS* stars, but to also refine their masses. Over 40 per cent of our sample do not have TIC stellar mass values, as they are giant stars and prioritised less than their dwarf counterparts by *TESS*.

Included within Fig. 5 is the comparison between our derived isochronic masses and those contained within the TIC. In our total sample, the median stellar mass is 1.21 $M_\odot$, compared to a slightly smaller mass of 1.11 $M_\odot$ for the subset of stars with mass measurements in the TIC. This is to be expected, since the TIC only includes mass measurements for dwarf stars. Our masses are slightly larger than those within the TIC, with a median increase of 11 per cent between our mass measurements and those in the TIC. This increase is slightly larger than our median relative error in stellar mass, being roughly 4 per cent. However, our median uncertainty is significantly smaller than that found within the TIC, with their median relative uncertainty being 13 per cent.

A Hertzsprung–Russell diagram of our results is shown in Fig. 6, based on GALAH DR2 $T_{\rm eff}$, log g, and ISOCHRONES-derived stellar luminosity. This sanity check confirms that none of our GALAH-*TESS* stars fall in unphysical regions of the H–R diagram parameter space. Using the definitions used in Sharma et al. (2018), hot dwarfs dominate the GALAH–*TESS* catalogue, accounting for 62 per cent of the stars (with 38 per cent being giant stars). A very small fraction of our sample are cool dwarfs, with only 52 such stars. This number of cool dwarf stars is consistent with GALAH being a magnitude-limited survey and the *TESS* goals of detecting exoplanets primarily around bright, nearby stars.

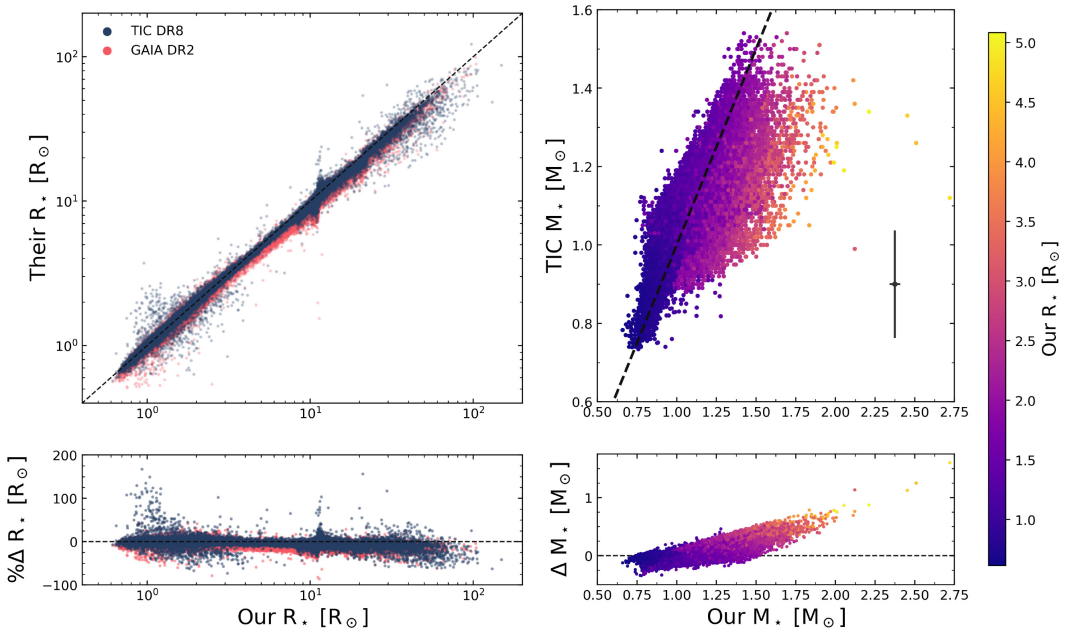

Figure 5. Left: Comparing the stellar radii of GALAH–*TESS* stars with the TIC (blue) and *Gaia* (pink). There is good overall agreement between the derived radius values, with a relative rms of 10 per cent and 14 per cent for *Gaia* DR2 and TIC values, respectively. An equality line is present in both plots, in the form of the dark grey dashed line. Right: Comparing our GALAH–*TESS* stellar masses with TIC-derived stellar masses. There is a good overall agreement between the derived `isochrone` masses and the TICs, with an rms of 0.12 $M_{\odot}$. Only dwarf stars within the TIC have mass measurements, and thus these comparisons are only valid for this luminosity class. Each star is coloured by its stellar radius, with median error bars given in the bottom-right corner.

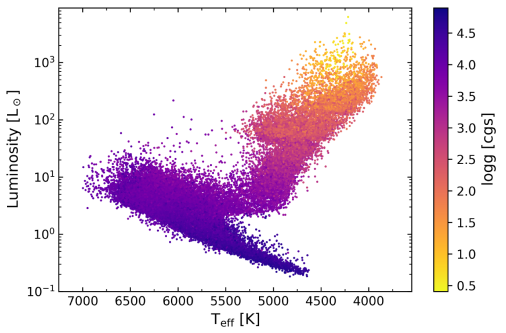

Figure 6. A Hertzsprung–Russell diagram of our GALAH–*TESS* catalogued stars using GALAH DR2's $T_{\rm eff}$ and our isochrone-derived luminosity values. Stars selected for our catalogue include both those on the main-sequence (lower right to mid-left; high log g) and evolved stars (mid-left to upper left; low log g). We have included giant stars within our catalogue as these stars are also known to host exoplanets, and it seems likely that analysis of *TESS*'s full-frame images will yield a number of new discoveries of this type.

3.2 Chemical abundances of GALAH–*TESS* stars

Our catalogue of ∼47 000 stars provides elemental abundances for up to 23 unique species derived from GALAH DR2 abundances. It is not possible, however, to provide accurate elemental abundances for all 23 elements for all of our target stars – and so we have only provided abundances for those species which can be reliably determined from each star's spectrum. As a result, 90 per cent of our sample have reliable O, Si, Mg, Si, Zn, and Y abundances, whilst just 2 per cent of the stars cataloged yield reliable Co abundances. In the most extreme case, only 23 stars in our catalogue have reliable, measured Li abundances. The median abundance values, along with the number of stars of which we have a particular abundance value for, can be found in Table 1. Generally, our catalogue median values are near Solar, with C, O, Al, K, and Fe median values being significantly sub-Solar, and Li, Co, Y, and La being significantly super-Solar (though Li suffers from small number statistics). Our distribution between selected elements and the measured Fe abundance is shown in Fig. 7. Given the paucity of Li measurements, we do not discuss the abundances of that element further in this work.[6]

To validate our stellar abundances, we made use of the online, interactive stellar abundance catalogue, the Hypatia Catalog Hinkel & Burger (2017a). The Hypatia Catalog is an amalgamation of stellar abundances, including physical and planetary parameters, for stars within 150 pc of the Sun (Hinkel et al. 2014, 2016; Hinkel & Burger 2017b). Comprised of mostly FGKM-type stars, the catalogue is compiled from more than 190 literature sources that can be normalized by several Solar normalizations, particularly Lodders et al. (2009). By using the Hypatia Catalog alongside the abundances within our sample, we can directly compare our abundances that use the same Solar normalization. We accessed the Hypatia Catalog on

[6]We direct the interested reader to Martell et al. (2020), and references therein, for a discussion of Li abundances from GALAH data, with a particular focus on the mechanisms by which different populations of stars can end up with dramatically different Li distributions.

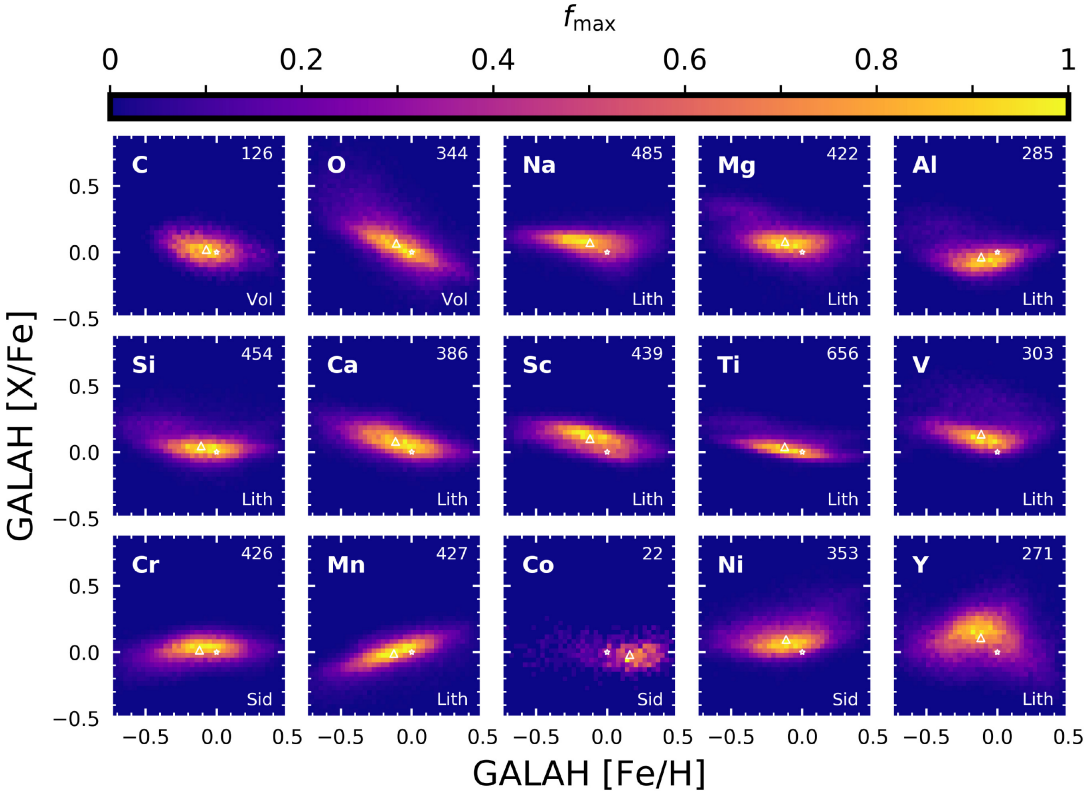

Figure 7. 2D histogram distributions of elemental abundances versus iron abundance for planet-building lithophile (Lith), siderophile (Sid), and volatile (Vol) elements. The Sun's values are represented on each plot by a white-bordered, hollow star, with the median values depicted by triangles. Since there are some elements that are easier to detect in a stellar photosphere than others, each bin is coloured by the fraction of the maximum bin value in each plot. The maximum bin value for each plot is given in the plot's top right-hand corner.

2020 August 6 and cross-matched our GALAH–*TESS* stars with stars within Hypatia by directly comparing their 2MASS identifiers.

Our GALAH–*TESS* catalogue contains data for 606 stars that are within 150 pc of the Sun, of which five matched with the Hypatia Catalog. Fig. 8 shows the comparison of elemental abundances for the five cross-matched stars, namely HD 121004, HD 138799, HD 139536, HD 89920, and HD 103197. HD 121004 is the only metal-poor star within our sample that was cross-matched with Hypatia, with the other four stars boasting super-Solar abundances. HD 121004, a G2V dwarf, has elemental abundances that show the best agreement with the abundances within Hypatia, with a median difference of 0.03 dex with those nine specific elements. The four iron-rich stars, which are all K dwarfs, show a minor discrepancy between their elemental abundances, with the GALAH abundances being enriched by 0.12–0.14 dex compared to Hypatia.

In terms of the abundance difference per element between our data and those presented in the Hypatia catalogue, the Ti abundances agree to within a median value of 0.03 dex, which is within the median 1σ error of GALAH–*TESS* and Hypatia Ti abundances for this sample, being 0.03 and 0.05 dex, respectively. The values for Ca, Al, and Na between the two catalogues differ by 0.08 dex, with the Fe, O, Si, Mg, and Ni abundances varying between the catalogues by between 0.12 and 0.16 dex. The GALAH DR2 abundances include non-Local Thermodynamic Equilibrium (non-LTE) effects for O (Amarsi et al. 2016a), Na, Mg (Osorio et al. 2015; Osorio & Barklem 2016), Al, Si (Amarsi & Asplund 2017), and Fe (Amarsi et al. 2016b) (Buder et al. 2018; Gao et al. 2018), whereas the Hypatia abundances (from Adibekyan et al. 2012) do not take into account non-LTE affects, which may explain the discrepancy between the difference in elemental abundance values.

We calculated the Mg/Si, Fe/Mg, Fe/Mg, and C/O abundance ratios using our GALAH–*TESS* [X/H] values and Solar values from Lodders et al. (2009). We only returned a ratio value if stars had both elements available to us, with 43 162 Fe/Si, 44 968 Fe/Mg, 41 741 Mg/Si, and 9521 C/O abundance measurements available. The limited C/O ratio measurements reflect the one atomic C line and two O lines available for reliable abundance measurements across HERMES' wavelength coverage and resulting detection limits. The median and 1σ error values for our selected GALAH–*TESS* abundance ratios are presented in Table 2. For reference, the Solar values for Fe/Si, Fe/Mg, Mg/Si, and C/O using Lodders et al. (2009) are 0.85, 0.81, 1.05, and 0.46, respectively.[7] Our abundance ratios all tend to have sub-Solar Fe/Si, Fe/Mg, Mg/Si, and C/O ratios. The

[7]Solar abundance ratios are calculated by $\log_{10}(X/Y)_{\odot} = A(X)_{\odot} - A(Y)_{\odot}$.

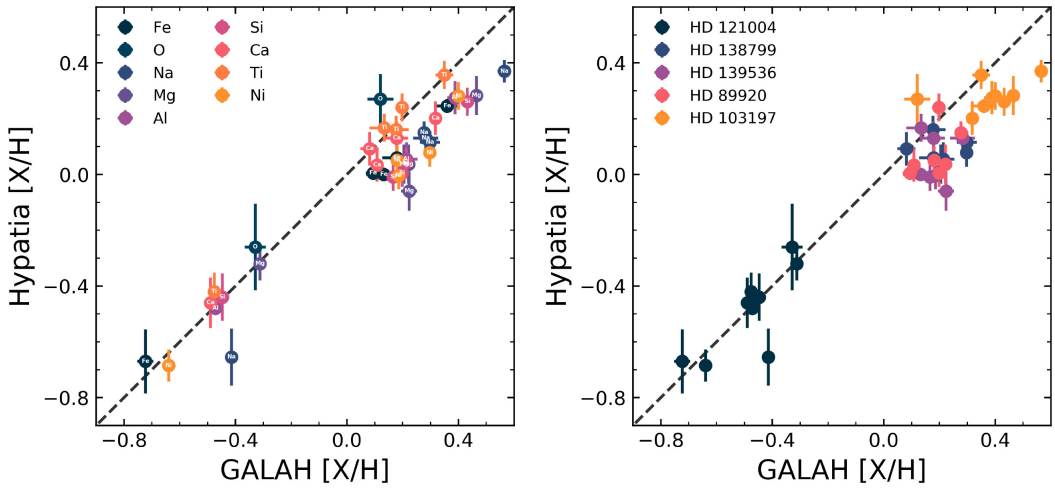

Figure 8. Both of these plots compare the elemental abundances for nine different elements across five stars cross-matched with the Hypatia Catalog (Hinkel & Burger 2017a). Left: Comparing by element with each element given a unique colour identifier. Right: Same plot as the left; however, abundances are now grouped by star, labeled by their Henry Draper catalogue (HD) identifier.

Table 1. Here, we present the median and 1σ error values for [X/H] abundances derived in our GALAH–*TESS* catalogue normalized by Lodders et al. (2009). We also give the number of stars in our catalogue for which a reliable value for the abundance in question was obtained. The 1σ error values here quoted are the median 1σ error values for each elemental abundance. The paucity of stars with a reliable Li abundance is particularly apparent.

X	Number of stars	[X/H] (dex)	X	Number of stars	[X/H] (dex)
Li	28	2.02 ± 0.06	Cr	38771	−0.07 ± 0.04
C	9716	−0.16 ± 0.07	Mn	39214	−0.07 ± 0.04
O	43297	−0.15 ± 0.07	Fe	47289	−0.12 ± 0.07
Na	44762	0.13 ± 0.05	Co	1057	0.14 ± 0.05
Mg	44972	−0.05 ± 0.03	Ni	39450	−0.00 ± 0.03
Al	24068	−0.14 ± 0.06	Cu	22598	0.04 ± 0.04
Si	43164	0.00 ± 0.01	Zn	43976	0.09 ± 0.02
K	34258	−0.29 ± 0.06	Y	43490	0.33 ± 0.04
Ca	41491	−0.06 ± 0.05	Ba	28751	0.02 ± 0.06
Sc	41641	−0.04 ± 0.05	La	8522	0.17 ± 0.05
Ti	39205	−0.07 ± 0.06	Eu	5799	−0.06 ± 0.05
V	27403	0.09 ± 0.04	–	–	–

Table 2. Median and 1σ error values for our GALAH–*TESS* abundance ratios. The majority of our stars have Mg/Si, Fe/Mg, and Fe/Mg values; however, only 20 per cent have reliable C/O measurements.

	Number of stars	(X/Y)	$(X/Y)^a_\odot$
Fe/Si	43162	0.65 ± 0.22	0.85
Fe/Mg	44968	0.68 ± 0.23	0.81
Mg/Si	41741	0.98 ± 0.22	1.05
C/O	9521	0.44 ± 0.13	0.65

[a]Solar values from Lodders et al. (2009).

distribution of our C/O and Mg/Si values are plotted against each other in Fig. 13, and are discussed in more detail in Section 4.2.

Stellar elemental abundances can change slightly, depending upon the Solar normalization used to derive such abundances. To illustrate this, we have then created Fig. 9 to show the distribution of our [X/H] abundances for planet-building elements scaled to the various Solar normalizations that are widely used within exoplanetary science. These rocky-planet building elements include the volatiles, which typically reside in the atmosphere (C, O), the lithophiles, which are present in the crust/mantle of rocky planets (Na, Mg, Al, Si, Ca, Sc, Ti, V, Mn, Y), and the siderophiles, which easily alloy with Fe and primarily reside in the core (Cr, Fe, Co, Ni) (Hinkel et al. 2019). Having six different normalizations means that each star in the sample is counted six times. However, this allows the skewed distributions from the different methods to be assessed in a single figure, and forms the basis for Fig. 9, where we present the skews for all sixteen planet-building elements.

From Fig. 9, it is readily apparent that there is general overall agreement among our abundances normalized by Lodders et al. (2009), when compared to other distributions with the total median of the distributions falling within 1σ of our L09 values. Volatile elements such as C and O and lithophiles Na and Mg tend to negative [X/H] values in older normalizations compared to newer normalizations that instead peak towards super-Solar values. We have incorporated Fig. 9 into this work to show the exoplanetary community the importance of referencing what Solar normalizations are used within their work, as abundance values will differ depending upon these normalizations. Larger changes can be seen in the spread of median C/O, Mg/Si, and Fe/Mg abundance ratios for these different Solar normalizations. The spread of our median C/O values vary from 0.44 to 0.64, from 0.98 to 1.35 for Mg/Si, and from 0.58 to 1.39 for Fe/Mg depending upon what Solar normalization is used. Changing the value of Mg/Si for a given planet would have the primary effect of altering the mantle mineralogy between olivine rich and pyroxene rich (Hinkel & Unterborn 2018; Unterborn & Panero 2017; Brewer & Fischer 2016; Thiabaud et al. 2014a, 2015). These differences in composition are known to change the degree of melting and crustal composition (Brugman, Phillips & Till 2020), but the degree that that composition changes the interior behaviour of a rocky exoplanet remains an area of active research. These results therefore highlight the importance of normalizing abundances to the same Solar normalizations when comparing chemical abundances

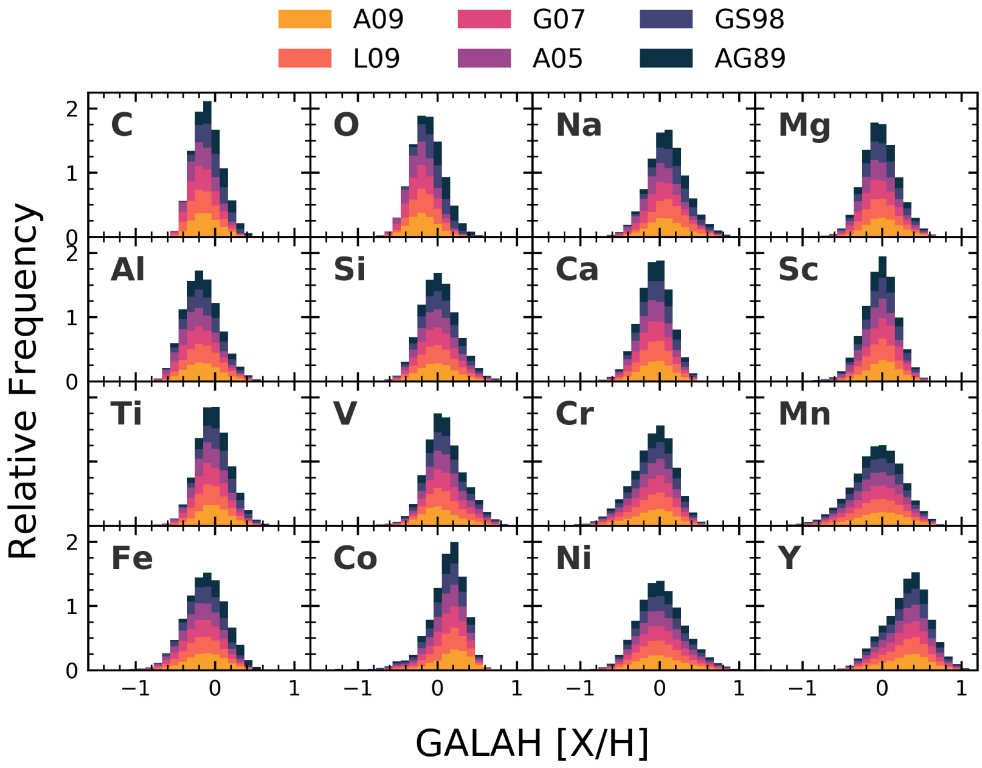

Figure 9. The same distribution of planet-building elements as found in Fig. 7. Here, however, we have normalized our [X/H] values to various Solar normalizations including Asplund et al. (2009), Lodders et al. (2009), Grevesse, Asplund & Sauval (2007), Asplund, Grevesse & Sauval (2005), Grevesse & Sauval (1998), and Anders & Grevesse (1989), displayed in yellow, orange, pink, purple, violet, and navy, respectively. Combining the stellar abundances in this manner with different Solar normalizations shows the general trends within a certain element, unbiased by using a specific Solar normalization.

from different surveys and considering the implications those results might have on inferring the structure of rocky exoplanets.

4 DISCUSSION

In this section, we discuss the refinement of planetary systems with the newly derived GALAH–*TESS* stellar parameters (Section 4.1) and how the X/Y molar abundance ratios of stars within GALAH–*TESS* can inform us in forward predicting what possible planetary systems and makeups these stars may host (Section 4.2).

4.1 Refining planetary system parameters

Within our GALAH–*TESS* sample, we cross-matched our GALAH–*TESS* sample with the catalogue of known planetary systems on NASA's Exoplanet Archive and TOIs or CTOIs by accessing the Exoplanet Follow-up Observing Program for *TESS* (ExOFOP–TESS)[8] website. At the time of writing, the GALAH–*TESS* catalogue contains three confirmed single-planet systems: WASP-61 (Smith et al. 2012), WASP-182 (Nielsen et al. 2019a), and HD 103197 (Mordasini et al. 2011). Our catalogue also includes five single-planet candidate systems namely TOI-745, TOI-815, TOI-1031, TOI-777, and TOI-1126. We should note that WASP-61b is also known as TOI 439.01. Lastly, there are also three CTOI planetary systems, two of which host two candidates, TIC 201256771 and TIC 220402290. The other CTOI system is a three-planet candidate system, TIC 300903537. A brief summary of the revised stellar parameters for these 11 confirmed and candidate exoplanet hosts are summarized in Table 3.

The calculated radius of an exoplanet is directly related to the radius of its host star – so any change in stellar radius will change the radius of the planet. All of our exoplanets and candidates have transit depth measurements from *TESS*, which we obtain from ExOFOP-TESS, except for WASP-182b and HD 103197b. For the short-period transiting exoplanet WASP-182b, there is currently no transit data from *TESS*. Instead, we use the transit depth values from its discovery paper (Nielsen et al. 2019a) to refine its radius. Unfortunately, at the time of writing, the longer-period exoplanet HD 103197b has not been observed to transit its host, and no direct size determination is possible.

A brief summary of the revised planetary radii for the 14 confirmed and candidate exoplanets are summarized in Table 4 along with the transit depth and literature planetary radii against which we are able to compare our results.

By far the most surprising result from our refinement of planetary radii is the refinements of two planetary candidates orbiting the

[8]https://exofop.ipac.caltech.edu/; accessed 6 August 2020 August 6.

Table 3. Our stellar physical parameters of matched confirmed and candidate exoplanet hosts. For CTOI hosts, since their CTOI ID is simply their TIC ID, we have omitted this column from the table. [M/H] in this table is the overall metallicity and not the host star's iron abundance, [Fe/H].

Catalogue ID	TOI ID	TIC ID	$T_{\rm eff}$ (K)	[M/H] (dex)	log g (cgs)	$M_\star$ ($M_\odot$)	$R_\star$ ($R_\odot$)
WASP-61	439	13021029	6245 ± 58	-0.06 ± 0.08	4.03 ± 0.17	1.20 ± 0.03	1.38 ± 0.02
UCAC4 238-060232	754	72985822	6096 ± 59	0.13 ± 0.08	4.16 ± 0.17	1.16 ± 0.04	1.21 ± 0.03
CD-43 6219	815	102840239	4954 ± 34	0.13 ± 0.05	4.46 ± 0.11	0.83 ± 0.01	0.76 ± 0.01
UNSW-V 320	–	201256771	4979 ± 50	0.04 ± 0.07	3.42 ± 0.15	1.29 ± 0.09	3.22 ± 0.07
CD-57 956	–	220402290	5817 ± 41	0.08 ± 0.06	4.33 ± 0.13	1.04 ± 0.03	1.10 ± 0.01
UCAC4 306-282520	–	300903537	4841 ± 83	0.2 ± 0.09	4.41 ± 0.19	0.82 ± 0.02	0.80 ± 0.01
HD 81655	1031	304021498	6415 ± 44	-0.19 ± 0.06	3.88 ± 0.14	1.32 ± 0.04	1.89 ± 0.02
HD 106100	777	334305570	6187 ± 35	0.12 ± 0.05	3.82 ± 0.11	1.28 ± 0.02	1.54 ± 0.02
WASP-182	–	369455629	5615 ± 50	0.32 ± 0.07	4.15 ± 0.15	1.05 ± 0.03	1.25 ± 0.02
HD 103197	–	400806831	5223 ± 32	0.35 ± 0.04	4.43 ± 0.11	0.94 ± 0.02	0.90 ± 0.01
TYC 7914-01572-1	1126	405862830	5108 ± 55	0.09 ± 0.08	4.66 ± 0.17	0.82 ± 0.02	0.74 ± 0.01

Table 4. Our refined planetary radii values for confirmed and TESS candidate exoplanets. All literature radius values and transit depth values come from ExOFOP-TESS except for WASP-182b, where its literature planetary radius and transit depth values are from Nielsen et al. (2019a). We have flagged problematic planetary candidates in bold. From our revised planetary radii, CTOI 201256771.01 and CTOI 201256771.02 now have radii comparable to the Sun, and thus are not exoplanets. The orbital periods of CTOI 220402290.01, CTOI 220402290.02, CTOI 300903537.01, and CTOI 300903537.02 are problematic and are likely duplications of the same event. This is discussed further in Section 4.1. Since some of these planet candidates are comparable in scale to that of Jupiter, the conversion between Jupiter's radius to Earth's is $R_J = 11.209\ R_\oplus$.

TOI/CTOI ID	TIC ID	ΔF (mmag)	Our R_p ($R_\oplus$)	Literature R_p ($R_\oplus$)
439.01	13021029	9.04283 ± 0.00143	13.68 ± 0.20	13.27 ± 0.47
754.01	72985822	8.93564 ± 0.50239	12.00 ± 0.48	13.90 ± 13.91
815.01	102840239	1.25 ± 0.00155	2.81 ± 0.03	2.87 ± 0.13
201256771.01	**201256771**	**84.34287 ± 8.98023**	**96.17 ± 5.34**	**24.72**
201256771.02	**201256771**	**97.59384 ± 10.39110**	**103.15 ± 5.69**	**26.51**
220402290.01	**220402290**	**21.84594 ± 2.32600**	**17.02 ± 0.93**	**17.15**
220402290.02	**220402290**	**44.09427 ± 4.69485**	**24.05 ± 1.30**	**24.25**
300903537.01	**300903537**	**94.16304 ± 10.02582**	**25.06 ± 1.33**	**25.10**
300903537.02	**300903537**	**11.02043 ± 1.17338**	**8.74 ± 0.48**	**8.75**
300903537.03	300903537	3.74782 ± 0.39904	5.10 ± 0.28	5.11
1031.01	304021498	1.18 ± 0.00172	6.80 ± 0.08	6.91 ± 0.46
777.01	334305570	2.80673 ± 0.08351	8.56 ± 0.16	7.32 ± 1.15
WASP-182 b	369455629	0.01067 ± 0.00000	8.90 ± 0.15	9.53 ± 0.34
1126.01	405862830	1.06 ± 0.00144	2.53 ± 0.02	2.62 ± 0.11

star TIC 201256771. Currently, TIC 201256771 hosts two CTOIs, 201256771.01 and 201256771.02, which are recorded on ExOFOP–TESS as having radii of $24.72 R_\oplus$ and $26.51 R_\oplus$, respectively. With our revised radii, these candidate events observed in TESS Sector 1 now have radii comparable with stellar radii (Chen & Kipping 2017) of $96.17 \pm 5.34 R_\oplus$ and $103.15 \pm 5.69 R_\oplus$, respectively. This casts serious doubts about the planetary nature of these candidate events, especially with their orbital periods being only separated by 17 min, with the orbital periods of CTOI-201256771.01 and CTOI-201256771.02's being stated as 3.754861 and 3.766667 d, respectively. Upon further investigation, this system is a known eclipsing binary that has an orbital period nearly equal to the candidates, being 3.76170 d (Christiansen et al. 2008). From this data alone, we conclude that CTOI 201256771.01 and CTOI 201256771.01 are candidates of the same event, being the transit of the eclipsing companion to UNSW-V 320. Apart from this extreme example, the rest of our planetary radii fall nicely within the current literature values and their uncertainties, all of which can be found in Table 4. Upon the revision of this CTOI system, we re-checked the sensibility of the other CTOI systems within our planet-host sample. The orbital periods of CTOI 220402290.01 and CTOI 220402290.02 are 0.7833 and 0.7222 d, respectively, or roughly 90 min. This would mean that their orbital separation would be comparable to their radii, which deems this system as extremely unstable. These transit events are likely caused by a single candidate, rather than two. Similarly, the orbital periods of CTOI 300903537.01 and CTOI 300903537.02 only differ by 36 min and are likely caused by the same candidate.

Of our known confirmed and candidate exoplanets, only three have measured mass values. The most conventional way that an exoplanet's mass is determined is through the radial velocity technique. Specifically, an exoplanet's line-of-sight mass, $M_p \sin i$ is determined through measurement of the semi-amplitude of the host's radial velocities measurement, K_{RV}, orbital eccentricity, e, period P, and stellar mass $M_\odot$ (Lovis & Fischer 2010). If the orbital inclination, i, of the system is known, traditionally found through fitting models to the photometric transit curve, we can then calculate the planet's true mass, M_p.

We use literature values for these planetary systems, namely WASP-182b values from Nielsen et al. (2019a) as well as WASP-61b and HD 103197b values from Stassun, Collins & Gaudi (2017). We combine these with the masses of their host stars in order to revise the planetary mass of the exoplanets. Our revised planetary mass values, along with the previous literature values, can be found in Table 5. As with the refined radii results, there is excellent overall

Table 5. With our newly derived stellar mass values, we have refined the mass of three exoplanets, WASP-61 b, WASP-182b, and HD 103197 b. In this table, we have used our new stellar mass values, along with literature semi-amplitude (K) and orbital eccentricity (e), period (P), and inclination (i) values to derive the new planetary mass values.

Planet Name	TIC ID	K_{RV} (ms^{-1})	P (d)	e	i (deg)	Our M_p ($M_\oplus$)	Literature M_p ($M_\oplus$)
WASP-61 b	13021029	233 ± 0	3.8559 ± 3.00e-06	0	89.35 ± 0.56	646.01 ± 9.82	851.784 ± 266.977
WASP-182 b	369455629	19 ± 1.2	3.376985 ± 2.00e-06	0	83.88 ± 0.33	46.41 ± 3.05	47.039 ± 3.496
HD 103197 b	400806831	5.9 ± 0.3	47.84 ± 0.03	0	–	32.06 ± 1.67*	28.605 ± 6.357*

Note. Literature values for WASP-182b come from Nielsen et al. (2019a) and WASP-61b and HD 103197b's values are from Stassun et al. (2017). Asterisk (∗) denotes that HD 103187b's mass is actually $M_p \sin i$ in this current form, as there is yet to be any inclination data retrieved from this particular planetary system. Since some of these exoplanets are comparable in scale to that of Jupiter, the conversion between Jupiter's mass to Earth's is $M_J = 317.83\ M_\oplus$.

agreement with our mass values compared to the literature. All three refined planetary mass values fall within 1σ error bars of the previous literature values. The biggest increase of planetary mass precision with our results comes from the Jovian type exoplanet HD 103197 b. We have refined the mass of HD 103197b from a percentage error of 31 per cent down to 2 per cent, thanks largely due to the refinement in the stellar mass of HD 103197.

Overall, our refined planetary mass and radius results are in good agreement with their literature values. This also validates the overall good agreement with our refined stellar mass and radius values. Even though the change in planetary mass or radius of 10–20 per cent might intuitively be insignificant in re-characterizing Jovian worlds, it does however have larger implications for smaller planets like our own.

For example if an Earth-like planet in mass and radius ($1.0R_\oplus$,$1.0M_\oplus$), characterized by the TIC, was discovered orbiting around any of our GALAH–*TESS* stars, would this planet still be 'Earth-like' with our revised stellar parameters? Using a similar approach to that of Johns et al. (2018), we can refine the planetary radius and mass of this fictitious Earth using both GALAH-*TESS* and TIC catalogue values of stellar and planetary mass and radius values.

Our refined radius and mass values for these fictitious Earth-like exoplanets are displayed in Fig. 10. Roughly 85 per cent of our planets fall within ±10 per cent of Earth-like mass and radius values. Beyond this ±10 per cent, there is a wide variety of mass and radius values throughout the plot, which would suggest that these exoplanets that were once thought to be Earth-like, are now anything but. From Fig. 10, there are varying degrees of bulk composition for these 'Earth-like' worlds. In extreme cases, a putative 'Earth-like' planet's bulk density varies between a scaled-up Enceladus-like world (i.e. dominated by layers of water and a silicate core) (Schubert et al. 2007; Zolotov et al. 2011), to a possible remnant Jovian-world core dominated by iron (Benz et al. 2007; Mocquet, Grasset & Sotin 2014) with the habitability of such worlds still up for debate (Noack, Snellen & Rauer 2017; Kite & Ford 2018; Lingam & Loeb 2019). This shows that not only do we need better precision for stellar masses and radii, which better constrain the planetary mass and radius values, but there also needs to be a level of consistency across these fundamental parameters for future follow-up characterization.

There are already a wide variety of planetary radius and mass values for known super-Earth and Earth-sized worlds and thus there will be a wide variety of planetary compositions. A fundamental problem with inferring planetary compositions through mass–radius or ternary/quaternary diagrams (Rogers & Seager 2010; Brugger et al. 2017) is that they cannot uniquely predict the interior composition of a given exoplanet. A variety of different interior compositions can lead to identical mass and radius values (Dorn et al. 2015; Unterborn et al. 2016; Suissa et al. 2018; Unterborn & Panero 2019). This gives rise to an inherent density degeneracy problem. A wide variety of planetary compositions are allowed, especially if the models used have three or more layers. This is typical for most that assume a three (core, mantle, ocean) or four-layered planet (core, mantle, ocean, atmosphere). Current Bayesian inference (Dorn et al. 2015) and forward models (Unterborn et al. 2018a; Unterborn, Desch & Panero 2018b) break down this degeneracy, using stellar abundance ratios to infer an exoplanet's composition. These abundance ratios and their importance are described in Section 4.2.

4.2 Importance of stellar abundances to exoplanetary science

Within our own Solar system, observations show that the relative abundances of refractory elements such as Fe, Mg, and Si, elements crucial in forming rocky material for planets like ours to build upon, are similar within the Sun, Earth, Moon, and Mars (Wang et al. 2019b; Lodders 2003; McDonough & Sun 1995; Wanke & Dreibus 1994). The bulk planetary and stellar ratios of these elements during planetary formation are also similar, suggesting that stellar Fe/Mg and Mg/Si can assist with determining the building blocks of the planets they host (Bond et al. 2010b; Thiabaud et al. 2015, 2014a). These elemental abundances can help us understand what elements favour certain planetary architectures and can also provide constraints on the internal geological composition of exoplanets (Brugger et al. 2017; Dorn et al., 2015, 2017a; Unterborn et al. 2018a).

In particular, the elemental abundance ratios of Mg/Si, Fe/Mg, and C/O are fundamental for probing the mineralogy and structure of rocky exoplanets. The formation, structure, and composition of exoplanets is extremely complex, with these generalizations not taking into account planetary migration or secondary processes such as giant impacts. A more comprehensive analysis of GALAH DR2's abundances trends, galactic populations and implications for planet-building elements can be found in Bitsch & Battistini (2020) and Carrillo et al. (2020).

4.2.1 Estimating the size of a rocky planet's core through stellar Fe/Si ratios

The amount of mass contained within a rocky exoplanet's core is determined by its Fe/Si ratio (Brugger et al. 2017; Dorn et al. 2015; Unterborn et al. 2018a). An increasing Fe/Si ratio would result in a larger core mass fraction compared to a larger mantle core fraction for smaller values of Fe/Si. Within our Solar system, Earth (McDonough 2003; McDonough & Sun 1995), and Mars (Wanke & Dreibus 1994) have comparable bulk Fe/Si values to that of photospheric Solar values (Lodders et al. 2009; Lodders 2003). Mercury, however, is an anomaly with its bulk Fe/Si value estimates ranging from ∼5 to 10,

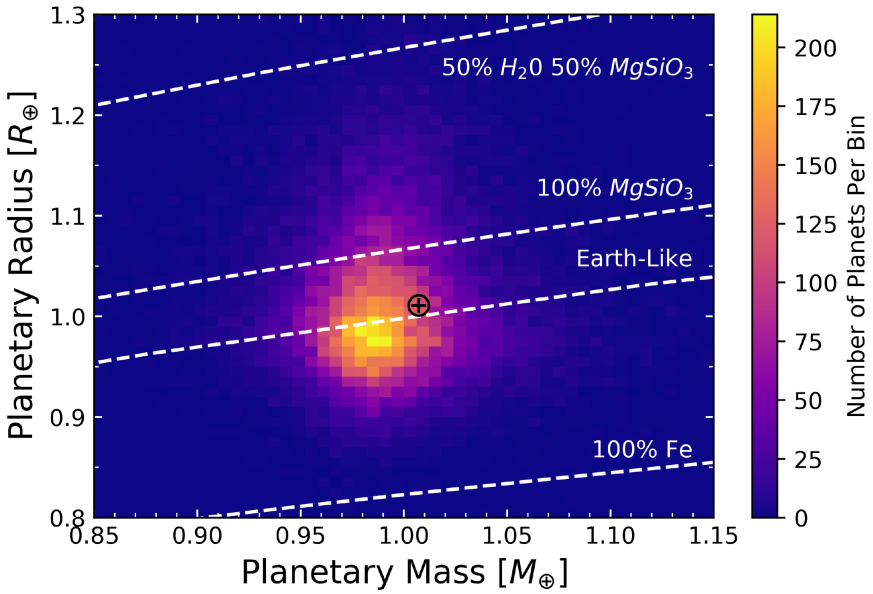

Figure 10. Simulation for the effects of parameter refinement on the mass and radius for a fictitious Earth-like planet discovered using the TIC catalogue. The mass–radius relationships used for the dashed lines to show density curves for a 50 per cent water-50 per centrocky, pure rocky (containing pure post-perovskite $MgSiO_3$), 'Earth-like' (33 per cent Fe and 67 per cent rock) and pure iron worlds are from (Zeng, Sasselov & Jacobsen 2016). The black symbol '⊕' represents the Earth's mass and radius. In extreme cases, a putative 'Earth-like' planet varies between a scaled-up Enceladus-like world (i.e. dominated by layers of water and a silicate core), to a Fe-enriched, Mercury-like planet. This simulation shows the need for consistency and precision in exoplanetary mass and radius determination for meaningful comparative planetology.

corresponding to a core mass fraction of ∼45–75 per cent compared to a Fe/Si ratio near ∼1.00 and a core mass fraction of 32 per cent for Earth (Nittler et al. 2017; Brugger et al. 2018; Wang et al. 2019b).

It is possible for the majority of iron to be contained within silicate material including bridgmanite ($MgSiO_3$/$FeSiO_3$), magnesiowüstite (MgO/FeO), olivine (Mg_2SiO_4/Fe_2SiO_4), and pyroxenes ($Mg_2Si_2O_6$/$Fe_2Si_2O_6$) for bulk Fe/Si values less than 1.13 (Alibert 2014). For Fe/Si $>$ 1.13, models suggest that an iron core needs to be present within a rocky exoplanet to explain such a high ratio. This limit is calculated by simple stoichiometry and may not reflect the actual distribution of iron throughout a rocky exoplanet's core and mantle. The oxygen fugacity can also affect the distribution of a planet's iron distribution (Bitsch & Battistini 2020), oxidizing with mantle constituents instead of being differentiated into a core if the oxygen fugacity is too high (Elkins-Tanton & Seager 2008). This would result in a lower core mass fraction compared to situations of lower fugacity. Current models show that iron can be taken up in the mantle (Dorn et al. 2015; Unterborn et al. 2018a) as well as silicon being taken up within an iron core (Hirose, Labrosse & Hernlund 2013). Thus, Fe/Mg is a better proxy for core-to-mantle ratio and is produced within the GALAH–*TESS* catalogue.

Fig. 11 shows the distribution of Fe, Mg, and Si for our sample of GALAH–*TESS* stars. We can calculate the core mass fraction of potential rocky planets hosted by GALAH-*TESS* stars, using stiochiometry by the equation:

$$\mathrm{CMF} = \frac{\#\mathrm{Fe}\mu_{\mathrm{Fe}}}{\#\mathrm{Mg}(\mu_{\mathrm{Mg}} + \mu_O) + \#\mathrm{Si}(\mu_{\mathrm{Si}} + 2\mu_O) + \#\mathrm{Fe}\mu_{\mathrm{Fe}}} \quad (3)$$

where $\#X$ represents the molar abundance of element X and μ_X is the molar weight of that element. We are able to use this estimation as Fe, Mg, and Si all have similar condensation temperature (Lodders et al. 2009) and thus thermal processes are unlikely to fractionate the elements relative to each other. That is while a planet may have significantly fewer atoms of Fe and Mg than the host star, the Fe/Mg ratio of the star and planet may only be different by ∼10 per cent (Bond et al. 2010a; Thiabaud et al. 2014b; Unterborn & Panero 2017). While mantle stripping by large impacts may increase the planet's Fe/Mg ratio (e.g. Bonomo et al. 2019), equation (3) represents a reasonable upper-bound for CMF for most systems. As mentioned above, changes in oxygen fugacity will convert some core Fe into mantle FeO, which will lower the CMF for a given bulk composition. From this ternary we can see that stellar abundances outline a wide range of CMF compared to the Earth and Sun, with their abundances falling near the middle of the distribution (Fig. 12). Less than 0.3 per cent of our stars have Fe/Si $>$ 1.13 (Fig. 12); therefore, the rocky planets possibly orbiting GALAH-*TESS* stars may have their iron content distributed between both core and mantle layers with marginally lower CMF than predicted in Fig. 11.

4.2.2 Mantle compositions of rocky exoplanets through stellar host Mg/Si and C/O ratios

The structure and composition of super-Earths and sub-Neptunes can be constrained through theoretical models using their host's Mg/Si and C/O elemental ratios. The stellar C/O abundance chemically controls the silicon distribution amongst oxides and carbides (Bond et al. 2010b; Carter-Bond et al. 2012; Duffy, Madhusudhan & Lee 2015). For those stars with C/O values less than 0.8, Mg/Si controls the mantle chemistry by varying the relative proportions of olivine,

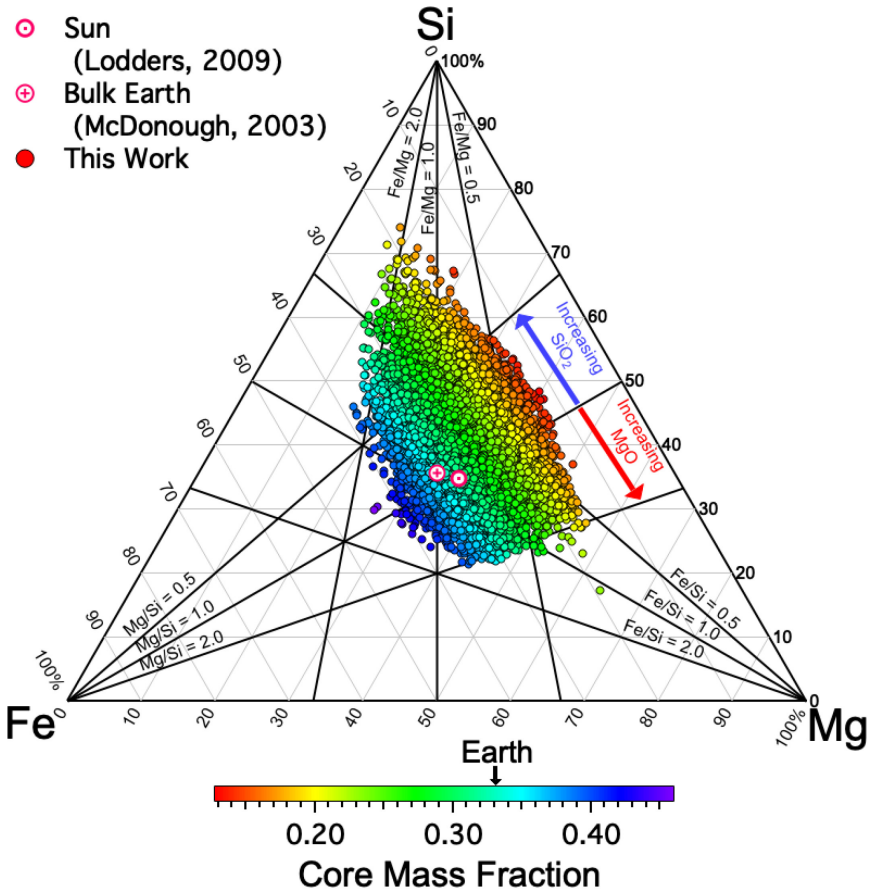

Figure 11. Ternary diagram of the Fe, Mg, and Si abundances from the for our GALAH–*TESS* stars, assuming a Solar abundance model of Lodders et al. (2009). In general, the closer to an individual corner of the ternary a data point falls the greater the proportion of that element in the resulting planet assuming stellar composition roughly reflects planetary composition (Bond et al. 2010a; Thiabaud et al. 2014b; Unterborn & Panero 2017). Individual points are colour coded to show the maximum core mass fraction (CMF) of the planet, assuming all Fe is present in the core and Mg and Si are in their oxide forms (MgO, SiO_2). The Earth (McDonough 2003) and Solar (Lodders et al. 2009) abundances are shown for reference.

pyroxenes and oxides. However, within this realm of low C/O values, there are two distinct regimes in which the Mg and Si are distributed within the mantle:

(i) In a 'silicon-rich' environment, whereby the Mg/Si < 1, the upper mantle will be dominated by ortho- and clino-pyroxene, majoritic garnet ($Mg_3(MgSi)(SiO_4)_3$) as well as SiO_2 (either as quartz or coesite) with the lower mantle consisting of bridgmanite ($(Mg,Fe)SiO_3$) and stishovite (SiO_2). As Mg/Si decreases, the proportion of stishovite will increase at the cost of brigmanite in the lower mantle.

(ii) For larger values of Mg/Si, where Mg/Si > 1, a rocky planet's upper mantle will mostly comprise of olivine (Mg_2SiO_4), pyroxenes and majoritic garnet, with bridgmanite and magnesiowüstite (or ferropericlase) ((Mg,Fe)O) in lower mantle. As the Mg/Si ratio increases, so does the amount of olivine and ferropericlase within the rocky planet's upper and lower mantle respectively. This regime of planetary composition is akin to rocky worlds (i.e. Mars and Earth) within our Solar system and thus labelled as 'terrestrial-like' mantle compositions within our paper (Unterborn & Panero 2017; Duffy et al. 2015; Carter-Bond et al. 2012; Bond et al. 2010b). As Mg/Si increases, the proportion of magnesiowüstite will increase at the cost of brigmanite in the lower mantle.

However, these compositions only extend for C/O < 0.8. For C/O > 0.8, exotic mantle compositions of graphite and the carbides including SiC can start to dominate the geological composition of an exoplanet's core and mantle, when planets form within a protoplanetary disck's innermost region (Kuchner & Seager 2005; Carter-Bond et al. 2012; Unterborn et al. 2014; Wilson & Militzer 2014; Nisr et al. 2017; Miozzi et al. 2018;). These 'carbon-rich' worlds can extend out through carbon-rich discs and can even form with C/O ratios as low as 0.67 (Moriarty, Madhusudhan & Fischer 2014). However, the habitability of such worlds is still under debate, with some studies suggesting that habitability is unlikely. This is because theoretical models suggest that these worlds would likely be geodynamically inactive planets and would limit the amount of carbon-dioxide degassing into its atmosphere (Unterborn et al. 2014).

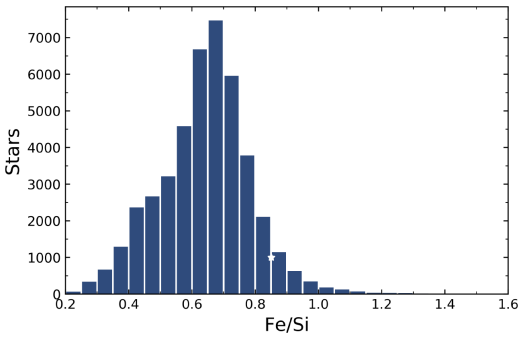

Figure 12. Of the 47 285 stars within our sample, only 134 have Fe/Si values greater than 1.13 which would indicate the vast majority of our possible rocky worlds will have their iron content distributed between their iron and mantle layers. An iron-core must be present beyond Fe/Si values of 1.13 to explain such a high Fe/Si ratio. The white star within the histogram depicts the Sun's photospheric Fe/Si value of 0.85 (Lodders et al. 2009).

Our C/O and Mg/Si distribution for the GALAH–*TESS* stars are found in Fig. 13. Of our 47 000+ sample, only 8832 stars have C/O and Mg/Si ratios as most stars' C or O abundances were flagged by *The Cannon*. This sample also includes exoplanet host WASP-61 and candidate hosts UCAC4 238-060232 (TOI-754) and HD 81655 (TOI-1031). A total of 53.6 per cent of these stars have C/O < 0.8 and Mg/Si > 1 values, suggesting that these stars may potentially host exoplanets that would have compositions akin to planets found within our own Solar system, including both known exoplanet-hosting stars WASP-61 and TOI-754. Both WASP-61 and TOI-754 however are only known to host Jupiter-sized worlds that would have significantly different core structures to that of smaller super-Earth and sub-Neptune exoplanets (Mocquet et al. 2014; Fortney & Nettelmann 2010; Buhler et al. 2016). However, future studies may discover smaller worlds around these stars. Within our GALAH-*TESS* sample, 46.4 per cent of stars have Mg/Si and C/O ratios suggesting that these stars could possibly host rocky planets that are 'silicon-rich' compared to planets found within our Solar system. The candidate exoplanet host TOI-1031 is such a system that could boast Silicon-rich worlds with an Mg/Si value of 0.91 ± 0.20.

Distributions of Mg/Si similar to the ones we find within our sample have also been discovered with other surveys: ∼60 per cent of the Brewer & Fischer (2016) sample of FGK dwarfs in the local neighbourhood also falls between $1 <$ Mg/Si. Photospheric measurements of planet-hosting stars show a range of Mg/Si values ranging from 0.7 to 1.4 (Delgado Mena et al. 2010; Brewer & Fischer 2016), while our planet host and candidate stars Mg/Si values range from 0.9 to 1.1. Our median Mg/Si value is 0.98 ± 0.22 which is lower than Brewer & Fischer (2016)'s Mg/Si median value of 1.02. The larger spread of Mg/Si values in other surveys might be due to different Solar normalizations but seems more likely that this is due to a different stellar sample and methodologies to derive chemical abundances. Hinkel et al. (2014) showed that even for iron, the spread in for the same stars gathered from various groups was 0.16 dex. Thus, more work is needed to better understand the underlying systematics and variations of stellar abundances from various surveys and research groups (Hinkel et al. 2016; Jofré et al. 2017; Jofré, Heiter & Soubiran 2019).

Surprisingly, less than 1 per cent of GALAH–*TESS* stars have a C/O ratio greater than 0.8, suggesting that these stars may host 'Carbon-Rich' worlds, that will have geological structures unlike any object within our Solar system. Our median C/O value is 0.44 ± 0.13 which is somewhat comparable to other stellar surveys (Delgado Mena et al. 2010; Petigura & Marcy 2011; Amarsi et al. 2016a; Brewer & Fischer 2016; Suárez-Andrés et al. 2018) and population statistics (Fortney 2012) – but could be an overestimate from galactic chemical evolution models (Fortney 2012). The discrepancies between these surveys are likely due to different stellar populations, methodologies used to derive stellar abundances, the single C line used in GALAH DR2 (658.761 nm), or Solar normalizations used as discussed in Section 3.2.

We should note that GALAH's [O/H] abundances do account for non-LTE effects but are only taken from the triplet O_I lines near ∼777.5 nm (Amarsi et al. 2016a; Buder et al. 2018; Gao et al. 2018). This triplet is known to over-estimate abundances if non-LTE effects are not taken into account (Teske et al. 2013). Brewer & Fischer (2016)'s approach considers molecular OH lines and numerous more carbon lines, such that our results might be overestimated with respect to theirs. Teske et al. (2014) found that there is currently no significant trend between planet hosts, in particular the occurrence of hot-Jupiters, and their C/O values.

4.2.3 How are stellar abundances linked to planetary formation?

There is theoretical evidence suggesting that the abundance ratios of refractory materials stay relatively constant throughout a protoplanetary disc, but it is misleading to suggest that volatile abundance ratios will be constant through the disc. This evidence includes the fact that the relative ratios of many elements in the protoplanetary disc do not change during planet formation, including the dominant rocky-planet-building elements: Fe, Mg, and Si (Bond et al. 2010b; Thiabaud et al. 2015). For example, 95 per cent of all atoms in the Earth can be accounted for via Fe, Mg, and Si, along with the constituent oxygen brought in their oxide forms (e.g. rocks containing Mg as MgO, Si as SiO_2 etc., McDonough 2003). In addition, the Sun, Earth, and Mars all agree to within 10 per cent in the relative proportions of the major rocky planet building elements (Waenke & Dreibus 1988; Lodders 2003; McDonough 2003). Mercury, due to its high CMF, does not follow the same similarity; however, stellar abundances can better help us classify planets as Mercury like. Recent work by Schulze et al. (2020) confirms that the molar ratios for refractory elements will be similar for rocky worlds and their host stars. But, work done by Plotnykov & Valencia (2020) contradicts this result, showing that the composition of rocky worlds likely spans a greater range than their host stars. Now with Adibekyan et al. (2021) showing that there might be a linear relationship with a planet's composition and that of its host-star, this assumption is starting to weaken.

Elemental abundance ratios can also change through a protoplanetary disc depending upon the concentration of material and temperature profile of the disk (Bond et al. 2010b; Carter-Bond et al. 2012; Unterborn & Panero 2017). There are studies that suggest that estimates of the devolatilization process within a protoplanetary disc could aid in determining the bulk elemental abundances of rocky worlds, assuming they have formed where they are currently situated within their own planetary system (Wang et al. 2019b).

If we want to determine if a world has bulk composition as the earth, studies suggest that the errors with the elemental abundances themselves need to be further refined with uncertainties better than ∼0.04 dex needed for such a comparison (Hinkel & Unterborn 2018; Wang et al. 2019b). Even further, if we want to differentiate between unique planetary structures within a rocky exoplanet population, the

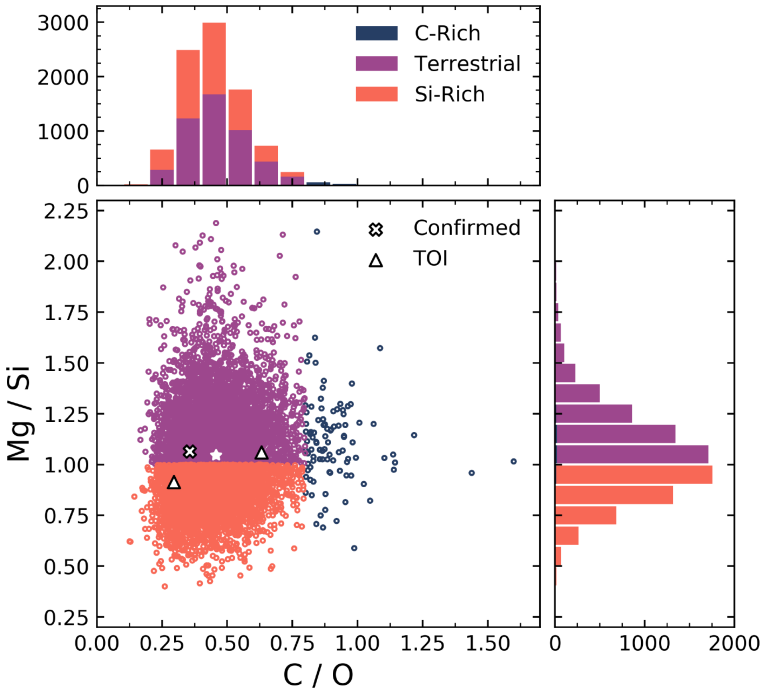

Figure 13. Distribution of all stars that have both measured C/O and Mg/Si ratios. These ratios can help inform astronomers on the likely composition of probable rocky worlds these stars may host. A total of 53.6 per cent of these stars have C/O < 0.8 and Mg/Si > 1 values that would suggest that these stars may potentially host planets that would be similar in geological composition to Earth and Mars. These potential rocky worlds would host olivine and pyroxene within their upper mantle and bridgmanite and magnesiowüstite (or ferropericlase) in their lower mantle. That leaves 46.4 per cent of stars that will host planets unlike any worlds within our Solar system. These include 45.4 per cent of stars potentially hosting 'Silicon-Rich' rocky worlds with stellar abudance ratios C/O < 0.8 and Mg/Si < 1, indicating that these worlds could contain pyroxene + SiO within both their upper and lower mantles. Only 1 per cent of GALAH–*TESS* stars have C/O > 0.8, indicating that they might host rocky worlds with carbon-rich mantles. Planet-hosting (cross) and candidate stars [TOI (upright triangle)] measured Mg/Si and C/O values are displayed on the figure with the Sun's Mg/Si and C/O values depicted with a white star (Lodders et al. 2009).

absolute errors for Fe, Si, Al, Mg, and Ca abundances need to be less than 0.02, 0.01, 0.002, 0.001, and 0.001 dex, respectively (Hinkel & Unterborn 2018). These uncertainties, especially for Al, Mg, and Ca are unobtainable with current detection methods and Solar abundance normalizations. Hence, if we do want to accurately determine an exoplanet's interior and composition, which has vast implications for its habitability, then precision on spectroscopic abundances and Solar normalizations themselves also have to significantly increased.

The relationship between elemental abundances and planetary architectures is a complex one. There is an overall trend that hot-Jupiter systems favour iron-rich hosts (Fischer & Valenti 2005; Mortier et al. 2013) and early evidence that super-Earths are predominantly found around metal-poor and α-rich stars (Adibekyan et al. 2012) and new work with machine-learning algorithms suggest elemental indicators for hot-Jupiter hosting stars apart from Fe are O, C, and Na (Hinkel et al. 2019). The orbits of super-Earths might also be correlated with their host-stars iron abundance, as work by Adibekyan et al. (2013b), Adibekyan, Figueira & Santos (2016), Sousa et al. (2019), and Petigura et al. (2018) shows super-Earths orbiting metal-rich stars have orbits that are shorter than their metal-poor hosted peers.

Sousa et al. (2019) also suggest the mass of planets increases with the host star metallicity, but contradicts Teske et al. (2019), which did not find such a correlation. Brewer et al. (2018) found that compact-multi systems are more common around metal-poor stars, showing a large [Fe/H] versus Si/Fe parameter space unfilled by single hot-Jupiters but filled with compact-multi systems for planet hosts with [Fe/H] values below 0.2 and Si/Fe values higher than 1.4. Similarly, Adibekyan et al. (2012) also showed that most planets orbiting metal-poor stars are enhanced in alpha elements, leading to higher Si/Fe ratios, and belong to the Milky Way's thick disc.

We have created a similar figure for our small exoplanetary sample, to somewhat forward predict the types of planetary architectures our GALAH–*TESS* stars might host. Fig. 14 shows that the majority of planet hosts and candidates fill quadrant B of this phase-space, where Brewer et al. (2018) found a diverse range of planetary architectures occupying this space. All of our confirmed and candidate systems favour iron-rich, silicon-poor stars, where a diverse range of exoplanetary architectures are likely to be found. This matches our current, though very small sample with single-planet systems hosting sub-Neptune to Jovian-like worlds.

5 CONCLUSION

The aim of this paper is to aid *TESS* follow-up teams with a catalogue of high precision atmospheric, physical and chemical stellar parameters for stars being observed with the space-based exoplanet survey satellite. We have cross-matched GALAH DR2 with the TIC to provide the characteristics for over ~47 000 stars, eleven of which

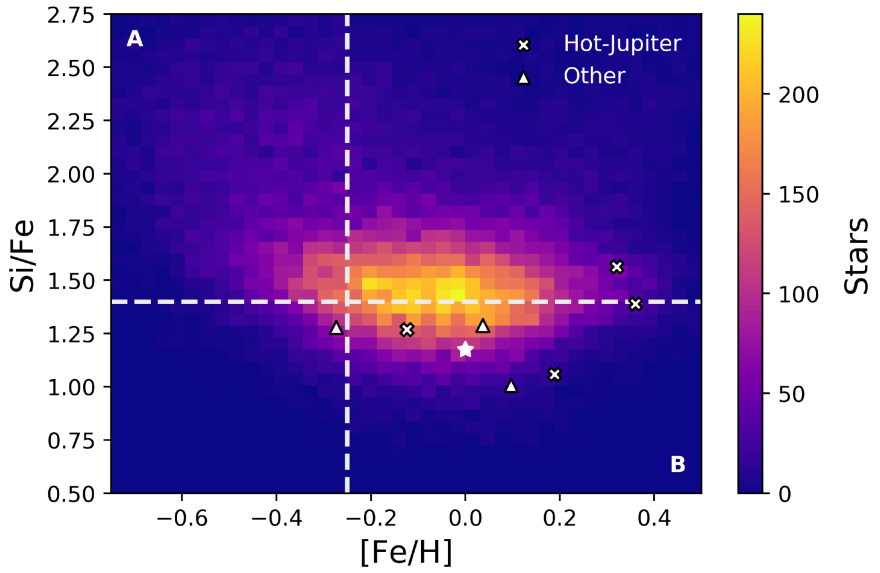

Figure 14. In Brewer et al. (2018), the authors discovered that compact multiplanet systems favoured iron-poor, silicon-rich stars with a higher population of multiplanetary systems favouring the A quadrant in this figure. A wider range of planetary systems, including single-systems consisting of hot-Jupiters were more common within quadrant B of this figure. This figure shows our [Fe/H] and Si/Fe abundance ratios for 43162 GALAH–*TESS* stars. Based upon our results, a more diverse range of planetary systems will be uncovered around GALAH–*TESS* stars, with the majority of our stars lying in quadrant B. The white star represents the Sun's [Fe/H] and Si/Fe values with known confirmed or candidate hot-Jupiter (cross) and other (triangle) planetary systems shown for comparison.

confirmed planet-hosts or planetary candidates discovered by the *TESS* mission. The refinement of stellar radii and masses of those planet-hosting stars have improved the mass and radius measurements of the confirmed and candidate exoplanets they host, with a median relative uncertainty for our planetary mass and radius values being 5 per cent and 4 per cent, respectively. From these refinements, we have increased the planetary radii of CTOI-201256771.01 and CTOI-201256771.02 to near Solar values of 96.17$R_{\odot}$ and 103.15$R_{\odot}$, and with further investigation, have indicated that these transit events were likely caused by the eclipsing binary companion of UNSW-V 320 A. We also cast serious doubts over the candidate events CTOI-220402290.01, CTOI-220402290.02, CTOI-300903537.01, and CTOI 300903537.02 as their orbital periods alone suggest that these candidate systems are likely coming from one source and not two. Our updated mass and radius values changed on the order of 10–20 per cent from literature values, which have minor implications for the large exoplanets currently within the GALAH–*TESS* catalogue, but would have profound impacts on the refinement of a fictitious 'Earth-like' world orbiting these stars, with a range of densities that would render some uninhabitable by current theories of habitability.

Our catalogue contains the elemental abundances for 23 elements that have been normalized by Lodders et al. (2009) to not only drive consistency within the community, but to also make it easier for comparisons of elemental abundances from other abundance driven, stellar surveys to ours. The GALAH–*TESS* catalogue includes the elemental abundance ratios for C/O, Mg/Si, Fe/Mg, and Fe/Si which can help astronomers and planetary scientists make predictions about the composition and structure of potential rocky worlds orbiting our GALAH–*TESS* stars. Our stellar C/O and Mg/Si distributions suggest that the majority of GALAH-*TESS* stars will likely host worlds similar in composition to that of Earth and Mars, with over 54 per cent of stars hosting Mg/Si $>$ 1, and C/O $<$ 0.8. However, 46 per cent of stars have atmospheric abundance ratios of either Mg/Si $<$ 1 and C/O $<$ 0.8 or C/O $>$ 0.8, suggesting that these stars may host rocky worlds with geological compositions unlike any planet found within our Solar system. These values will change dependent upon the Solar normalization used, hence the need for a standard Solar normalization within the exoplanetary community. It is important in our language that a truly Earth-like planet has yet to be discovered (Tasker et al. 2017). But our characterization of GALAH stars being observed by *TESS* might one day be used to determine the composition of a world just like ours.

SOFTWARE

ASTROPY (Astropy Collaboration et al. 2013), ASTROQUERY (Ginsburg et al. 2019), ISOCHRONES (Morton 2015), MATPLOTLIB (Hunter 2007), MULTINEST (Feroz et al. 2019; Feroz, Hobson & Bridges 2009; Feroz & Hobson 2008), MULTIPROCESSING (McKerns et al. 2012), NUMPY (Oliphant 2006; van der Walt, Colbert & Varoquaux 2011), OPENBLAS (Xianyi, Qian & Yunquan 2012; Wang et al. 2013), PANDAS (McKinney et al. 2010), SCIPY (Virtanen et al. 2020).

ACKNOWLEDGEMENTS

Our research is based upon data acquired through the Australian Astronomical Observatory. We acknowledge the traditional owners of the land on which the AAT stands, the Gamilaraay people, and pay our respects to elders past, present and emerging.

This research has made use of the NASA Exoplanet Archive, which is operated by the California Institute of Technology, under

contract with the National Aeronautics and Space Administration under the Exoplanet Exploration Program

This paper makes use of data from the first public release of the WASP data (Butters et al. 2010) as provided by the WASP consortium and services at the NASA Exoplanet Archive, which is operated by the California Institute of Technology, under contract with the National Aeronautics and Space Administration under the Exoplanet Exploration Program.

This work has made use of the TIC and CT Stellar Properties Catalog, through the *TESS* Science Office's target selection working group (architects K. Stassun, J. Pepper, N. De Lee, M. Paegert, R. Oelkers). The Filtergraph data portal system is trademarked by Vanderbilt University.

This research has made use of the Exoplanet Follow-up Observation Program website, which is operated by the California Institute of Technology, under contract with the National Aeronautics and Space Administration under the Exoplanet Exploration Program.

This work has made use of data from the European Space Agency (ESA) mission *Gaia* (http://www.cosmos.esa.int/gaia), processed by the *Gaia* Data Processing and Analysis Consortium (DPAC; http://www.cosmos.esa.int/web/gaia/dpac/ consortium). Funding for the DPAC has been provided by national institutions, in particular the institutions participating in the *Gaia* Multilateral Agreement.

The research shown here acknowledges use of the Hypatia Catalog Database, an online compilation of stellar abundance data as described in Hinkel et al. (2014), which was supported by NASA's Nexus for Exoplanet System Science (NExSS) research coordination network and the Vanderbilt Initiative in Data-Intensive Astrophysics (VIDA).

JTC would like to thank SW, BC, and DN, and is supported by the Australian Government Research Training Program (RTP) Scholarship. JTC would also like to thank Vardan Adibekyan for their valuable comments which have significantly improved the science of this manuscript. JDS and SM acknowledges the support of the Australian Research Council through Discovery Project grant DP180101791. SB acknowledges funds from the Australian Research Council (grants DP150100250 and DP160103747). Parts of this research were supported by the Australian Research Council (ARC) Centre of Excellence for All Sky Astrophysics in 3 Dimensions (ASTRO 3D), through project number CE170100013. YST is grateful to be supported by the NASA Hubble Fellowship grant *HST*-HF2-51425.001 awarded by the Space Telescope Science Institute.

DATA AVAILABILITY

The data underlying this article are available in Data Central at https://datacentral.org.au/.

REFERENCES

Addison B. C. et al., 2021, MNRAS, 502, 3704
Addison B. et al., 2019, PASP, 131, 115003
Adibekyan V., Figueira P., Santos N. C., 2016, Origins Life Evolution Biosphere, 46, 351
Adibekyan V., Gonçalves da Silva H. M., Sousa S. G., Santos N. C., Delgado Mena E., Hakobyan A. A., 2017, ApJ, 60, 325
Adibekyan V. et al., 2021, preprint (arXiv:2102.12444)
Adibekyan V. Z. et al., 2012, A&A, 543, A89
Adibekyan V. Z. et al., 2013a, A&A, 554, A44
Adibekyan V. Z. et al., 2013b, A&A, 560, A51
Alibert Y., 2014, A&A, 561, A41
Amarsi A. M., Asplund M., 2017, MNRAS, 464, 264
Amarsi A. M., Asplund M., Collet R., Leenaarts J., 2016a, MNRAS, 455, 3735
Amarsi A. M., Lind K., Asplund M., Barklem P. S., Collet R., 2016b, MNRAS, 463, 1518
Anders E., Grevesse N., 1989, Geochim. Cosmochim. Acta, 53, 197
Asplund M., Grevesse N., Sauval A. J., 2005, in Barnes T. G., III, Bash F. N., eds, The Solar Chemical Composition. Astronomical Society of the Pacific Conference Series, San Francisco, p. 25
Asplund M., Grevesse N., Sauval A. J., Scott P., 2009, ARA&A, 47, 481
Astropy Collaboration et al., 2013, A&A, 558, A33
Barclay T., Pepper J., Quintana E. V., 2018, ApJS, 239, 2
Barclay T. et al., 2013, ApJ, 768, 101
Batalha N. M. et al., 2013, ApJS, 204, 24
Benz W., Anic A., Horner J., Whitby J. A., 2007, Space Sci. Rev., 132, 189
Bitsch B., Battistini C., 2020, A&A, 633, A10
Bond J. C., Lauretta D. S., O'Brien D. P., 2010a, Icarus, 205, 321
Bond J. C., O'Brien D. P., Lauretta D. S., 2010b, ApJ, 715, 1050
Bonomo A. S. et al., 2019, Nature Astron., 3, 416
Borucki W. J. et al., 2010, Science, 327, 977
Brewer J. M., Fischer D. A., 2016, ApJ, 831, 20
Brewer J. M., Fischer D. A., Madhusudhan N., 2017, AJ, 153, 83
Brewer J. M., Wang S., Fischer D. A., Foreman-Mackey D., 2018, ApJ, 867, L3
Brugger B., Mousis O., Deleuil M., Deschamps F., 2017, ApJ, 850, 93
Brugger B., Mousis O., Deleuil M., Ronnet T., 2018, Characterizing the deviations of Mercury's bulk composition from solar abundances. European Planetary Science Congress, Berlin, p. EPSC2018–404
Brugman K. K., Phillips M. G., Till C. B., 2019, Experimental Determination of Rocky Exoplanet Crust Compositions. AGU Fall Meeting Abstracts, San Francisco, p. 3016
Buchhave L. A., Latham D. W., 2015, ApJ, 808, 187
Buchhave L. A. et al., 2014, Nature, 509, 593
Buder S. et al., 2018, MNRAS, 478, 4513
Buhler P. B., Knutson H. A., Batygin K., Fulton B. J., Fortney J. J., Burrows A., Wong I., 2016, ApJ, 821, 26
Butters O. W. et al., 2010, A&A, 520, L10
Carrillo A., Hawkins K., Bowler B. P., Cochran W., Vanderburg A., 2020, MNRAS, 491, 4365
Carter-Bond J. C., O'Brien D. P., Delgado Mena E., Israelian G., Santos N. C., González Hernández J. I., 2012, ApJ, 747, L2
Chen J., Kipping D., 2017, ApJ, 834, 17
Choi J., Dotter A., Conroy C., Cantiello M., Paxton B., Johnson B. D., 2016, ApJ, 823, 102
Christiansen J. L. et al., 2008, MNRAS, 385, 1749
Coughlin J. L. et al., 2016, ApJS, 224, 12
Cui X.-Q. et al., 2012, Res. Astron. Astrophys., 12, 1197
Dalba P. A. et al., 2020, AJ, 159, 241
Davis A. B. et al., 2020, AJ, 160, 229
Delgado Mena E., Israelian G., González Hernández J. I., Bond J. C., Santos N. C., Udry S., Mayor M., 2010, ApJ, 725, 2349
De Silva G. M. et al., 2015, MNRAS, 449, 2604
Dorn C., Harrison J. H. D., Bonsor A., Hands T. O., 2019, MNRAS, 484, 712
Dorn C., Hinkel N. R., Venturini J., 2017b, A&A, 597, A38
Dorn C., Khan A., Heng K., Connolly J. A. D., Alibert Y., Benz W., Tackley P., 2015, A&A, 577, A83
Dorn C., Venturini J., Khan A., Heng K., Alibert Y., Helled R., Rivoldini A., Benz W., 2017a, A&A, 597, A37
Duffy T., Madhusudhan N., Lee K., 2015, in Schubert G., ed., Treatise on Geophysics (Second Edition), 2nd edn. Elsevier, Oxford, p. 149
Eisner N. et al., 2020, MNRAS, 494, 750
Elkins-Tanton L. T., Seager S., 2008, ApJ, 685, 1237
Endl M. et al., 2016, ApJ, 818, 34
Feroz F., Hobson M. P., 2008, MNRAS, 384, 449
Feroz F., Hobson M. P., Bridges M., 2009, MNRAS, 398, 1601
Feroz F., Hobson M. P., Cameron E., Pettitt A. N., 2019, OJAp, 2, 10
Fischer D. A., Valenti J., 2005, ApJ, 622, 1102
Fischer D. A. et al., 2008, ApJ, 675, 790
Fortney J. J., 2012, ApJ, 747, L27

Fortney J. J., Nettelmann N., 2010, Space Sci. Rev., 152, 423
Fuhrmann K., 1998, A&A, 338, 161
Gaia Collaboration et al., 2018, A&A, 616, A1
Gao X. et al., 2018, MNRAS, 481, 2666
Gilbert E. A. et al., 2020, AJ, 160, 116
Gillon M. et al., 2017, Nature, 542, 456
Ginsburg A. et al., 2019, AJ, 157, 98
Gonzalez G., 1997, MNRAS, 285, 403
Grevesse N., Asplund M., Sauval A. J., 2007, Space Sci. Rev., 130, 105
Grevesse N., Sauval A. J., 1998, Space Sci. Rev., 85, 161
Hardegree-Ullman K. K., Zink J. K., Christiansen J. L., Dressing C. D., Ciardi D. R., Schlieder J. E., 2020, ApJS, 247, 28
Harris C. R. et al., 2020, Nature, 585, 357
Hellier C. et al., 2012, MNRAS, 426, 739
Hinkel N. R., Burger D., 2017a, preprint (arXiv:1712.04944)
Hinkel N. R., Burger D., 2017b, preprint (arXiv:1712.04944)
Hinkel N. R., Timmes F. X., Young P. A., Pagano M. D., Turnbull M. C., 2014, AJ, 148, 54
Hinkel N. R., Unterborn C., Kane S. R., Somers G., Galvez R., 2019, ApJ, 880, 49
Hinkel N. R., Unterborn C. T., 2018, ApJ, 853, 83
Hinkel N. R. et al., 2016, ApJS, 226, 4
Hirose K., Labrosse S., Hernlund J., 2013, AREPS, 41, 657
Horner J., Jones B. W., 2010, IJAsB, 9, 273
Horner J. et al., 2020, PASP, 132, 102001
Huang C. X. et al., 2018, ApJ, 868, L39
Huber D. et al., 2019, AJ, 157, 245
Hunter J. D., 2007, CSE, 9, 90
Jofré P., Das P., Bertranpetit J., Foley R., 2017, MNRAS, 467, 1140
Jofré P., Heiter U., Soubiran C., 2019, ARA&A, 57, 571
Johns D., Marti C., Huff M., McCann J., Wittenmyer R. A., Horner J., Wright D. J., 2018, ApJS, 239, 14
Johnson J. A. et al., 2011, ApJS, 197, 26
Jones M. I. et al., 2016, A&A, 590, A38
Jordán A. et al., 2020, AJ, 159, 145
Kite E. S., Ford E. B., 2018, ApJ, 864, 75
Kopparapu R. K. et al., 2013, ApJ, 765, 131
Kos J. et al., 2017, MNRAS, 464, 1259
Kuchner M. J., Seager S., 2005, preprint(astro-ph/0504214)
Latham D. W., Mazeh T., Stefanik R. P., Mayor M., Burki G., 1989, Nature, 339, 38
Lawton A. T., Wright P., 1989, J. Br. Interplanet. Soc., 42, 335
Lewis I. J. et al., 2002, MNRAS, 333, 279
Ligi R. et al., 2019, A&A, 631, A92
Lingam M., Loeb A., 2019, Int. J. Astrobiol., 18, 112
Lodders K., 2003, ApJ, 591, 1220
Lodders K., Palme H., Gail H. P., 2009, Landolt Börnstein, 4B, 712
Lovis C., Fischer D., 2010, in Seager S., ed., Exoplanets. University of Arizona Press, Tucson, p. 27
Lovis C. et al., 2011, A&A, 528, A112
Madhusudhan N., Lee K. K. M., Mousis O., 2012, ApJ, 759, L40
Martell S. et al., 2020, preprint (arXiv:2006.02106)
Martell S. L. et al., 2016, MNRAS, 465, 3203
Mayor M., Queloz D., 1995, Nature, 378, 355
McDonough W. F., 2003, TrGeo, 2, 568
McDonough W. F., Sun S. s., 1995, Chem. Geol., 120, 223
McKerns M. M., Strand L., Sullivan T., Fang A., Aivazis M. A., 2012, preprint (arXiv:1202.1056)
McKinney W., 2010, Data Structures for Statistical Computing in Python. Proc. 9th Python in Science Conference, Austin, p. 51
Miozzi F., Morard G., Antonangeli D., Clark A. N., Mezouar M., Dorn C., Rozel A., Fiquet G., 2018, J. Geophys. Res. Planets, 123, 2295
Mocquet A., Grasset O., Sotin C., 2014, RSPTA, 372, 20130164
Mordasini C. et al., 2011, A&A, 526, A111
Moriarty J., Madhusudhan N., Fischer D., 2014, ApJ, 787, 81
Mortier A., Santos N. C., Sousa S. G., Adibekyan V. Z., Delgado Mena E., Tsantaki M., Israelian G., Mayor M., 2013, A&A, 557, A70
Morton T. D., 2015, Astrophysics Source Code Library, record ascl:1503.010
Muirhead P. S. et al., 2012, ApJ, 747, 144
Naef D. et al., 2001, A&A, 375, L27
Ness M., Hogg D. W., Rix H. W., Ho A. Y. Q., Zasowski G., 2015, ApJ, 808, 16
Nielsen L. D. et al., 2019a, MNRAS, 489, 2478
Nielsen L. D. et al., 2019b, A&A, 623, A100
Nisr C., Meng Y., MacDowell A. A., Yan J., Prakapenka V., Shim S.-H., 2017, JGRE, 122, 124
Nittler L. R., Chabot N. L., Grove T. L., Peplowski P. N., 2017, preprint (arXiv:1712.02187)
Noack L., Snellen I., Rauer H., 2017, Space Sci. Rev., 212, 877
Noyes R. W. et al., 2008, ApJ, 673, L79
Osborn A., Bayliss D., 2019, MNRAS, 491, 4481
Osorio Y., Barklem P. S., 2016, A&A, 586, A120
Osorio Y., Barklem P. S., Lind K., Belyaev A. K., Spielfiedel A., Guitou M., Feautrier N., 2015, A&A, 579, A53
Petigura E. A., Marcy G. W., 2011, ApJ, 735, 41
Petigura E. A. et al., 2018, AJ, 155, 89
Plotnykov M., Valencia D., 2020, MNRAS, 499, 932
Putirka K. D., Rarick J. C., 2019, Am. Mineral., 104, 817
Recio-Blanco A. et al., 2014, A&A, 567, A5
Reddy B. E., Lambert D. L., Allende Prieto C., 2006, MNRAS, 367, 1329
Ricker G. R. et al., 2014, J. Astron. Telesc. Instr. Syst., 1, 1
Rogers L. A., Seager S., 2010, ApJ, 712, 974
Rowe J. F. et al., 2014, ApJ, 784, 45
Salaris M., Chieffi A., Straniero O., 1993, ApJ, 414, 580
Santerne A. et al., 2014, A&A, 571, A37
Santos N. C., Israelian G., Mayor M., 2001, A&A, 373, 1019
Schubert G., Anderson J. D., Travis B. J., Palguta J., 2007, Icarus, 188, 345
Schulze J. G., Wang J., Johnson J. A., Gaudi B. S., Unterborn C. T., Panero W. R., 2020, preprint (arXiv:2011.08893)
Seager S., Kuchner M., Hier-Majumder C. A., Militzer B., 2007, ApJ, 669, 1279
Shallue C. J., Vanderburg A., 2018, AJ, 155, 94
Sharma S. et al., 2018, MNRAS, 473, 2004
Sharma S. et al., 2019, MNRAS, 490, 5335
Sheinis A. et al., 2015, JATIS, 1, 035002
Skrutskie M. F. et al., 2006, AJ, 131, 1163
Smith A. M. S. et al., 2012, MNRAS, 426, 739
Sousa S. G. et al., 2019, MNRAS, 485, 3981
Stassun K. G., Collins K. A., Gaudi B. S., 2017, AJ, 153, 136
Stassun K. G. et al., 2018, AJ, 156, 102
Stassun K. G. et al., 2019, AJ, 158, 138
Steinmetz M. et al., 2006, AJ, 132, 1645
Suárez-Andrés L., Israelian G., González Hernández J. I., Adibekyan V. Z., Delgado Mena E., Santos N. C., Sousa S. G., 2018, A&A, 614, A84
Suissa G., Chen J., Kipping D., 2018, MNRAS, 476, 2613
Sullivan P. W. et al., 2015, ApJ, 809, 77
Tasker E. et al., 2017, NatAs, 1, 0042
Taylor M. B., 2005, TOPCAT & STIL: Starlink Table/VOTable Processing Software. Astronomical Data Analysis Software and Systems XIV ASP Conference Series, San Francisco, p. 29
Teske J. K., Cunha K., Schuler S. C., Griffith C. A., Smith V. V., 2013, ApJ, 778, 132
Teske J. K., Cunha K., Smith V. V., Schuler S. C., Griffith C. A., 2014, ApJ, 788, 39
Teske J. K., Thorngren D., Fortney J. J., Hinkel N., Brewer J. M., 2019, AJ, 158, 239
Thiabaud A., Marboeuf U., Alibert Y., Cabral N., Leya I., Mezger K., 2014a, A&A, 562, A27
Thiabaud A., Marboeuf U., Alibert Y., Cabral N., Leya I., Mezger K., 2014b, A&A, 562, A27
Thiabaud A., Marboeuf U., Alibert Y., Leya I., Mezger K., 2015, A&A, 580, A30
Torres G. et al., 2015, ApJ, 800, 99

Unterborn C. T., Desch S. J., Hinkel N. R., Lorenzo A., 2018a, Nature Astron., 2, 297
Unterborn C. T., Desch S. J., Panero W. R., 2018b, Fall Meeting 2018. American Geophysical Union, Washington D.C., p. P42A
Unterborn C. T., Dismukes E. E., Panero W. R., 2016, ApJ, 819, 32
Unterborn C. T., Kabbes J. E., Pigott J. S., Reaman D. M., Panero W. R., 2014, ApJ, 793, 124
Unterborn C. T., Panero W. R., 2017, ApJ, 845, 61
Unterborn C. T., Panero W. R., 2019, JGRE, 124, 1704
Valencia D., O'Connell R. J., Sasselov D., 2006, Icarus, 181, 545
Valenti J. A., Piskunov N., 1996, A&AS, 118, 595
Vanderspek R. et al., 2019, ApJ, 871, L24
van der Walt S., Colbert S. C., Varoquaux G., 2011, CSE, 13, 22
Virtanen P. et al., 2020, NatMe, 17, 261
Vogt S. S. et al., 2010, ApJ, 708, 1366
Waenke H., Dreibus G., 1988, RSPTA, 325, 545
Wang H. S., Liu F., Ireland T. R., Brasser R., Yong D., Lineweaver C. H., 2019b, MNRAS, 482, 2222
Wang Q., Zhang X., Zhang Y., Yi Q., 2013, AUGEM: automatically generate high performance dense linear algebra kernels on x86 CPUs. Proceedings of the International Conference on High Performance Computing, Networking, Storage and Analysis, Denver, p. 1
Wang S. et al., 2019a, AJ, 157, 51
Wanke H., Dreibus G., 1994, RSPTA, 349, 285
Wilson H. F., Militzer B., 2014, ApJ, 793, 34
Wittenmyer R. A. et al., 2014, ApJ, 783, 103
Wittenmyer R. A. et al., 2017, AJ, 154, 274
Wittenmyer R. A. et al., 2018, AJ, 155, 84
Wittenmyer R. A. et al., 2020, MNRAS, 491, 5248
Wolszczan A., Frail D. A., 1992, Nature, 355, 145
Xianyi Z., Qian W., Yunquan Z., 2012, Model-driven Level 3 BLAS Performance Optimization on Loongson 3A Processor. IEEE 18th International Conference on Parallel and Distributed Systems, Washington D.C., p. 684
Zeng L., Sasselov D. D., Jacobsen S. B., 2016, ApJ, 819, 127
Zolotov M. Y., Tobie G., Postberg F., Magee B., Waite J. H., Esposito L., 2011, Chemical and Phase Composition of Enceladus: Insights from Cassini Observations. EPSC-DPS Joint Meeting 2011, Nantes, p. 1330

APPENDIX A

See Table A1.

Table A1. Column names, units, data types and descriptions for the GALAH-*TESS* parameters table.

Name	Units	Data type	Description
TIC_ID		int64	*TESS* Input Catalog (TIC) Identifier
TWOMASS		int64	Two Micron All-Sky Survey (2MASS) identifier
GAIADR2		long64	*Gaia* DR2 Identifier
PRIORITY		float64	TIC v8 priority
RA	deg	float64	J2000 right ascension from 2MASS
DEC	deg	float64	J2000 declination from 2MASS
TEFF	K	int64	GALAH DR2 Effective temperature
E_TEFF	K	int64	Uncertainty in TEFF
LOGG	dex	float64	GALAH DR2 Surface gravity
E_LOGG	dex	float64	Uncertainty in LOGG
M_H	dex	float64	GALAH DR2 overall metallicity
E_MH	dex	float64	Uncertainty in M_H
ALPHA_FE	dex	float64	[α/Fe] abundance
E_ALPHA_FE	dex	float64	Uncertainty in ALPHA_FE
VMAG	mag	float64	V magnitude from TIC
E_VMAG	mag	float64	Uncertainty in VMAG
TMAG	mag	float64	*TESS* magnitude from TIC
E_TMAG	mag	float64	Uncertainty in TMAG
HMAG	mag	float64	2MASS H magnitude from TIC
E_HMAG	mag	float64	Uncertainty in HMAG
JMAG	mag	float64	2MASS J magnitude from TIC
E_JMAG	mag	float64	Uncertainty in JMAG
KMAG	mag	float64	2MASS K magnitude from TIC
E_KMAG	mag	float64	Uncertainty in KMAG
GMAG	mag	float64	*Gaia* G magnitude from TIC
E_GMAG	mag	float64	Uncertainty in GMAG
GRPMAG	mag	float64	*Gaia* G_RP magnitude from TIC
E_GRPMAG	mag	float64	Uncertainty in GRPMAG
GBPMAG	mag	float64	*Gaia* G_BP magnitude from TIC
E_GBPMAG	mag	float64	Uncertainty in GBPMAG
PLX	mas	float64	Parallax from TIC
E_PLX	mas	float64	Uncertainty in PLX
DIST	pc	float64	Distance from TIC
E_DIST	pc	float64	Uncertainty in DIST
RADIUS	$R_\odot$	float64	isochrone Stellar radius
E_RADIUS	$R_\odot$	float64	Uncertainty in RADIUS
MASS	$M_\odot$	float64	isochrone Stellar mass
E_MASS	$M_\odot$	float64	Uncertainty in MASS
RHO	gcm^{-3}	float64	isochrone Stellar density
E_RHO	gcm^{-3}	float64	Uncertainty in RHO
LUM	$L_\odot$	float64	Stellar luminosity
E_LUM	$L_\odot$	float64	Uncertainty in LUM
AGE	Gyr	float64	isochrone Stellar age
E_AGE	Gyr	float64	Uncertainty in AGE
EEP		int64	MIST isochrone equivalent evolutionary phase
E_EEP		int64	Uncertainty in EEP
RV	$km\ s^{-1}$	float64	GALAH DR2 Radial velocity from internal cross-correlation against data
E_RV	$km\ s^{-1}$	float64	Uncertainty in RV
VSINI	$km\ s^{-1}$	float64	GALAH DR2 Line of sight rotational velocity
E_VSINI	$km\ s^{-1}$	float64	Uncertainty in VSINI
VMIC	$km\ s^{-1}$	float64	GALAH DR2 Microturbulence velocity
E_VMIC	$km\ s^{-1}$	float64	Uncertainty in VMIC
HZRECVEN	au	float64	Recent Venus Habitable Zone
HZRUNGRN	au	float64	Runaway Greenhouse Habitable Zone
HZMOIGRN	au	float64	Moist Greenhouse Habitable Zone
HZMAXGRN	au	float64	Maximum Greenhouse Habitable Zone
HZEARMAR	au	float64	Early Mars Habitable Zone
X_H	dex	float64	[X/H] abundance for element X
E_X_H	dex	float64	[X/H] Uncertainty in X_H
C_O		float64	(C/O) abundance ratio
E_C_O		float64	Uncertainty in C_O
MG_SI		float64	(Mg/Si) abundance ratio
E_MG_SI		float64	Uncertainty in MG_SI
FE_MG		float64	(Fe/Mg) abundance ratio
E_FE_MG		float64	Uncertainty in FE_MG
FE_SI		float64	(Fe/Si) abundance ratio
E_FE_SI		float64	Uncertainty in FE_SI

This paper has been typeset from a TEX/LATEX file prepared by the author.

I don't know what to do anymore
My life is pointless that's something I can't ignore
But that just makes me want to do it even more
Cause everything is meaningless
So why take it so serious?

– Dregg

3

IMPROVING OUR UNDERSTANDING OF CONFIRMED AND CANDIDATE PLANETARY SYSTEMS WITH GALAH

The published paper Clark et al. (2021), "The GALAH Survey: Improving our understanding of confirmed and candidate planetary systems with large stellar surveys" follows.

Monthly Notices of the ROYAL ASTRONOMICAL SOCIETY

MNRAS **00,** 1 (2021) https://doi.org/10.1093/mnras/stab3498
Advance Access publication 2021 December 2

The GALAH Survey: improving our understanding of confirmed and candidate planetary systems with large stellar surveys

Jake T. Clark [1]★ Duncan J. Wright,[1] Robert A. Wittenmyer,[1]★ Jonathan Horner [1]★ Natalie R. Hinkel,[2] Mathieu Clerté,[1] Brad D. Carter [1] Sven Buder [3,4] Michael R. Hayden,[4,5] Joss Bland-Hawthorn [4,5] Andrew R. Casey [6,7] Gayandhi M. De Silva,[8,9] Valentina D'Orazi,[10] Ken C. Freeman,[3] Janez Kos,[11] Geraint F. Lewis [5] Jane Lin,[3,4] Karin Lind,[12,13] Sarah L. Martell [4,14] Katharine J. Schlesinger,[3] Sanjib Sharma [4,5] Jeffrey D. Simpson [4,14] Dennis Stello,[4,5,14] Daniel B. Zucker,[9,15] Tomaž Zwitter [11] Ulisse Munari [10] and Thomas Nordlander [3,4]

[1]*Centre for Astrophysics, University of Southern Queensland, West Street, Toowoomba, QLD 4350, Australia*
[2]*Space Science and Engineering Division, Southwest Research Institute, San Antonio, TX 78238, USA*
[3]*Research School of Astronomy & Astrophysics, Australian National University, ACT 2611, Australia*
[4]*Centre of Excellence for Astrophysics in Three Dimensions (ASTRO-3D), Australia*
[5]*Sydney Institute for Astronomy, School of Physics, A28, The University of Sydney, NSW 2006, Australia*
[6]*Monash Centre for Astrophysics, Monash University, Clayton VIC 3800, Australia*
[7]*School of Physics and Astronomy, Monash University, Clayton VIC 3800, Australia*
[8]*Australian Astronomical Optics, Faculty of Science and Engineering, Macquarie University, Macquarie Park, NSW 2113, Australia*
[9]*Macquarie University Research Centre for Astronomy, Astrophysics & Astrophotonics, Sydney, NSW 2109, Australia*
[10]*Istituto Nazionale di Astrofisica, Osservatorio Astronomico di Padova, vicolo dell'Osservatorio 5, I-35122, Padova, Italy*
[11]*Faculty of Mathematics and Physics, University of Ljubljana, Jadranska 19, 1000 Ljubljana, Slovenia*
[12]*Department of Astronomy, Stockholm University, AlbaNova University Centre, SE-106 91 Stockholm, Sweden*
[13]*Department of Physics and Astronomy, Macquarie University, Sydney, NSW 2109, Australia*
[14]*School of Physics, University of New South Wales – Sydney, Sydney 2052, Australia*
[15]*Max Planck Institute for Astronomy, K onigstuhl 17, D-69117 Heidelberg, Germany*

Accepted 2021 November 27. Received 2021 November 24; in original form 2021 April 13

ABSTRACT

Pioneering photometric, astrometric, and spectroscopic surveys is helping exoplanetary scientists better constrain the fundamental properties of stars within our galaxy and the planets these stars host. In this study, we use the third data release from the stellar spectroscopic GALAH Survey, coupled with astrometric data of eDR3 from the *Gaia* satellite, and other data from NASA's Exoplanet Archive, to refine our understanding of 279 confirmed and candidate exoplanet host stars and their exoplanets. This homogenously analysed data set comprises 105 confirmed exoplanets, along with 146 K2 candidates, 95 TESS Objects of Interest (TOIs), and 52 Community TOIs (CTOIs). Our analysis significantly shifts several previously (unknown) planet parameters while decreasing the uncertainties for others. Our radius estimates suggest that 35 planet candidates are more likely brown dwarfs or stellar companions due to their new radius values. We are able to refine the radii and masses of WASP-47 e, K2-106 b, and CoRoT-7 b to their most precise values yet to less than 2.3 per cent and 8.5 per cent, respectively. We also use stellar rotational values from GALAH to show that most planet candidates will have mass measurements that will be tough to obtain with current ground-based spectrographs. With GALAH's chemical abundances, we show through chemo-kinematics that there are five planet hosts that are associated with the galaxy's thick disc, including NGTS-4, K2-183, and K2-337. Finally, we show that there is no statistical difference between the chemical properties of hot Neptune and hot rocky exoplanet hosts, with the possibility that short-period rocky worlds might be the remnant cores of hotter, gaseous worlds.

Key words: surveys – planets and satellites: detection – planets and satellites: fundamental parameters – planets and satellites: terrestrial planets – stars: fundamental parameters.

1 INTRODUCTION

Over the past three decades, new discoveries have moved the study of alien worlds from science fiction to science fact. We now know that planets are ubiquitous – that virtually every star in the sky is accompanied by a retinue of exoplanets (Batalha et al. 2013; Dressing & Charbonneau 2013, 2015; Hsu et al. 2019; Kunimoto & Matthews 2020; Yang, Xie & Zhou 2020). One of the great revelations of the first 30 yr of the exoplanet era is the diversity exhibited by the physical properties of the planets we have discovered. We have found massive planets with extremely inflated, tenuous atmospheres,

★ E-mail: jake.clark@usq.edu.au (JTC); rob.wittenmyer@usq.edu.au (RAW); jonti.horner@usq.edu.au (JH)

resulting in bulk densities lower than that of cotton candy (Deleuil et al. 2008; Bailes et al. 2011; Siverd et al. 2012; Rowe et al. 2014a; Dragomir et al. 2019), and others whose density far exceeds that of the planets in the Solar system (Steffen et al. 2013; Masuda 2014; Rowe et al. 2014b; Hartman et al. 2016; Lam et al. 2017; Zhou et al. 2017; Hartman et al. 2019). Such studies have even revealed systems with similar-sized planets of very disparate mass – such as the Kepler-107 system; Kepler-107 b and c both have radii of $\sim$1.5$R_\oplus$, but while b has an Earth-like density of 5.3 g cm^{-3}, c has a density at least twice as large, 12.6 g cm^{-3}; Bonomo et al. 2019).

In the coming years, our ability to determine the true mass and radius of newly discovered exoplanets will become even more important, as the search for exoplanets becomes a dedicated effort to find planets that could be considered truly 'Earth-like'. Those planets will require significant effort to measure their atmospheres in an attempt to look for potential biomarkers. As a result, it will be vitally important to be able to work out which of those planets are most likely to be truly Earth-like (see e.g. Horner & Jones 2010, and references therein).

One of the key pieces of information for that selection process will be precise estimates of the mass and density of the planets in question – data that can be used to estimate the physical makeup and internal structure of those planets. However, the precision with which we can determine both the mass and the radius of a given planet is limited by the precision with which we can categorize that planet's host star. The less precisely we know the mass or radius of that star, the less accurate will be the parameters we derive for the planets orbiting the star. Our knowledge of the worlds we discover is limited by our knowledge of their host stars.

The problem has become even more pronounced since the launch of *TESS*, which has already delivered a plethora of new discoveries (e.g. Huang et al. 2018; Nielsen et al. 2019; Vanderburg et al. 2019; Jordán et al. 2020; Plavchan et al. 2020; Addison et al. 2021; Rodriguez et al. 2021) along with candidate systems waiting for their planetary status to be confirmed, such as *TESS* Object of Interest (TOIs) and Community TOIs (CTOIs). Currently, the median error for TOI planetary radii is in excess of 10 per cent. Fortunately, vast galactic archaeology surveys are now gathering high-quality spectroscopic data on hundreds of thousands of stars in the local solar neighbourhood, as well as stars within the galaxy's thick and thin discs (Steinmetz et al. 2006; Cui et al. 2012; Gilmore et al. 2012; De Silva et al. 2015; Majewski et al. 2017). The GALAH (GALactic Archeology with HERMES) survey (De Silva et al. 2015; Martell et al. 2016; Buder et al. 2018, 2020) is one such program, with the aim of gathering high-quality spectra for up to one million nearby stars. In GALAH's latest data release, GALAH DR3 (DR3; Buder et al. 2020), the GALAH team provides the results of its observations of 588 571 stars – including elemental abundances for up to 27 different elements. The resulting data set is a treasure trove of information that is of vital importance to the exoplanet community. In particular, the GALAH stellar abundances can assist in determining the compositions of the planets these stars might host (Rogers & Seager 2010; Dorn et al. 2017, 2015; Unterborn et al. 2018a; Bitsch & Battistini 2020; Clark et al. 2020), and even the types of planets the stars could potentially host (Hinkel et al. 2019). At the same time, the *Gaia* spacecraft is taking incredibly precise distance measurements of the stars being surveyed by GALAH (surveying up to $\sim$2 per cent of all stars in the Galaxy).

In this work, we use data from the GALAH DR3 and *Gaia* EDR3 to refine the stellar parameters for a total of 273 stars in the *TESS* Input Catalog (TIC). We show how GALAH data can greatly improve the precision of our characterization of potential planet hosting stars. Section 2 determines the stellar parameters for our sample and comparing them to our surveys. In Section 3, we use these stellar parameters to then recharacterize confirmed and candidate planetary systems. We discuss our results in Section 4, identifying false positives, using our stellar $v \sin i$ values to determine how difficult it will be to determine mass measurements for our candidates, discuss the ultra short-period planets within our sample, confirm thick-disc host stars, compare the chemical abundances of hot Neptune and hot rocky worlds, and assess the radius valley and super-Earth desert of our sample. Finally, we give our conclusions in Section 5.

2 DETERMINING STELLAR PARAMETERS

2.1 Combining input data

All three GALAH Data Releases (DR1; DR2; DR3; Martell et al. 2016; Buder et al. 2018, 2020, respectively) contain physical and chemical parameters for stars observed on the 3.9-m Anglo-Australian Telescope (AAT), situated on Gamilaraay land in New South Wales, Australia. There are 392 science fibres attached to the two degree-field prime focus top-end (2dF; Lewis et al. 2002) that feed into the High Efficiency and Resolution Multi Element Spectrograph (HERMES) (Sheinis et al. 2015), delivering high-resolution ($R \approx 28\,000$) spectra in four distinct wavelength arms covering 471.3–490.3 nm, 564.8–587.3 nm, 647.8–673.7 nm, and 758.5–788.7 nm, respectively. Systematic and atmospheric effects are corrected for each spectrum and then continuum normalized with detailed physical parameters including $T_{\rm eff}$, $\log g$, [M/H] and individual abundances derived from each stellar spectrum using 1D stellar atmospheric models via the Spectroscopy Made Easy (or SME, Valenti & Piskunov 1996) package.

2.1.1 *GALAH DR3*

GALAH DR3 is slightly different from its previous two counterparts (GALAH DR2; Buder et al. 2018, and DR1; Martell et al. 2016) in a few ways. First, GALAH DR3 includes other stellar surveys, such as *TESS*–HERMES (Sharma et al. 2018) and K2-HERMES (Wittenmyer et al. 2018; Sharma et al. 2019), which have also used the AAT and HERMES instrument. This creates a catalogue with more coverage across the ecliptic and southern ecliptic pole. It also creates a catalogue that includes stars specifically observed for exoplanet detection and characterization.

Secondly, GALAH DR3 solely uses SME to derive stellar parameters for all $\sim$600 000 stars, whereas SME was used only in a subset of stars within DR1 and DR2 with these results and then propagated through the rest of the catalogue thanks to The Cannon (Ness et al. 2015). Quality flags have been determined for each star, encoded as a bitmask with flags raised indicating various problems with the analysis. For our analysis, we include only stars within our analysis that had an SME flag `flag_sp` $= 0$ and also required the Fe abundance flag `flag_X_fe` $= 0$ in the GALAH DR3 release.

2.1.2 *Cross-matching with other stellar and planetary catalogues*

For our analysis, we first cross-matched GALAH DR3 with the TIC DR8 (Stassun et al. 2018), *Gaia* DR2 (Gaia Collaboration 2018), and *Gaia* EDR3 (Gaia Collaboration 2020) using the TOPCAT (Taylor 2005) tool, cross-matching both catalogues with a position tolerance of $\pm$1 arcsec. Because we are interested in re-characterizing

confirmed or candidate exoplanetary systems, we then cross-matched GALAH DR3 with four different exoplanet and exoplanet candidate catalogues. These four catalogues include the NASA's Exoplanet Archive (NEA) and exoplanetary candidates from the K2[1] and TESS missions.[2] We cross-matched the NEA and TESS TOI and CTOI catalogues by comparing their TIC identifiers with those found within our catalogue and cross-matched the K2 candidate list with our catalogue by comparing 2MASS identifiers. We accepted only a K2 cross-match if the planet candidate was flagged as a 'CANDIDATE' within the K2 Candidate Catalog, rejecting those that are already confirmed exoplanets, which would be picked up through the Exoplanet catalogue cross-match, and already known false positives. We have included all TOIs and CTOIs, regardless of their disposition currently described by the *TESS* Follow-up Observing Program Working Group (TFOPWG) within the TOI and CTOI catalogues. From this cross-matching, we have identified 280 stars within GALAH DR3 that host either confirmed or candidate exoplanets.

2.2 Stellar masses, radii, luminosities, ages via ISOCHRONES

To derive the physical parameters of these host stars from the GALAH catalogue, we use a similar approach to Clark et al. (2020), implementing the PYTHON package ISOCHRONES (Morton 2015). ISOCHRONES derives physical parameters from observed stellar parameters using the stellar evolution grid, MESA Isochrones & Stellar Tracks (MIST; Choi et al. 2016). For our analysis, we used the star's effective temperature ($T_{\rm eff}$), surface gravity ($\log g$), and colour excess (E(B-V)) from GALAH, Johnson-Morgan (V; taken from the TIC), 2MASS (J, H, $K_{\rm s}$) and *Gaia* EDR3 (G, $G_{\rm RP}$, $G_{\rm BP}$) photometric magnitudes,[3] along with parallax values obtained by *Gaia* EDR3 (Gaia Collaboration 2020) where available as input observables for ISOCHRONES. We incorporated the associated errors for each measurement from their respective catalogues but inflated the associated errors in the photometric bands to 0.05 mag. By inflating the magnitude errors rather than including their associated errors, we found the stars to better converge on more realistic results, with ISOCHRONES producing better estimates on the error of the derived parameters. We also include the star's global metallicity, [M/H], derived by GALAH's [Fe/H] and [α/Fe] abundances formulated by Salaris & Cassisi (2006) as:

$$[\mathrm{M/H}] = [\mathrm{Fe/H}] + \log_{10}\left(0.694\, f_{\alpha} + 0.306\right) , \quad (1)$$

where f_{α} is the α-element enhancement factor given by $f_{\alpha} = 10^{[\frac{\alpha}{Fe}]}$. When the model reaches convergence, the median and corresponding 1-σ uncertainties for stellar mass, radius, density, age, and equivalent evolution phase values are calculated from their respective posterior distributions. A star's stellar luminosity is then calculated through the Stefan–Boltzmann relationship, with these resulting luminosities used to derive the habitable zone boundaries for each star, as formulated by Kopparapu et al. (2013). We include all five HZ boundaries within Kopparapu et al. (2013) including Recent Venus, Runaway Greenhouse, Moist Greenhouse, Maximum Greenhouse, and Early Mars. Rotational, radial and microturbulence velocities from GALAH DR3 have also been included in our stellar parameter table (Table A1) to assist ground-based radial velocity teams to better prioritize follow-up targets, including K2, TOI, and CTOI candidates.

[1] https://exoplanetarchive.ipac.caltech.edu/; accessed 2021 November 23.
[2] https://exofop.ipac.caltech.edu/; accessed 2021 November 23.
[3] We note that the transmission curves for *Gaia*'s photometric bands are different from DR2 to EDR3. Currently, ISOCHRONES handles only *Gaia* DR2 photometric bands. We ran tests during this analysis for the impact of using the different photometric values from DR2 to EDR3 and found changes to the astrophysical properties of the stars well within their 1-sigma error bars.

Table 1. Median and 1-σ values of our exoplanet/candidate-hosting population.

Quantity	$\mu \pm \sigma$
$T_{\rm eff}$ (K)	5633 ± 88
$\log g$ (cgs)	4.28 ± 0.19
[Fe/H] (dex)	− 0.01 ± 0.08
[α/Fe] (dex)	0.02 ± 0.04
[M/H] (dex)	0.03 ± 0.10
$R_{\star}$ ($R_{\odot}$)	1.18 ± 0.03
$M_{\star}$ ($M_{\odot}$)	1.02 ± 0.04
$L_{\star}$ ($L_{\odot}$)	1.49 ± 0.11
Age (Gyr)	4.98 ± 2.90

2.3 Comparison of stellar parameter estimates

Because our methodology uses cross-matched data with *Gaia* DR2 and TIC DR8, we can use stellar parameter values from these catalogues to determine any biases from our own data. The median value and median 1-σ errors for our stellar parameters can be found in Table 1 with the full stellar parameter catalogue being found in Table A1. Fig. 1 shows the comparison of GALAH DR3 $\log g$ and $T_{\rm eff}$ values with those determined by *Gaia* and the TIC.

2.3.1 Stellar T_{eff}

There is an overall good agreement between the catalogues, with a mean difference between $T_{\rm eff}$ values from GALAH and TIC of -11^{+121}_{-127} K, and *Gaia* of 32^{+281}_{-163} K, with an rms difference of 10 and 21 K, respectively. Just as Hardegree-Ullman et al. (2020) and Clark et al. (2020) showed in their work, we also find a horizontal structure within our *Gaia* $T_{\rm eff}$ comparison near 5000 K. This further suggests that *Gaia* $T_{\rm eff}$ values preferentially converge on to some $T_{\rm eff}$ values over others. For our comparison of TIC $T_{\rm eff}$ values, we compare only GALAH's values to those found with the TIC that have been derived photometrically and not spectroscopically. This is to avoid the potential comparison of GALAH DR2 values, as the TIC incorporated GALAH DR2's $T_{\rm eff}$ measurements into their catalogue. Our median planet-hosting temperature of 5514 K is slightly cooler than candidate hosts with a median temperature of 5698 K.

2.3.2 Stellar log g

Because the *Gaia* catalogue contains no $\log g$ values for its stellar catalogue, we compare only our $\log g$ results to those found within the TIC. In its current iteration, the TIC has $\log g$ values for only dwarf stars and not giants to fit within the science requirements of the *TESS* mission. Fig. 1 also shows the comparison with our dwarf $\log g$ values to those found in the TIC. There is a strong overall agreement with our $\log g$ values and those found within the TIC with a bias and rms of $0.00^{+0.06}_{-0.08}$ and 0.01 dex, respectively. Only one star seemed to be a significant outlier with the CTOI-host star TIC 179582003 having a $\log g$ of 4.45 ± 0.19 dex compared to a slightly lower surface gravity found within the TIC of 3.91 ± 0.08 dex.

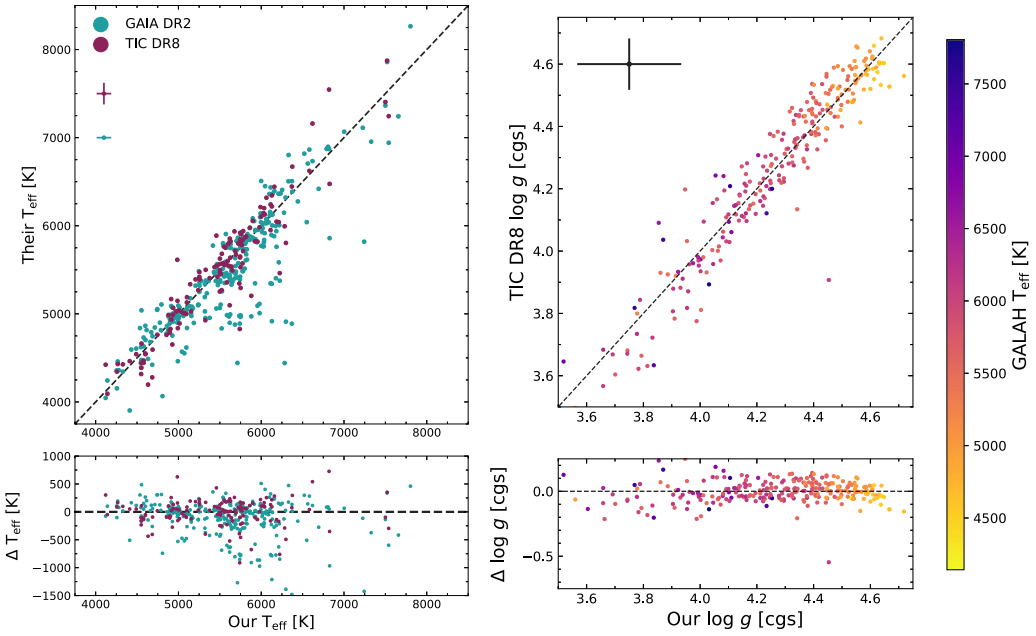

Figure 1. *Left*: GALAH DR3's $T_{\rm eff}$ results are plotted against the $T_{\rm eff}$ measurements found within the *Gaia* DR2 (blue) and TIC (purple) catalogues, respectively. An equality line (grey dashed) is plotted for comparison. Only stars within the TIC that were flagged as obtaining their effective temperature values from photometric surveys are plotted on this graph. A median GALAH-TIC and GALAH-*Gaia* $T_{\rm eff}$ error bars are found in the figure's top left (purple and blue crosses, respectively). Because the *Gaia* DR2 catalogue currently does not produce errors for their $T_{\rm eff}$ values, there is no median y-error bar for *Gaia* in the plot. The differences in our results are plotted in the bottom plot with $\Delta X = X_{\rm Other} - X_{\rm GALAH}$. *Right*: GALAH's log g values compared to the TICs with each star colour-coded by their $T_{\rm eff}$ values. As with the $T_{\rm eff}$ figure to the left, an equality line (grey-dashed line) is shown along with the median TESS and GALAH log g error bar shown in the top left (grey cross). log g values for giant stars are not derived in the TIC and are thus not compared with GALAH's values within this figure.

2.3.3 *Stellar [M/H]*

Overall metallicity values, [M/H], are found within Table A1 and were calculated from GALAH DR3's [Fe/H] and [α/Fe] abundances. We should note that the current TIC catalogue directly incorporates GALAH DR2's iron abundances, [Fe/H], as a star's overall metallicity [M/H]. As such, a direct comparison between such values is left to a more thorough analysis of iron abundance improvements from DR2 and DR3 in Buder et al. (2020).

2.3.4 *Stellar radius and mass*

From GALAH's DR3 $T_{\rm eff}$, log g and [M/H] measurements, alongside photometric and astrometric parameters, we have been able to constrain stellar mass, radius, age, and thus luminosity values from ISOCHRONES. For a sanity check, we created a Hertzsprung–Russell diagram found in Fig. 2 to check if our stars fell into any non-physical areas of the diagram. A vast majority of our planet-hosting or candidate-hosting stars lie on the main sequence with only 21 giant stars within our sample (Note, we classify a star as a giant by it being cooler than 5500 K and having a surface gravity of less than 3.5; Sharma et al. 2019).

Fig. 3 compares our stellar radius and mass values against other internal and external catalogues. Our stellar radius values are compared against those found within the TIC, *Gaia* DR2, and the GALAH DR3 BSTEP Value Added Catalog (VAC). The BSTEP VAC results

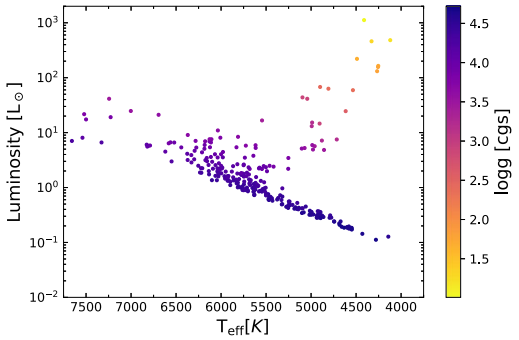

Figure 2. This Hertzsprung–Russell diagram of our GALAH DR3 $T_{\rm eff}$ and ISOCHRONES luminosity values colour coded by GALAH DR3's log g values shows that the vast majority of planet-hosting or candidate-system stars lie on the main sequence. Of our 280 stars, only 21 are giants ($T_{\rm eff} < 5500$ and log $g < 3.5$).

for K2-HERMES and *TESS*–HERMES stars are being released in a future paper. Briefly, stellar parameters such as age, mass, and radius were computed with the BSTEP code (Sharma et al. 2018) making use of PARSEC–COLIBRI stellar isochrones (Marigo et al. 2017). BSTEP provides a Bayesian estimate of intrinsic stellar parameters from observed stellar parameters by making use of stellar isochrones.

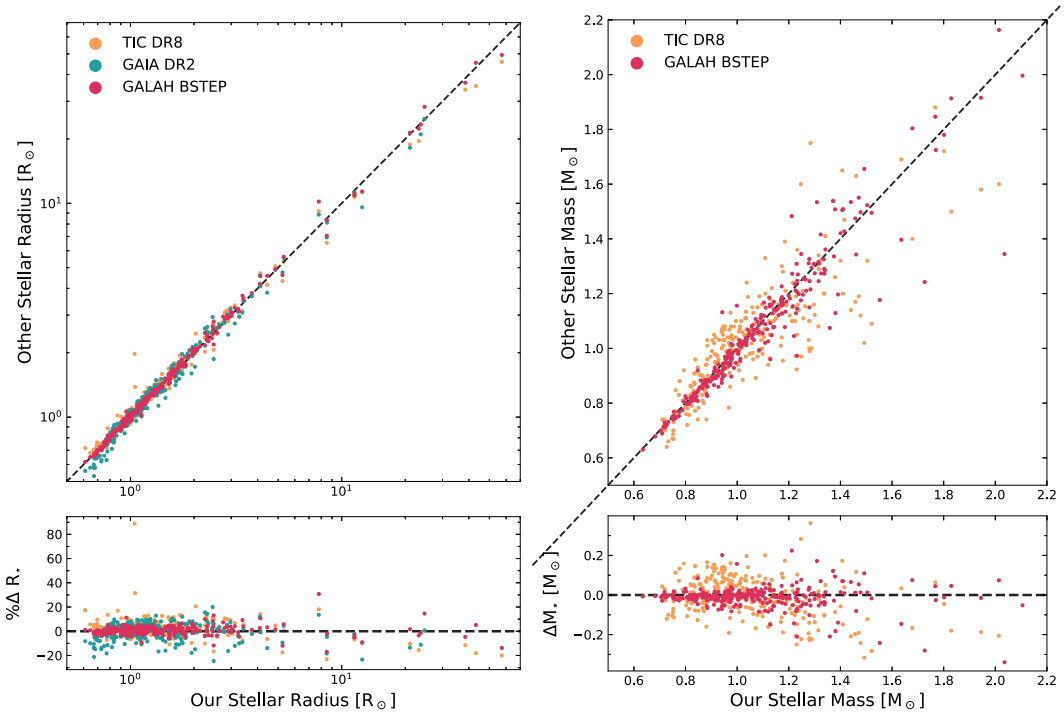

Figure 3. *Left*: Our stellar radius values are compared to other surveys and methodologies to confirm the validity of our values. Radius values derived from ISOCHRONES are compared with values found within the TIC (yellow), *Gaia* DR2 (blue), and GALAH's BSTEP VAC (red). Error bars are suppressed for clarity. An equality line in both plots is depicted in a grey dashed line. *Right*: Our stellar mass values are compared against those that are found within the TIC (yellow) and GALAH's BSTEP VAC (red). 1-σ median error bars for each comparison can be found in the top-right corner of the figure.

It is unsurprising, given the same data and similar methodology, that our stellar radius values agree well against those found in BSTEP, with a stellar radius bias and rms of $-0.01^{+0.03}_{-0.04}\,R_\odot$ and $0.04\,R_\odot$, respectively. These values are comparable to comparisons we make to the TIC and *Gaia* DR2, with median biases of $-0.02^{+0.05}_{-0.08}$ $R_\odot$ and $-0.01^{+0.09}_{-0.07}$ $R_\odot$, and rms values of 0.06 $R_\odot$ and 0.02 $R_\odot$, respectively.

While GALAH DR3 does not come with stellar masses, the BSTEP VAC catalogue does, such that our isochrone-derived results are compared with BSTEP and the TIC values found in Fig. 3. There are 25 stars within our sample that have no mass measurements found within the TIC (including confirmed planet hosts K2-97 b (Livingston et al. 2018b), NGC 2682 Sand 364 b (Stassun, Collins & Gaudi 2017), and NGC 2682 Sand 978 b (Brucalassi et al. 2017), due to the TIC-only deriving masses for dwarf stars and hence no comparison between their masses is shown in Fig. 3.

As with the stellar radii, there seems to be an overall good agreement with our derived mass values and those found within the TIC, with a bias and rms of $0.01^{+0.11}_{-0.09}\,M_\odot$ and $0.01\,M_\odot$, respectively. Our stellar mass results are comparable with stellar mass values found in GALAH's BSTEP VAC, with bias of $0.01^{+0.04}_{-0.03}\,M_\odot$ and rms of $0.01\,M_\odot$, respectively. However, there seems to be a larger scatter for stars more massive than $1.4\,M_\odot$, with our results preferentially favouring larger mass values compared to the other catalogues. These mass and radius measurements become fundamental parameters for constraining the mass and size of the planets they host, which will be discussed in the next section.

3 REFINING PLANETARY SYSTEMS

With our new stellar parameters, we can now refine and redetermine the planetary or potential planetary systems that these stars host. We previously cross-matched GALAH DR3 with the NEA for known planet hosts and K2 candidates. We also cross-matched GALAH DR3 with stars known to host TOI and CTOIs. From these cross-matches, we have 105 confirmed exoplanets, and 293 exoplanet candidates with 146 K2 candidates, 95 TOIs, and 52 CTOIs. The refined planetary parameters can be found in Table A2.

As there are multiple catalogues with differing definitions of transit depth (i.e. some report it in mmag, others as a percentage or as $(R_s/R_p)^2$), we convert all transit depths to percentages. Thus, the exoplanet's radius is defined by:

$$\frac{R_p}{R_\oplus} = \sqrt{0.01\Delta F}\,\frac{R_s}{R_\odot}\,, \tag{2}$$

where R_p is the planet's radius, ΔF is the percentage transit depth, and R_s is the host star's radius. The planet's semimajor axis is calculated by Kepler's third law, incorporating our revised stellar mass values. These semimajor axis values were then used alongside stellar luminosities ($L_\star$) to derive insolation flux values, S_{eff}, for each confirmed and candidate exoplanet. These stellar luminosities and the newly derived temperatures can then be used to determine a planet's effective temperature. If an exoplanet's atmosphere is 'well mixed', that being there is no obvious phase function at IR wavelengths, its

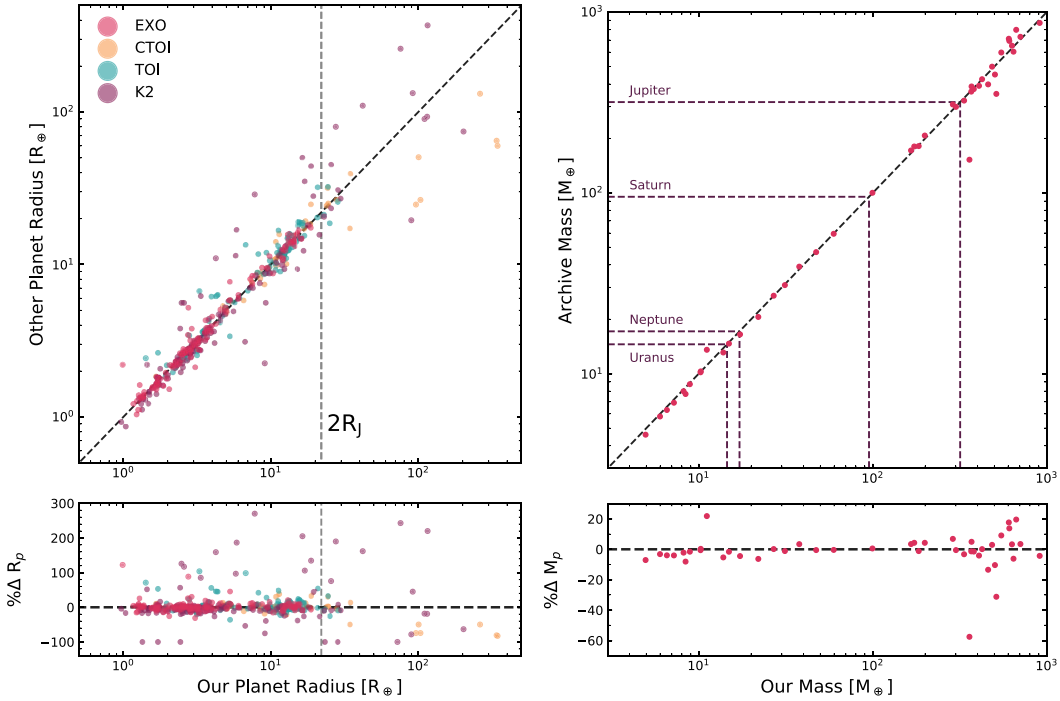

Figure 4. *Left*: Our planetary radii values are compared with literature values found within the NEA (red) K2 candidate catalogue (purple) and TOI (blue) and CTOI (yellow) catalogues found on ExoFOP. No confirmed exoplanet thus far has a radius larger than twice that of Jupiter's (vertical grey-dashed line). As such, any candidate beyond the right of this line is most likely non-planetary in nature and more likely a sub-stellar or stellar companion to its host star. *Right*: We compare our planetary mass values to those found within the NEA. Lines representing the masses of Uranus, Neptune, Saturn, and Jupiter are depicted as purple dashed lines across the plot.

effective temperature will be:

$$T_{\rm p} = \left(\frac{L_\star(1-A)}{\alpha\pi\sigma r^2}\right)^{\frac{1}{4}}, \tag{3}$$

where $\alpha = 16$, the spherical (Bond) albedo is given by A, σ is the Stefan–Boltzmann constant, and r is the star–planet separation, which we have defaulted to be the semimajor axis (Kane & Gelino 2011) of the star–planet system. For a hot-dayside exoplanet, whereby its atmosphere is inefficient with respect to heat distribution, its effective temperature is calculated also using equation (3), but in this instance, $\alpha = 8$ instead (Kane & Gelino 2011). Because an exoplanet's rotational period (exo-day) is currently difficult to determine, we have included both values within Table A2.

We have used the geometric albedos from Sheets & Deming (2017) with geometric albedos assumed to be 0.11 ± 0.06, 0.05 ± 0.04, and 0.11 ± 0.08 for planets 1–2 $R_\oplus$, 2–4 R⊕, and 4–6 $R_\oplus$, respectively. Bond albedos are then calculated from these geometric albedos using the relationship $A_{\rm B} = 3A_{\rm g}/2$ (Seager 2010). We also used the 1–2 $R_\oplus$ albedo value for planets $R_{\rm p} < 1R_\oplus$ and used the Bond albedo value of 0.35 ± 0.05 (Mallonn et al. 2019) for planets >6 $R_\oplus$.

For known exoplanets that have measured line of sight, $M_{\rm P}\sin i$, or true mass measurements, we refine their masses, given our stellar mass values given by the formula:

$$\frac{M_{\rm P}\sin i}{M_\oplus} = \frac{K_{\rm RV}\sqrt{1-e^2}}{0.0895{\rm ms}^{-1}}\left(\frac{M_*}{M_\odot}\right)^{2/3}\left(\frac{P}{\rm yr}\right)^{1/3}, \tag{4}$$

where $K_{\rm RV}$ is the radial velocity's semi-amplitude in ms^{-1}, e is the orbital eccentricity, and P is the orbital period. This equation also assumes that $M_{\rm p} \ll M_\star$ (Lovis & Fischer 2010). If the orbital inclination of the system is known, we then refine the planet's true mass, $M_{\rm p}$.

Because the NEA is designed now to have multiple entries for a single exoplanet or planetary system, the challenge then becomes what observables we use to refine and re-characterize these exoplanets and planetary systems. We have used a weighted mean approach to determine a single value for our K2 candidate transit depths and orbital inclinations. We have also used a weighted mean approach to derive exoplanet transit depths, radial velocity semi-amplitudes, and orbital eccentricities, inclinations, and periods where available. The weighted mean of observable X is calculated by:

$$\bar{X} = \frac{\sum_{i=1}^{n} w_i X_i}{\sum_{i=1}^{n} w_i}, \tag{5}$$

where the weight of the i-th data point w_i is related by its error, σ_i as $w_i = \sigma_i^{-2}$. The error in the standard mean is then calculated to be:

$$\sigma_{\bar{X}} = \left(\sqrt{\sum_{i=1}^{n} w_i}\right)^{-1}. \tag{6}$$

These weighted mean values are then used to refine the planetary mass and radii values found in Fig. 4 with our new planetary properties found in Table A2.

4 DISCUSSION

4.1 Identifying false positives

Fig. 4 shows the comparison of our planetary radii and mass values compared to catalogue values found either on the NEA or NASA's ExoFOP data bases. If there were multiple planetary mass or radius values, we have compared our results to the latest values within their respective data bases. Using the same definition found in Wittenmyer et al. (2018), we use an upper limit of $R_P < 2\ R_J \approx 22R_\oplus$ for a planetary object. We have used this cutoff as there is currently no confirmed exoplanet on the archive with a planetary radius larger than this value.

There are 12 CTOIs that have radii comparable to sub-stellar and stellar objects, being larger than our $2R_P$ limit. Of these, Clark et al. (2020) also found the planetary radii values for CTOI 201256771.01, CTOI 201256771.02, and CTOI 300903537.01 to be too large for a planetary object. The two candidates orbiting TIC 141622065, both have radii of $344.62 \pm 6.50R_\oplus$ and $339.57 \pm 6.40R_\oplus$, with an orbital period separation of 0.05 d. These two candidate events are more akin to a single 3 $R_\odot$ binary star companion. Similarly, the radii for all candidates in the CTOI 91369561 system including TIC 91369561.02 and TIC 91369561.03 have radii comparable to FGK-type stars. CTOI 140830390.01 and CTOI 220402290.02 have planetary radii on the cusp of the 'planetary limit' of $\sim 22R_\oplus$, but it was further suggested in Clark et al. (2020) that the candidate events within the CTOI 220402290 system are also from a single object, which is likely caused by a sub-stellar or stellar companion. CTOIs 31869740.01 and 219322317.01 are both recorded as having sub-stellar radius values of $31.61R_\oplus$ and $39.24 \pm 2.64R_\oplus$, respectively, on TFOP. With our revised radius values, these two candidates also have non-physical planetary radii, with their radii now being $24.27 \pm 2.13R_\oplus$ and $34.59 \pm 0.71R_\oplus$ for CTOI events 31869740.01 and 219322317.01, respectively. Planetary candidate CTOI 140830390.01, also known as TOI 1072.01, is more likely a brown dwarf with a planetary radius of $27.91 \pm 0.68R_\oplus$. These results highlight the need for vetting of CTOI systems before they are made publicly available.

With our refined radii, there are five exoplanetary TOI candidates that have radii $R_p > 2R_J$. These being TOI 147.01, 565.01, 959.01, 1072.01, and 2391.01. The TESS Follow-up team contains five specialist sub-groups, with TFOP Science Group 1 (SG1) specializing in seeing limited photometry. Members attempt to confirm and refine orbital parameters from TOIs, with the project lead then up- or down-ranking the candidates' disposition depending upon their follow-up observations. Currently, TOI 147.01 and TOI 959.01 have their dispositions labelled as 'false positives', with our work also confirming that their radii alone are too big to be considered planetary in nature. TOI 565.01 was originally labelled as a 'false positive' under the TFOPWG Disposition in April 2019 but is now an 'ambiguous planetary candidate' as of November 2020. With an archive planetary radius of $18.62R_\oplus$ and now an updated radius of $25.07 \pm 0.65R_\oplus$, this candidate is also now too large to be exoplanetary in nature and is likely an eclipsing binary event.

There are only two TOIs above our planetary radius limit, TOI 1072.01 and TOI 2391.01, which are currently labelled as potential candidates on TFOP, with TOI 1072.01's planetary nature already being discussed. TOI 2379.01 is on the borderline of our defined planetary radii boundary, having a radius of $21.21 \pm 1.34R_\oplus$ on TFOP, with our radius only being slightly higher of $22.89 \pm 0.58R_\oplus$. Notes on TFOP suggest that this event is likely an eclipsing binary, with our revised radii also being too large for a planet-like event. If confirmed to be an exoplanet, however, it would be one of the largest ever to be discovered.

There are 18 K2 candidates that have problematic radii with 13 having been found to be false positives in previous work (Wittenmyer et al. 2018, 2020). Of the five K2 candidates remaining, three candidates EPIC 210769880.01, EPIC 205050711.01, and EPIC 204546592.01 all have candidate radii $>0.35\ R_\odot$, which far exceeds the physical radius needed to be a planetary event. There are two candidate events observed by K2 that are much closer to having radii nearer to the $2R_J$ radius limit, these being EPIC 214611894.01 and EPIC 210598340.01.

EPIC 214611894.01 is a candidate event discovered through K2's seventh campaign by Petigura et al. (2018) with a candidate radius of $20.5^{+2.8}_{-2.1}R_\oplus$. Its refined stellar host radius of $1.35 \pm 0.02\ R_\odot$ is larger compared to Petigura et al.'s (2018) value of 1.21 $R_\odot$. This increase has meant that the candidate's radius is now $28.50 \pm 0.63R_\oplus$, which is too large to be planetary in nature. A candidate first announced by Barros, Demangeon & Deleuil (2016), EPIC 210598340.01's radius was first determined by Kruse et al. (2019) as being $30.71^{+0.54}_{-6.89}R_\oplus$. Our newly revised candidate radius for EPIC 210598340.01 sits right on our defined radius limit, being $22.92 \pm 0.45R_\oplus$. This candidate radius is also smaller than the one derived by Hardegree-Ullman et al. (2020), with their derived planetary radius for EPIC 210598340.01 of $26.764^{1.724}_{-1.633}R_\oplus$. With our revised radii, it is possible that this candidate is planetary in nature, but more follow-up is needed.

4.2 Follow-up and mass confirmation from ground-based surveys

TESS is delivering thousands of candidate exoplanets in which the community will have to confirm and characterize by both space and ground-based observations. The radius measurements of these candidates will be derived mostly from TESS photometry, with confirmation mass measurements being derived from ground-based radial velocity follow-up. On the biggest considerations for radial velocity follow-up is considering a star's rotational velocity – or in most cases, its projected rotational velocity ($v \sin i$). Slow rotating stars are the most preferred stellar companions, as they generally have well-defined absorption lines. As $v \sin i$ increases, the absorption lines needed for high-precision radial velocity measurements will broaden out, with some lines blending completely. This broadening decreases the number of well-defined lines needed to obtain better radial velocity measurements, thus deteriorating the radial velocity precision. We have thus included $v \sin i$ values in Table A1 to assist follow-up teams in better allocating telescope time to feasible RV targets.

We have decided to forward model the likely mass and thus predicted radial velocity semi-amplitudes for confirmed and candidate exoplanets within our sample to check which are the most viable targets for mass confirmation. To model the predicted radial velocity semi-amplitudes, we have used the Chen & Kipping (2017) mass–radius relationship to derive predicted mass values for exoplanets for which there exists no current mass measurements. From this, we have used equation (4), along with the host's stellar mass, the predicted planetary mass, observed orbital period, and assuming circular orbits for these planets to then obtain the predicted semi-amplitudes. These predicted semi-amplitude values are plotted against the host star's $v \sin i$ in Fig. 5. In Fig. 5, we have also included confirmed exoplanets with known mass measurements from NEA for comparison to our predicted RV values.

For the majority of our candidates, their host star's $v \sin i$ values are above $5\ \mathrm{km\,s^{-1}}$; however, the planet's predicted RV signal is

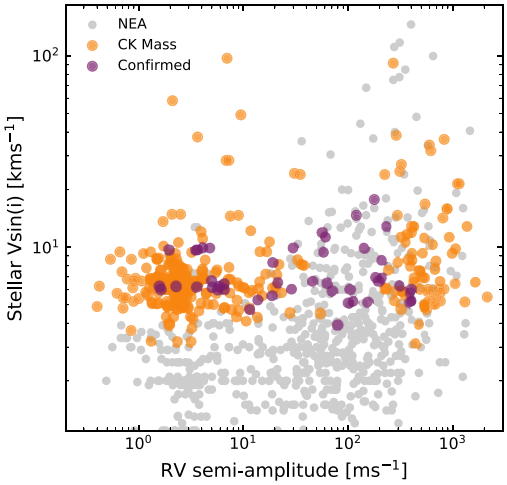

Figure 5. Expected radial velocity amplitudes for candidate and known exoplanets have been derived from expected mass values from Chen & Kipping (2017) (in yellow) and compared to exoplanets with known mass values in our sample (purple) and those within NASA's Exoplanet Archive (grey).

less than 5 m s^{-1}. For context, only 19 confirmed exoplanets have RV signals less than 5 m s^{-1} orbiting stars with $v \sin i$ values greater than 5 km s^{-1}. We then predict that it will be difficult, with current methodology, to obtain mass confirmations for most of the smaller planet candidates orbiting stars found within our sample. In the extreme cases for smaller planets orbiting rapid-rotating stars, it will be highly improbable to derive their mass measurements.

For example, the star TOI-1219 (TIC 294981566) is a rapid rotator ($v \sin i = 58.3 \pm 2.5$ km s^{-1}) with a $1.97 \pm 0.13 R_\oplus$ planet candidate orbiting around it every 1.91 d. We wanted to see what the expected radial velocity precision would be for such candidate orbiting around such a rapid rotator and compare that to the expected RV signal of the exoplanet. To do this, we created a template spectrum that roughly matched the stellar properties of the host star, resampling the spectrum to match modern extreme precision radial velocity spectrographs (spectral range = 400–650 nm, $R \sim 100\,000$ and 3.5 pixels per full width at half-maximum). We then recreated this stellar template for its observed $v \sin i$ value, calculating the intrinsic error in radial velocities using Butler et al. (1996). With its current rotational velocity, the expected RV precision for TOI-1219 is 20.5 m s^{-1}, nearly an order of magnitude difference compared to the predicted RV signal of TOI-1219.01 being an estimated 2.1 m s^{-1}. Since we know what the expected RV signal of the planet candidate is predicted to be ($K = 2.1$ m s^{-1}) and have an intrinsic RV precision ($\sigma_{\bar{V}} = 20.5$ m s^{-1}), we can use the formula found in Wittenmyer et al. (2011):

$$N = \left(\frac{12.3 \times \sigma_{\bar{V}}}{K + 0.02} \right)^2 \quad (7)$$

to then determine the number of observations (N) needed to detect the radial velocity signal of TOI-1219.01. In this case, the number of observations needed to confirm the mass measurement of TOI-1219.01 would be over 14 000. For context, the number of radial velocity observation we currently use for RV detection is in the order of tens or in some case nearing to 100 or 200 observations. Thus, for a relatively hot ($T_{\rm eff} = 6600$ K) and rapidly rotating star, the precision needed to obtain a 3-sigma RV signal for TOI-1219.01 is unobtainable with current technology and methodology. Higher-resolution spectrographs will be needed to determine the mass measurements of small planets orbiting rapid rotating stars. For reference, there is only one exoplanet that has a confirmed mass measurement smaller than $4 R_\oplus$ orbiting a star with a $v \sin i$ greater than 20 km s^{-1}, with Kepler-462 b's mass being determined through transit timing variations orbiting the rapid rotating star ($v \sin i = 80 \pm 3$ km s^{-1}) Kepler-462 (Masuda & Tamayo 2020). Transit timing variations can therefore be another great avenue to determine the mass measurements of these candidates, rather than utilizing RV measurements. Our data, along with other large stellar surveys, then provide a useful data base for ground-based follow-up teams to determine what are the most suitable targets to follow up for mass confirmation to maximize their resource efficiency.

4.3 Planetary compositions from mass–radius relations

4.3.1 Our results

Within GALAH's latest data release, there are 105 confirmed planet-hosting stars. There was only one planet that was omitted in our analysis, this being the exoplanet Pr0211 c, as its orbital period error was too large to facilitate in the Markov chain Monte Carlo (MCMC) analysis of our work. With our previous line of thought, there are no planets with revised radii measurements that exceed the $2 R_J$ limit. Nor do any revised mass measurements, where available, exceed the theoretical exoplanet mass limit of $\sim 13 M_J$ (Boss 2001). Fig. 4 shows our newly derived mass values compared to those found in the literature. We should note that in Fig. 4, the comparison of literature values is median mass and radius values taken from the NEA. There are three visible outliers within the comparison mass plot, CoRoT-7 c ($11.12 \pm 0.79 M_\oplus$), K2-97 b ($359.26 \pm 38.56 M_\oplus$), and K2-34 b ($512.48 \pm 17.39 M_\oplus$). With further inspection, these three outliers are mainly caused by various anomalies within the NEA, rather than drastic changes with the refined stellar parameters, for example, K2-97 b.

An example of the caveats of both our methodology and utilizing any form of heterogeneous archival data comes from the revision of planetary system K2-97. First discovered by Grunblatt et al. (2016), K2-97 b is a Jupiter-sized exoplanet that had an initial radial velocity semi-amplitude of 103 ± 8 m s^{-1}, inferring a planetary mass of $350 \pm 35 M_\oplus$, where our refined value is $359.26 \pm 38.56 M_\oplus$.

However, its radial velocity semi-amplitude was later revised by Grunblatt et al. (2017) through additional radial velocity measurements to be $42.1^{+4.3}_{-4.2}$ m s^{-1}, a decrease of over 56 per cent. These new measurements imply a revised mass of $153 \pm 22 M_\oplus$. But this RV value is not included within the NEA and hence was not used within our methodology until now.

If these literature values were treated as independent measurements, our weighted mean approach would yield an estimated mass for K2-97 b of $146.7 \pm 18.4 M_\oplus$. But, if you then incorporate both of these values in our weighted mean approach, the mass of K2-97 b then becomes $194.54 \pm 19.54 M_\oplus$. Additionally, if we were to use only the default parameters (DEFAULT_FLAG) used by the NEA, K2-97 b's parameters would include its planet radius but no information would be present in regard to its planetary mass (Livingston et al. 2018b).

With 469 independent records for our sample of 105 exoplanets within the NEA, it would be inefficient to independently review every record entry on the archive. The community can utilize only the information that is present within its current iteration. As the

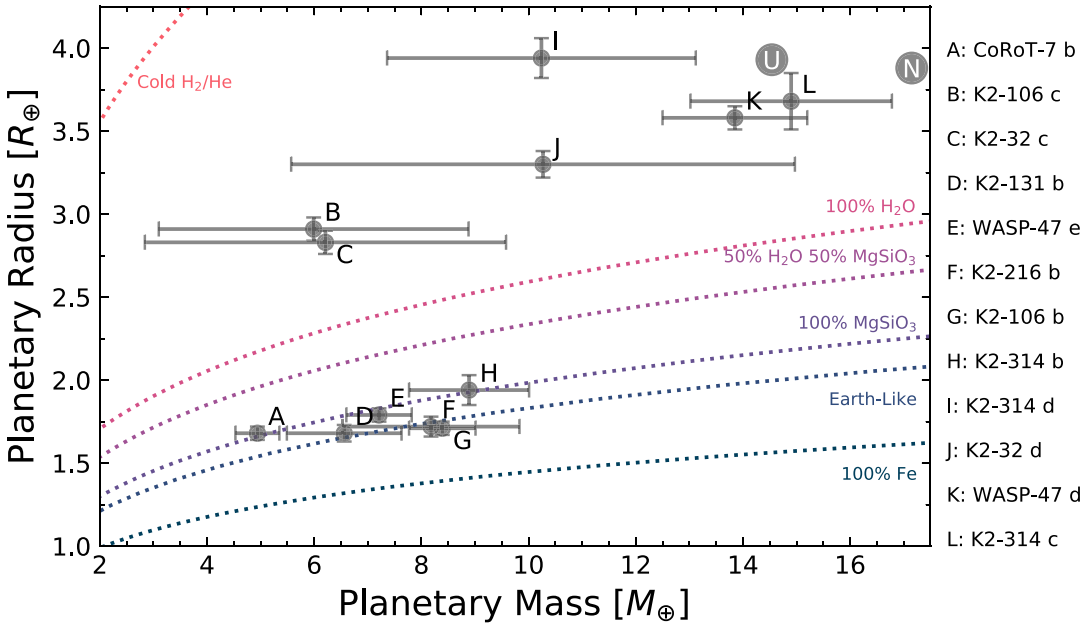

Figure 6. Revised planetary mass and radius values for confirmed super-Earth and mini-Neptune exoplanets within our sample. Each planet is labelled alphabetically, with its corresponding name to the right of the plot. 1-σ error bars are given for each exoplanet, with Uranus and Neptune depicted on the plot as 'U' and 'N' in the plot's right-hand corner. The mass–radius relationships used for the dashed lines to show density curves for cold H_2/He, 100 per cent water, 50 per cent water, and 50 per cent rocky, pure rocky (containing pure post-perovskite $MgSiO_3$), 'Earth-like' (33 per cent Fe and 67 per cent rock), and pure iron worlds are from Zeng, Sasselov & Jacobsen (2016).

field becomes more reliant on heterogeneous data to infer exoplanet populations and demographics, it is crucial that all of these data are accounted for. Hence, there needs to be a discussion within our community on making data and fundamental parameters within our literature more accessible and refine our best practice on updating information on exoplanetary systems.

Because mass and radius measurements of an exoplanet are derived through independent techniques, there is a small overlap for exoplanets with both mass and radius measurements within our sample. We can plot some of our 39 exoplanets with both inferred mass and radius values on to a mass–radius diagram. In Fig. 6, we have plotted all of the exoplanets within our sample with a planetary radius, $R_p \leq 4R_\oplus$, with known mass and radius measurements. Even within our relatively small sample, there is a large variation of planetary mass for a particular planetary radius, showing the compositional diversity of known exoplanets. There are two distinct exoplanet groups contained with this phase space, sub-Neptunes (i.e. WASP-47 d, K2-314 c etc.) and super-Earths (i.e. CoRoT-7 b, K2-106 b etc.).

Of these 12 exoplanets, six have radii that put them within the exoplanet category known as super-Earths. All of these super-Earths either straddle or sit within the super-Earth radius gap, a scarcity of planets with radii, $1.5R_\oplus \leq R\_p \leq 2R_\oplus$ (Fulton et al. 2017), indicating that these planets may be transitioning between their radii being dominated by their rocky bodies, rather than gaseous envelopes. We show in Fig. 7 a zoom-in of our refined mass and radius values, compared to the latest entry in the NEA. There are some cases, where there are only single values for a given exoplanet's mass and radius value (e.g. K2-314 b) where there is a shift in mass and radius values, given our change in stellar values. But there are also several cases here where we have combined multiple mass and radius measurements within the archive, as well as our refined stellar values, to better refine the characteristics of these known super-Earths (e.g. CoRoT-7 b and K2-106 b). More detail for each of these planets is discussed below.

4.3.2 Fundamental properties of our ultra short-period exoplanet sample

(i) **K2-314 b:** K2-314 b, also known as EPIC 249893012 b, is a super-Earth-sized exoplanet first discovered in 2020 by Hidalgo et al. (2020) orbiting a slightly evolved, metal-rich ([Fe/H] $= 0.19$) G-type star. Our stellar parameters for K2-314, $1.71 \pm 0.03\,R_\odot$, and $1.07 \pm 0.03\,M_\odot$, compared to those found in Hidalgo et al. (2020), $1.71 \pm 0.04\,R_\odot$ and $1.05 \pm 0.05\,M_\odot$, are almost identical with only a very slight adjustment to the star's mass values. This small discrepancy in stellar values translates to an insignificant change in the exoplanet's mass and radius values, with our values of $1.94 \pm 0.09R_\oplus$ and $8.89 \pm 1.12M_\oplus$ for K2-314 b, compared to its original values of $1.95^{+0.09}_{-0.08}R_\oplus$ and $8.75^{+1.09}_{-1.08}M_\oplus$ (Hidalgo et al. 2020). This small discrepancy is also found with its exoplanetary siblings K2-314 c and K2-314 d found in Fig. 6.

(ii) **K2-106 b:** Found within the Pisces constellation is a two-planet system, orbiting the GV star K2-106, also known as EPIC 220674823 (Guenther et al. 2017). One of these planets is the ultra short-period ($P = 0.567$ d) super-Earth K2-106 b. Combining multiple radial-velocity and photometric measurements, our revised planetary radius and mass values for K2-106 b are $1.71 \pm 0.04R_\oplus$ and

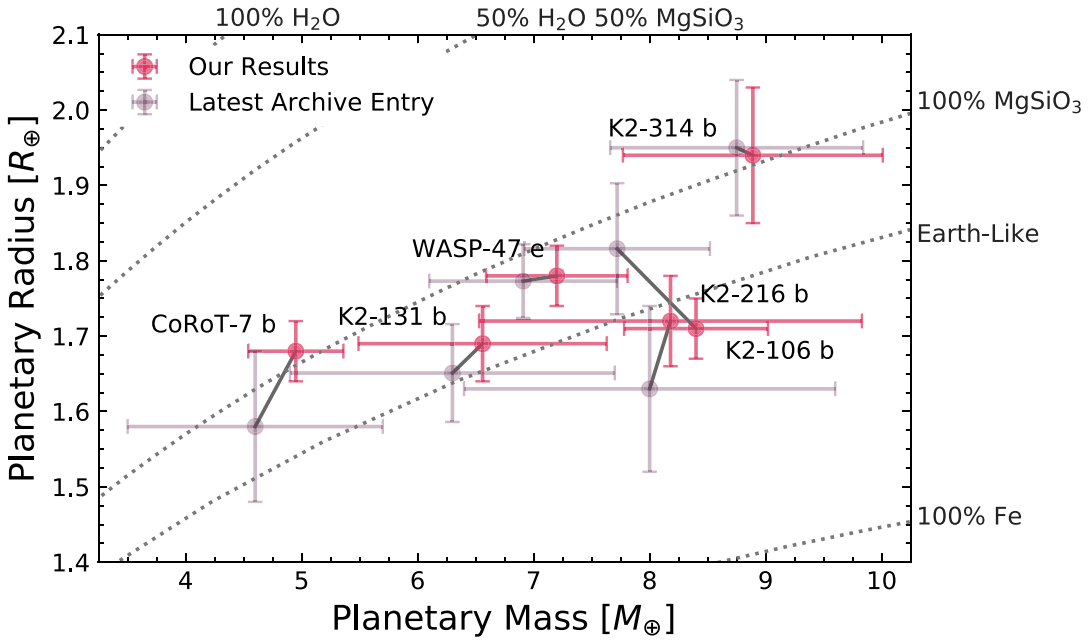

Figure 7. Combining the weighted mean and updated stellar parameters approach of our work (labelled as red crosses) has improved the mass and radius errors on several exoplanets that are thought to be rocky in nature within our work. The latest entry within the NEA is shown for reference as grey crosses.

8.39 ± 0.62$M_\oplus$, respectively. These revised planetary radii and mass values now place K2-106 b underneath the density curve of a planetary body with a density like that of Earth.

By far, the most interesting aspect of K2-106 b is the amount of incoming insolation flux being received on its surface, 4330 times that of Earth. K2-106 b's well mixed and hot dayside equilibrium temperatures of 2160 K and 2570 K, respectively, far exceeded the condensation temperatures of most refractory elements. The dayside equilibrium temperature would be more akin to that on the surface, as tidal locking would become likely with an orbit so short. With an equilibrium temperature of 2568 ± 74 K, our newly revised parameters for K2-106 b make it the hottest known super-Earth to date. There are only eight exoplanets on the NEA that have higher equilibrium temperatures. However, as shown by Konatham, Martin-Torres & Zorzano (2020), ultra-hot worlds like K2-106 b, WASP-47 e, and CoRoT-7 b (discussed later in this section) could retain atmospheres, even atmospheric constituents such as O, H_2O, and CH_4, given their relatively high escape velocities. K2-106 b's escape velocity is 24.76 ± 0.97 kms^{-1}, comparable to Neptune's escape velocity of 23.5 kms^{-1}.

(iii) **K2-216 b:** Also contained within the Pisces constellation is the K5 V dwarf, K2-216, with a single super-Earth companion, K2-216 b (Mayo et al. 2018; Petigura et al. 2018). Our stellar radius and mass values for K2-216 are consistent with other surveys, them being 0.69 ± 0.01 $R_\odot$ and 0.72 ± 0.02 $M_\odot$, respectively. As with K2-106 b, the planet is also on an ultra-short orbit of 9 h, with a single radial velocity (Persson et al. 2018) and several transit detections used within our methodology to revise its fundamental parameters. We have revised the planetary radius and mass of K2-216 b to be 1.72 ± 0.06$R_\oplus$ and 8.18 ± 1.65$M_\oplus$, respectively. With K2-216 b's relatively high density (8.85 ± 1.99 gcm^{-3}), high escape velocity (24.38 ± 2.55 kms^{-1}), and moderate equilibrium temperature (1217 ± 34 K), it can be capable of an atmosphere comprising H_2O, N_2, and CO_2 (Konatham et al. 2020).

(iv) **WASP-47 e:** Contained within a four-planet system is a super-Earth exoplanet known as WASP-47 e, first discovered in 2015 (Becker et al. 2015; Dai et al. 2015). Orbiting around an iron-rich ([Fe/H] = 0.45 ± 0.09 dex) G9V dwarf every 0.78 d, this exoplanet and its companions have been characterized by numerous studies since its discovery (Weiss et al. 2017; Dorn et al. 2019; Kane, Fetherolf & Hill 2020). With our refined stellar parameters (1.13 ± 0.02 $R_\odot$, 1.06 ± 0.05 $M_\odot$) and combining multiple independent archive observations, we have determined the radius and mass of WASP-47 e to be 1.79 ± 0.04$R_\oplus$ and 7.21 ± 0.61$M_\oplus$, respectively. Its equilibrium temperature rivals that of K2-106 b, with our derived T_{eq} being 2514 ± 70 K. Dorn et al. (2019) have postulated that WASP-47 e may have an exotic composition of a Ca and Al-rich interior without any atmosphere. But if there is an atmosphere, with an escape velocity of 22.44 ± 0.99 $km\,s^{-1}$, it may contain ionic calcium, silicon, magnesium, and maybe even aluminium with its extreme equilibrium temperature (Dorn et al. 2019). The albedo of such worlds is still a field of active research, with Kane et al. (2020) being able to constrain the geometric albedo of its sibling, WASP-47 b, to be 0.0016 but were unable to constrain WASP-47 e's. However, there was some evidence to suggest that WASP-47 e's geometric albedo could also be as low as WASP-47 b, but a wide range of geometric albedo solutions were also found. Contrary to this, Modirrousta-Galian, Ito & Micela (2021) found that high spherical albedos for super-Earths could be explained by molten Fe-rich magma oceans on the surface of ultra short-period worlds (Rouan et al. 2011).

(v) **K2-131 b:** Orbiting around the K dwarf K2-131 is an ultra short-period exoplanet known as K2-131 b (Dai et al. 2017). Currently a single planet system, our stellar mass and radius values of $0.75 \pm 0.01\,R_\odot$ and $0.82 \pm 0.02\,M_\odot$ are comparable to values found within the archive. Discovered in 2017, we have combined our stellar parameters and observed parameters from other surveys to revise K2-131b's radius and mass to be $1.68 \pm 0.05 R_\oplus$ and $6.56 \pm 1.07 M_\oplus$, respectively. K2-131 b is another super-Earth predicted to host an ocean of molten lava, with a hot-dayside equilibrium temperature of 2496 ± 66 K. Its density, escape velocity, and insolation flux of 7.52 ± 1.37 gcm^{-3} , 22.09 ± 1.86 kms^{-1}, and $3865 \pm 300\ S_\oplus$, respectively, are comparable to that of K2-141 b (Barragán et al. 2018). Theoretical models have predicted that K2-141 b could have an atmosphere of Na, Si, and SiO_2 that is continually replenished from the upcycling of vapourized refractory material being displaced back into its atmosphere (Nguyen et al. 2020). Such atmospheres could potentially be detected through space-based telescopes such as JWST, which will be launched later this year.

(vi) **CoRoT-7 b:** While there have been smaller exoplanets discovered since, CoRoT-7 b (Léger et al. 2009; Queloz et al. 2009) was one of the first ultra short-period super-Earths to be discovered, the origins and evolution of which are still an active area of research (Léger et al. 2011; Winn, Sanchis-Ojeda & Rappaport 2018; Dai et al. 2019; Lichtenberg et al. 2021). We have determined the stellar radius and mass of CoRoT-7 to be $0.84 \pm 0.01\,R_\odot$ and $0.87 \pm 0.03\,M_\odot$, respectively. Given the observed transit depths and semi-amplitudes of CoRoT-7 b found within the literature, and our derived astrophysical parameters for CoRoT-7, we have refined its planetary radius and mass to now be $1.68 \pm 0.04 R_\oplus$ and $4.94 \pm 0.41 M_\oplus$. That is, we have increased its radius and mass precision to 2.4 per cent and 8.3 per cent, respectively, the most precise physical values for CoRoT-7 b currently available.

With these precise values, CoRoT-7 b's radius is now large enough for an atmosphere to contribute to its overall radius (Rogers 2015), with its density being, 5.73 ± 0.61 gcm^{-3}, comparable to that of Earth's, $\rho_\oplus = 5.51$ gcm^{-3} (Perryman 2018). Receiving $1682 \pm 122\ S_\oplus$, CoRoT-7 b's well-mixed and hot dayside equilibrium temperatures of 1705 K and 2027 K make it one of the cooler ultra short-period planets discussed in this section.

4.4 Chemical abundances of confirmed and candidate exoplanets

One of the biggest strengths of all-sky surveys such as GALAH is the not only access to the physical properties of these stellar hosts within our sample but also the numerous chemical abundances that are included as well. The chemical links between stars and the planets that they host have been widely studied (Fischer & Valenti 2005; Adibekyan 2019; Teske et al. 2019). We are interested within our sample if there are any thick-disc hosts within our sample, and to see if there is a trend between stars that hosts close in gaseous worlds, compared to their rocky hosting counterparts.

4.4.1 Searching for thick-disc hosts within GALAH

The density and populations of stars vary significantly within the Milky Way's disc. The thin disc is contained within the galaxy's innermost plane, hosting relatively young (6 Gyr), iron-rich ($[Fe/H]_{thin} \sim 0.0$ dex), α-poor ($[\alpha/Fe]_{thin} \sim -0.1$ dex), and low total space velocity ($v_{tot} \leq 50$ kms^{-1}) stars (Nissen 2004; Sharma et al. 2019). However, the thick disc, lying in the Milky Way's outer plane, consists of a much higher proportion of older stars, with a mean stellar age around 9.5 Gyr (Sharma et al. 2019). Not only are these stars older, but their iron abundance is lower ($[Fe/H]_{thick} \sim -0.367$ dex), their α-process (i.e. Mg, Si, Ca, and Ti) elemental abundances are enriched ($[\alpha/Fe]_{thick} \sim 0.218$ dex), and have faster velocities ($70 \leq v_{tot} \leq 200$ kms^{-1}) compared to their thin-disc counterparts (Nissen 2004; Sharma et al. 2019). Within the Solar neighbourhood, 1 per cent to 12 per cent of stars are estimated to be considered members of the Milky Way's thick disc (Bland-Hawthorn & Gerhard 2016), with a few exoplanets being announced orbiting thick-disc stars (Bouchy et al. 2010; Gan et al. 2020; Weiss et al. 2021). With the above population statistics, there should be in the order of 35–400 exoplanet hosts from the thick disc in which we can then better understand the underlying exoplanetary population and architectures of thick-disc planetary systems.

With this motivation, we used GALAH DR3 stellar abundances, specifically the iron and α abundances, along with the galactic kinematic and dynamic information within GALAH's value-added catalogue to constrain the stellar populations of known and candidate exoplanetary systems. In Fig. 8, we plot the iron abundance of known confirmed and candidate systems against the stars' α and magnesium abundances (a more thorough discussion between the populations outlined in the figure is discussed in Section 4.4.2). Fig. 8 shows a host star's iron abundance against its α abundance, with dashed lines within the plot chemically separating stars within the thick and thin disc regions of the Milky Way as per Adibekyan et al. (2012b). We also use a one-sigma cutoff of the α and iron abundances from the separation line to determine the stellar populations from these chemical abundances. From these cutoffs, we have 13 stars, or 5 per cent of our host stars potentially from the thick disc. These stars, along with their α and iron abundances, can be found within Table 2.

Another way to determine the stellar populations of stars within the galaxy is through kinematic and dynamic data. A star's velocity towards the Galactic Centre (U), in the direction of rotation (V) and upwards from the disc (W), can be determined though large spectroscopic surveys combining astrometric data from *Gaia* (Gaia Collaboration 2020) and radial velocity data from GALAH (Bland-Hawthorn & Gerhard 2016; Buder et al. 2020). We have used these stellar velocities from GALAH DR3 to create a Toomre diagram found in Fig. 9. The Toomre diagram shows the radial and perpendicular ($\sqrt{U_{LSR}^2 + W_{LSR}^2}$) stellar velocities for all known confirmed and candidate exoplanet hosts, corrected for the local standard of rest (LSR). We have included in Table 2 stars will total space velocities ($v_{tot} = \sqrt{U_{LSR}^2 + V_{LSR}^2 + W_{LSR}^2}$) greater than 70 km s^{-1} to bring the number of potential thick-disc host stars to 30. We can also see in the figure that there are stars that have chemical abundances suggesting that they are from the thick disc and yet have stellar velocities similar to that of thin-disc stars. However, past surveys have also shown that galactic thick-disc stars will often have similar kinematics to those stars found in the thin disc (Kovalev et al. 2019; Chen et al. 2021).

We have also included in Fig. 9 the stellar dynamics of our exoplanet hosts: L_z and J_R. L_z is the azimuthal angular momentum of a star and describes the amount of rotation a star's orbit has around the Galactic centre (Bland-Hawthorn & Gerhard 2016; Trick, Coronado & Rix 2019). J_R is described the radial action of a star and can be considered a measure of a star's orbital eccentricity (Bland-Hawthorn & Gerhard 2016; Trick et al. 2019). Thick-disc stars would be considered to have higher J_R, as thick-disc stars have more eccentric orbits than their thin-disc counter parts (Buder et al. 2020)

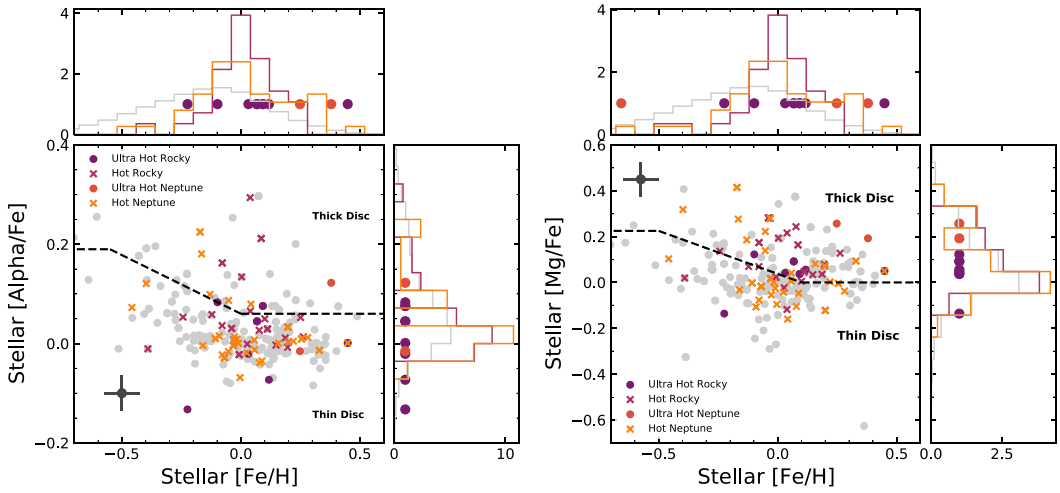

Figure 8. Left: Stellar iron abundance values are plotted against their α (left) and magnesium (right) abundances for our confirmed and candidate planet host stars. The dashed lines represent the distinction between the different stellar populations of thick- and thin-disc stars as shown in Adibekyan et al. (2012b) and Hayden et al. (2017) for our α and Mg abundances, respectively. Different short (terrestrial – pink cross; Neptune – yellow cross) and ultra-short (terrestrial – purple disc; Neptune – orange disc) period planet populations are highlighted within the figure. Thick-disc stars are typically associated with being above the plane of the dark grey-dashed line, with thin-disc stars being associated below it. Median error bars are shown within each plot as grey markers.

Table 2. Our potential thick-disc host stars are presented in this table with their chemical, kinematic, and dynamic information. The table is sorted by the star's radial action. TD/D probability values are taken from Carrillo et al. (2020) for stars within our sample that had matching TIC IDs.

Star name	(Fe/H) dex	(α/Fe) dex	V_{SLR} km s^{-1}	$\sqrt{U_{SLR}^2 + W_{SLR}^2}$ km s^{-1}	J_R kpc km s^{-1}	L_Z kpc km s^{-1}	TD/D
EPIC 211064647	−0.44 ± 0.18	0.07 ± 0.1	−259.1	79.94	715.6	−91	
K2-64	−0.08 ± 0.12	0.09 ± 0.07	−3.241	119.2	168.4	1935	
K2-181	0.25 ± 0.07	0.01 ± 0.04	−20.8	85.45	126.2	1910	0.221
EPIC 211770696	−0.36 ± 0.09	0.2 ± 0.05	−82.53	75.71	121.8	1425	4.52
TOI-933	−0.61 ± 0.06	0.26 ± 0.03	−54.8	68.13	116.1	1573	0.291
K2-204	−0.11 ± 0.06	0.01 ± 0.02	−70.77	62.55	110.2	1500	
EPIC 212624936	−0.07 ± 0.08	0.09 ± 0.05	−7.493	106.3	109.4	1916	
EPIC 213546283	−0.17 ± 0.06	0.18 ± 0.02	−43.53	105.1	103.6	1619	0.545
EPIC 210961508	0.1 ± 0.12	0.1 ± 0.06	−45.32	84.32	99.61	1794	
EPIC 216111905	−0.23 ± 0.12	0.17 ± 0.07	−82.87	47.34	98.95	1293	
EPIC 212495601	−0.2 ± 0.09	0.05 ± 0.04	−54.8	100	97.81	1562	0.294
EPIC 201561956	−0.64 ± 0.12	0.13 ± 0.06	−69.25	46.21	93.35	1453	
TOI-832	0.4 ± 0.08	−0.02 ± 0.04	−78.89	14.48	82.26	1403	
K2-248	−0.13 ± 0.08	0.1 ± 0.04	−31.36	63.91	81.33	1748	
TOI-348	0.08 ± 0.09	−0.01 ± 0.05	−59.44	60.31	80.61	1531	0.261
TOI-844	−0.03 ± 0.08	0.03 ± 0.04	−55.98	60.92	80.3	1622	0.18
NGTS-4	−0.17 ± 0.06	0.22 ± 0.03	−77.27	82.75	73.46	1435	103
EPIC 211800191	−0.7 ± 0.13	0.21 ± 0.06	−3.113	87.5	70.26	2090	0.577
K2-7	−0.4 ± 0.09	0.19 ± 0.05	−60.47	50.56	64.63	1544	
TOI-924	−0.28 ± 0.05	0.1 ± 0.02	−52.45	87.46	56.11	1624	0.367
TOI-868	−0.1 ± 0.05	0.08 ± 0.01	−61.64	47	53.85	1528	0.0956
K2-73	0.02 ± 0.05	−0.02 ± 0.02	−22.03	72.03	51.98	1825	0.0252
TIC 287328202	−0.06 ± 0.12	0.14 ± 0.06	−41.16	87.24	50.73	1749	0.105
HATS-52	−0.31 ± 0.11	0.06 ± 0.05	2.438	77.06	48.78	2119	
EPIC 211736305	0.13 ± 0.15	0.19 ± 0.08	−65.79	57.32	47.15	1572	
K2-183	0.07 ± 0.11	0.04 ± 0.06	−43.32	80.45	45.97	1741	2.7
EPIC 211978988	0.02 ± 0.08	−0.0 ± 0.05	−13.67	74.74	45.32	2008	0.0737
EPIC 212646483	−0.27 ± 0.08	0.13 ± 0.04	−68.48	51.5	43.55	1348	
EPIC 218901589	−0.12 ± 0.05	0.06 ± 0.02	−31.92	69.22	43.24	1748	0.033
EPIC 220674823	0.09 ± 0.09	0.08 ± 0.05	−44.9	56.29	43.21	1681	0.0579
TOI-810	−0.24 ± 0.05	0.12 ± 0.02	−38.64	64.44	11.85	1709	2.53

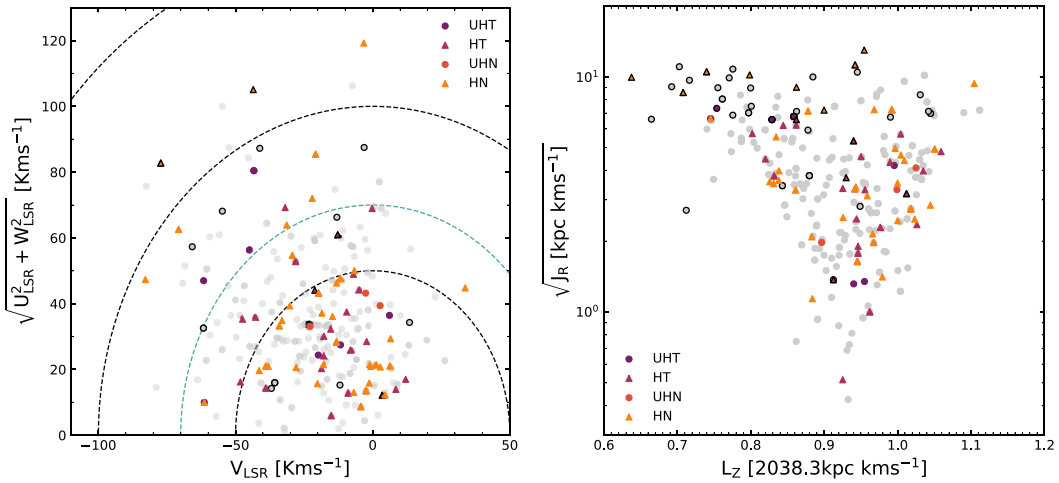

Figure 9. Left: Toomre diagram for the planet hosting and stars without planets. The red squares and blue triangles represent stars with Jupiter- and Neptune-mass planets, respectively. The magenta circles and green asterisks refer to the high-α metal-poor (chemically defined thick disc) and high-α metal-rich stars without planets, and the black dots refer to the chemically defined thin-disc non-host stars. Dotted grey lines indicate total space velocities of 50, 100, and 150 km s^{-1} with the teal dashed line of 70 km s^{-1} being our thick–thin-disc kinematic cutoff line. Stars with total velocities greater than 70 km s^{-1} are also outlined in the right figure. Right: Stellar dynamics of our planet-hosting stars including the dynamic actions J_R and L_z. L_z of the Sun is determined to be 2038.3 kpc km s^{-1}(Buder et al. 2020).

and have L_z values diverging away from the solar neighbourhood L_z value of 2038.3 kpc km s^{-1}.

Carrillo et al. (2020) collated a large chemo-kinematic data base for stars being observed by *TESS* and determined probable likelihoods of stars within their data base to be members of the thick-disc (TD/D) as per Bensby, Feltzing & Oey (2014). These probabilities determined by Carrillo et al. (2020) suggest that stars with a TD/D $>$ 2 would be likely members of the thick-disc, with stars having TD/D $<$ 0.5 being associated more with the thin-disc and stars in between these values being transitional-disc stars. We have cross-matched the catalogue of Carrillo et al. (2020), with our 30 thick-disc candidate stars, with 18 confirmed cross-matches. All of the above information can now better inform us of what stellar populations these planet hosts are likely to be a part of.

From the above information we have four stars including confirmed planet hosts NGTS-4, K2-183, and EPIC 211770696 along with the multiplanet hosting candidate star TOI-810 to be members of the thick disc. West et al. (2019) announced the discovery of NGTS-4 b, showing that its host star's kinematics made it a member of the thick disc. With GALAH's chemical abundances, [Fe/H] $= -0.17 \pm 0.06$, [α/Fe] $= 0.22 \pm 0.03$, we independently confirm that NGTS-4 is indeed a member of the thick disc. With the highest J_R within our candidates, along with a low iron abundance ([Fe/H] $= -0.44 \pm 0.18$) and enriched α abundance ([α/Fe] $= 0.07 \pm 0.1$), we also consider candidate planet host EPIC 211064647 to also be a member of the thick disc. It is interesting to note that TOI-810 has one of the lowest J_R values within the potential thick-disc members; however, it has a TD/D value of 2.53. This shows that all chemo-kinematic and dynamical information needs to be considered before determining what population a star is associated with. With data base of Carrillo et al. (2020) and our results, we also consider EPIC 211800191 and EPIC 213546283 to be members of the transition area of the Milky Way. During the writing of this paper, EPIC 211770696.01 and EPIC 211978988.01 were confirmed as exoplanets and were given the designation of K2-337 b and K2-341 b, respectively (de Leon et al. 2021). However, our work shows for the first time that K2-337 b has characteristics associated with being a thick-disc planetary system and K2-341 b is orbiting a star likely associated with the Milky Way's thin disc. Due to the complex and non-linear nature that the chemical, kinematic, and dynamic information that stars have with their associated stellar groups, we leave the rest to be characterized in further studies. Having a homogeneous and more inclusive sample of thick-disc stars, such as Chen et al. (2021) and others, would allow exoplanetary scientists to better probe the characteristic planetary population differences between the stellar populations, leading on to implications for astrobiology and habitability across the Milky Way (Santos et al. 2017).

4.4.2 Chemical abundance relationships between short-period and ultra short-period planets

There has been a great range of studies to link the chemical abundances of stars to the planets they host. The first link was discovering hot Jupiters tending to favour iron-rich host stars (Gonzalez 1997; Santos, Israelian & Mayor 2001; Fischer & Valenti 2005). Adibekyan et al. (2012a) showed that there is an overabundance of alpha elements in short-period exoplanet hosts, in particular, Neptune and super-Earth-sized exoplanets, compared to stars hosting larger planets. Winn et al. (2017) showed through iron abundances of planet hosts that there was a population difference between hot Jupiters and their ultra short-period (USP) counterparts, concluding that rocky USP planets might not necessarily be remnants of hot-Jovian cores. Further, Dai et al. (2019) also argued that short-period rocky worlds are more than likely exposed rocky cores of sub-Neptunes, rather than hot Jupiters. Per the discovery of the USP TOI-1444b, Dai et al. (2021) showed that hot Neptunes tended to favour iron-rich stars, compared to their rockier counterparts. All of the above then motivate us, with our homogenous sample to

explore the abundance trends between different short-period planet types.

First, we split up our sample into five different categories; ultra hot rocky (UHR) exoplanets ($R_P < 2$ R$_\oplus$; $P_p < 1$ d; $N = 9$), hot rocky (HR) exoplanets ($R_p < 2$ R$_\oplus$; 1 d $\leq P_p < 10$ d; $N = 36$), ultra hot Neptune (UHN) exoplanets (2 R$_\oplus \leq R_p < 4$ R$_\oplus$; $P_p < 1$ d; $N = 3$), hot Neptune (HN) exoplanets (2 R$_\oplus \leq R_p < 4$ R$_\oplus$; 1 d $\leq P_p < 10$ d; $N = 48$), and all other candidates that fit outside of these parameters. We plot the iron abundance against the α-element and magnesium abundances for these populations in Fig. 8. Within Fig. 8, we see a range of iron abundances for both HN and HR worlds. Near solar values, there is a similar distribution of these two populations; however, beyond [Fe/H] > 0.15, there are a greater fraction of HNs compared to their rocky counterparts. We do see a difference in the magnesium abundances, however, between the two populations, as HR worlds tend to favour a wider range of magnesium abundances. In contrast, HNs are seen in more magnesium-poor environments peaking at near Solar values. Adibekyan et al. (2012a) showed an over-abundance of magnesium for Neptune and super-Earth hosting stars, but these two populations were entangled within the same distribution for their comparison between hot Jupiters; thus, it is difficult to compare our results with theirs in this particular case. As with Dai et al. (2021), we do see UHNs around stars enriched in iron compared to ultra hot rocky (UHRs), with the one exception being the USP exoplanet WASP-47 e, orbiting around an extremely iron-rich host ([Fe/H] $= 0.45 \pm 0.09$). There does also seem to be a trend in UHNs being preferentially found around higher [Mg/Fe] stars compared to UHRs, but this trend for ultra-short exoplanets severely weakens out for the α-abundance (which is a combination of Ca, Mg, Ti, and Al). With an exceedingly small sample size for both ultra short-period populations ($N_{UHR} = 9$, $N_{UHN} = 3$), more data and planets are needed to confirm the existence of such trends and their implications.

Similar to Winn et al. (2017), we wanted to see if there is a difference between the populations of HRs and HNs. In our case, we have access to not only [Fe/H] but also over 20 abundances, which provides a more rigorous chemical test to see if our visual discrepancy in magnesium and α-abundances between the two populations is real or not. We perform a two-sample Kolmogorov–Smirnov test between the HN and HR populations for all GALAH abundances. The Kolmogorov–Smirnov statistic and p value for each element are shown in Table 3, sorted by their lowest p value. Surprisingly, the p value between the two populations for the magnesium abundance was 0.052, meaning that there is no statistical evidence that the magnesium abundances for the two populations are significantly different from one another. Of the 29 abundances, only three distributions had p values smaller than 0.05, those elements being Y, Ce, and Al. We have plotted the yttrium, cerium, and aluminium abundances in Fig. 10.

The overall yttrium abundance distribution for HN and HR worlds is similar to the overall GALAH distribution; however, we do see a trend where by more HR exoplanets are found around a broader range of [Y/Fe] values. We also see a higher fraction of HR planets orbiting stars enriched in yttrium ([Y/Fe] > 0.2) compared to their gaseous counterparts. As yttrium is known as a 'chemical-clock' element, whereby stars enriched in yttrium are typically younger, we see this trend as a possibility that HR planets tend to favour younger stars (Slumstrup et al. 2017; Titarenko et al. 2019). However, we also see a trend whereby HR worlds tend to favour magnesium-enriched stars. Magnesium is also a 'chemical-clock' element, but enhanced magnesium abundances are often a reflection of orbiting around older stars (Titarenko et al. 2019). Thus, this positive correlation between magnesium and yttrium needs further investigation to determine as to why HR planets tend to favour stars enriched in both of these elements. Cerium has similar trends, with HR stars being enriched with Ce compared to HN hosting stars. However, both HN and HR [Ce/Fe] abundances peak super-Solar, compared to the Solar-like abundance peak for the overall GALAH sample, with the interpretation to this distribution remaining an interesting development for future work.

Table 3. Our two-sample Kolmogorov–Smirnov test results between our hot Neptune and hot rocky planet samples for each GALAH abundance.

Element	D-statistic	p value
Y	0.364	0.01
Ce	0.476	0.024
Al	0.303	0.037
Mg	0.299	0.052
Na	0.25	0.132
Cr	0.238	0.169
Ba	0.236	0.176
α	0.217	0.254
Cu	0.212	0.275
K	0.21	0.302
Mo	0.625	0.303
Zr	0.326	0.311
C	0.571	0.318
O	0.235	0.323
La	0.367	0.357
Si	0.2	0.357
Mn	0.19	0.39
Rb	0.889	0.4
Sm	0.667	0.4
Sc	0.183	0.46
Li	0.333	0.5
Ca	0.166	0.571
Co	0.201	0.573
Fe	0.16	0.622
Zn	0.16	0.629
Ti	0.147	0.707
V	0.159	0.821
Ni	0.11	0.945
Nd	0.667	1.0

Overall, there does not seem to be a statistical difference between the chemical properties of stars that host HNs and those that host HRs. Thus, following the conclusions of Dai et al. (2021) and Winn et al. (2017), our more robust chemical abundance results show that there is a possibility that short-period rocky worlds might be the remnant cores of hotter gaseous Neptune worlds. The reason being is that there are only three of the 29 elemental abundances that had KS statistics significant enough to show that HRs and HNs come from different populations. Even with these three elements, the smallest p value of 0.01, along with a relatively small sample size of our HRs and HNs, there is still more research to be done to determine the similarities in these populations and thus determine the origins and evolution of short-period exoplanets.

4.5 Assessing the radius valley and super-Earth desert

Because we have four ultra short-period exoplanets within our sample straddling the super-Earth radius gap, we show in Fig. 11(a) their location in the so-called two-dimensional radius gap, i.e. the planetary radius compared to the orbital period (Fulton et al. 2017; Van Eylen et al. 2018). None of the ultra short-period super-Earths

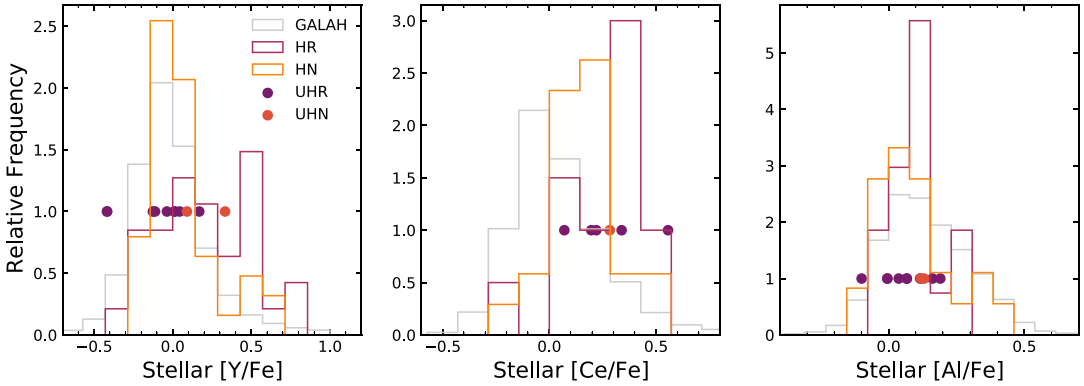

Figure 10. Chemical abundance distributions for the three elements, yttrium (left), cerium (middle), and aluminium (right), that had p values indicative of UN (pink) and HR (yellow) worlds being derived from different populations. We have included the overall GALAH abundance distributions (grey) along with the UHR (purple discs) and UHN (orange discs) for comparison as well.

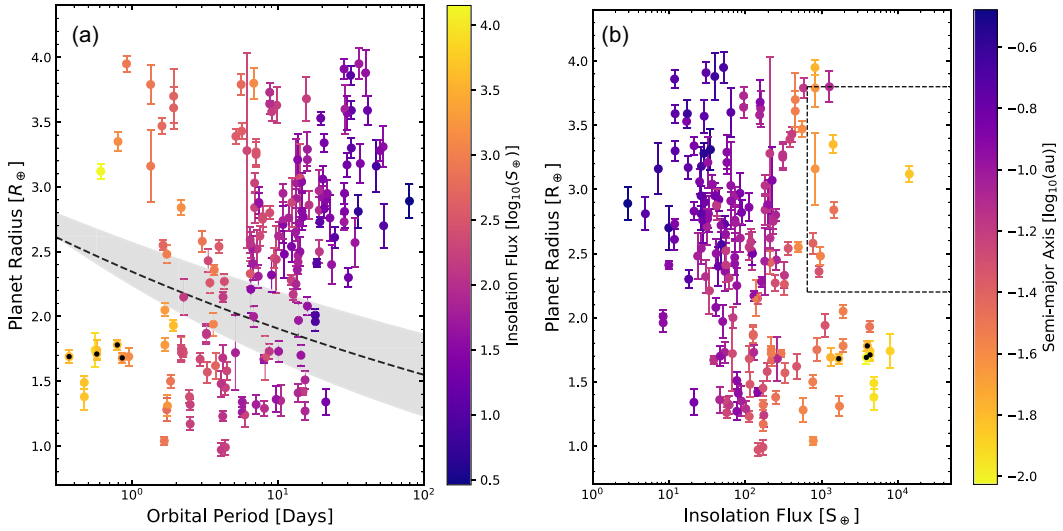

Figure 11. A: Our confirmed and candidate exoplanet planetary radius values are plotted against their orbital periods, each being coloured by their insolation flux values. The dashed line and shaded region around it indicate the slope and error in the radius valley as noted by Van Eylen et al. (2018). B: Planet and candidate radius values are plotted against their incident flux, coloured by their semimajor axis values. The dashed lines enclose the hot super-Earth desert noted by Lundkvist et al. (2016). Our four ultra short-period super-Earths are depicted in each plot by black dots.

within our sample lie within the photoevaporation valley, the grey dashed line within the Fig. 11(a), all below this line. Nor do any of these ultra short periods have periods smaller than the expected Roche limits of their host stars (Rappaport et al. 2013). They do, however, have orbits that are smaller than the dust sublimation radius of their host stars (Isella, Testi & Natta 2006), meaning that *in situ* formation of these exoplanets is unlikely. There is only one confirmed exoplanet that lies within 1-sigma of the line proposed by Van Eylen et al. (2018), that being K2-247 b (P: 2.25 d, R_p: 2.15 $\pm$ 0.14 $R_\oplus$) (Livingston et al. 2018a).

We show also in Fig. 11 the insolation flux of confirmed and candidate exoplanets compared to their estimated radii; the dashed lines enclose a region of parameter space known as the Neptunian desert, proposed by (Lundkvist et al. 2016). This Neptunian desert is a region of flux–radius phase space where super-Earths are less common, explained by evaporation of volatile elements. The sub-Neptune NGTS-4 b (S_{eff}: 824 $\pm$ 62 $S_\oplus$, R_p: 3.16 $\pm$ 0.29$R_\oplus$) is the only confirmed exoplanet within this region (West et al. 2019) with two TOIs, 1926.01 and 1948.01, also being contained within the Neptunian desert.

As mentioned previously, the origin of ultra short-period super-Earths remains an active field of science (Wagner et al. 2012; Lundkvist et al. 2016; Nguyen et al. 2020; Spaargaren et al. 2020). The elemental abundances of refractory elements, such as Mg, Si, Fe, and molar ratios of such elements, can help constrain the interiors of rocky worlds (Valencia, O'Connell & Sasselov 2006; Seager et al. 2007; Unterborn, Dismukes & Panero 2016). Modelling the interiors of ultra short period can help determine if these worlds are likely

remnants of Jovian cores, or super-Earths that have migrated inwards to their current positions (Benz et al. 2007; Mocquet, Grasset & Sotin 2014). 44 per cent of ultra short-period super-Earths discovered are enriched with iron, with exoplanet candidate KOI 1843.03 predicted to have a core-mass fraction as high as mercury's. However, there seems to be no trend between a rocky planet's core-mass fraction and its received flux values (Price & Rogers 2020). Mg/Si and Fe/Si ratios from GALAH DR3 could be used to further constrain the chemical and geological composition of these super-Earths using models such as Dorn et al. (2015), Dorn et al. (2017), Wang et al. (2019), and Unterborn, Desch & Panero (2018b). But this is outside the scope of this paper and is left for further future investigation.

5 CONCLUSION

The wealth of astronomical data in large galactic archaeology surveys like GALAH can be used in numerous astrophysical fields, including exoplanetary science. We have cross-matched GALAH's latest release with the latest astrometric data from *Gaia* EDR3 to determine the physical parameters of 279 confirmed and candidate exoplanet hosting stars. With these new stellar parameters and combining planetary observables from transit photometry and Doppler spectroscopy where applicable, we have determined and refined the physical characteristics of 105 confirmed exoplanets, 146 K2 candidates, 95 TOIs, and 52 CTOIs, along with analysing the chemical abundances of these host stars. From our study, we have uncovered:

(i) 30 CTOI and K2 candidates have radii larger than our planetary limit of $R_P < 2\ R_J$, meaning that these candidates would be more akin to brown dwarfs or stellar companions. TOIs 147.01, 565.01, 959.01, 1072.01, and 2391.01 are also too large to be planetary in nature.

(ii) For the majority of our candidates, their host star's $v \sin i$ values are above $5\,\mathrm{km\,s^{-1}}$, with predicted RV signals being less than $5\,\mathrm{m\,s^{-1}}$. We then predict that it will be difficult, with current methodology, to obtain mass confirmations for most of the smaller planet candidates orbiting stars found within our sample. In the extreme cases for smaller planets orbiting rapid-rotating stars, it will be highly improbable to derive their mass measurements, with TOI-1219.01 needing over 14 000 RV measurements to confirm its mass from a typical modern spectrograph.

(iii) Out of the homogeneous data set of 105 exoplanets with new planetary parameters, we have updated parameters for five ultra short-period super-Earths – K2-106 b, K2-216 b, WASP-47 e, K2-131 b, and CoRoT- 7 b – which make up 28 per cent of all such planets with known mass and radius values. In particular, our refined radius and mass values for WASP-47 e, K2-106 b, and CoRoT-7 b have uncertainties smaller than 2.3 per cent and 8.5 per cent, respectively. From these refinements, K2-106 b's equilibrium temperature of 2570 K far exceeds the condensation temperature of most refractory elements, making it the hottest super-Earth to date. With our mass and radius measurements of CoRoT-7 b, $1.68 \pm 0.04 R_\oplus$, and $4.94 \pm 0.41 M_\oplus$, respectively, its radius is now large enough for an atmosphere to contribute to its overall radius and now straddles the super-Earth radius gap.

(iv) Through stellar chemo-kinematic and dynamical data, we announce that three confirmed planet hosts, including NGTS-4, K2-183, and K2-337, along with candidate host stars TOI-810 and EPIC 211064647 to be members of the Milky Way's thick disc. By knowing more thick-disc hosts, we will be able to better determine the statistics of planetary architectures across stellar populations and determine the habitability of systems across the galaxy.

(v) With GALAH chemical abundances, we have shown that there does not seem to be a statistical difference between the chemical properties of stars that host hot Neptunes and those that host hot rocky exoplanets. Thus, there is a possibility that short-period rocky worlds might be the remnant cores of hotter-gaseous Neptune-sized worlds.

SOFTWARE

ASTROPY (Astropy Collaboration 2013), ASTROQUERY (Ginsburg et al. 2019), ISOCHRONES (Morton 2015), MATPLOTLIB (Hunter 2007), MULTINEST (Feroz & Hobson 2008; Feroz, Hobson & Bridges 2009; Feroz et al. 2019), MULTIPROCESSING (McKerns et al. 2012), NUMPY (Oliphant 2006; van der Walt, Colbert & Varoquaux 2011), PANDAS (McKinney et al. 2010), and SCIPY (Virtanen et al. 2020).

ACKNOWLEDGEMENTS

We thank the Australian Time Allocation Committee for their generous allocation of AAT time, which made this work possible. Our research is based upon data acquired through the Australian Astronomical Observatory. We acknowledge the traditional owners of the land on which the AAT stands, the Gamilaraay people, and pay our respects to elders past, present and emerging.

This research has made use of the NASA Exoplanet Archive, which is operated by the California Institute of Technology, under contract with the National Aeronautics and Space Administration under the Exoplanet Exploration Program.

This work has made use of the TIC and CT Stellar Properties Catalog, through the *TESS* Science Office's target selection working group (architects K. Stassun, J. Pepper, N. De Lee, M. Paegert, and R. Oelkers). The Filtergraph data portal system is trademarked by Vanderbilt University.

This research has made use of the Exoplanet Follow-up Observation Program website, which is operated by the California Institute of Technology, under contract with the National Aeronautics and Space Administration under the Exoplanet Exploration Program.

This work has made use of data from the European Space Agency (ESA) mission *Gaia* (http://www.cosmos.esa.int/gaia), processed by the *Gaia* Data Processing and Analysis Consortium (DPAC, http://www.cosmos.esa.int/web/gaia/dpac/ consortium). Funding for the DPAC has been provided by national institutions, in particular, the institutions participating in the *Gaia* Multilateral Agreement.

JTC would like to thank BC and DN, and is supported by the Australian Government Research Training Program (RTP) Scholarship.

DATA AVAILABILITY

The data underlying this article are available in the article and in its online supplementary material.

REFERENCES

Addison B. C. et al., 2021, MNRAS, 502, 3704
Adibekyan V. Z. et al., 2012a, A&A, 543, A89
Adibekyan V. Z., Sousa S. G., Santos N. C., Delgado Mena E., González Hernández J. I., Israelian G., Mayor M., Khachatryan G., 2012b, A&A, 545, A32
Adibekyan V., 2019, Geosciences, 9, 105
Astropy Collaboration 2013, A&A, 558, A33

Bailes M. et al., 2011, Science, 333, 1717
Barragán O. et al., 2018, A&A, 612, A95
Barros S. C. C., Demangeon O., Deleuil M., 2016, A&A, 594, A100
Batalha N. M. et al., 2013, ApJS, 204, 24
Becker J. C., Vanderburg A., Adams F. C., Rappaport S. A., Schwengeler H. M., 2015, ApJ, 812, L18
Bensby T., Feltzing S., Oey M. S., 2014, A&A, 562, A71
Benz W., Anic A., Horner J., Whitby J. A., 2007, Space Sci. Rev., 132, 189
Bitsch B., Battistini C., 2020, A&A, 633, A10
Bland-Hawthorn J., Gerhard O., 2016, ARA&A, 54, 529
Bonomo A. S. et al., 2019, Nature Astron., 3, 416
Boss A. P., 2001, ApJ, 551, L167
Bouchy F. et al., 2010, A&A, 519, A98
Brucalassi A. et al., 2017, A&A, 603, A85
Buder S. et al., 2018, MNRAS, 478, 4513
Buder S. et al., 2020, MNRAS, 506, 150
Butler R. P., Marcy G. W., Williams E., McCarthy C., Dosanjh P., Vogt S. S., 1996, PASP, 108, 500
Carrillo A., Hawkins K., Bowler B. P., Cochran W., Vanderburg A., 2020, MNRAS, 491, 4365
Chen D.-C. et al., 2021, ApJ, 909, 115
Chen J., Kipping D., 2017, ApJ, 834, 17
Choi J., Dotter A., Conroy C., Cantiello M., Paxton B., Johnson B. D., 2016, ApJ, 823, 102
Clark J. T. et al., 2020, MNRAS, 504, 4968
Cui X.-Q. et al., 2012, Res. Astron. Astrophys., 12, 1197
Dai F. et al., 2015, ApJ, 813, L9
Dai F. et al., 2017, AJ, 154, 226
Dai F. et al., 2021, AJ, 162, 62
Dai F., Masuda K., Winn J. N., Zeng L., 2019, ApJ, 883, 79
de Leon J. P. et al., 2021, MNRAS, 508, 195
De Silva G. M. et al., 2015, MNRAS, 449, 2604
Deleuil M. et al., 2008, A&A, 491, 889
Dorn C., Harrison J. H. D., Bonsor A., Hands T. O., 2019, MNRAS, 484, 712
Dorn C., Khan A., Heng K., Connolly J. A. D., Alibert Y., Benz W., Tackley P., 2015, A&A, 577, A83
Dorn C., Venturini J., Khan A., Heng K., Alibert Y., Helled R., Rivoldini A., Benz W., 2017, A&A, 597, A37
Dragomir D. et al., 2019, ApJ, 875, L7
Dressing C. D., Charbonneau D., 2013, ApJ, 767, 95
Dressing C. D., Charbonneau D., 2015, ApJ, 807, 45
Feroz F., Hobson M. P., 2008, MNRAS, 384, 449
Feroz F., Hobson M. P., Bridges M., 2009, MNRAS, 398, 1601
Feroz F., Hobson M. P., Cameron E., Pettitt A. N., 2019, Open J. Astrophys., 2, 10
Fischer D. A., Valenti J., 2005, ApJ, 622, 1102
Fulton B. J. et al., 2017, AJ, 154, 109
Gaia Collaboration 2018, A&A, 616, A1
Gaia Collaboration 2020, A&A, 649, A1
Gan T. et al., 2020, AJ, 159, 160
Gilmore G. et al., 2012, Messenger, 147, 25
Ginsburg A. et al., 2019, AJ, 157, 98
Gonzalez G., 1997, MNRAS, 285, 403
Grunblatt S. K. et al., 2016, AJ, 152, 185
Grunblatt S. K. et al., 2017, AJ, 154, 254
Guenther E. W. et al., 2017, A&A, 608, A93
Hardegree-Ullman K. K., Zink J. K., Christiansen J. L., Dressing C. D., Ciardi D. R., Schlieder J. E., 2020, ApJS, 247, 28
Hartman J. D. et al., 2016, AJ, 152, 182
Hartman J. D. et al., 2019, AJ, 157, 55
Hayden M. R., Recio-Blanco A., de Laverny P., Mikolaitis S., Worley C. C., 2017, A&A, 608, L1
Hidalgo D. et al., 2020, A&A, 636, A89
Hinkel N. R., Unterborn C., Kane S. R., Somers G., Galvez R., 2019, ApJ, 880, 49
Horner J., Jones B. W., 2010, Int. J. Astrobiology, 9, 273
Hsu D. C., Ford E. B., Ragozzine D., Ashby K., 2019, AJ, 158, 109
Huang C. X. et al., 2018, ApJ, 868, L39
Hunter J. D., 2007, Comput. Sci. Eng., 9, 90
Isella A., Testi L., Natta A., 2006, A&A, 451, 951
Jordán A. et al., 2020, AJ, 159, 145
Kane S. R., Fetherolf T., Hill M. L., 2020, AJ, 159, 176
Kane S. R., Gelino D. M., 2011, ApJ, 741, 52
Konatham S., Martin-Torres J., Zorzano M., 2020, Proc. R. Soc. A Math. Phys. Eng. Sci., 476, 20200148
Kopparapu R. K. et al., 2013, ApJ, 765, 131
Kovalev M., Bergemann M., Ting Y.-S., Rix H.-W., 2019, A&A, 628, A54
Kruse E., Agol E., Luger R., Foreman-Mackey D., 2019, ApJS, 244, 11
Kunimoto M., Matthews J. M., 2020, AJ, 159, 248
Lam K. W. F. et al., 2017, A&A, 599, A3
Léger A. et al., 2009, A&A, 506, 287
Léger A. et al., 2011, Icarus, 213, 1
Lewis I. J. et al., 2002, MNRAS, 333, 279
Lichtenberg T., Bower D. J., Hammond M., Boukrouche R., Sanan P., Tsai S.-M., Pierrehumbert R. T., 2021, J. Geophys. Res. Planets, 126, e06711
Livingston J. H. et al., 2018a, AJ, 156, 78
Livingston J. H. et al., 2018b, AJ, 156, 277
Lovis C., Fischer D., 2010, in Seager S., ed., Exoplanets. University of Arizona Press, Tucson, USA, p. 27
Lundkvist M. S. et al., 2016, Nature Commun., 7, 11201
Majewski S. R. et al., 2017, AJ, 154, 94
Mallonn M., Köhler J., Alexoudi X., von Essen C., Granzer T., Poppenhaeger K., Strassmeier K. G., 2019, A&A, 624, A62
Marigo P. et al., 2017, ApJ, 835, 77
Martell S. L. et al., 2016, MNRAS, 465, 3203
Masuda K., 2014, ApJ, 783, 53
Masuda K., Tamayo D., 2020, AJ, 160, 224
Mayo A. W. et al., 2018, AJ, 155, 136
McKerns M. M., Strand L., Sullivan T., Fang A., Aivazis M. A., 2012, preprint (arXiv:1202.1056)
McKinney W., et al., 2010, Data Structures for Statistical Computing in Python, Proceedings of the 9th Python in Science Conference. Austin, p. 51
Mocquet A., Grasset O., Sotin C., 2014, Phil. Trans. R. Soc. London Ser. A, 372, 20130164
Modirrousta-Galian D., Ito Y., Micela G., 2021, Icarus, 358, 114175
Morton T. D., 2015, Astrophysics Source Code Library, record ascl:1503.010
Ness M., Hogg D. W., Rix H. W., Ho A. Y. Q., Zasowski G., 2015, ApJ, 808, 16
Nguyen T. G., Cowan N. B., Banerjee A., Moores J. E., 2020, MNRAS, 499, 4605
Nielsen L. D. et al., 2019, A&A, 623, A100
Nissen P. E., 2004, in McWilliam A., Rauch M., eds, Origin and Evolution of the Elements. Cambridge University Press. Cambridge, England, p. 154
Oliphant T. E., 2006, A guide to NumPy.Trelgol Publishing, USA
Perryman M., 2018, The Exoplanet Handbook. Cambridge University Press, Cambridge, England
Persson C. M. et al., 2018, A&A, 618, A33
Petigura E. A. et al., 2018, AJ, 155, 21
Plavchan P. et al., 2020, Nature, 582, 497
Price E. M., Rogers L. A., 2020, ApJ, 894, 8
Queloz D. et al., 2009, A&A, 506, 303
Rappaport S., Sanchis-Ojeda R., Rogers L. A., Levine A., Winn J. N., 2013, ApJ, 773, L15
Rodriguez J. E. et al., 2021, AJ, 161, 194
Rogers L. A., 2015, ApJ, 801, 41
Rogers L. A., Seager S., 2010, ApJ, 712, 974
Rouan D., Deeg H. J., Demangeon O., Samuel B., Cavarroc C., Fegley B., Léger A., 2011, ApJ, 741, L30
Rowe J. F. et al., 2014a, ApJ, 784, 45
Rowe J. F. et al., 2014b, ApJ, 784, 45
Salaris M., Cassisi S., 2006, Evolution of Stars and Stellar Populations. Wiley, Hoboken, NJ
Santos N. C. et al., 2017, A&A, 608, A94
Santos N. C., Israelian G., Mayor M., 2001, A&A, 373, 1019

Seager S., 2010, Exoplanet Atmospheres: Physical Processes. Princeton University Press, Princeton, NJ
Seager S., Kuchner M., Hier-Majumder C. A., Militzer B., 2007, ApJ, 669, 1279
Sharma S. et al., 2018, MNRAS, 473, 2004
Sharma S. et al., 2019, MNRAS, 490, 5335
Sheets H. A., Deming D., 2017, AJ, 154, 160
Sheinis A. et al., 2015, J. Astron. Telesc. Instrum. Syst., 1, 035002
Siverd R. J. et al., 2012, ApJ, 761, 123
Slumstrup D., Grundahl F., Brogaard K., Thygesen A. O., Nissen P. E., Jessen-Hansen J., Van Eylen V., Pedersen M. G., 2017, A&A, 604, L8
Spaargaren R. J., Ballmer M. D., Bower D. J., Dorn C., Tackley P. J., 2020, A&A, 643, A44
Stassun K. G. et al., 2018, AJ, 156, 102
Stassun K. G., Collins K. A., Gaudi B. S., 2017, AJ, 153, 136
Steffen J. H. et al., 2013, MNRAS, 428, 1077
Steinmetz M. et al., 2006, AJ, 132, 1645
Taylor M. B., 2005, TOPCAT & STIL: Starlink Table/VOTable Processing Software. Astronomical Data Analysis Software and Systems XIV ASP-Conference Series. San Francisco, CA, p. 29
Teske J. K., Thorngren D., Fortney J. J., Hinkel N., Brewer J. M., 2019, AJ, 158, 239
Titarenko A., Recio-Blanco A., de Laverny P., Hayden M., Guiglion G., 2019, A&A, 622, A59
Trick W. H., Coronado J., Rix H.-W., 2019, MNRAS, 484, 3291
Unterborn C. T., Desch S. J., Hinkel N. R., Lorenzo A., 2018a, Nature Astron., 2, 297
Unterborn C. T., Desch S. J., Panero W. R., 2018b, in AGU Fall Meeting Abstracts. American Geophysical Union, Washington D.C, p. P42A–02
Unterborn C. T., Dismukes E. E., Panero W. R., 2016, ApJ, 819, 32
Valencia D., O'Connell R. J., Sasselov D., 2006, Icarus, 181, 545
Valenti J. A., Piskunov N., 1996, A&AS, 118, 595
van der Walt S., Colbert S. C., Varoquaux G., 2011, Comput. Sci. Eng., 13, 22
Van Eylen V., Agentoft C., Lundkvist M. S., Kjeldsen H., Owen J. E., Fulton B. J., Petigura E., Snellen I., 2018, MNRAS, 479, 4786
Vanderburg A. et al., 2019, ApJ, 881, L19
Virtanen P. et al., 2020, Nature Methods, 17, 261
Wagner F. W., Tosi N., Sohl F., Rauer H., Spohn T., 2012, A&A, 541, A103
Wang H. S., Liu F., Ireland T. R., Brasser R., Yong D., Lineweaver C. H., 2019, MNRAS, 482, 2222
Weiss L. M. et al., 2017, AJ, 153, 265
Weiss L. M. et al., 2021, AJ, 161, 56
West R. G. et al., 2019, MNRAS, 486, 5094
Winn J. N. et al., 2017, AJ, 154, 60
Winn J. N., Sanchis-Ojeda R., Rappaport S., 2018, New A Rev., 83, 37
Wittenmyer R. A. et al., 2018, AJ, 155, 84
Wittenmyer R. A. et al., 2020, MNRAS, 496, 851
Wittenmyer R. A., Tinney C. G., O'Toole S. J., Jones H. R. A., Butler R. P., Carter B. D., Bailey J., 2011, ApJ, 727, 102
Yang J.-Y., Xie J.-W., Zhou J.-L., 2020, AJ, 159, 164
Zeng L., Sasselov D. D., Jacobsen S. B., 2016, ApJ, 819, 127
Zhou G. et al., 2017, AJ, 153, 211

SUPPORTING INFORMATION

Supplementary data are available at *MNRAS* online.

Table A1. Our stellar parameters for confirmed and candidate exoplanet hosting stars.
Table A2. Our refined confirmed and candidate exoplanet parameters.

Please note: Oxford University Press is not responsible for the content or functionality of any supporting materials supplied by the authors. Any queries (other than missing material) should be directed to the corresponding author for the article.

APPENDIX A: DATA TABLES

Table A1. Our stellar parameters for confirmed and candidate exoplanet hosting stars. The full table of which can be found on the online version of this paper.

TIC ID	2MASS ID	GAIA DR3 ID	RA (deg)	Dec (deg)	T_{eff} (K)	log g (cgs)	[Fe/H] (dex)	[α/Fe] (dex)	[M/H] (dex)	–
355703913	00030587 − 6228096	4904523077718046720	0.7745 ± 0.0099	−62.4693 ± 0.0096	5451 ± 112	4.50 ± 0.19	0.23 ± 0.10	0.05 ± 0.06	0.30 ± 0.14	–
70785910	00062006 − 3020105	2320600658577841536	1.5836 ± 0.0152	−30.3364 ± 0.0115	5819 ± 96	4.09 ± 0.19	0.08 ± 0.09	−0.01 ± 0.05	0.06 ± 0.12	–
201256771	00071640 − 5827263	4918333184280735232	1.8187 ± 0.0083	−58.4573 ± 0.0084	4960 ± 81	3.42 ± 0.18	−0.34 ± 0.05	0.19 ± 0.02	−0.04 ± 0.06	–
328066864	00392335 + 0443037	2554244130700741504	9.8475 ± 0.0148	4.7178 ± 0.0077	4742 ± 123	4.59 ± 0.19	−0.12 ± 0.12	0.06 ± 0.08	−0.04 ± 0.17	–
299897516	00403884 − 6052497	4903399170675741568	10.1621 ± 0.0099	−60.8804 ± 0.0092	5417 ± 98	3.86 ± 0.18	−0.83 ± 0.09	0.26 ± 0.05	−0.42 ± 0.12	–
418761354	00455526 + 0620490	2556231154370582400	11.4802 ± 0.0200	6.3470 ± 0.0111	4602 ± 88	4.61 ± 0.18	−0.04 ± 0.07	0.03 ± 0.03	0.01 ± 0.09	–
234504626	00474568 − 6225232	4902237021244807296	11.9408 ± 0.0091	−62.4232 ± 0.0091	5001 ± 90	4.55 ± 0.18	0.18 ± 0.07	0.03 ± 0.03	0.23 ± 0.09	–
257394133	00485666 + 0524595	2552929320952237952	12.2361 ± 0.0169	5.4164 ± 0.0086	5617 ± 96	4.32 ± 0.19	0.27 ± 0.08	−0.02 ± 0.04	0.25 ± 0.10	–
257218673	00490407 + 0215596	2549922465888108032	12.2670 ± 0.0146	2.2666 ± 0.0080	5579 ± 93	4.06 ± 0.18	0.21 ± 0.08	0.04 ± 0.04	0.27 ± 0.10	–
405336406	00493540 + 1001123	2582183683235097728	12.3975 ± 0.0185	10.0200 ± 0.0142	4490 ± 76	1.67 ± 0.25	−0.74 ± 0.05	0.20 ± 0.01	−0.43 ± 0.05	–
266012991	00510476 + 0931003	2581918597853527424	12.7700 ± 0.0204	9.5168 ± 0.0144	5554 ± 77	4.38 ± 0.18	−0.02 ± 0.05	0.04 ± 0.02	0.04 ± 0.06	–
333605244	00510570 − 0111452	2535901287452166400	12.7737 ± 0.0167	−1.1959 ± 0.0089	4975 ± 125	4.59 ± 0.19	0.04 ± 0.11	0.07 ± 0.06	0.14 ± 0.14	–
257434940	00511854 + 0520004	2552891834477747200	12.8273 ± 0.0152	5.3334 ± 0.0093	5254 ± 98	3.91 ± 0.19	−0.13 ± 0.08	0.13 ± 0.05	0.06 ± 0.11	–
266015990	00521914 + 1047409	2582617711154563968	13.0800 ± 0.0146	10.7947 ± 0.0105	5499 ± 104	4.40 ± 0.19	0.09 ± 0.09	0.08 ± 0.05	0.21 ± 0.12	–
257435562	00523368 + 0330277	2551651031310145024	13.1404 ± 0.0162	3.5078 ± 0.0090	5750 ± 88	4.21 ± 0.18	0.10 ± 0.07	0.05 ± 0.03	0.18 ± 0.09	–
266017624	00524666 + 0941345	2581916673708201216	13.1944 ± 0.0163	9.6929 ± 0.0129	5014 ± 91	4.54 ± 0.19	0.33 ± 0.07	−0.01 ± 0.04	0.31 ± 0.09	–
344586726	00530642 + 0606009	2553369877222007168	13.2768 ± 0.0152	6.1002 ± 0.0108	4935 ± 116	4.61 ± 0.19	−0.05 ± 0.10	−0.02 ± 0.06	−0.07 ± 0.14	–
266030611	00534179 + 1002417	2581964605543263104	13.4241 ± 0.0130	10.0448 ± 0.0107	5652 ± 88	4.44 ± 0.18	0.35 ± 0.07	−0.00 ± 0.03	0.35 ± 0.09	–
–	–	–	–	–	–	–	–	–	–	–

R_s ($R_\odot$)	M_s ($M_\odot$)	L_s ($L_\odot$)	Age [$\log_{10}$(Gyr)]	RV (kms^{-1})	vsini (kms^{-1})	HZ_1 (au)	HZ_2 (au)	HZ_3 (au)	HZ_4 (au)	HZ_5 (au)
0.925 ± 0.015	0.977 ± 0.040	0.677 ± 0.060	9.526 ± 0.424	17.286 ± 0.096	5.168 ± 2.488	0.626	0.823	0.828	1.429	1.495
1.610 ± 0.033	1.106 ± 0.065	2.660 ± 0.208	9.851 ± 0.130	31.222 ± 0.123	5.488 ± 2.350	1.222	1.597	1.617	2.745	2.871
3.233 ± 0.059	1.220 ± 0.098	5.664 ± 0.425	9.693 ± 0.130	−11.577 ± 0.071	6.509 ± 2.133	1.845	2.442	2.441	4.314	4.513
0.727 ± 0.011	0.761 ± 0.025	0.240 ± 0.026	9.805 ± 0.398	−2.143 ± 0.081	6.950 ± 2.492	0.382	0.507	0.506	0.904	0.946
1.765 ± 0.036	0.928 ± 0.037	2.400 ± 0.200	10.041 ± 0.056	1.605 ± 0.117	9.993 ± 2.320	1.180	1.553	1.561	2.699	2.823
0.688 ± 0.010	0.723 ± 0.019	0.190 ± 0.016	9.719 ± 0.419	−26.481 ± 0.081	6.666 ± 2.247	0.342	0.454	0.453	0.814	0.853
0.801 ± 0.011	0.865 ± 0.024	0.359 ± 0.028	9.533 ± 0.425	20.991 ± 0.073	6.239 ± 2.250	0.464	0.614	0.614	1.082	1.132
1.167 ± 0.027	1.019 ± 0.042	1.214 ± 0.100	9.912 ± 0.128	−4.166 ± 0.104	6.379 ± 2.301	0.832	1.092	1.101	1.887	1.973
1.602 ± 0.035	1.078 ± 0.054	2.228 ± 0.178	9.952 ± 0.188	4.115 ± 0.114	7.170 ± 2.284	1.129	1.482	1.494	2.564	2.681
	1.212 ± 0.296	220.397 ± 25.991	9.593 ± 0.280	−148.747 ± 0.085	7.090 ± 2.096	11.700	15.531	15.481	27.974	29.309
24.617 ± 1.181										
1.010 ± 0.017	0.929 ± 0.029	0.868 ± 0.057	9.951 ± 0.124	13.396 ± 0.082	4.899 ± 2.143	0.706	0.927	0.934	1.604	1.678
0.767 ± 0.011	0.825 ± 0.025	0.323 ± 0.034	9.522 ± 0.449	18.833 ± 0.104	3.666 ± 2.651	0.440	0.583	0.582	1.028	1.076
1.794 ± 0.039	1.003 ± 0.035	2.195 ± 0.190	10.033 ± 0.081	11.729 ± 0.115	10.051 ± 2.262	1.135	1.498	1.502	2.618	2.738
0.969 ± 0.017	0.969 ± 0.045	0.769 ± 0.064	9.756 ± 0.321	−16.011 ± 0.096	6.027 ± 2.367	0.665	0.875	0.880	1.517	1.586
1.337 ± 0.024	1.086 ± 0.043	1.749 ± 0.124	9.837 ± 0.129	−6.373 ± 0.109	5.812 ± 2.260	0.994	1.300	1.315	2.239	2.342
0.817 ± 0.013	0.871 ± 0.028	0.378 ± 0.030	9.677 ± 0.407	−5.682 ± 0.068	6.797 ± 2.251	0.475	0.629	0.629	1.109	1.160
0.728 ± 0.012	0.773 ± 0.025	0.282 ± 0.028	9.655 ± 0.444	8.326 ± 0.083	6.188 ± 2.447	0.412	0.545	0.545	0.964	1.009
1.037 ± 0.019	1.062 ± 0.042	0.982 ± 0.071	9.527 ± 0.378	−9.459 ± 0.098	7.432 ± 2.237	0.747	0.980	0.989	1.692	1.769
–	–	–	–	–	–	–	–	–	–	–

Table A2. Our refined confirmed and candidate exoplanet parameters. The full table of which can be found on the online version of this paper.

TIC ID	Candidate name	Period (days)	Semimajor axis (au)	R_p/R_*	au/R_*	Transit depth (%)	Inclination (deg)	Eccentricity	K_{amp} (ms^{-2})	–
677945	K2-128 b	5.675729 ± 0.0001680	0.0559 ± 0.0004	0.01709 ± 0.00059	17.8385 ± 0.268	0.029239 ± 0.001693	88.331 ± 0.574	0.23 ± 0.221	–	–
677945	EPIC 212686205.01	5.67556 ± 0.0002900	0.0559 ± 0.0004	0.01822 ± 0.00058	17.8382 ± 0.268	0.0332 ± 0.001700	–	–	–	–
678699	EPIC 212560683.01	13.7043 ± 0.0037000	0.1134 ± 0.0012	0.01257 ± 0.0006	23.7383 ± 0.463	0.0158 ± 0.001300	–	–	–	–
706595	K2-194 b	39.72342 ± 0.0031880	0.2358 ± 0.0034	0.02562 ± 0.00128	36.5615 ± 0.898	0.06572 ± 0.005381	89.065 ± 0.46	–	–	–
706595	EPIC 212672300.01	39.703624 ± 0.0021210	0.2358 ± 0.0034	0.02721 ± 0.00093	36.5523 ± 0.897	0.0741 ± 0.002800	–	–	–	–
707724	EPIC 212585579.01	3.021889 ± 0.0000460	0.0411 ± 0.0007	0.03443 ± 0.00114	7.8281 ± 0.188	0.1186 ± 0.004500	–	–	–	–
743782	EPIC 212652418.01	19.1324 ± 0.0031010	0.1416 ± 0.0024	0.01912 ± 0.00075	22.5198 ± 0.579	0.0366 ± 0.002000	–	–	–	–
771548	EPIC 212587672.01	23.231764 ± 0.0008410	0.1579 ± 0.0025	0.02175 ± 0.00135	33.5908 ± 0.802	0.047326 ± 0.005322	89.421 ± 0.422	–	–	–
771548	EPIC 212587672.02	15.2841 ± 0.0020000	0.1195 ± 0.0019	0.01367 ± 0.00066	25.4093 ± 0.607	0.0187 ± 0.001500	–	–	–	–
771548	EPIC 212587672 b	15.2841 ± 0.0017600	0.1195 ± 0.0019	0.01152 ± 0.00065	25.4108 ± 0.606	0.01328 ± 0.001324	–	–	–	–
1103432	565.01	3.727891 ± 0.0004550	0.0496 ± 0.001	0.13363 ± 0.00451	6.2069 ± 0.178	19.571261 ± 0.548862	–	–	–	–
2621212	K2-199 c	7.374442 ± 0.0000660	0.0663 ± 0.0006	0.03868 ± 0.0012	20.9489 ± 0.324	0.149668 ± 0.007299	88.893 ± 0.557	–	–	–
2621212	K2-199 b	3.225392 ± 0.0000320	0.0382 ± 0.0004	0.02522 ± 0.00089	12.0707 ± 0.187	0.063616 ± 0.003787	87.182 ± 1.475	–	–	–
2621212	EPIC 212779596.01	3.225349 ± 0.0000430	0.0382 ± 0.0004	0.02506 ± 0.001	12.0704 ± 0.187	0.062827 ± 0.004389	–	–	–	–
2621212	EPIC 212779596.02	7.374284 ± 0.0001100	0.0663 ± 0.0006	0.03876 ± 0.00161	20.9486 ± 0.324	0.150314 ± 0.011041	–	–	–	–
2670610	EPIC 213546283.01	9.770225 ± 0.0001750	0.0898 ± 0.0012	0.02896 ± 0.00123	16.8145 ± 0.375	0.083943 ± 0.005663	88.885 ± 0.815	–	–	–
2712931	EPIC 212645891.01	0.328227 ± 0.0000010	0.0092 ± 0.0002	0.04742 ± 0.00135	1.7434 ± 0.048	0.224802 ± 0.001692	41.646 ± 5.432	–	–	–
2764004	EPIC 212624936.01	11.81387 ± 0.0008500	0.0994 ± 0.0015	0.02686 ± 0.00108	22.7423 ± 0.555	0.0722 ± 0.004200	–	–	–	–
–	–	–	–	–	–	–	–	–	–	–

R_p $R_\oplus$	M_p $M_\oplus$	$Flag_{mass}$	ρ_p gcm^{-3}	S_{eff} $S_\oplus$	$T_{eq\,WM}$ (K)	$T_{eq\,HD}$ (K)	g_p (ms^{-2})	v_e (ms^{-1})	$Flag_{cat}$
1.26 ± 0.04	–	–	–	57.26 ± 4.49	732 ± 19	871 ± 23	–	–	EXO
1.34 ± 0.04	–	–	–	57.26 ± 4.48	732 ± 19	871 ± 23	–	–	K2
1.41 ± 0.07	–	–	–	81.14 ± 5.28	799 ± 19	950 ± 23	–	–	K2
3.88 ± 0.18	–	–	–	39.93 ± 3.14	687 ± 15	817 ± 18	–	–	EXO
4.12 ± 0.12	–	–	–	39.95 ± 3.14	630 ± 30	749 ± 35	–	–	K2
4.24 ± 0.12	–	–	–	797.66 ± 62.96	1331 ± 63	1583 ± 75	–	–	K2
2.82 ± 0.1	–	–	–	89.55 ± 7.88	840 ± 20	999 ± 24	–	–	K2
2.4 ± 0.15	–	–	–	44.41 ± 3.51	705 ± 16	839 ± 19	–	–	K2
1.51 ± 0.07	–	–	–	77.63 ± 6.14	790 ± 21	940 ± 25	–	–	K2
1.27 ± 0.07	–	–	–	77.63 ± 6.14	790 ± 21	940 ± 25	–	–	EXO
25.07 ± 0.65	–	–	–	1429.21 ± 119.76	1420 ± 84	1689 ± 99	–	–	TOI
2.87 ± 0.08	–	–	–	42.3 ± 3.22	697 ± 15	828 ± 18	–	–	EXO
1.87 ± 0.07	–	–	–	127.37 ± 9.71	894 ± 23	1063 ± 28	–	–	EXO
1.86 ± 0.07	–	–	–	127.39 ± 9.71	894 ± 23	1064 ± 28	–	–	K2
2.88 ± 0.12	–	–	–	42.29 ± 3.22	697 ± 15	828 ± 18	–	–	K2
3.63 ± 0.14	–	–	–	159.39 ± 11.64	971 ± 20	1154 ± 24	–	–	K2
5.87 ± 0.12	–	–	–	13416.93 ± 1670.66	2692 ± 143	3201 ± 171	–	–	K2
2.75 ± 0.1	–	–	–	73.34 ± 6.44	799 ± 19	951 ± 23	–	–	K2
–	–	–	–	–	–	–	–	–	–

This paper has been typeset from a TEX/LATEX file prepared by the author.

Don't feel obliged to live a life you never wanted to
the best way out is straight through
let intuition guide you.

– Hellions

4

THE DETECTION AND CHARACTERISATION TOI-778 B

The submitted manuscript paper Clark et al. (2022), "Spinning up a Daze: *TESS* uncovers a hot-Jupiter hosted by the rapid-rotator TOI-778 b" follows.

Draft version July 17, 2022
Typeset using LaTeX **twocolumn** style in AASTeX63

Spinning up a Daze: *TESS* Uncovers a Hot Jupiter orbiting the Rapid-Rotator TOI-778

Jake T. Clark,[1] Jack Okumura,[1] Sydney Vach,[2] Alexis Heitzmann,[1] Joseph E. Rodriguez,[3] Brett C. Addison,[1] Duncan J. Wright,[1] Mathieu Clerté,[1] Carolyn J. Brown,[1] Tara Fetherolf,[4,*] Robert A. Wittenmyer,[1] Peter Plavchan,[5] Stephen R. Kane,[6] Jonathan Horner,[1] John F. Kielkopf,[7] Avi Shporer,[8] C.G. Tinney,[9] Liu Hui-Gen,[10] Sarah Ballard,[11] Brendan P. Bowler,[12] Matthew W. Mengel,[1] George Zhou,[1] Annette S. Lee,[13,14,15,1] Avelyn David,[14,13] Jessica Heim,[14,13] Michele E. Lee,[16,13] Verónica Sevilla,[14,13] Naqsh E. Zafar,[14,13] Natalie R. Hinkel,[17] Bridgette E. Allen,[18,19] Daniel Bayliss,[20] Arthur Berberyan,[18,21] Perry Berlind,[2] Allyson Bieryla,[2] François Bouchy,[22] Rafael Brahm,[23,24,25] Edward M. Bryant,[26,27] Jessie L. Christiansen,[18] David R. Ciardi,[18] Krystina N. Ciardi,[18,28] Karen A. Collins,[29] Jules Dallant,[22] Allen B. Davis,[30] Matías R. Díaz,[31,32] Courtney D. Dressing,[33] Gilbert A. Esquerdo,[2] Jan-Vincent Harre,[34] Steve B. Howell,[35] Jon M. Jenkins,[35] Eric L. N. Jensen,[36] Matías I. Jones,[37] Andrés Jordán,[23,24,25] David W. Latham,[2] Michael B. Lund,[18] James McCormac,[38] Louise D. Nielsen,[22] Jon Otegi,[22] Samuel N. Quinn,[2] Don J. Radford,[39] George R. Ricker,[8] Richard P. Schwarz,[40] Sara Seager,[8,41,42] Alexis M. S. Smith,[43] Chris Stockdale,[44] Thiam-Guan Tan,[45,46] Stéphane Udry,[22] Roland Vanderspek,[8] Songhu Wang,[47] Geof Wingham,[48] and Joshua N. Winn[49]

[1] *University of Southern Queensland, Centre for Astrophysics, USQ Toowoomba, West Street, QLD 4350 Australia*
[2] *Center for Astrophysics | Harvard & Smithsonian, 60 Garden St, Cambridge, MA 02138, USA*
[3] *Department of Physics and Astronomy, Michigan State University, East Lansing, MI 48824, USA*
[4] *Department of Earth and Planetary Sciences, University of California Riverside, 900 University Avenue, Riverside, CA 92521, USA*
[5] *Department of Physics & Astronomy, George Mason University, 4400 University Drive MS 3F3, Fairfax, VA 22030, USA*
[6] *Department of Earth and Planetary Sciences, University of California, Riverside, CA 92521, USA*
[7] *Department of Physics and Astronomy, University of Louisville, Louisville, KY 40292, USA*
[8] *Department of Physics and Kavli Institute for Astrophysics and Space Research, Massachusetts Institute of Technology, Cambridge, MA 02139, USA*
[9] *Exoplanetary Science at UNSW, School of Physics, UNSW Sydney, NSW 2052, Australia*
[10] *School of Astronomy and Space Science, Key Laboratory of Modern Astronomy and Astrophysics in Ministry of Education, Nanjing University, Nanjing 210046, Jiangsu, China*
[11] *Department of Astronomy, University of Florida, 211 Bryant Space Science Center, Gainesville, FL, 32611, USA*
[12] *Department of Astronomy, The University of Texas at Austin, TX 78712, USA*
[13] *The Native Skywatchers Initiative, MN USA*
[14] *Department of Physics and Astronomy, St. Cloud University, MN USA*
[15] *Department of Astronomy and Astrophysics, University of California, Santa Cruz, CA 95064, USA*
[16] *Jeremiah Horrocks Institute, University of Central Lancashire, Preston, PR1 2HE, UK*
[17] *Space Science and Engineering Division, Southwest Research Institute, San Antonio, TX 78238, USA*
[18] *NASA Exoplanet Science Institute - Caltech/IPAC, 1200 E. California Blvd, Pasadena, CA 91125 USA*
[19] *University of Wisconsin Stout, 712 South Broadway Street, Menomonie, WI 54751 USA*
[20] *Dept. of Physics, University of Warwick, Gibbet Hill Road, Coventry, CV4 7AL, UK*
[21] *College of the Canyons, 26455 Rockwell Canyon Rd., Santa Clarita, CA 91355, USA*
[22] *Geneva Observatory, University of Geneva, Chemin Pegasi 51, 1290 Versoix, Switzerland*
[23] *Facultad de Ingeniería y Ciencias, Universidad Adolfo Ibáñez, Av. Diagonal las Torres 2640, Peñalolén, Santiago, Chile*
[24] *Millennium Institute for Astrophysics, Chile*
[25] *Data Observatory Foundation, Chile*
[26] *Dept. of Physics, University of Warwick, Gibbet Hill Road, Coventry CV4 7AL, UK*
[27] *Centre for Exoplanets and Habitability, University of Warwick, Gibbet Hill Road, Coventry CV4 7AL, UK*
[28] *Rhode Island College, 600 Mount Pleasant Avenue Providence, RI 02908 USA*
[29] *Center for Astrophysics | Harvard & Smithsonian, 60 Garden Street, Cambridge, MA 02138, USA*
[30] *Department of Astronomy, Yale University, 52 Hillhouse Avenue, New Haven, CT 06511, USA*
[31] *Las Campanas Observatory, Carnegie Institution of Washington, Colina el Pino, Casilla 601 La Serena, Chile*

Corresponding author: Jake Clark
jake.clark@usq.edu.au

[32] Departamento de Astronomía, Universidad de Chile, Camino El Observatorio 1515, Las Condes, Santiago, Chile
[33] Astronomy Department, University of California, Berkeley, CA 94720, USA
[34] Institute of Planetary Research, German Aerospace Center (DLR), Rutherfordstraße 2, 12489 Berlin, Germany
[35] NASA Ames Research Center, Moffett Field, CA 94035, USA
[36] Dept. of Physics & Astronomy, Swarthmore College, Swarthmore PA 19081, USA
[37] European Southern Observatory, Alonso de C'ordova 3107, Vitacura, Casilla 19001, Santiago, Chile
[38] Dept. Physics, University of Warwick, Gibbet Hill Road, CV4 7AL, UK
[39] Brierfield Observatory, New South Wales, Australia
[40] Patashnick Voorheesville Observatory, Voorheesville, NY 12186, USA
[41] Department of Earth, Atmospheric and Planetary Sciences, Massachusetts Institute of Technology, Cambridge, MA 02139, USA
[42] Department of Aeronautics and Astronautics, MIT, 77 Massachusetts Avenue, Cambridge, MA 02139, USA
[43] Institute of Planetary Research, German Aerospace Center, Rutherfordstr. 2, 12489 Berlin, Germany
[44] Hazelwood Observatory, Australia
[45] Perth Exoplanet Survey Telescope, Perth, Western Australia
[46] Curtin Institute of Radio Astronomy, Curtin University, Bentley, Western Australia 6102
[47] Department of Astronomy, Indiana University, Bloomington, IN 47405, USA
[48] Mt. Stuart Observatory, New Zealand
[49] Department of Astrophysical Sciences, Princeton University, Princeton, NJ 08544, USA

Submitted to Astronomical Journal

ABSTRACT

NASA's *Transiting Exoplanet Survey Satellite* (*TESS*) mission, has been uncovering a growing number of exoplanets orbiting nearby, bright stars. Most exoplanets that have been discovered by *TESS* orbit narrow-line, slow-rotating stars, facilitating the confirmation and mass determination of these worlds. We present the discovery of a hot Jupiter orbiting a rapidly rotating ($v \sin(i)$ = 28.9±3.7 km s^{-1}) early F3V-dwarf, HD 115447 (TOI-778). The transit signal taken from Sectors 10 and 37 of *TESS*'s initial detection of the exoplanet is combined with follow-up ground-based photometry and velocity measurements taken from MINERVA-Australis, TRES, CORALIE and CHIRON to confirm and characterise TOI-778 b. A global analysis of the light curves and the radial velocity measurements yield a mass, radius, and orbital period for TOI-778 b of 2.774±0.204 $M_{\rm J}$, 1.344±0.027 $R_{\rm J}$ and 4.634 days, respectively. The planet orbits a bright (V = 9.1 mag) F3-dwarf with M = 1.39±0.02 $M_{\odot}$, R = 1.70±0.02 $R_{\odot}$, and $\log g$ = 4.05±0.17. We observed a spectroscopic transit of TOI-778 b, which allowed us to derive a sky-projected spin-orbit angle of 19.1±9.6 degrees, consistent with an aligned planetary system. This discovery demonstrates the capability of smaller aperture telescopes such as MINERVA-Australis to detect the radial velocity signals produced by planets orbiting broad-line, rapidly rotating stars.

Keywords: stars: individual (HD 115447) — techniques: radial velocities – techniques: transits

1. INTRODUCTION

In the late 1980s the first exoplanetary candidates around main sequence stars were discovered orbiting Gamma Cephei (Campbell et al. 1988) and HD 114672 (Latham et al. 1989)[1]. Soon after Mayor & Queloz (1995) announced the discovery of 51 Peg b, the first planet found orbiting a Sun-like star – marking the start of the Exoplanet Era.

In the decade that followed that seminal discovery, the radial velocity technique dominated the search for alien worlds, revealing a plethora of "hot Jupiters" – giant planets orbiting their host stars with periods of just a few days (e.g. Butler et al. 1997; Henry et al. 2000; Tinney et al. 2001). Based solely on knowledge of the Solar system, it was broadly expected that planetary systems would feature giant planets on long period or-

* UC Chancellor's Fellow
[1] This companion is likely a low-mass star in a face-on orbit (Kiefer 2019).

bits, and small, rocky worlds on short period orbits[2]. Instead, it became obvious that a significant number of stars (∼1%, e.g. Wittenmyer et al. 2011; Wright et al. 2012; Kunimoto & Matthews 2020) host scorching hot giant planets – marking their planetary systems as being truly alien when compared to our own.

Such planets (commonly known as "hot Jupiters") are by far the easiest exoplanets to detect – a fact made clear by the great success of the *Kepler* mission. *Kepler* launched in 2008, and spent slightly over four years staring continuously at a single patch of the night sky – in the northern constellation of Cygnus – monitoring the brightness of more than 150,000 stars. By recording minuscule dips in brightness exhibited by some of those stars, *Kepler*'s primary mission led to the discovery of 3184 planets[3].

The successor to *Kepler* is the *Transiting Exoplanet Survey Satellite*, *TESS* (Ricker et al. 2015). Launched in April 2018, *TESS* is currently in the process of scouring the sky, observing hundreds of thousands of the nearest and brightest stars, in an attempt to find short-period planets around them. *TESS* observes the majority of its targets for two consecutive 13.7 day periods, separated by a short window where the spacecraft pivots to broadcast data back to Earth, meaning that it is particularly well adapted for the discovery of hot Jupiters. Indeed, the majority of the 177 planets[4] confirmed by *TESS* are either hot Jupiters or their smaller siblings, the "hot Neptunes" (e.g. Nielsen et al. 2019; Kossakowski et al. 2019; Addison et al. 2021; Jordán et al. 2020; Plavchan et al. 2020).

The origin of such planets has been the source of much debate. It is widely accepted that such planets cannot have formed on their current orbits, so close to their host stars. Instead, it is thought that they originate at much greater distances, beyond the "ice-line" – the location in the protoplanetary disk around their host at which temperatures were sufficiently low for water ice to be present (e.g. Pollack et al. 1996; Ida & Lin 2004; Wittenmyer et al. 2020).

Several different mechanisms have been proposed to explain this migration – all of which likely occur in some, but not all, planetary systems. The current proposals include a smooth process of migration through the protoplanetary disks of their host stars, as the young planet interacts with the material from which it is feeding (e.g. Lin et al. 1996; Tanaka et al. 2002); planet-planet scattering shifting the planet onto an extremely eccentric orbit, followed by a process of tidal circularisation (e.g. Chatterjee et al. 2008; Beaugé & Nesvorný 2012; Li et al. 2019a); and secular perturbations imposed by a highly inclined unseen massive companion (the Kozai-Lidov mechanism; Kozai 1962; Lidov 1962; Nagasawa et al. 2008a; Nagasawa & Ida 2011).

The techniques we use to characterise exoplanets are built upon observations of hot Jupiter systems about bright stars. Though it is the best studied of the exoplanet demographic, questions remain on the origins and evolution of close-in Jovian planets. Mechanisms are likely responsible for the population (see review in Dawson & Johnson 2018), though their timescales and proclivity are not well understood.

For individual hot Jupiters, tell-tale signs of their formation pathways may still remain. The orbits of planets that migrate purely as a result of interaction with their host star's protoplanetary disk are expected to remain co-planar with the star's equator, as long as the initial disk isn't tilted (as is the case for < 100 Myr close-orbital giants AU Mic b, DS Tuc Ab, HIP 67522 b, V1298 Tau b and c and TOI 942 c Plavchan et al. 2020; Zhou et al. 2020; Heitzmann et al. 2021; Gaidos et al. 2022), whilst a process of planet-planet scattering can act to moderately incline a planet's orbit relative to that plane. Planets whose migration is driven by the Kozai-Lidov mechanism can become dramatically misaligned with the equators of their host stars – sometimes even being injected to polar or retrograde orbits (e.g. Albrecht et al. 2012; Addison et al. 2018; Siverd et al. 2018; Temple et al. 2019).

Studies of the inclination of the orbits of hot Jupiters have revealed a correlation between planetary inclination and host star mass/temperature. The more massive (and hotter) the host star, the more likely it is that any short-period planets discovered in orbit will be strongly misaligned to the star's equatorial plane (e.g. Collier Cameron et al. 2010; Addison et al. 2013; Rodríguez Martínez et al. 2020).

Given that more massive stars are more likely to exhibit binarity (Preibisch et al. 1999; Böhm-Vitense 2007), it is possible that the increased numbers of misaligned planets orbiting such stars is a direct result of those stars having undetected massive companions. Equally, more massive stars tend to form more massive planets (e.g. Ida & Lin 2005; Johnson et al. 2007; Bowler et al. 2010; Jones et al. 2016), and so mechanisms in-

[2] For a detailed overview of our knowledge of the Solar system, and its impact on our understanding of exoplanetary science, we direct the interested reader to Horner et al. (2020), and references therein.

[3] As of 27th January, 2022; statistics taken from the NASA Exoplanet Archive counts page, at https://exoplanetarchive.ipac.caltech.edu/docs/counts_detail.html.

[4] As of 27th January, 2022; data courtesy of the NASA Exoplanet Archive's counts page.

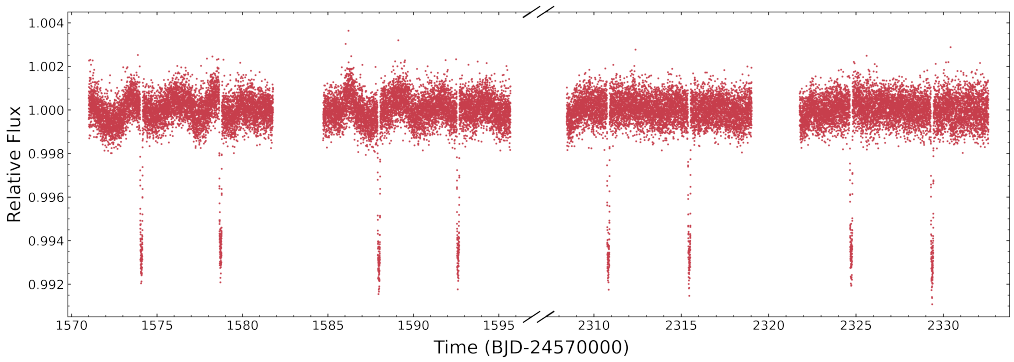

Figure 1. Full TESS light curves for TOI-778 from Sector 10 and Sector 37

volving planet-planet scattering are also more likely to play a role in determining the obliquities of short period planets.

To determine the degree to which these different mechanisms contribute to the overall population of short-period planets, it is important to discover and characterise as many such planets, orbiting as wide a variety of stars, as possible. In this work, we present the discovery of a new hot Jupiter orbiting HD 115447 (also known as TOI-778), an F3-dwarf with a mass of 1.39±0.02 $M_{\odot}$ and a surface temperature of 6875±190 K. The candidate planet was detected by *TESS* during Sector 10, in the first year of operation as it surveyed the southern sky. Here, we used follow-up observations from a variety of ground-based facilities to confirm the existence of TOI-778 b, and characterise both the planet and its orbit around TOI-778.

Following in Section 2, we provide the latest characterisation of TOI-778 and then describe the observations of that star in Section 3. We then present the results of our analysis in Section 4, discuss those results in Section 5, and then conclude in Section 6.

2. STELLAR PROPERTIES OF HD 115447

The planetary properties of TOI-778 b depend upon the stellar properties of its host star. We first combine the MINERVA-Australis spectra of TOI-778 to create a median spectrum to input into `iSpec` (Blanco-Cuaresma et al. 2014; Blanco-Cuaresma 2019). `iSpec` uses a grid-modelling approach to calculate the effective temperature ($T_{\rm eff}$), surface gravity (log g) and overall metallicity ([M/H]) from the input spectra. These spectroscopic properties are then used along with other photometric and astrometric data as input for the Bayesian isochrone modelling program `isochrones`. We used the *Gaia* DR2 (Gaia Collaboration et al. 2018) parallax and *Gaia* DR2 magnitudes (G, G_R and G_B), 2MASS (Cutri et al. 2003) magnitudes (J, H and K_s) V-band magnitude (V) and colour excess (E(B-V)), with the `iSpec` values as input for the `isochrones` analysis. The resulting derived `isochrone` properties for TOI-778, including stellar mass, radius, luminosity, and age are given in Table 1. Our results are consistent with version 9 of the *TESS* Input Catalog (Stassun et al. 2019) and are the parameters used to further characterise the planetary nature of TOI-778 b. The above procedure of determining the stellar properties of TOI-778 is similar to that of Addison et al. (2021).

We also calculated the rotation period of TOI-778 through the light curve obtained by *TESS* (discussed in more detail within Section 3.1). Using SCIPY's Lomb-Scargle periodogram (Virtanen et al. 2020) on the light curves collected by *TESS* (plotted in Figure 1), we calculated the stellar rotation period for TOI-778 to be 2.567 ± 0.095 days. Figure 2 shows a phase-folded plot of the TOI-778's light curve to the period of 2.567 days. There seems to be no correlation between the light curve modulation and the momentum dumps of TESS shown in Figure 2 and the normalized power of the periodogram is sufficiently high, such that we are confident that this modulation is astrophysical in nature. We include our derived stellar rotation value in Table 1.

3. OBSERVATIONS AND DATA REDUCTION

In this section, we describe the photometric, spectroscopic, and imaging data sets used to validate the planetary nature of TOI-778 b.

3.1. *Photometric Observations*

3.1.1. *TESS Light Curve*

TOI-778 (TIC 335630746) was observed by *TESS* during Sector 10 of its primary mission, from March 26 to

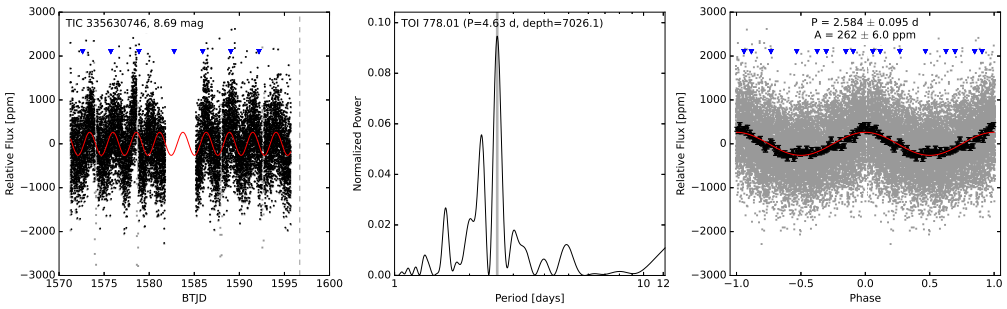

Figure 2. Left: Relative flux values from TOI-778 during Sector 10 (black dots). The transit events of TOI-778 b that have been removed for the periodogram analysis are shown as grey points. The baseline is shown in green with the periodic signal of 2.584 days is over-plotted in red. Momentum dumps from *TESS* are shown by the blue triangles. Centre: The periodogram from the *TESS* light curve with the peak period being nearer to the orbital period of TESS-778 b. Right: A phase-folded version of Left figure, with the period and semi-amplitude of the periodic variations listed at the top of the figure.

April 21, 2019, and extended via Sector 37 observations, taken between April 2 and April 28, 2021. The target star was identified as a planet host candidate via the analyses of the Science Processing Observation Center (SPOC, Jenkins et al. 2016), as described by Twicken et al. (2018) and Li et al. (2019b), using light curves extracted from the two minute target pixel files. We used the Pre-search Data Conditioning Simple Aperture Photometry flux values from the *TESS* light curve, removing nonzero flagged data (such as momentum dumps) that could contaminate the light curve analysis. The light curves were then normalised by the median flux values and used in the analysis for TOI-778 b's confirmation. The resulting light curves are found in Figure 1.

3.1.2. *Next Generation Transit Survey*

A transit egress of TOI-778 b was observed using the Next Generation Transit Survey (NGTS; Wheatley et al. 2018) on UTC 2019 June 22. NGTS is an exoplanet hunting facility located at the ESO Paranal Observatory in Chile, which consists of twelve independently operated robotic telescopes. Each telescope has a 20 cm diameter and an 8 square-degree field-of-view. The NGTS telescopes use the DONUTS auto-guiding algorithm (McCormac et al. 2013) to achieve sub-pixel guiding. TOI-778 was observed simultaneously using two NGTS telescopes, and such multi-telescope observations have been shown to significantly improve the photometric precision of the observations (Smith et al. 2020; Bryant et al. 2020). A total of 1486 images were obtained using an exposure time of 10 s and the custom NGTS filter (520 - 890 nm). The airmass of the target was kept below 2 and the sky conditions were optimal throughout the observations.

The images were reduced using a custom aperture photometry pipeline (Bryant et al. 2020) which uses the `SEP` library (Bertin & Arnouts 1996; Barbary 2016) for source extraction and photometry. The pipeline automatically identifies comparison stars using *Gaia* DR2 (Gaia Collaboration et al. 2016, 2018), ranking the stars in the field based on their similarity to TOI-778 in terms of brightness, colour and CCD position.

3.1.3. *Perth Exoplanet Survey Telescope*

We observed an egress of TOI-778 on UTC 2020 March 31 in V-band from the Perth Exoplanet Survey Telescope (PEST) near Perth, Australia. The 0.3 m telescope is equipped with a 1530 × 1020 SBIG ST-8XME camera with an image scale of $1\farcs2$ pixel^{-1} resulting in a $31' \times 21'$ field of view. A custom pipeline based on `C-Munipack`[5] was used to calibrate the images and extract the differential photometry, using an aperture with radius $7\farcs4$. The images have typical stellar point spread functions (PSFs) with a FWHM of $\sim 4''$.

3.1.4. *LCO SAAO*

We observed a full transit of TOI-778 in Pan-STARSS z-short band on UTC 2020 May 30 from the LCOGT (Brown et al. 2013) 1.0 m network node at South Africa Astronomical Observatory. We used the ***`TESS`*** `Transit Finder`, which is a customized version of the `Tapir` software package (Jensen 2013), to schedule our transit observations. The 4096 × 4096 LCOGT SINISTRO cameras have an image scale of $0.389''$ per pixel, resulting in a $26' \times 26'$ field of view. The images were calibrated by the standard LCOGT `BANZAI` pipeline (Mc-

[5] http://c-munipack.sourceforge.net

Table 1. Stellar Parameters for HD 115447

Stellar Parameters	Value	Source
Catalog Information		
Right Ascension (h:m:s)	13:17:20.189	1
Declination (d:am:as)	-15:16:24.944	1
Parallax (mas)	6.15415 ± 0.04231	1
$\mu_{\rm R.A}$ (mas yr^{-1})	-60.600 ± 0.083	1
$\mu_{\rm Dec.}$ (mas yr^{-1})	-26.012 ± 0.065	1
Gaia DR2 ID	3607877948613218304	1
2MASS ID	J13172019-1516248	2
HD ID	115447	
TIC ID	335630746	3
TOI ID	778	
Spectroscopic Properties		
Spectral type	F2	4
	F3V	5
$T_{\rm eff}$ (K)	6715 ± 128	3
	6875 ± 190	7
$\log g$ (cgs)	4.144 ± 0.085	3
	4.05 ± 0.17	7
Metallicity, [M/H]*	0.00 ± 0.08	7
$v \sin i$ (km s^{-1})	28.94 ± 3.65	7
Photometric Properties		
G (mag)	8.99436 ± 0.000672	1
G_{BP} (mag)	9.22647 ± 0.001553	1
G_{RP} (mag)	8.64796 ± 0.001898	1
J (mag)	8.246 ± 0.021	2
H (mag)	8.09 ± 0.026	2
K_s (mag)	8.055 ± 0.033	2
V (mag)	9.11 ± 0.02	6
T (mag)	8.6901 ± 0.0062	3
Derived Properties		
$M_\star$ ($M_\odot$)	1.428 ± 0.094	3
	1.39 ± 0.02	7
$R_\star$ ($R_\odot$)	1.677 ± 0.068	3
	1.70 ± 0.02	7
$\rho_\star$ (g cm^{-3})	0.40 ± 0.01	7
$L_\star$ ($L_\odot$)	5.153 ± 0.269	3
	5.76 ± 0.65	7
Age (Gyr)	$1.9498\ ^{+0.1395}_{-0.1301}$	7
Distance (pc)	162.493 ± 1.117	1
Rotation Period (days)	2.584±0.095	7

References—1. Gaia Collaboration et al. (2018); 2. Cutri et al. (2003) ; 3. Stassun et al. (2019); 4. Cannon & Pickering (1993); 5. Houk & Smith-Moore (1988), 6. Høg et al. (2000), 7. This work.

Cully et al. 2018), and photometric data were extracted with `AstroImageJ` (Collins et al. 2017). The images were defocused to a full-width-half-maximum (FWHM) of $\sim 6\farcs7$, and circular apertures with radius $8\farcs2$ were used to extract the differential photometry.

3.1.5. *Mount Kent Observatory*

On 2020 June 5 at the Mount Kent Observatory, a photometric transit observation of TOI-778 was taken simultaneously with radial velocity observations from MINERVA-Australis. The observation was preformed with the Shared Skies Partnership's Planewave CDK700 telescope equipped with an Alta U16M Apogee camera. All data was taken using a Sloan i' filter with a 27.3'x27.3' field of view. All data reduction and analysis was completed using the `AstroImageJ` software package.

3.1.6. *Mt. Stuart*

We observed TOI-778 b on UTC 2020 April 28 in Sloan r' band from the Mt. Stuart Observatory near Dunedin, New Zealand. The 0.32 m telescope is equipped with a 3072 × 2048 SBIG STXL6303E camera with an image scale of $0\farcs88$ pixel^{-1} resulting in a $44' \times 30'$ field of view. The images were calibrated and photometric data were extracted with `AstroImageJ` using a circular aperture with radius $3\farcs5$.

3.2. *Spectroscopic Observations*

In order to obtain precise radial velocity follow-up data for TOI-778, we carried out observations using four different facilities. Here we give details about the observations carried out by each instrument.

Table 2. Radial Velocities for TOI-778

Time [BJD]	Velocity [m s^{-1}]	Uncertainty [m s^{-1}]	Instrument
2458662.635267	175.05	77.77	Chiron
2458664.593833	0.27	68.85	Chiron
2458666.604267	190.92	88.77	Chiron
2458667.6084	-110.02	72.73	Chiron
2458668.6492	-347.35	98.36	Chiron
2458652.690111	-6229.16	132.58	Coralie
2458653.673741	-6089.93	130.86	Coralie
2458654.685435	-5971.39	105.6	Coralie
2458670.487533	-5466.47	56.06	Coralie
2458676.511537	-5934.62	66.24	Coralie
2458679.556439	-5559.42	71.34	Coralie
2458680.515732	-5679.11	62.03	Coralie
2458691.532747	-6115.06	62.46	Coralie
2458693.538366	-5422.17	88.7	Coralie
2458694.501064	-5568.92	63.81	Coralie

Table 2 *continued*

Table 2 *(continued)*

Time [BJD]	Velocity [m s^{-1}]	Uncertainty [m s^{-1}]	Instrument
2458695.469491	-6048.16	57.82	Coralie
2458696.505111	-5671.52	113.86	Coralie
2458709.46814	-6144.97	90.64	Coralie
2458710.466932	-6021.12	136.78	Coralie
2458712.493358	-5809.26	91.72	Coralie
2458713.471968	-5989.96	82.57	Coralie
2458714.472638	-5884.07	76.8	Coralie
2458715.469593	-5805.4	78.4	Coralie
2458716.483157	-5627.43	66.24	Coralie
2458717.472442	-5579.16	105.59	Coralie
2458718.473601	-5803.01	68.28	Coralie
2458721.47271	-5398.83	74.93	Coralie
2458723.475732	-5989.71	70.39	Coralie
2458724.472153	-5717.1	65.55	Coralie
2458725.474141	-5515.44	64.28	Coralie
2458726.473827	-5468.42	70.46	Coralie
2458728.474083	-6132.56	92.31	Coralie
2458647.926208	-6527.96	149.17	Minerva T1
2458647.947619	-7041.7	227.72	Minerva T1
2458654.026804	-6794.14	188.55	Minerva T1
2458665.047428	-6479.67	249.21	Minerva T1
2458673.955227	-6875.54	96.16	Minerva T1
2458673.976637	-6606.27	183.97	Minerva T1
2458674.985359	-6779.37	166.03	Minerva T1
2458675.006769	-6394.48	152.48	Minerva T1
2458677.004458	-7318.43	180.87	Minerva T1
2458677.958648	-6870.83	206.74	Minerva T1
2458677.980047	-6807.1	174.71	Minerva T1
2458678.97892	-6682.21	133.2	Minerva T1
2458679.000318	-6414.22	266.15	Minerva T1
2458679.982075	-6941.1	430.08	Minerva T1
2458680.003473	-6178.08	319.36	Minerva T1
2458680.988875	-6629.58	180.78	Minerva T1
2458681.941607	-7003.08	177.44	Minerva T1
2458681.963017	-6943.91	165.46	Minerva T1
2458682.924197	-6994.76	189.53	Minerva T1
2458686.917908	-6895.76	172.31	Minerva T1
2458686.939318	-6853.55	169.26	Minerva T1
2458688.871712	-6352.02	197.59	Minerva T1
2458688.893111	-6332.18	164.89	Minerva T1

Note—Table 2 is published in its entirety in machine-readable format online. A portion is shown here for guidance regarding its form and content.

3.2.1. *MINERVA-Australis*

We carried out the spectroscopic observations of TOI-778 using the Minerva-Australis facility (Wittenmyer et al. 2018; Addison et al. 2019, 2021). Minerva-Australis consists of an array of four independently operated 0.7 m CDK700 telescopes situated at the Mount Kent Observatory in Queensland, Australia (Addison et al. 2019). Each telescope simultaneously feeds stellar light via fiber optic cables to a single KiwiSpec R4-100 high-resolution ($R = 80,000$) spectrograph (Barnes et al. 2012) with wavelength coverage from 480 to 620 nm. TOI-778 was observed on 71 epochs with three telescopes (labelled 'T1, T3, T4') between June 13, 2019 and June 4, 2020. Each epoch consists of two 30-minute exposures, and the resulting radial velocities are given in Table 2. Radial velocities for the observations are derived for each telescope by cross-correlation, where the template being matched is the mean spectrum of each telescope. The instrumental variations are corrected by using simultaneous Thorium-Argon (ThAr) arc lamp observations. Radial velocities computed from different Minerva-Australis telescopes are modeled in Section 4 as originating from independent instruments.

3.2.2. *TRES*

We obtained additional observations of TOI-778 via the Tillinghast Reflector Echelle Spectrograph (TRES, Fűrész 2008) on the 1.5 m reflector at the Fred Lawrence Whipple Observatory in USA. TRES is a fiber fed echelle with a resolving power of $R \sim 44,000$ over the wavelength range of $3850-9100$. The observing strategy and spectral extraction procedures are outlined in Buchhave et al. (2010). Radial velocities are derived from a multi-order cross correlation between each observed spectrum and a master template derived from the median combination of the observations as per Quinn et al. (2012).

3.2.3. *CORALIE*

The high resolution spectrograph CORALIE (Queloz et al. 2001) is mounted on the Swiss 1.2m Euler telescope in La Silla Observatories, Chile. The instrument is fibre fed with a 2″ science fibre on sky and simultaneous Fabry-Pérot wavelength calibration, with a resolution of $R = 60,000$. A total of 28 spectra of TOI-778 were obtained between June 17, 2019 and September 1, 2019 by the Swiss CORALIE team and the WINE-collaboration. One epoch was discarded due to low S/N, leaving 27 remaining spectra with S/N 10-50 at wavelength 550 nm. All spectra were extracted using the standard CORALIE data reduction pipeline.

RVs were extracted through the cross-correlation technique (Baranne et al. 1996). We used a weighted binary mask corresponding to an A0-star dominated by hydrogen and Fe lines. This mask highly favours the strongest 1000 absorption lines seen in hot stars (Wyttenbach et al. 2020). TOI-778 is a rapidly rotating star, resulting in non-Gaussian absorption lines. We therefore fit a rotational profile to the cross-correlation functions, as done for WASP-189 in Anderson et al. (2018). Through this method we achieve a typical RV precision of 80 m s^{-1}.

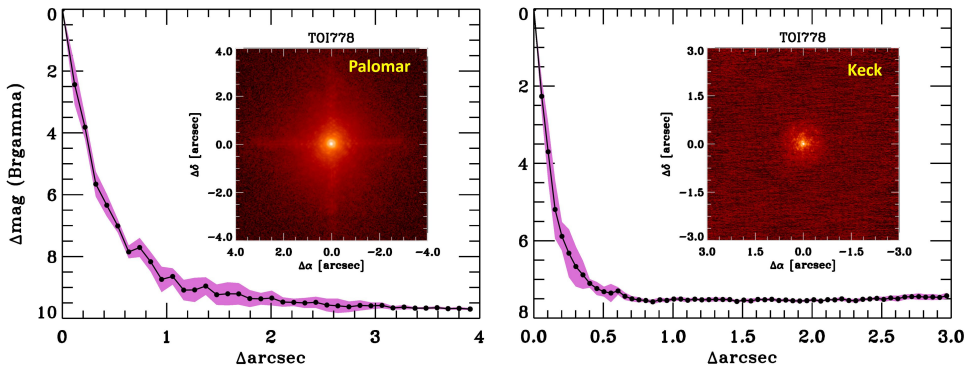

Figure 3. Companion sensitivity for the near-infrared adaptive optics imaging. The black points represent the 5σ limits and are separated in steps of 1 FWHM; the purple represents the azimuthal dispersion (1σ) of the contrast determinations (see text). The inset image is of the primary target showing no additional close-in companions.

3.2.4. *CHIRON*

We obtained fifteen spectra of TOI-778 using the CHIRON spectrograph (Tokovinin et al. 2013) on the Small and Moderate Aperture Research Telescope System (SMARTS) 1.5 m telescope at Cerro Tololo, Chile. The CHIRON spectra were obtained using the $R = 80,000$ slicer mode, and each spectrum is bracketed by a pair of ThAr lamp exposures for wavelength calibration. This combination allows for higher throughput at the cost of some instrumental RV precision. For this early-type star, however, the RV uncertainties are dominated by the broad and sparse spectral lines, rather than wavelength calibration error or line-spread function drift (both of which are better addressed with iodine, rather than ThAr). CHIRON's fiber has an on-sky radius of $1\farcs35$ with individual exposure times set to 5 minutes in length. Three back-to-back exposures were taken per night that we observed TOI-778.

The RVs were derived following the procedure described in Jones et al. (2017); Wang et al. (2019); Davis et al. (2020). To summarise, each set of observations of TOI-778 during a night were bracketed by a pair of ThAr exposures, and the CHIRON pipeline uses these to correct for possible instrumental drift; this yields a demonstrated long-term stability better than 10 m s^{-1}. Individual CHIRON spectra are shifted to a common rest frame and then stacked to form a template. We compute the Cross-Correlation Function (CCF) between each observed spectrum and this template. We then fit a Gaussian function plus linear trend to the CCF, and take the maximum of the fit to be the RV for that observation. This method is repeated for the 33 echelle orders between ∼4700–6500 Å where we have good wavelength calibration. The final RV at each epoch is obtained from the median of the individual order velocities, after applying a 3σ rejection method. RV uncertainties are computed from the error in the mean of the non-rejected velocities (as in Jones et al. 2017). For this star, the typical RV error found was about 150 m s^{-1}.

3.3. *High Angular Resolution Imaging*

As part of our standard process for validating transiting exoplanets to assess the possible contamination of bound or unbound companions on the derived planetary radii (Ciardi et al. 2015), we observed TOI-778 with high-resolution near-infrared adaptive optics (AO) imaging at Palomar and Keck Observatories and with optical speckle interferometric imaging at Gemini-South. The infrared observations provide the deepest sensitivities to faint companions while the optical speckle observations provide the highest resolution imaging making the two techniques complementary.

3.3.1. *Near-Infrared AO*

The Palomar Observatory observations were made with the Palomar High Angular Resolution Observer (PHARO) instrument (Hayward et al. 2001) behind the natural guide star AO system P3K (Dekany et al. 2013) on 2020 Jun 12 UT in a standard 5-point quincunx dither pattern with steps of $5''$ in the narrow-band $Br{-}\gamma$ filter ($\lambda_o = 2.1686; \Delta\lambda = 0.0326$ μm). Each dither position was observed three times, offset in position from each other by $0.5''$ for a total of 15 frames; with an integration time of 10 seconds per frame, the total on-

source time was 150 seconds. PHARO has a pixel scale of 0.025″ per pixel for a total field of view of ∼ 25″.

The Keck Observatory observations were made with the NIRC2 instrument on Keck-II behind the natural guide star AO system (Wizinowich et al. 2000) on June 25, 2019 in the standard 3-point dither pattern that is used with NIRC2 to avoid the left lower quadrant of the detector which is typically noisier than the other three quadrants. The dither pattern step size was 3″ and was repeated twice, with each dither offset from the previous dither by 0.5″. NIRC2 was used in the narrow-angle mode with a full field of view of ∼ 10″ and a pixel scale of approximately 10 milliarcsec per pixel. The Keck observations were made in both the narrow-band filters $Br-\gamma$ filter ($\lambda_o = 2.1686; \Delta\lambda = 0.0326$ μm) and $J-cont$ ($\lambda_o = 1.2132; \Delta\lambda = 0.0198$ μm) with an integration time in each filter of 1 second for a total of 9 seconds on target.

The AO data were processed and analyzed with a custom set of IDL tools. The science frames were flat-fielded and sky-subtracted. The flat fields were generated from a median average of dark subtracted flats taken on-sky. The flats were normalised such that the median value of the flats is unity. The sky frames were generated from the median average of the 15 dithered science frames; each science image was then sky-subtracted and flat-fielded. The reduced science frames were combined into a single combined image using a intra-pixel interpolation that conserves flux, shifts the individual dithered frames by the appropriate fractional pixels, and median-coadds the frames. The final resolution of the combined dithers was determined from the full-width half-maximum of the point spread function; 0.105″ and 0.050″ for the Palomar and Keck observations respectively.

To within the limits of the AO observations, no stellar companions were detected. The sensitivities of the final combined AO image were determined by injecting simulated sources azimuthally around the primary target every 20° at separations of integer multiples of the central source's FWHM (Furlan et al. 2017; Lund 2021 submitted). The brightness of each injected source was scaled until standard aperture photometry detected it with 5σ significance. The resulting brightness of the injected sources relative to TOI-778 set the contrast limits at that injection location. The final 5σ limit at each separation was determined from the average of all of the determined limits at that separation and the uncertainty on the limit was set by the rms dispersion of the azimuthal slices at a given radial distance (Figure 3).

3.4. *Optical Speckle Interferometry*

TOI-778 was observed on March 16, 2020, using the Zorro speckle interferometric instrument mounted on the 8 m Gemini South telescope on the summit of Cerro Pachon in Chile. Zorro simultaneously obtains diffraction-limited images at 562 and 832 nm. Our data set consisted of 3 minutes of total integration time on source taken as sets of 1000 x 0.06 s images plus a consecutive observation of a Point Spread Function (PSF) standard star. Following Howell et al. (2011), we combined all images and subjected them to Fourier analysis to produce speckle reconstructed imagery from which the 5σ contrast curves are derived for each passband and nearby companion stars searched for (Figure 4). Our data reveal TOI-778 to be a single star to contrast limits of 5–8.5 magnitudes covering a spatial range of ∼3 to 196 au at the distance to TOI-778.

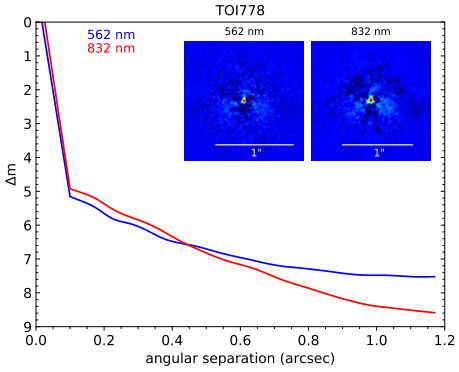

Figure 4. Speckle interferometric contrast curves and reconstructed images for the 562 nm and 832 nm observations. No companion was detected within the spatial limits of the diffraction limit and 1.2" equaling 3-4 to 196 au at the distance of TOI-778

4. JOINT ANALYSIS AND RESULTS

To determine the planetary nature of TOI-778 b, and its host star's obliquity, we used `Allesfitter` (Günther & Daylan 2019, 2021) to perform a joint analysis of the *TESS* light curve segments, the photometric ground-based light curves, and the radial velocity measurements. We include both light curves from the *TESS* Sectors 10 and 37, keeping them as separate observations with possible brightness offsets between the sectors. We also split the observations from each Sector into two parts, since there is a clear break in each sector during the data download. Thus, we have four independent *TESS* light curves we use for the analysis. We

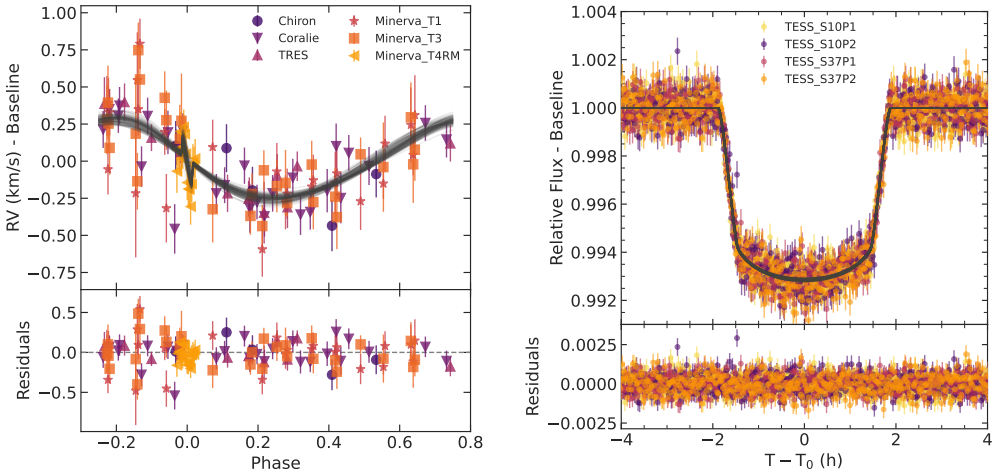

Figure 5. Left: A phase-folded radial velocity model of TOI-778 b from our `AllesFitter` analysis with the Rossiter-Mclaughlin effect. Each radial velocity instrument's data is shown, with CHIRON in violet circles, CORALIE in purple down arrows, TRES in burgundy triangles, MINERVA-Australis Telescope 1 in pink stars, MINERVA-Australis Telescope 3 in orange squares and MINERVA-Australis Telescope 4 in yellow left arrows. 100 randomly drawn posterior radial velocity models are drawn out in grey lines. Residual velocities are also shown for reference. Right: Phase-folded Light curve model for the TOI-778 b just from TESS data. Phase-folded Light curve models for the ground-based follow-up is plotted in Figure 6.

use all ground-based photometric observations of TOI-778 that had full transits of TOI-778 b. These facilities included the NGTS, PEST, LCO, Mt. Kent, and Mt. Stuart observations. We used all radial velocity measurements taken from MINERVA-Australis, TRES, CORALIE, and CHIRON. These radial velocities include the data from MINERVA-Australis that were taken during the Rossiter-Mclaughlin observation on June 4, 2020. TOI-778's stellar radius, mass and effective temperature are used within the `Allesfitter` analysis, as these values are needed for deriving the planetary mass, radius, and equilibrium temperature.

Since `Allesfitter` utilises priors for its fitting routine for a more accurate analysis, we assigned priors for values to be fitted during the analysis. The priors used for our analysis can be found in Table 3 and Table 4. For each of our light curves, we calculated the quadratic limb darkening coefficients used by Eastman et al. (2013), an interpolation of the quadratic limb darkening tables derived by Claret & Bloemen (2011). These calculated values were then used as median values for priors used within the `Allesfitter` analysis. Since the NGTS has a unique Band-pass filter, we set its quadratic limb darkening coefficients to both 0.5. We also applied a prior on the dilution parameter (D_0). In `Allesfitter`, $D_0 = 1 -$ CROWDSAP. CROWDSAP is defined to be a parameter that corrects the target star's flux, accounting for crowding from other stars in the target field. We used the CROWDSAP value from the *TESS* SPOC light curve meta data. The orbital period, transit mid-time and planet radius values were taken from NASA's Exoplanet Follow-up Observing Program database and were incorporated for the planet-to-star radius ratio ($R_p/R_\star$), the ratio of the sum of the planet and star radii to the semi-major axis ($(R_\star + R_p)/a_p$), mid-transit time ($T_{0;b}$) and orbital period (P_p) priors. We used reasonable boundaries and starting values for other physical model parameters including the cosine of the inclination angle ($\cos i_p$), the radial velocity semi-amplitude (K), and eccentricity ($\sqrt{e_p}\cos\omega_p$ and $\sqrt{e_p}\sin\omega_p$). For the light curves we used priors for the flux error scaling ($\ln\sigma_{F_{inst}}$) and a radial velocity baseline offset (ΔRV_{inst}) and jitter term ($\log\sigma_{RV_{inst}}$) for each radial velocity instrument. Since we wanted to also model the Rossiter-McLaughlin effect with the global fit, we used our derived stellar rotational velocity ($v\sin(i)$) from Table 1 as a prior for the Rossiter-McLaughlin model.

We utilise `Allesfitter`'s nested sampling approach to sample the model posteriors by implementing the `dynesty` package (Speagle 2020). We used a dynamic nested sampling, with random walk sample, 1680 live points and a tolerance of 0.01. We ran our analysis

until a tolerance of 0.01 was achieved with the derived stellar, planetary and instrumental parameters shown in Table 3 and 4. Median values are shown in Table 3 and 4 along with their associated 1-sigma errors.

Table 3. Astrophysical parameters for TOI-778 b as derived by `Allesfitter`. Priors are shown as uniform $\mathcal{U}$(a,b) or normal $\mathcal{N}(\nu,\sigma)$. Parameters used for the transit and radial velocity fits that are not located in this Figure, can be found in Figure 4.

Parameter	Prior	Best-Fit
Planetary Parameters		
K_b(km/s)	$\mathcal{U}$(0,1)	0.267 ± 0.019
$R_p/R_\star$	$\mathcal{U}$(0,1)	0.08260 ± 0.00024
$(R_\star + R_p)/a_p$	$\mathcal{U}$(0.05,0.2)	0.1372 ± 0.0027
$\cos i$	$\mathcal{U}$(0,1)	0.0826 ± 0.0037
$T_{0;b}$ - 2450000 (BJD)	$\mathcal{N}$(8569.4484,0.0004)	8578.71604 ± 0.00015
P_b (d)	$\mathcal{N}$(4633751,0.00011)	4.6336115 ± 0.0000014
$\sqrt{e_b}\cos\omega_b$	$\mathcal{U}$(-0.3,0.3)	$0.220^{+0.053}_{-0.11}$
$\sqrt{e_b}\sin\omega_b$	$\mathcal{U}$(-0.3,0.3)	$0.235^{+0.039}_{-0.054}$
$R_\star/a_\mathrm{p}$		0.1268 ± 0.0025
$a_\mathrm{p}/R_\star$		$7.89^{+0.16}_{-0.15}$
$R_\mathrm{p}/a_\mathrm{p}$		0.01047 ± 0.00021
R_p ($\mathrm{R}_\oplus$)		15.07 ± 0.30
i_p (deg)		85.26 ± 0.21
e_p		0.101 ± 0.028
w_p (deg)		$47^{+19}_{-10.}$
R_p ($\mathrm{R_{jup}}$)		1.344 ± 0.027
M_p ($\mathrm{M_{jup}}$)		2.774 ± 0.204
a_p ($\mathrm{R}_\odot$)		13.19 ± 0.37
a_p (AU)		0.0613 ± 0.0017
$b_\mathrm{tra;p}$		0.601 ± 0.015
$T_\mathrm{tot;p}$ (hr)		$3.768^{+0.013}_{-0.012}$
$T_\mathrm{full;p}$ (hr)		2.897 ± 0.017
ρ_p (cgs)		766^{+54}_{-51}
g_p (cgs)		3810^{+340}_{-310}
$T_\mathrm{eq;p}$ (K)		1583 ± 47
Stellar Parameters		
$v \sin i$ (km/s)	$\mathcal{N}$(29,18)	49.9 ± 7.5
λ (deg)	$\mathcal{U}$(-180,180)	19.1 ± 9.6
$\rho_\star$ (cgs)		$0.432^{+0.027}_{-0.024}$

The resulting transit light curve model for the TESS and ground-based photometry can be found in Figure 5 and Figure 6 respectively. Figure 5 also includes the radial velocity model for TOI-778 b with our Doppler spectroscopy data. From our global analysis, TOI-778 b's orbital period is 4.6336115±0.0000015 days, in line with the 4.63361±0.00011 days found by *TESS* in Sector 10. It has a relatively large radial velocity semi-amplitude, with a 13-sigma detection of $\mathrm{K} = 267 \pm 19\ \mathrm{m\,s^{-1}}$. Given these parameter posteriors, and our estimates of the stellar mass, radius and their uncertainties given in Table 1, we derive a planetary mass and radius for TOI-778 b to be 2.774±0.204 M_J and 1.344±0.027 R_J respectively. With its radius, and orbital period, we confirm the planetary nature of TOI-778 b as a hot Jupiter.

TOI-778 b was found to have a statistically significant non-zero orbital eccentricity, of 0.101±0.028. With previous research showing that eccentric orbits can be due to hidden planetary companions (e.g. Wittenmyer et al. 2013; Trifonov et al. 2017; Boisvert et al. 2018; Wittenmyer et al. 2019) we additionally inspected the RV residuals with general Lomb-Scargle periodograms, but found no significant signal. We also performed an independent analysis of our radial velocity and photo-

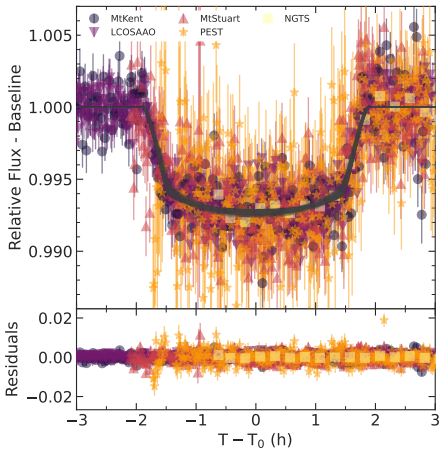

Figure 6. Right: Phase-folded Light curve model for TOI-778 b from the ground-based observations, including Mt. Kent (violet circles), Mt. Stuart (pink triangles), NGTS (yellow squares), LCO (purple down arrows) and PEST (orange stars). 100 randomly drawn posteriors are shown in grey, with the residuals of the fits shown in bottom plot.

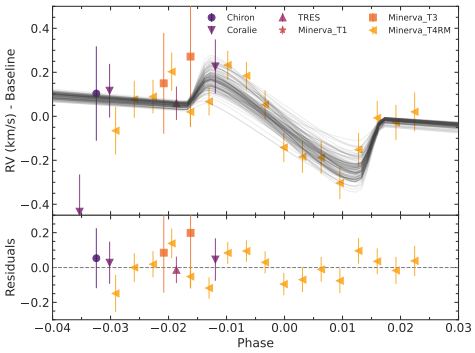

Figure 7. A phase-folded radial velocity model of the Rossiter-McLaughlin effect from TOI-778 b on TOI-778. Each radial velocity instrument's data is shown with CHIRON in violet circles, CORALIE in purple down arrows, TRES in burgundy triangles, MINERVA-Australis Telescope 3 in orange squares and MINERVA-Australis Telescope 4 in yellow left arrows. 100 randomly drawn posterior radial velocity models are drawn out in grey lines. Residual velocities are also shown for reference.

metric data through `EXOFASTv2` (Eastman et al. 2019; Eastman 2017), and found consistent results at the 1-σ level.

We also conducted a joint analysis on our Rossiter-Mclaughlin observation with the global fit. The resulting effect can clearly be seen in Figure 5 and 7. The global fit analysis yields a sky-projected spin-orbit angle of 19.1±9.6°. In addition, following Masuda & Winn (2020), we find the stellar inclination to be well aligned to the line of sight, with $I_\star > 50°$ at 3σ significance. This result is consistent with an aligned system and is discussed further in Section 5.

5. TOI-778 B IN CONTEXT

We have confirmed the planetary nature of TOI-778 b, detected by *TESS* in Sector 10 of its primary mission. It is a hot Jupiter with radius 1.344±0.027 R_J and mass 2.774±0.204 M_J orbiting a rapidly-rotating early-F star. In Figure 8 we plot TOI-778 b's mass and radius against other known transiting exoplanets with a mass measurement precision better than 20%. From this graph, it is apparent that TOI-778 b is somewhat inflated compared to other exoplanets with the same mass values.

The confirmation and mass measurement of TOI-778 b was challenging due to the relatively rapid $\sim$30 km s^{-1} rotation of its early-F type host star. Figure 9 shows

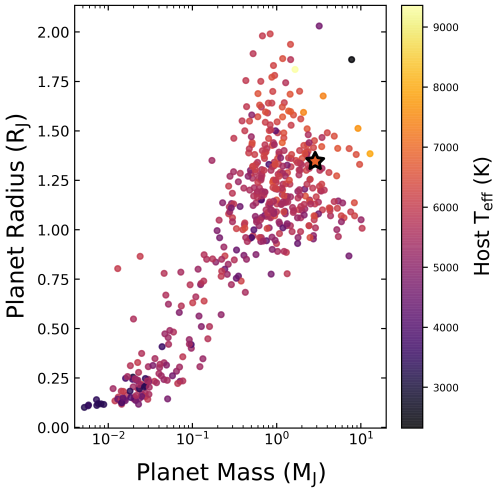

Figure 8. A mass-radius plot of all known transiting exoplanets with a measured mass precision better than 20%. TOI-778 b is shown as the star in the figure. All points, including our new exoplanet, are coloured according to their host star's effective temperature.

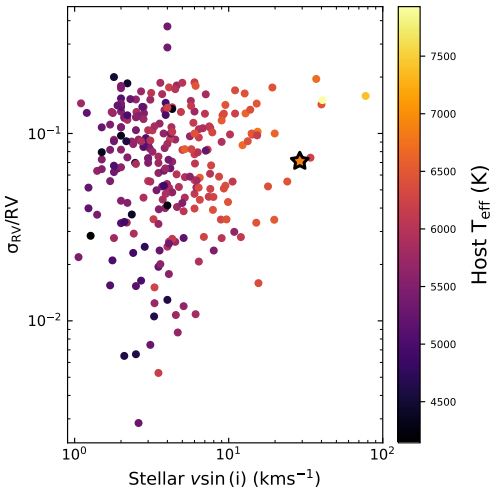

Figure 9. Host-star $v \sin i$ as a function of radial velocity amplitude precision, for 842 planets for which masses have been measured with a precision of better than 20%.

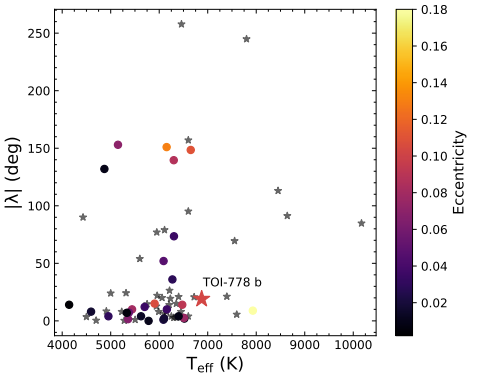

Figure 10. We show all known hot Jupiters ($R_p > 0.7$ R_J, $P_P < 10$ days) with obliquity measurements and plot those measurements against their host star's effective temperature. Points are coloured by the planet's orbital eccentricity, albeit planet's in circular orbits shown in grey stars. TOI-778 b is shown as the filled in star.

the stellar rotational velocity against the semi-amplitude radial velocity precision of all known exoplanets with a mass measurement precision better than 20%.

There are only five other planets that have been discovered with a mass precisions better than 20%, orbiting around a more rapidly rotating stars. These include CoRoT-11 b (Gandolfi et al. 2010), HAT-P-69 b (Zhou et al. 2019a), HATS-70 b (Zhou et al. 2019b), Kepler-1658 b (Chontos et al. 2019) and WASP-93 b (Hay et al. 2016). In the most extreme case, HAT-P-69 b was found around the rapidly rotating A star ($v \sin i = 77.44 \pm 0.56\,\mathrm{km\,s^{-1}}$), and achieved a semi-amplitude radial velocity precision of $K = 309 \pm 49\,\mathrm{m\,s^{-1}}$. Our results demonstrates how a facility like MINERVA-Australis, with an effective telescope radius of 1.20m, can be utilised to follow up and confirm planetary candidates around such rapidly rotating stars. The occurrence of such systems seems to be quite uncommon too, with Zhou et al. (2019c) discovering an occurrence rate in *TESS* data of only 0.43±0.15% for hot Jupiters orbiting main-sequence F stars, and 0.26±0.11% for A-type stars. These low occurrence rates for earlier-type stars are consistent with those found for their evolved kin (Grunblatt et al. 2019).

The rapid rotation, brightness ($V = 9.1$ mag), and large radius of the planet all work in favour of measuring the spin-orbit angle for this system. From Rossiter-McLaughlin observations of a transit of TOI-778 b, we find the planet's orbit to be aligned with the stellar rotation, with a host star sky-projected obliquity of 19.1±9.6 degrees.

An obliquity measurement can aid in better determining the origin and formation history of exoplanets, especially large and relatively close-in orbiting ones like TOI-778 b. Since the star's effective temperature ($T_{\rm eff}$ 7800 K) is beyond the Kraft break temperature of $\sim$ 6200 K, it is unlikely to have realigned from a high obliquity orbit (Kraft 1967). Thus we may be seeing the exoplanet's primordial obliquity, rather than the result of a secondary realignment. It therefore seems most likely that TOI-778 b sedately migrated through its host's disk, rather than reaching its current location through more chaotic means. Indeed, with a low obliquity angle and a stellar age of 2 Gyr, we can rule out migration mechanisms such as high-eccentricity, planet-planet scattering, Kozai–Lidov tidal and secular chaos migrations (Masset & Papaloizou 2003; Nagasawa et al. 2008b; Dawson & Johnson 2018). Figure 10 shows the planetary obliquity as a function of host star temperature with TOI-778 b and the sample of known hot Jupiters with obliquity measurements. From Figure 10, TOI-778 b joins a cohort of other hot Jupiters with well-aligned obliquities, suggesting that disk migration is the likely case of their evolution to their current positions.

6. CONCLUSION

During Sector 10 of *TESS*'s primary mission, an exoplanet candidate was discovered around the rapidly ro-

tating star HD 115447, also known as TOI-778. This 4.63 day signal was subsequently followed up by the exoplanetary community through transit observations from PEST, LCO, NGTS, Mount Kent and Mt. Stuart. Coinciding with these efforts, radial velocity measurements from TOI-778 were collected from MINERVA-Australis, TRES, CORALIE and CHIRON to then determine the exoplanetary nature of TOI-778.01. From our `AllesFitter` global model, we confirm the presence of the hot Jupiter TOI 778 b (1.344±0.027 R_J, 2.774±0.204 M_J). We conducted a Rossiter-Mclaughlin observation of TOI-778 b and discovered its spin-orbit angle to its host is 19.1±9.6°, which is consistent with an aligned planetary system. These results also highlight how smaller telescope arrays such as MINERVA-Australiscan lead the charge of confirming and characterising exoplanets around rapidly rotating stars.

ACKNOWLEDGMENTS

We respectfully acknowledge the traditional custodians of all lands throughout Australia, and recognise their continued cultural and spiritual connection to the land, waterways, cosmos, and community. We pay our deepest respects to all Elders, ancestors and descendants of the Giabal, Jarowair, and Kambuwal nations, upon whose lands the MINERVA-Australis facility at Mt Kent is situated.

MINERVA-Australis is supported by Australian Research Council LIEF Grant LE160100001, Discovery Grants DP180100972 and DP220100365, Mount Cuba Astronomical Foundation, and institutional partners University of Southern Queensland, UNSW Sydney, MIT, Nanjing University, George Mason University, University of Louisville, University of California Riverside, University of Florida, and The University of Texas at Austin.

This paper includes data collected at the Keck Telescopes. We recognise and acknowledge the cultural role and reverence that the summit of Maunakea has within the indigenous Hawaiian community. We are deeply grateful to have the opportunity to conduct observations from this mountain.

Funding for the *TESS* mission is provided by NASA's Science Mission directorate. We acknowledge the use of public *TESS* Alert data from pipelines at the *TESS* Science Office and at the *TESS* Science Processing Operations Center. This research has made use of the Exoplanet Follow-up Observation Program website, which is operated by the California Institute of Technology, under contract with the National Aeronautics and Space Administration under the Exoplanet Exploration Program. Resources supporting this work were provided by the NASA High-End Computing (HEC) Program through the NASA Advanced Supercomputing (NAS) Division at Ames Research Center for the production of the SPOC data products. This paper includes data collected by the *TESS* mission, which are publicly available from the Mikulski Archive for Space Telescopes (MAST).

Some of the observations in the paper made use of the High-Resolution Imaging instrument Zorro. Zorro was funded by the NASA Exoplanet Exploration Program and built at the NASA Ames Research Center by Steve B. Howell, Nic Scott, Elliott P. Horch, and Emmett Quigley. Data were reduced using a software pipeline originally written by Elliott Horch and Mark Everett. Zorro was mounted on the Gemini South telescope of the international Gemini Observatory, a program of NSF's OIR Lab, which is managed by the Association of Universities for Research in Astronomy (AURA) under a cooperative agreement with the National Science Foundation. on behalf of the Gemini partnership: the National Science Foundation (United States), National Research Council (Canada), Agencia Nacional de Investigación y Desarrollo (Chile), Ministerio de Ciencia, Tecnología e Innovación (Argentina), Ministério da Ciência, Tecnologia, Inovações e Comunicações (Brazil), and Korea Astronomy and Space Science Institute (Republic of Korea).

We thank the Swiss National Science Foundation (SNSF) and the Geneva University for their continuous support to our planet search programs. This work has been in particular carried out in the frame of the National Centre for Competence in Research *PlanetS* supported by the Swiss National Science Foundation (SNSF).
This publication makes use of The Data & Analysis Center for Exoplanets (DACE), which is a facility based at the University of Geneva (CH) dedicated to extrasolar planets data visualisation, exchange and analysis. DACE is a platform of the Swiss National Centre of Competence in Research (NCCR) PlanetS, federating the Swiss expertise in Exoplanet research. The DACE platform is available at https://dace.unige.ch.

This work makes use of observations from the LCOGT network.

J.T.C would like to thank BC and DN, and is supported by the Australian Government Research Training Program (RTP) Scholarship. T.F. acknowledges support from the University of California President's Postdoctoral Fellowship Program. A.J. and R.B. acknowledge support from ANID – Millennium Science Initia-

tive – ICN12_009. A.J. acknowledges additional support from FONDECYT project 1210718.

Facilities: Minerva-Australis, Euler1.2m (CORALIE), LCOGT, CHIRON

Software: `dynesty` (Speagle 2020), `ExoFAST` (Eastman 2017), `isochrones` (Morton 2015), `Allesfitter` (Günther & Daylan 2019, 2021)

APPENDIX

A. EXTRA FITTING INFORMATION

Table 4. Fitted parameters from the `Allesfitter` analysis for TOI-778's photometry and radial velocities curves.

Parameter	Prior	Best-Fit
Radial Velocity Model Parameters		
$\log \sigma_{\rm jitter}$ (RV Chiron)(km/s)	$\mathcal{U}$(-10,-1)	$-1.83^{+0.42}_{-0.55}$
$\log \sigma_{\rm jitter}$ (RV Coralie)(km/s)	$\mathcal{U}$(-10,-1)	$-2.32^{+0.26}_{-0.30}$
$\log \sigma_{\rm jitter}$ (RV TRES)(km/s)	$\mathcal{U}$(-10,-1)	$-6.4^{+2.5}_{-2.4}$
$\log \sigma_{\rm jitter}$ (RV Minerva;T1)(km/s)	$\mathcal{U}$(-10,-1)	$-4.2^{+2.1}_{-3.8}$
$\log \sigma_{\rm jitter}$ (RV Minerva;T3)(km/s)	$\mathcal{U}$(-10,-1)	-5.8 ± 2.7
$\log \sigma_{\rm jitter}$ (RV Minerva;T4RM)(km/s)	$\mathcal{U}$(-10,-1)	$-5.3^{+2.1}_{-3.0}$
offset CHIRON (km/s)	$\mathcal{U}$(-1.5,1.5)	0.080 ± 0.081
offset CORALIE (km/s)	$\mathcal{U}$(-7.3,-4.3)	$-5.784^{+0.024}_{-0.026}$
offset TRES (km/s)	$\mathcal{U}$(-1.3,1.6)	0.233 ± 0.036
offset $\mathrm{Minerva_{T1}}$ (km/s)	$\mathcal{U}$(-8.3,-5.3)	-6.730 ± 0.037
offset $\mathrm{Minerva_{T3}}$ (km/s)	$\mathcal{U}$(-8.3,-5.3)	-6.719 ± 0.033
offset $\mathrm{Minerva_{T4RM}}$ (km/s)	$\mathcal{U}$(-1.5,1.5)	-0.000 ± 0.030
Photometric Model Parameters		
$D_{0;\rm TESS}$	$\mathcal{N}(0.0127, 0.0001)$	0.012690 ± 0.000092
$q_{1;\rm TESS}$	$\mathcal{U}(0.166, 0.203)$	$0.1797^{+0.012}_{-0.0089}$
$q_{2;\rm TESS}$	$\mathcal{U}(0.293, 0.358)$	$0.324^{+0.022}_{-0.020}$
$q_{1;\rm MtKent}$		0.184005
$q_{2;\rm MtKent}$		0.325575
$q_{1;\rm LCOSAAO}$		0.135055
$q_{2;\rm LCOSAAO}$		0.325575
$q_{1;\rm LCOMcD}$		0.135055
$q_{2;\rm LCOMcD}$		0.325575
$q_{1;\rm MtStuart}$		0.25579
$q_{2;\rm MtStuart}$		0.337465
$q_{1;\rm PEST}$		0.319775
$q_{2;\rm PEST}$		0.32764
$q_{1;\rm NGTS}$	$\mathcal{U}(0, 1)$	$0.30^{+0.17}_{-0.13}$
$q_{2;\rm NGTS}$	$\mathcal{U}(0, 1)$	$0.33^{+0.32}_{-0.22}$
offset TESS	$\mathcal{U}(0.98, 1.02)$	$1.001^{+0.012}_{-0.014}$
$\ln \sigma_{\rm TESS}$ ($\ln$ rel.flux.)	$\mathcal{U}(-10, -3)$	-7.480 ± 0.013
offset Mount Kent	$\mathcal{U}(0.98, 1.02)$	0.999 ± 0.013
$\ln \sigma_{\rm MountKent}$ ($\ln$ rel.flux.)	$\mathcal{U}(-10, -3)$	-6.390 ± 0.042
offset LCO AAO	$\mathcal{U}(0.98, 1.02)$	1.000 ± 0.013
$\ln \sigma_{\rm LCOAAO}$ ($\ln$ rel.flux.)	$\mathcal{U}(-10, -3)$	-6.651 ± 0.034
offset LCO McD	$\mathcal{U}(0.98, 1.02)$	0.999 ± 0.013
$\ln \sigma_{\rm LCOMcD}$ ($\ln$ rel.flux.)	$\mathcal{U}(-10, -3)$	$-5.097^{+0.065}_{-0.060}$
offset Mount Stuart	$\mathcal{U}(0.98, 1.02)$	$1.002^{+0.012}_{-0.014}$

Table 4 *continued*

Table 4 *(continued)*

Parameter	Prior	Best-Fit
$\ln \sigma_{\rm MountStuart}$ (ln rel.flux.)	$\mathcal{U}(-10,-3)$	-6.032 ± 0.037
offset PEST	$\mathcal{U}(0.98,1.02)$	$1.001^{+0.013}_{-0.013}$
$\ln \sigma_{\rm PEST}$ (ln rel.flux.)	$\mathcal{U}(-10,-3)$	-5.562 ± 0.029
offset NGTS	$\mathcal{U}(0.98,1.02)$	$1.000^{+0.013}_{-0.013}$
$\ln \sigma_{\rm NGTS}$ (ln rel.flux.)	$\mathcal{U}(-10,-3)$	-5.345 ± 0.014
$\delta_{\rm tr;undil;TESS;S10P1}$ (ppt)		0.007239 ± 0.000029
$\delta_{\rm tr;dil;TESS;S10P1}$ (ppt)		0.007147 ± 0.000029
$\delta_{\rm tr;undil;TESS;S10P2}$ (ppt)		0.007240 ± 0.000028
$\delta_{\rm tr;dil;TESS;S10P2}$ (ppt)		0.007149 ± 0.000027
$\delta_{\rm tr;undil;TESS;S37P1}$ (ppt)		$0.007238^{+0.000028}_{-0.000030}$
$\delta_{\rm tr;dil;TESS;S37P1}$ (ppt)		$0.007147^{+0.000028}_{-0.000029}$
$\delta_{\rm tr;undil;TESS;S37P2}$ (ppt)		0.007241 ± 0.000029
$\delta_{\rm tr;dil;TESS;S37P2}$ (ppt)		0.007149 ± 0.000028
$\delta_{\rm tr;MtKent}$ (ppt)		0.007246 ± 0.000025
$\delta_{\rm tr;LCOSAAO}$ (ppt)		0.007175 ± 0.000028
$\delta_{\rm tr;LCOMcD}$ (ppt)		0.007176 ± 0.000027
$\delta_{\rm tr;MtStuart}$ (ppt)		0.007333 ± 0.000027
$\delta_{\rm tr;PEST}$ (ppt)		0.007401 ± 0.000027
$\delta_{\rm tr;NGTS}$ (ppt)		0.00739 ± 0.00014
$u_{1;\rm TESS;S10P1}$		0.276 ± 0.018
$u_{2;\rm TESS;S10P1}$		$0.150^{+0.017}_{-0.019}$
$u_{1;\rm NGTS}$		$0.35^{+0.28}_{-0.23}$
$u_{2;\rm NGTS}$		$0.17^{+0.30}_{-0.32}$

REFERENCES

Addison, B., Wright, D. J., Wittenmyer, R. A., et al. 2019, PASP, 131, 115003, doi: 10.1088/1538-3873/ab03aa

Addison, B. C., Tinney, C. G., Wright, D. J., et al. 2013, ApJL, 774, L9, doi: 10.1088/2041-8205/774/1/L9

Addison, B. C., Wang, S., Johnson, M. C., et al. 2018, AJ, 156, 197, doi: 10.3847/1538-3881/aade91

Addison, B. C., Wright, D. J., Nicholson, B. A., et al. 2021, MNRAS, 502, 3704, doi: 10.1093/mnras/staa3960

Albrecht, S., Winn, J. N., Johnson, J. A., et al. 2012, ApJ, 757, 18, doi: 10.1088/0004-637X/757/1/18

Anderson, D. R., Temple, L. Y., Nielsen, L. D., et al. 2018, arXiv e-prints, arXiv:1809.04897. https://arxiv.org/abs/1809.04897

Baranne, A., Queloz, D., Mayor, M., et al. 1996, A&AS, 119, 373

Barbary, K. 2016, The Journal of Open Source Software, 1, 58, doi: 10.21105/joss.00058

Barnes, S. I., Gibson, S., Nield, K., & Cochrane, D. 2012, in Society of Photo-Optical Instrumentation Engineers (SPIE) Conference Series, Vol. 8446, Ground-based and Airborne Instrumentation for Astronomy IV, ed. I. S. McLean, S. K. Ramsay, & H. Takami, 844688, doi: 10.1117/12.926527

Beaugé, C., & Nesvorný, D. 2012, ApJ, 751, 119, doi: 10.1088/0004-637X/751/2/119

Bertin, E., & Arnouts, S. 1996, A&AS, 117, 393, doi: 10.1051/aas:1996164

Blanco-Cuaresma, S. 2019, MNRAS, 486, 2075, doi: 10.1093/mnras/stz549

Blanco-Cuaresma, S., Soubiran, C., Heiter, U., & Jofré, P. 2014, A&A, 569, A111, doi: 10.1051/0004-6361/201423945

Böhm-Vitense, E. 2007, AJ, 133, 1903, doi: 10.1086/512124

Boisvert, J. H., Nelson, B. E., & Steffen, J. H. 2018, MNRAS, 480, 2846, doi: 10.1093/mnras/sty2023

Bowler, B. P., Johnson, J. A., Marcy, G. W., et al. 2010, ApJ, 709, 396, doi: 10.1088/0004-637X/709/1/396

Brown, T. M., Baliber, N., Bianco, F. B., et al. 2013, PASP, 125, 1031, doi: 10.1086/673168

Bryant, E. M., Bayliss, D., McCormac, J., et al. 2020, MNRAS, 494, 5872, doi: 10.1093/mnras/staa1075

Buchhave, L. A., Bakos, G. Á., Hartman, J. D., et al. 2010, ApJ, 720, 1118, doi: 10.1088/0004-637X/720/2/1118

Butler, R. P., Marcy, G. W., Williams, E., Hauser, H., & Shirts, P. 1997, ApJL, 474, L115, doi: 10.1086/310444

Campbell, B., Walker, G. A. H., & Yang, S. 1988, ApJ, 331, 902, doi: 10.1086/166608

Cannon, A. J., & Pickering, E. C. 1993, VizieR Online Data Catalog, III/135A
Chatterjee, S., Ford, E. B., Matsumura, S., & Rasio, F. A. 2008, ApJ, 686, 580, doi: 10.1086/590227
Chontos, A., Huber, D., Latham, D. W., et al. 2019, AJ, 157, 192, doi: 10.3847/1538-3881/ab0e8e
Ciardi, D. R., Beichman, C. A., Horch, E. P., & Howell, S. B. 2015, ApJ, 805, 16, doi: 10.1088/0004-637X/805/1/16
Claret, A., & Bloemen, S. 2011, A&A, 529, A75, doi: 10.1051/0004-6361/201116451
Collier Cameron, A., Guenther, E., Smalley, B., et al. 2010, MNRAS, 407, 507, doi: 10.1111/j.1365-2966.2010.16922.x
Collins, K. A., Kielkopf, J. F., Stassun, K. G., & Hessman, F. V. 2017, AJ, 153, 77, doi: 10.3847/1538-3881/153/2/77
Cutri, R. M., Skrutskie, M. F., van Dyk, S., et al. 2003, VizieR Online Data Catalog, II/246
Davis, A. B., Wang, S., Jones, M., et al. 2020, AJ, 160, 229, doi: 10.3847/1538-3881/aba49d
Dawson, R. I., & Johnson, J. A. 2018, ARA&A, 56, 175, doi: 10.1146/annurev-astro-081817-051853
Dekany, R., Roberts, J., Burruss, R., et al. 2013, ApJ, 776, 130, doi: 10.1088/0004-637X/776/2/130
Eastman, J. 2017, EXOFASTv2: Generalized publication-quality exoplanet modeling code, Astrophysics Source Code Library. http://ascl.net/1710.003
Eastman, J., Gaudi, B. S., & Agol, E. 2013, PASP, 125, 83, doi: 10.1086/669497
Eastman, J. D., Rodriguez, J. E., Agol, E., et al. 2019, arXiv e-prints, arXiv:1907.09480. https://arxiv.org/abs/1907.09480
Fűrész, G. 2008, PhD thesis, Univ. of Szeged, Hungary
Furlan, E., Ciardi, D. R., Everett, M. E., et al. 2017, AJ, 153, 71, doi: 10.3847/1538-3881/153/2/71
Gaia Collaboration, Prusti, T., de Bruijne, J. H. J., et al. 2016, A&A, 595, A1, doi: 10.1051/0004-6361/201629272
Gaia Collaboration, Brown, A. G. A., Vallenari, A., et al. 2018, A&A, 616, A1, doi: 10.1051/0004-6361/201833051
Gaidos, E., Hirano, T., Beichman, C., et al. 2022, MNRAS, 509, 2969, doi: 10.1093/mnras/stab3107
Gandolfi, D., Hébrard, G., Alonso, R., et al. 2010, A&A, 524, A55, doi: 10.1051/0004-6361/201015132
Grunblatt, S. K., Huber, D., Gaidos, E., et al. 2019, AJ, 158, 227, doi: 10.3847/1538-3881/ab4c35
Günther, M. N., & Daylan, T. 2019, Allesfitter: Flexible Star and Exoplanet Inference From Photometry and Radial Velocity, Astrophysics Source Code Library. http://ascl.net/1903.003
—. 2021, ApJS, 254, 13, doi: 10.3847/1538-4365/abe70e
Hay, K. L., Collier-Cameron, A., Doyle, A. P., et al. 2016, MNRAS, 463, 3276, doi: 10.1093/mnras/stw2090
Hayward, T. L., Brandl, B., Pirger, B., et al. 2001, PASP, 113, 105, doi: 10.1086/317969
Heitzmann, A., Zhou, G., Quinn, S. N., et al. 2021, ApJL, 922, L1, doi: 10.3847/2041-8213/ac3485
Henry, G. W., Marcy, G. W., Butler, R. P., & Vogt, S. S. 2000, ApJL, 529, L41, doi: 10.1086/312458
Høg, E., Fabricius, C., Makarov, V. V., et al. 2000, A&A, 355, L27
Horner, J., Kane, S. R., Marshall, J. P., et al. 2020, PASP, 132, 102001, doi: 10.1088/1538-3873/ab8eb9
Houk, N., & Smith-Moore, M. 1988, Michigan Catalogue of Two-dimensional Spectral Types for the HD Stars. Volume 4, Declinations -26.0 to -12.0., Vol. 4
Ida, S., & Lin, D. N. C. 2004, ApJ, 616, 567, doi: 10.1086/424830
—. 2005, ApJ, 626, 1045, doi: 10.1086/429953
Jenkins, J. M., Twicken, J. D., McCauliff, S., et al. 2016, in Proc. SPIE, Vol. 9913, Software and Cyberinfrastructure for Astronomy IV, 99133E, doi: 10.1117/12.2233418
Jensen, E. 2013, Tapir: A web interface for transit/eclipse observability. http://ascl.net/1306.007
Johnson, J. A., Butler, R. P., Marcy, G. W., et al. 2007, ApJ, 670, 833, doi: 10.1086/521720
Jones, M. I., Brahm, R., Wittenmyer, R. A., et al. 2017, A&A, 602, A58, doi: 10.1051/0004-6361/201630278
Jones, M. I., Jenkins, J. S., Brahm, R., et al. 2016, A&A, 590, A38, doi: 10.1051/0004-6361/201628067
Jordán, A., Brahm, R., Espinoza, N., et al. 2020, AJ, 159, 145, doi: 10.3847/1538-3881/ab6f67
Kiefer, F. 2019, A&A, 632, L9, doi: 10.1051/0004-6361/201936942
Kossakowski, D., Espinoza, N., Brahm, R., et al. 2019, MNRAS, 490, 1094, doi: 10.1093/mnras/stz2433
Kozai, Y. 1962, AJ, 67, 591, doi: 10.1086/108790
Kraft, R. P. 1967, ApJ, 150, 551, doi: 10.1086/149359
Kunimoto, M., & Matthews, J. M. 2020, AJ, 159, 248, doi: 10.3847/1538-3881/ab88b0
Latham, D. W., Mazeh, T., Stefanik, R. P., Mayor, M., & Burki, G. 1989, Nature, 339, 38, doi: 10.1038/339038a0
Li, D., Mustill, A. J., & Davies, M. B. 2019a, MNRAS, 488, 1366, doi: 10.1093/mnras/stz1794
Li, J., Tenenbaum, P., Twicken, J. D., et al. 2019b, PASP, 131, 024506, doi: 10.1088/1538-3873/aaf44d
Lidov, M. L. 1962, Planet. Space Sci., 9, 719, doi: 10.1016/0032-0633(62)90129-0
Lin, D. N. C., Bodenheimer, P., & Richardson, D. C. 1996, Nature, 380, 606, doi: 10.1038/380606a0
Lund, M. B. 2021 submitted, MNRAS

Masset, F. S., & Papaloizou, J. C. B. 2003, ApJ, 588, 494, doi: 10.1086/373892
Masuda, K., & Winn, J. N. 2020, AJ, 159, 81, doi: 10.3847/1538-3881/ab65be
Mayor, M., & Queloz, D. 1995, Nature, 378, 355, doi: 10.1038/378355a0
McCormac, J., Pollacco, D., Skillen, I., et al. 2013, PASP, 125, 548, doi: 10.1086/670940
McCully, C., Volgenau, N. H., Harbeck, D.-R., et al. 2018, in Society of Photo-Optical Instrumentation Engineers (SPIE) Conference Series, Vol. 10707, Software and Cyberinfrastructure for Astronomy V, ed. J. C. Guzman & J. Ibsen, 107070K, doi: 10.1117/12.2314340
Morton, T. D. 2015, isochrones: Stellar model grid package. http://ascl.net/1503.010
Nagasawa, M., & Ida, S. 2011, ApJ, 742, 72, doi: 10.1088/0004-637X/742/2/72
Nagasawa, M., Ida, S., & Bessho, T. 2008a, ApJ, 678, 498, doi: 10.1086/529369
—. 2008b, ApJ, 678, 498, doi: 10.1086/529369
Nielsen, L. D., Bouchy, F., Turner, O., et al. 2019, A&A, 623, A100, doi: 10.1051/0004-6361/201834577
Plavchan, P., Barclay, T., Gagné, J., et al. 2020, Nature, 582, 497, doi: 10.1038/s41586-020-2400-z
Pollack, J. B., Hubickyj, O., Bodenheimer, P., et al. 1996, Icarus, 124, 62, doi: 10.1006/icar.1996.0190
Preibisch, T., Balega, Y., Hofmann, K.-H., Weigelt, G., & Zinnecker, H. 1999, NewA, 4, 531, doi: 10.1016/S1384-1076(99)00042-1
Queloz, D., Mayor, M., Udry, S., et al. 2001, The Messenger, 105, 1
Quinn, S. N., Bakos, G. Á., Hartman, J., et al. 2012, ApJ, 745, 80, doi: 10.1088/0004-637X/745/1/80
Ricker, G. R., Winn, J. N., Vanderspek, R., et al. 2015, Journal of Astronomical Telescopes, Instruments, and Systems, 1, 014003, doi: 10.1117/1.JATIS.1.1.014003
Rodríguez Martínez, R., Gaudi, B. S., Rodriguez, J. E., et al. 2020, AJ, 160, 111, doi: 10.3847/1538-3881/ab9f2d
Siverd, R. J., Collins, K. A., Zhou, G., et al. 2018, AJ, 155, 35, doi: 10.3847/1538-3881/aa9e4d
Smith, A. M. S., Eigmüller, P., Gurumoorthy, R., et al. 2020, Astronomische Nachrichten, 341, 273, doi: 10.1002/asna.202013768
Speagle, J. S. 2020, MNRAS, 493, 3132, doi: 10.1093/mnras/staa278
Stassun, K. G., Oelkers, R. J., Paegert, M., et al. 2019, AJ, 158, 138, doi: 10.3847/1538-3881/ab3467
Tanaka, H., Takeuchi, T., & Ward, W. R. 2002, ApJ, 565, 1257, doi: 10.1086/324713
Temple, L. Y., Hellier, C., Anderson, D. R., et al. 2019, MNRAS, 490, 2467, doi: 10.1093/mnras/stz2632
Tinney, C. G., Butler, R. P., Marcy, G. W., et al. 2001, ApJ, 551, 507, doi: 10.1086/320097
Tokovinin, A., Fischer, D. A., Bonati, M., et al. 2013, PASP, 125, 1336, doi: 10.1086/674012
Trifonov, T., Kürster, M., Zechmeister, M., et al. 2017, A&A, 602, L8, doi: 10.1051/0004-6361/201731044
Twicken, J. D., Catanzarite, J. H., Clarke, B. D., et al. 2018, PASP, 130, 064502, doi: 10.1088/1538-3873/aab694
Virtanen, P., Gommers, R., Oliphant, T. E., et al. 2020, Nature Methods, 17, 261, doi: 10.1038/s41592-019-0686-2
Wang, S., Jones, M., Shporer, A., et al. 2019, AJ, 157, 51, doi: 10.3847/1538-3881/aaf1b7
Wheatley, P. J., West, R. G., Goad, M. R., et al. 2018, MNRAS, 475, 4476, doi: 10.1093/mnras/stx2836
Wittenmyer, R. A., Bergmann, C., Horner, J., Clark, J., & Kane, S. R. 2019, MNRAS, 484, 4230, doi: 10.1093/mnras/stz236
Wittenmyer, R. A., Horner, J., Carter, B. D., et al. 2018, arXiv e-prints, arXiv:1806.09282. https://arxiv.org/abs/1806.09282
Wittenmyer, R. A., Tinney, C. G., Butler, R. P., et al. 2011, ApJ, 738, 81, doi: 10.1088/0004-637X/738/1/81
Wittenmyer, R. A., Wang, S., Horner, J., et al. 2013, ApJS, 208, 2, doi: 10.1088/0067-0049/208/1/2
—. 2020, MNRAS, 492, 377, doi: 10.1093/mnras/stz3436
Wizinowich, P., Acton, D. S., Shelton, C., et al. 2000, PASP, 112, 315, doi: 10.1086/316543
Wright, J. T., Marcy, G. W., Howard, A. W., et al. 2012, ApJ, 753, 160, doi: 10.1088/0004-637X/753/2/160
Wyttenbach, A., Mollière, P., Ehrenreich, D., et al. 2020, A&A, 638, A87, doi: 10.1051/0004-6361/201937316
Zhou, G., Huang, C. X., Bakos, G. Á., et al. 2019a, AJ, 158, 141, doi: 10.3847/1538-3881/ab36b5
Zhou, G., Bakos, G. Á., Bayliss, D., et al. 2019b, AJ, 157, 31, doi: 10.3847/1538-3881/aaf1bb
Zhou, G., Huang, C. X., Bakos, G. Á., et al. 2019c, AJ, 158, 141, doi: 10.3847/1538-3881/ab36b5
Zhou, G., Winn, J. N., Newton, E. R., et al. 2020, ApJL, 892, L21, doi: 10.3847/2041-8213/ab7d3c

The marks I left upon this world will wash away in time
In time, and so it ends
In time, it all finds an end.

– Parkway Drive

5 DISCUSSION AND CONCLUSIONS

5.1 The GALAH Survey: using galactic archaeology to refine our knowledge of *TESS* target stars

A key research theme in exoplanetary science can be described as "know the star, know the planet." So with the 2018 launch of the *TESS* mission and its extensive survey of relatively nearby stars and planets amenable to detailed studies, this thesis aims to provide a reliable, accurate and extended catalogue of the physical properties and chemical abundances of potential planet-hosting stars. In achieving this aim, a key outcome of this thesis is the improved stellar radius measurements that enables more accurate estimates of planetary radii and other related physical characteristics. The median uncertainty of stellar radii from this work is 2.8% compared to the seventh version of the TIC, which contained both misclassified giant stars and stars with substantial radius uncertainties of more than 10%. This thesis also includes mass estimates for all stars, including giant and evolved stars absent from the TIC because they

are not considered priority targets for the *TESS* mission.

I cross-matched the galactic archaeology survey catalogue GALAH with other surveys, such as *Gaia* DR2, and the TIC, to create a set of input values for the isochrone modelling software isochrones (Morton, 2015). This provides a catalogue of stellar masses, radii, ages, luminosities, and habitable zones, along with GALAH $T_{\rm eff}$, log g, [Fe/H], [α/Fe] and individual abundances for over 47,000 stars with refined mass and radius values down to a median precision of 5% and 4% respectively. The large improvement of stellar radii is largely due to the incorporation of *Gaia* DR2 parallax values, along with stellar magnitudes, that allow simultaneous spectral energy distribution fitting to be done, alongside of the isochrone modelling, to better constrain the physical parameters of our selected stars. Known as the GALAH-*TESS* catalogue, it is now being incorporated into NASA Exoplanet Science Institute's Exoplanet Followup database, the primary database for stellar and planetary characteristics for TOIs.

In addition to the GALAH-*TESS* catalogue, this thesis provides an improved characterisation for 13 candidate and confirmed exoplanets, where the results suggest that the systems discovered by Community *TESS* members including CTOI 201256771, CTOI 220402290 and CTOI 300903537 are more likely stellar or brown-dwarf companions.

Using the newly refined stellar mass and radius values, it was suggested that an "Earth-like" planet i.e. 1 $M_{\oplus}$, 1 $R_{\oplus}$, derived by one catalogue, might not "Earth-like" from using another set of stellar parameters from another catalogue. By using the GALAH values as this base for the "Earth-like" world, if one was to use the TIC values instead, roughly 85% of these fictitious "Earth-like" worlds would fall within 10% of Earth mass and radius values. For the other 15%, these planets would have different compositions from the Earth, ranging from scaled-up Enceladus-like planets to the possible remnant cores of Jovian-like planets. From this work, it is then important to

better contexualise how stellar parameters from one observation/survey are different or similar to one another. Large changes in these values then change the planetary mass and radius, as well as other properties of an exoplanet, such as the likely composition, which then influences the exoplanet's potential habitability. Thus consistency of stellar parameters across different surveys and teams are important to better understand the true nature of exoplanets and their underlying properties and populations.

The molar ratios of C/O, Mg/Si, and Fe/Si are critical in geological models to reliably constrain the composition and thus potential habitability of rocky exoplanets. These molar ratios were calculated for the 47,000 stars to then forward predict what types of rocky planets TESS is likely to uncover in our local neighbourhood. Using the measured C, O, Mg, Si and Fe abundances within 8800 stars, I determined that nearly 54% of GALAH-*TESS* stars have C/O and Mg/Si values that would suggest that they might potentially host planets that would be similar in geological composition to Earth and Mars. This implies that there are 46% of stars that will host planets unlike any worlds within our Solar system. The vast majority of this 46% have the potential to host silicon-rich rocky exoplanets, indicating that these likely found worlds could contain pyroxene + SiO within both their upper and lower mantles. Only 1% of GALAH-TESS stars had C/O molar ratios greater than 0.8, indicating that they might host rocky worlds with carbon-rich mantles of graphite and carbides including SiC. Thus, this thesis shows the necessity in the exoplanet community to better understand the geological processes, evolution and habitability of silicon-rich worlds, with almost half of the rocky worlds within the Milky Way having such compositions.

5.2 The GALAH Survey: Improving our understanding of confirmed and candidate planetary systems with large stellar surveys

There were several advancements in stellar surveys during this thesis that could be taken advantage of. GALAH released their third data release that included observed fields that overlapped with the fields observed by K2 and the *TESS* continuous view-

ing zone. With stellar parameters from dedicated planet surveys now available, the number of confirmed and candidate exoplanets within the GALAH survey increased from 11 confirmed and candidate exoplanet hosts to 279. *Gaia* also released a new data release, with an Early Data Release 3, that contained improvements in parallax and magnitude measurements, which would then improve the stellar parameters from isochrone and SED models. Furthermore NASA's Exoplanet Archive updated their database, so that more than one entry was available per exoplanet. This meant that users can pick and choose what their preferred stellar and/or planetary parameters are for a particular system. I could then exploit this through a weighted-mean approach, combining observables such as the semi-amplitudes of radial velocities or flux measurements from planet transits, to then increase the precision of an exoplanet's mass and radius. As argued in Chapter 1, an exoplanet's mass and radius will indicate a zeroth order bulk composition for an exoplanet. With better precision, a planet's bulk density will be further constrained to better understand its potential geological and chemical composition.

Using the plethora of available stellar surveys, it was possible to cross-match GALAH DR3, with *Gaia* EDR3 for every known confirmed and candidate planet host within GALAH DR3. Some cross-matched results have been used to derive stellar masses, radii, ages, luminosities and habitable zones, through ISOCHRONES for 279 stars. Output stellar parameters have been used, alongside the weighted mean values of an exoplanet's transit depth, orbital inclination, orbital period, orbital eccentricity, and radial velocity semi-amplitude where available, to better constrain an exoplanet's mass and radius values. Using this methodology, I recharacterised 105 confirmed exoplanets, along with 146 K2 candidates, 95 TOIs and 52 CTOIs.

With the newly derived planetary mass and radius values, this thesis cast doubt on the planetary nature of twelve CTOIs, 5 TOIs and 18 K2 candidates, all having radii beyond any known exoplanet to date ($R_P > 2\ R_J$). Candidates are then more akin to stellar companions, rather than being exoplanetary in nature. The increase

of precision in planetary mass and radius included exoplanets that are considered to be super-Earths, including CoRoT-7 b, K2-106 b, K2-131 b, K2-216 b, K2-314 b and WASP-47 e. All six exoplanets have revised radii indicative of them falling into the super-Earth "radius-gap" a scarcity of exoplanets with radii 1.5 $R_\oplus \leq R \leq 2\ R_\oplus$. This thesis includes the most precise mass and radius values for K2-106 b and CoRoT-7 b to date, assisting exogeologists to better determine the geological compositions of these worlds. For example K2-106 b's mass and radius precision have been improved to 7.4% and 2.4% respectively with its mass and radius now being 1.71±0.04 $R_\oplus$ and 8.39 ± 0.62 $M_\oplus$, with a density 1.67 times greater than that of earth, now being 9.22 ± 0.93 gcm^{-3}. A simple three body composition model, shown in Figure 5.1 suggests that K2-106 b's core mass fraction could be as high as 55%, with an iron core contributing to 63% of its radius (Zeng et al., 2016; Zeng & Sasselov, 2013). In contrast, CoRoT-7 b's new radius and mass measurements, also the most precise to date, of 1.68±0.04 $R_\oplus$ and 4.94±0.41 $M_\oplus$ respectively, now indicate that the molten super-Earth likely harbours an atmosphere to accommodate such a planetary radius compared to its mass.

Through the use of the stellar rotation velocities, and deriving predicted radial velocity signals for candidate and confirmed exoplanets with no known mass measurements, this thesis includes results that show that it will be difficult to detect the mass of most exoplanets within the GALAH catalogue. Most host stars' $v \sin i$ values are above 5 km s^{-1}, however the planet's predicted RV signal is less than 5 m s^{-1}. For context, only 19 confirmed exoplanets have RV signals less than 5 m s^{-1} orbiting stars with $v \sin i$ values greater than 5 km s^{-1}. In the extreme case of exoplanet candidate TOI-1219.01 orbiting a rapidly rotating star ($v \sin i$ = 58.3±2.5 km s^{-1}), this thesis has predicted that it will take 14,000 observations with current spectrographs to obtain a 1-sigma mass detection of this exoplanet. Thus catalogs such as GALAH can assist exoplanetary follow-up teams to better prioritise the best targets to follow-up with ground-based radial velocity facilities.

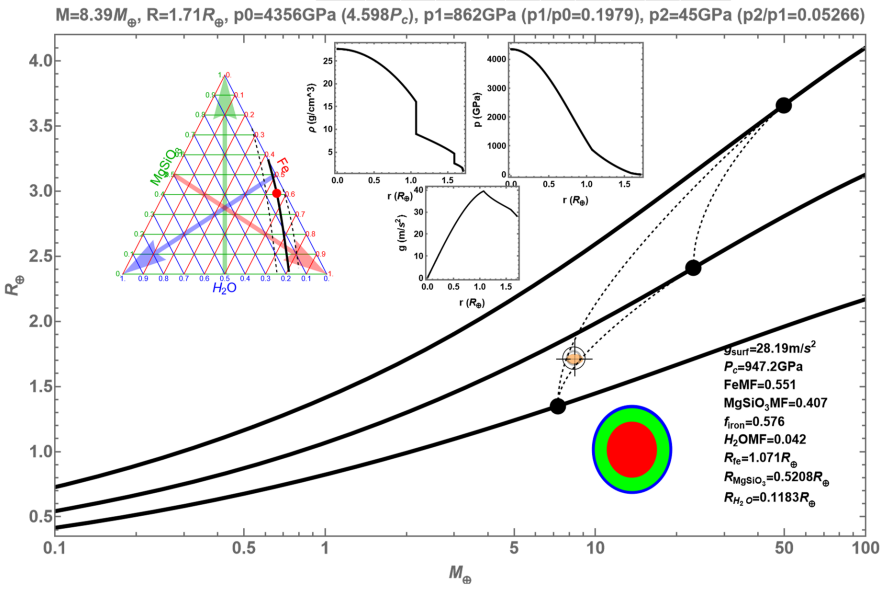

Figure 5.1: Using Zeng et al. (2016); Zeng & Sasselov (2013) models, this plot shows the potential composition of K2-106 b with this thesis' new mass and radius values. K2-106 b is shown in the yellow dot, with uncertainties plotted as cross-hairs. Solid black lines suggest a planetary body made from 100% Iron (bottom), 100% $MgSiO_2$ (middle) and 100% H_2O (top). Composition model of K2-106 b is found in the lower right-hand corner.

Through the analysis of stellar chemo-kinematic and dynamical data from GALAH DR3 and *Gaia* EDR3, the results of this thesis show that there are known planet hosts within GALAH DR3 that are thick-disk stars. Three confirmed planet hosts, including NGTS-4, K2-183 and K2-337 along with candidate host stars TOI-810 and EPIC 211064647 have iron abundances, and alpha abundances, along with radial and azimuthal velocities that suggest these stars are members of the Milky Way's thick-disk. There are nearly thirty more planetary systems that have either chemical abundances or stellar kinematics that also suggest that are also thick-disk members, but more research is needed to determine their stellar populations. By knowing more thick-disk hosts, we will be able to better determine the statistics of planetary architectures across stellar populations and determine the habitability of systems across the Galaxy.

It was suggested during this thesis that differences between short-period planet populations might be contained within the chemical abundances of their host stars. With chemical abundances from GALAH, this thesis has shown that there does not seem

to be a statistical difference between the chemical properties of stars that host hot-Neptunes and those that host hot-rocky worlds. Thus, following the conclusions of Dai et al. (2021) and Winn et al. (2017), the more robust chemical abundance results of 29 elemental abundances show that there is a possibility that short-period rocky worlds might be the remnant cores of hotter-gaseous Neptune worlds. The statistical analysis conducted suggests only a slight population difference in yttrium, cerium and aluminium. However, with these three elements, along with a relatively small sample size, there is still more research to be done to determine the similarities in such populations, and thus determine the origins and evolution of short-period exoplanets.

5.3 Spinning up a Daze: *TESS* uncovers a hot-Jupiter hosted by the rapid-rotator TOI-778 b

Chapter 4 shows that deriving the masses for both confirmed and candidate exoplanets will be immensely challenging due to their host star's rotational velocity. So much so, that for one particular exoplanet candidate, TOI-1219.01, we would need over 14,000 independent radial velocity measurements to have a 1-sigma mass detection. This realisation drove follow up *TESS* observations of targets around rapidly rotating stars with Minerva-Australis. This thesis confirmed the discovery of an exoplanet orbiting around the rapidly rotating ($v \sin(i) = 28$ km s^{-1}) early F dwarf HD 115447 (TOI-778). The hot Jupiter was discovered initially through Sector 10 of the *TESS* mission, designated TOI-778.01, showing how global, cooperative and collaborative the exoplanetary scientific community can be. Through the collection of the radial velocity measurements at Minerva-Australis, along with TRES, CORALIE and CHIRON radial velocities, with ground-based transit data, this thesis was able to confirm that the initial signal uncovered by *TESS* was indeed an exoplanet. With the assistance of students/co-authors, who participated in the *Indigenous Skywatchers-Searching for Earth 2.0* program, the team was able to constrain the stellar rotation period of TOI-778 to be 2.6±0.9 days compared to the orbital period of the transit signal to be 4.63373±0.00012 days.

Combining all of the photometric and radial velocity data, the team was able to use the global fitting model ALLESFITTER (Günther & Daylan, 2021, 2019) to constrain the exoplanetary nature of TOI-778 b, with seven light curves and radial velocity measurements from four observatories. From a global analysis of the light curves and the radial velocities measurements, this thesis was able to define the mass and radius of TOI-778 b to be 2.80±0.22 M_J, 1.336±0.027 R_J and respectively. There are only five planets with a mass precision better than 20% that have higher $v \sin i$ values. This outcome demonstrates how small telescope arrays like MINERVA-Australis , with an effective telescope size of 0.98 m, are able to characterise exoplanets orbiting around broad-lined, rapidly rotating stars.

Transit data, along with a spectroscopic transit data from MINERVA-Australis were also used in the global fit to measure the Rossiter–McLaughlin effect of the exoplanet upon the host star. This fit shows the spin-orbit angle of TOI-778 b to its host star is 19.1 ± 9.6°, which is consistent with an aligned planetary system. Having a stellar age of 2 Gyr, and an orbital eccentricity of 0.103±0.029, the most likely route for TOI-778 b's evolution to its current location would likely be either in-situ formation or disk migration. The formation and evolution of hot-Jupiters is still a very active field of research, thus two alternative formation mechanisms remain in contention for TOI-778 b.

5.4 Conclusions

This thesis has aimed to better understand current and potential exoplanetary systems, using the analysis of data from large stellar and galactic archaeology surveys. With the GALAH catalogue at the focal point, this thesis has utilised the abundantly rich amount of large survey data that can be extremely beneficial to the exoplanet community. From this thesis its been shown that only 36% of stars have Mg/Si and C/O molar ratios that fall within 2σ sigma of the Sun/Earth values. This suggests that

these stars may host rocky exoplanets with geological compositions similar to planets found within our own Solar system. For nearly half of rocky worlds across our galaxy however, these exoplanets will have compositions unlike any planet we currently have within our Solar system. This singular finding has come from the GALAH-*TESS* catalogue, curated here, and is now being ingested into the NASA Exoplanet Science Institute's Exoplanet Follow-up Observing Program database.

The GALAH-*TESS* catalogue will assist in the followup and characterisation of exoplanets discovered by the *TESS* mission and beyond to better understand the potential chemical and geological compositions of rocky planets orbiting nearby stars.

Current confirmed and candidate planetary systems have also been explored throughout this thesis. Here the evidence indicates that the chemical distribution of stars that host short-period super-Earth planets is currently indistinguishable from stars that host short-period sub-Neptune planets. Thus, there is a possibility that super-Earths might be the remnant cores of their gaseous counterparts. Stellar chemo-kinematics have also been used to detect thick-disk hosts, with a handful of planet hosts now considered to be part of the Galaxy's thick-disk. Very few planets have been discovered to orbit thick-disk stars and thus we have very little knowledge about the overall planetary architectures and population statistics of such worlds. As a result of the contributions provided by this thesis, more thick-disk hosts are now known, and the community is piecing together the information we need to then better understand how planets in different stellar populations form and evolve, not only through our local Solar neighbourhood, but all throughout the Milky Way.

Finally, the research undertaken for this thesis has also shown that confirming the mass and exoplanetary nature of some *TESS* candidates will be challenging with their host star's rotational velocity. This is especially true for smaller planets, in similar size to the Earth. However, planets with larger radial velocity amplitudes are still challenging to uncover, but can be discovered through smaller telescope arrays such as MINERVA-Australis. This thesis' discovery and mass measurement of TOI-778 b is evi-

dence that planets around such rapidly rotating stars can be confirmed, if their semi-amplitudes are large enough. As technology, methodologies and techniques improve, our understanding of planets around rapidly rotating stars will increase.

5.5 Into the Future

Gaia's third data release will be the first which includes the spectra for 100,000,000+ stars. Even though the spectra have a very limited resolution and wavelength coverage ($R \sim 11500$, 845–872 nm), it will cover absorption features of Fe, Si, N, Ca, S, Ti and Al (Cropper et al., 2018; Recio-Blanco et al., 2016). These elemental lines will lead to stellar abundances, particularly for α-elements, which can help better determine the stellar populations of the Milky Way for both stars with and without planets. This in turn will allow us to better distinguish any population or architectural differences there might be between thick- or thin-disk hosting stars.

At the time of writing, the APOGEE project team has delivered the final data release of the fourth phase of the Sloan Digital Sky Survey, DR17. APOGEE DR17 alone contains infra-red spectra of over 650,000 stars, with the expected GALAH DR4 being release in the next 12-24 months, it will also contain a catalogue larger than that of APOGEE DR17. This thesis only used one galactic archaeology survey, but there is no reason that a similar study or dissertation could be carried out with both of these surveys together. A future study could even incorporate all known galactic archaeology survey releases, such as GALAH, LAMOST, RAVE, APOGEE, Gaia-ESO etc., to obtain a higher fraction of known planet hosts. Having more planet-hosts would allow for a better analysis to be carried out upon the relationship between stellar abundances and planetary architectures, unveiling potential information on the formation and evolution of planetary systems. However, having a heterogeneous sample would be challenging due to survey biases, systematics, wavelength coverage, and varying line lists, to name a few. A future step would be to develop an homogeneous survey from two sites, one in each hemisphere, that would gather spectra for all known planet-

hosts. It would then be possible to determine the physical and chemical characteristics of known planet-hosting stars, that could lead to such discoveries as the California Kepler Survey's finding of a radius-gap; or maybe even fill in said gap!

With the James Webb Space Telescope nearing launch, to the future LUVOIR/HabEx hybrid direct-imaging telescope to be launched in the 2040's, there is a real need to characterise exoplanets, to the best of our ability from the ground. To increase the efficiency and maximise the scientific return from precious telescope time on such instruments, catalogues like GALAH-*TESS* can be used in conjunction with other information and models better inform us of the chemical, geological and atmospheric characterisation of planets being observed by space-based missions. Thus we can continue on our quest to answer one of humankind's grandest questions: are we truly alone?

REFERENCES

Note that the references presented here are for Chapters 1 and 5. References for the papers included in Chapters 2 - 4 are included in the references sections of the papers.

Addison, B., Wright, D. J., Wittenmyer, R. A., Horner, J., Mengel, M. W., Johns, D., Marti, C., Nicholson, B., Soutter, J., Bowler, B., Crossfield, I., Kane, S. R., Kielkopf, J., Plavchan, P., Tinney, C. G., Zhang, H., Clark, J. T., Clerte, M., Eastman, J. D., Swift, J., Bottom, M., Muirhead, P., McCrady, N., Herzig, E., Hogstrom, K., Wilson, M., Sliski, D., Johnson, S. A., Wright, J. T., Johnson, J. A., Blake, C., Riddle, R., Lin, B., Cornachione, M., Bedding, T. R., Stello, D., Huber, D., Marsden, S., & Carter, B. D. (2019). Minerva-Australis. I. Design, Commissioning, and First Photometric Results. *PASP*, 131(1005), 115003.

Addison, B. C., Knudstrup, E., Wong, I., Hébrard, G., Dorval, P., Snellen, I., Albrecht, S., Bello-Arufe, A., Almenara, J.-M., Boisse, I., Bonfils, X., Dalal, S., Demangeon, O. D. S., Hoyer, S., Kiefer, F., Santos, N. C., Nowak, G., Luque, R., Stangret, M., Palle, E., Tronsgaard, R., Antoci, V., Buchhave, L. A., Günther, M. N., Daylan, T., Murgas, F., Parviainen, H., Esparza-Borges, E., Crouzet, N., Narita, N., Fukui, A., Kawauchi, K., Watanabe, N., Rabus, M., Johnson, M. C., Otten, G. P. P. L., Jan Talens, G., Cabot, S. H. C., Fischer, D. A., Grundahl, F., Fredslund Andersen, M., Jessen-Hansen, J., Pallé, P., Shporer, A., Ciardi, D. R., Clark, J. T., Wittenmyer, R. A., Wright, D. J., Horner, J., Collins, K. A., Jensen, E. L. N., Kielkopf, J. F., Schwarz, R. P., Srdoc, G., Yilmaz, M., Senavci, H. V., Diamond, B., Harbeck, D., Komacek, T. D., Smith, J. C., Wang, S., Eastman, J. D., Stassun, K. G., Latham, D. W., Vanderspek, R., Seager, S., Winn, J. N., Jenkins, J. M., Louie, D. R., Bouma, L. G., Twicken, J. D., Levine, A. M., & McLean, B. (2021). TOI-1431b/MASCARA-5b: A Highly Irradiated Ultrahot Jupiter Orbiting One of the Hottest and Brightest Known Exoplanet Host Stars. *Astronomical Journal*, 162(6), 292.

Adibekyan, V., Gonçalves da Silva, H. M., Sousa, S. G., Santos, N. C., Delgado Mena, E., & Hakobyan, A. A. (2017). Mg/Si Mineralogical Ratio of Low-Mass Planet Hosts. Correction for the NLTE Effects. *Ap*, 60(3), 325–332.

Adibekyan, V., Santos, N. C., Figueira, P., Dorn, C., Sousa, S. G., Delgado-Mena, E., Israelian, G., Hakobyan, A. A., & Mordasini, C. (2015). From stellar to planetary composition: Galactic chemical evolution of Mg/Si mineralogical ratio. *Astronomy & Astrophysics*, 581, L2.

Adibekyan, V. Z., Santos, N. C., Sousa, S. G., Israelian, G., Delgado Mena, E., González Hernández, J. I., Mayor, M., Lovis, C., & Udry, S. (2012). Overabundance of α-elements in exoplanet-hosting stars. *A&A*, 543, A89.

Barclay, T., Pepper, J., & Quintana, E. V. (2018). A Revised Exoplanet Yield from the Transiting Exoplanet Survey Satellite (TESS). *ApJS*, 239(1), 2.

Barclay, T., Rowe, J. F., Lissauer, J. J., Huber, D., Fressin, F., Howell, S. B., Bryson, S. T., Chaplin, W. J., Désert, J.-M., Lopez, E. D., Marcy, G. W., Mullally, F., Ragozzine, D., Torres, G., Adams, E. R., Agol, E., Barrado, D., Basu, S., Bedding, T. R., Buchhave, L. A., Charbonneau, D., Christiansen, J. L., Christensen-Dalsgaard, J., Ciardi, D., Cochran, W. D., Dupree, A. K., Elsworth, Y., Everett, M., Fischer, D. A., Ford, E. B., Fortney, J. J., Geary, J. C., Haas, M. R., Handberg, R., Hekker, S., Henze, C. E., Horch, E., Howard, A. W., Hunter, R. C., Isaacson, H., Jenkins, J. M., Karoff, C., Kawaler, S. D., Kjeldsen, H., Klaus, T. C., Latham, D. W., Li, J., Lillo-Box, J., Lund, M. N., Lundkvist, M., Metcalfe, T. S., Miglio, A., Morris, R. L., Quintana, E. V., Stello, D., Smith, J. C., Still, M., & Thompson, S. E. (2013). A sub-Mercury-sized exoplanet. *Nature*, 494(7438), 452–454.

Barr, A. C., Dobos, V., & Kiss, L. L. (2018). Interior structures and tidal heating in the TRAPPIST-1 planets. *A&A*, 613, A37.

Barstow, J. K., Aigrain, S., Irwin, P. G., Kendrew, S., & Fletcher, L. N. (2016). Telling twins apart: Exo-Earths and Venuses with transit spectroscopy. *Monthly Notices of the Royal Astronomical Society*, 458(3), 2657–2666.

Batalha, N. M., Rowe, J. F., Bryson, S. T., Barclay, T., Burke, C. J., Caldwell, D. A., Christiansen, J. L., Mullally, F., Thompson, S. E., Brown, T. M., Dupree, A. K., Fabrycky, D. C.,

Ford, E. B., Fortney, J. J., Gilliland, R. L., Isaacson, H., Latham, D. W., Marcy, G. W., Quinn, S. N., Ragozzine, D., Shporer, A., Borucki, W. J., Ciardi, D. R., Thomas N. Gautier, I., Haas, M. R., Jenkins, J. M., Koch, D. G., Lissauer, J. J., Rapin, W., Basri, G. S., Boss, A. P., Buchhave, L. A., Carter, J. A., Charbonneau, D., Christensen-Dalsgaard, J., Clarke, B. D., Cochran, W. D., Demory, B.-O., Desert, J.-M., Devore, E., Doyle, L. R., Esquerdo, G. A., Everett, M., Fressin, F., Geary, J. C., Girouard, F. R., Gould, A., Hall, J. R., Holman, M. J., Howard, A. W., Howell, S. B., Ibrahim, K. A., Kinemuchi, K., Kjeldsen, H., Klaus, T. C., Li, J., Lucas, P. W., Meibom, S., Morris, R. L., Prša, A., Quintana, E., Sanderfer, D. T., Sasselov, D., Seader, S. E., Smith, J. C., Steffen, J. H., Still, M., Stumpe, M. C., Tarter, J. C., Tenenbaum, P., Torres, G., Twicken, J. D., Uddin, K., Cleve, J. V., Walkowicz, L., & Welsh, W. F. (2013). Planetary candidates observed by kepler. iii. analysis of the first 16 months of data. *The Astrophysical Journal Supplement Series*, 204(2), 24.

Bond, J. C., Lauretta, D. S., & O'Brien, D. P. (2010a). Making the Earth: Combining dynamics and chemistry in the Solar System. *Icarus*, 205(2), 321–337.

Bond, J. C., Lauretta, D. S., Tinney, C. G., Butler, R. P., Marcy, G. W., Jones, H. R. A., Carter, B. D., O' Toole, S. J., & Bailey, J. (2008). Beyond the iron peak: r- and s-process elemental abundances in stars with planets. *The Astrophysical Journal*, 682(2), 1234.

Bond, J. C., O'Brien, D. P., & Lauretta, D. S. (2010b). The Compositional Diversity of Extrasolar Terrestrial Planets. I. In Situ Simulations. *The Astrophysical Journal*, 715(2), 1050–1070.

Bond, J. C., Tinney, C. G., Butler, R. P., Jones, H. R. A., Marcy, G. W., Penny, A. J., & Carter, B. D. (2006). The abundance distribution of stars with planets. *Monthly Notices of the Royal Astronomical Society*, 370(1), 163–173.

Borucki, W. J., Koch, D., Basri, G., Batalha, N., Brown, T., Caldwell, D., Caldwell, J., Christensen-Dalsgaard, J., Cochran, W. D., DeVore, E., Dunham, E. W., Dupree, A. K., Gautier, T. N., Geary, J. C., Gilliland, R., Gould, A., Howell, S. B., Jenkins, J. M., Kondo, Y., Latham, D. W., Marcy, G. W., Meibom, S., Kjeldsen, H., Lissauer, J. J., Monet, D. G., Morrison, D., Sasselov, D., Tarter, J., Boss, A., Brownlee, D., Owen, T., Buzasi, D., Charbonneau, D., Doyle, L., Fortney, J., Ford, E. B., Holman, M. J., Seager, S., Steffen, J. H., Welsh, W. F., Rowe, J., Anderson, H., Buchhave, L., Ciardi, D., Walkowicz, L., Sherry, W.,

Horch, E., Isaacson, H., Everett, M. E., Fischer, D., Torres, G., Johnson, J. A., Endl, M., MacQueen, P., Bryson, S. T., Dotson, J., Haas, M., Kolodziejczak, J., Van Cleve, J., Chandrasekaran, H., Twicken, J. D., Quintana, E. V., Clarke, B. D., Allen, C., Li, J., Wu, H., Tenenbaum, P., Verner, E., Bruhweiler, F., Barnes, J., & Prsa, A. (2010). Kepler Planet-Detection Mission: Introduction and First Results. *Science*, 327, 977.

Borucki, W. J., Koch, D. G., Basri, G., Batalha, N., Brown, T. M., Bryson, S. T., Caldwell, D., Christensen-Dalsgaard, J., Cochran, W. D., DeVore, E., Dunham, E. W., Gautier, III, T. N., Geary, J. C., Gilliland, R., Gould, A., Howell, S. B., Jenkins, J. M., Latham, D. W., Lissauer, J. J., Marcy, G. W., Rowe, J., Sasselov, D., Boss, A., Charbonneau, D., Ciardi, D., Doyle, L., Dupree, A. K., Ford, E. B., Fortney, J., Holman, M. J., Seager, S., Steffen, J. H., Tarter, J., Welsh, W. F., Allen, C., Buchhave, L. A., Christiansen, J. L., Clarke, B. D., Das, S., Désert, J.-M., Endl, M., Fabrycky, D., Fressin, F., Haas, M., Horch, E., Howard, A., Isaacson, H., Kjeldsen, H., Kolodziejczak, J., Kulesa, C., Li, J., Lucas, P. W., Machalek, P., McCarthy, D., MacQueen, P., Meibom, S., Miquel, T., Prsa, A., Quinn, S. N., Quintana, E. V., Ragozzine, D., Sherry, W., Shporer, A., Tenenbaum, P., Torres, G., Twicken, J. D., Van Cleve, J., Walkowicz, L., Witteborn, F. C., & Still, M. (2011). Characteristics of Planetary Candidates Observed by Kepler. II. Analysis of the First Four Months of Data. *The Astrophysical Journal*, 736, 19.

Brooks, T., Stahl, H. P., & Arnold, W. R. (2015). Advanced Mirror Technology Development (AMTD) thermal trade studies. In M. A. Kahan & M. B. Levine-West (Eds.), *Optical Modeling and Performance Predictions VII*, volume 9577 of *Society of Photo-Optical Instrumentation Engineers (SPIE) Conference Series* (pp.Ẽ3).

Brugger, B., Mousis, O., Deleuil, M., & Deschamps, F. (2017). Constraints on Super-Earth Interiors from Stellar Abundances. *The Astrophysical Journal*, 850, 93.

Buder, S., Asplund, M., Duong, L., Kos, J., Lind, K., Ness, M. K., Sharma, S., Bland - Hawthorn, J., Casey, A. R., De Silva, G. M., D'Orazi, V., Freeman, K. C., Lewis, G. F., Lin, J., Martell, S. L., Schlesinger, K. J., Simpson, J. D., Zucker, D. B., Zwitter, T., Amarsi, A. M., Anguiano, B., Carollo, D., Casagrande, L., Čotar, K., Cottrell, P. L., Da Costa, G., Gao, X. D., Hayden, M. R., Horner, J., Ireland, M. J., Kafle, P. R., Munari, U., Nataf, D. M., Nordlander, T., Stello, D., Ting, Y.-S., Traven, G., Watson, F., Wittenmyer, R. A.,

Wyse, R. F. G., Yong, D., Zinn, J. C., & Žerjal, M. (2018). The GALAH Survey: second data release. *Monthly Notices of the Royal Astronomical Society*, 478, 4513–4552.

Buder, S., Sharma, S., Kos, J., Amarsi, A. M., Nordlander, T., Lind, K., Martell, S. L., Asplund, M., Bland-Hawthorn, J., Casey, A. R., de Silva, G. M., D'Orazi, V., Freeman, K. C., Hayden, M. R., Lewis, G. F., Lin, J., Schlesinger, K. J., Simpson, J. D., Stello, D., Zucker, D. B., Zwitter, T., Beeson, K. L., Buck, T., Casagrande, L., Clark, J. T., Čotar, K., da Costa, G. S., de Grijs, R., Feuillet, D., Horner, J., Kafle, P. R., Khanna, S., Kobayashi, C., Liu, F., Montet, B. T., Nandakumar, G., Nataf, D. M., Ness, M. K., Spina, L., Tepper-García, T., Ting, Y.-S., Traven, G., Vogrinčič, R., Wittenmyer, R. A., Wyse, R. F. G., Žerjal, M., & GALAH Collaboration (2021). The GALAH+ survey: Third data release. *Monthly Notices of the Royal Astronomical Society*, 506(1), 150–201.

Carter-Bond, J. C., O'Brien, D. P., Mena, E. D., Israelian, G., Santos, N. C., & Hernández, J. I. G. (2012). Low mg/si planetary host stars and their mg-depleted terrestrial planets. *The Astrophysical Journal Letters*, 747(1), L2.

Catanzaro, G. (2014). *How to Determine Surface Gravity from Stellar Spectra*, (pp. 97–109). Springer International Publishing: Cham.

Choi, J., Dotter, A., Conroy, C., Cantiello, M., Paxton, B., & Johnson, B. D. (2016). Mesa Isochrones and Stellar Tracks (MIST). I. Solar-scaled Models. *The Astrophysical Journal*, 823(2), 102.

Clark, J. T., Clerté, M., Hinkel, N. R., Unterborn, C. T., Wittenmyer, R. A., Horner, J., Wright, D. J., Carter, B., Morton, T. D., Spina, L., Asplund, M., Buder, S., Bland-Hawthorn, J., Casey, A., De Silva, G., D'Orazi, V., Duong, L., Hayden, M., Freeman, K., Kos, J., Lewis, G., Lin, J., Lind, K., Martell, S., Sharma, S., Simpson, J., Zucker, D., Zwitter, T., Tinney, C. G., Ting (丁源森), Y.-S., Nordlander, T., & Amarsi, A. M. (2021). The GALAH Survey: using galactic archaeology to refine our knowledge of TESS target stars. *Monthly Notices of the Royal Astronomical Society*, 504(4), 4968–4989.

Clark, J. T., Vach, S., Heitzmann, A., Rodriguez, J. E., Addison, B. C., Wright, D. J., Clerté, M., Brown, C. J., Fetherolf, T., Wittenmyer, R. A., Plavchan, P., Kane, S. R., Horner, J., Kielkopf, J. F., Shporer, A., Tinney, C. G., Hui-Gen, L., Ballard, S., Bedding, T., Bowler, B. P., Mengel, M. W., Zhou, G., Lee, A. S., David, A., Heim, J., Lee, M. E., Sevilla, V.,

Zafar, N. E., Hinkel, N. R., Allen, B. E., Berberyan, A., Berlind, P., Bieryla, A., Bouchy, F., Brahm, R., Bryant, E. M., Christiansen, J. L., Ciardi, D. R., Ciardi, K. N., Collins, K. A., Dallant, J., Davis, A. B., Díaz, M. R., Dressing, C. D., Esquerdo, G. A., Harre, J.-V., Howell, S. B., Jenkins, J. M., Jensen, E. L. N., Jones, M. I., Jordán, A., Latham, D. W., Lund, M. B., McCormac, J., Nielsen, L. D., Otegi, J., Quinn, S. N., Radford, D. J., Ricker, G. R., Schwarz, R. P., Seager, S., Smith, A. M. S., Stockdale, C., Tan, T.-G., Udry, S., Vanderspek, R., Wang, S., Wingham, G., & Winn, J. N. (2022). Spinning up a Daze: *TESS* Uncovers a Hot Jupiter orbiting the Rapid-Rotator TOI-778. *Astronomical Journal, Submitted*.

Clark, J. T., Wright, D. J., Wittenmyer, R. A., Horner, J., Hinkel, N. R., Clerté, M., Carter, B. D., Buder, S., Hayden, M. R., Bland-Hawthorn, J., Casey, A. R., De Silva, G. M., D' Orazi, V., Freeman, K. C., Kos, J., Lewis, G. F., Lin, J., Lind, K., Martell, S. L., Schlesinger, K. J., Sharma, S., Simpson, J. D., Stello, D., Zucker, D. B., Zwitter, T., Munari, U., & Nordlander, T. (2021). The GALAH Survey: improving our understanding of confirmed and candidate planetary systems with large stellar surveys. *Monthly Notices of the Royal Astronomical Society*, 510(2), 2041–2060.

Cropper, M., Katz, D., Sartoretti, P., Prusti, T., de Bruijne, J. H. J., Chassat, F., Charvet, P., Boyadjian, J., Perryman, M., Sarri, G., Gare, P., Erdmann, M., Munari, U., Zwitter, T., Wilkinson, M., Arenou, F., Vallenari, A., Gómez, A., Panuzzo, P., Seabroke, G., Allende Prieto, C., Benson, K., Marchal, O., Huckle, H., Smith, M., Dolding, C., Janßen, K., Viala, Y., Blomme, R., Baker, S., Boudreault, S., Crifo, F., Soubiran, C., Frémat, Y., Jasniewicz, G., Guerrier, A., Guy, L. P., Turon, C., Jean-Antoine-Piccolo, A., Thévenin, F., David, M., Gosset, E., & Damerdji, Y. (2018). Gaia Data Release 2. Gaia Radial Velocity Spectrometer. *A&A*, 616, A5.

Cui, X.-Q., Zhao, Y.-H., Chu, Y.-Q., Li, G.-P., Li, Q., Zhang, L.-P., Su, H.-J., Yao, Z.-Q., Wang, Y.-N., Xing, X.-Z., Li, X.-N., Zhu, Y.-T., Wang, G., Gu, B.-Z., Luo, A. L., Xu, X.-Q., Zhang, Z.-C., Liu, G.-R., Zhang, H.-T., Yang, D.-H., Cao, S.-Y., Chen, H.-Y., Chen, J.-J., Chen, K.-X., Chen, Y., Chu, J.-R., Feng, L., Gong, X.-F., Hou, Y.-H., Hu, H.-Z., Hu, N.-S., Hu, Z.-W., Jia, L., Jiang, F.-H., Jiang, X., Jiang, Z.-B., Jin, G., Li, A.-H., Li, Y., Li, Y.-P., Liu, G.-Q., Liu, Z.-G., Lu, W.-Z., Mao, Y.-D., Men, L., Qi, Y.-J., Qi, Z.-X., Shi, H.-M., Tang, Z.-H., Tao, Q.-S., Wang, D.-Q., Wang, D., Wang, G.-M., Wang, H., Wang, J.-N., Wang, J., Wang, J.-L., Wang, J.-P., Wang, L., Wang, S.-Q., Wang, Y., Wang, Y.-F., Xu, L.-

Z., Xu, Y., Yang, S.-H., Yu, Y., Yuan, H., Yuan, X.-Y., Zhai, C., Zhang, J., Zhang, Y.-X., Zhang, Y., Zhao, M., Zhou, F., Zhou, G.-H., Zhu, J., & Zou, S.-C. (2012). The Large Sky Area Multi-Object Fiber Spectroscopic Telescope (LAMOST). *Research in Astronomy and Astrophysics*, 12(9), 1197–1242.

Dai, F., Howard, A. W., Batalha, N. M., Beard, C., Behmard, A., Blunt, S., Brinkman, C. L., Chontos, A., Crossfield, I. J. M., Dalba, P. A., Dressing, C., Fulton, B., Giacalone, S., Hill, M. L., Huber, D., Isaacson, H., Kane, S. R., Lubin, J., Mayo, A., Močnik, T., Akana Murphy, J. M., Petigura, E. A., Rice, M., Robertson, P., Rosenthal, L., Roy, A., Rubenzahl, R. A., Weiss, L. M., Zandt, J. V., Beichman, C., Ciardi, D., Collins, K. A., Gonzales, E., Howell, S. B., Matson, R. A., Matthews, E. C., Schlieder, J. E., Schwarz, R. P., Ricker, G. R., Vanderspek, R., Latham, D. W., Seager, S., Winn, J. N., Jenkins, J. M., Caldwell, D. A., Colon, K. D., Dragomir, D., Lund, M. B., McLean, B., Rudat, A., & Shporer, A. (2021). TKS X: Confirmation of TOI-1444b and a Comparative Analysis of the Ultra-short-period Planets with Hot Neptunes. *Astronomical Journal*, 162(2), 62.

Dai, F., Masuda, K., Winn, J. N., & Zeng, L. (2019). Homogeneous Analysis of Hot Earths: Masses, Sizes, and Compositions. *The Astrophysical Journal*, 883(1), 79.

Dawson, R. I. & Fabrycky, D. C. (2010). Radial Velocity Planets De-aliased: A New, Short Period for Super-Earth 55 Cnc e. *The Astrophysical Journal*, 722, 937–953.

De Silva, G. M., Freeman, K. C., Bland-Hawthorn, J., Martell, S., de Boer, E. W., Asplund, M., Keller, S., Sharma, S., Zucker, D. B., Zwitter, T., Anguiano, B., Bacigalupo, C., Bayliss, D., Beavis, M. A., Bergemann, M., Campbell, S., Cannon, R., Carollo, D., Casagrande, L., Casey, A. R., Da Costa, G., D'Orazi, V., Dotter, A., Duong, L., Heger, A., Ireland, M. J., Kafle, P. R., Kos, J., Lattanzio, J., Lewis, G. F., Lin, J., Lind, K., Munari, U., Nataf, D. M., O'Toole, S., Parker, Q., Reid, W., Schlesinger, K. J., Sheinis, A., Simpson, J. D., Stello, D., Ting, Y. S., Traven, G., Watson, F., Wittenmyer, R., Yong, D., & Žerjal, M. (2015). The GALAH survey: scientific motivation. *Monthly Notices of the Royal Astronomical Society*, 449(3), 2604–2617.

Demarque, P., Woo, J.-H., Kim, Y.-C., & Yi, S. K. (2004). Y^2 Isochrones with an Improved Core Overshoot Treatment. *ApJS*, 155(2), 667–674.

Dorn, C., Bower, D. J., & Rozel, A. (2018a). *Assessing the Interior Structure of Terrestrial Exoplanets with Implications for Habitability*, (pp.66). Springer International Publishing: Cham.

Dorn, C., Khan, A., Heng, K., Connolly, J. A. D., Alibert, Y., Benz, W., & Tackley, P. (2015). Can we constrain the interior structure of rocky exoplanets from mass and radius measurements? *A&A*, 577, A83.

Dorn, C., Noack, L., & Rozel, A. B. (2018b). Outgassing on stagnant-lid super-Earths. *A&A*, 614, A18.

Dorn, C., Venturini, J., Khan, A., Heng, K., Alibert, Y., Helled, R., Rivoldini, A., & Benz, W. (2017). A generalized bayesian inference method for constraining the interiors of super earths and sub-neptunes. *A&A*, 597, A37.

Duffy, T., Madhusudhan, N., & Lee, K. K. (2015). *Mineralogy of Super-Earth Planets*, volume 2. Elsevier B.V.

Endl, M., Brugamyer, E. J., Cochran, W. D., MacQueen, P. J., Robertson, P., Meschiari, S., Ramirez, I., Shetrone, M., Gullikson, K., Johnson, M. C., Wittenmyer, R., Horner, J., Ciardi, D. R., Horch, E., Simon, A. E., Howell, S. B., Everett, M., Caldwell, C., & Castanheira, B. G. (2016). Two New Long-period Giant Planets from the McDonald Observatory Planet Search and Two Stars with Long-period Radial Velocity Signals Related to Stellar Activity Cycles. *The Astrophysical Journal*, 818(1), 34.

Espinoza, N., Brahm, R., Jordán, A., Jenkins, J. S., Rojas, F., Jofré, P., Mädler, T., Rabus, M., Chanamé, J., Pantoja, B., Soto, M. G., Morzinski, K. M., Males, J. R., Ward-Duong, K., & Close, L. M. (2016). Discovery and validation of a high-density sub-neptune from the k2 mission. *The Astrophysical Journal*, 830(1), 43.

Fischer, D. A., Howard, A. W., Laughlin, G. P., Macintosh, B., Mahadevan, S., Sahlmann, J., & Yee, J. C. (2014). Exoplanet Detection Techniques. *Protostars and Planets VI*, (pp. 715–737).

Fischer, D. A., Marcy, G. W., Butler, R. P., Vogt, S. S., Laughlin, G., Henry, G. W., Abouav, D., Peek, K. M. G., Wright, J. T., Johnson, J. A., McCarthy, C., & Isaacson, H. (2008). Five Planets Orbiting 55 Cancri. *The Astrophysical Journal*, 675(1), 790–801.

Fischer, D. A. & Valenti, J. (2005). The Planet-Metallicity Correlation. *The Astrophysical Journal*, 622(2), 1102–1117.

Fischer, D. A., Vogt, S. S., Marcy, G. W., Butler, R. P., Sato, B., Henry, G. W., Robinson, S., Laughlin, G., Ida, S., Toyota, E., Omiya, M., Driscoll, P., Takeda, G., Wright, J. T., & Johnson, J. A. (2007). Five intermediate-period planets from the n2k sample. *The Astrophysical Journal*, 669(2), 1336.

Fulton, B. J., Petigura, E. A., Blunt, S., & Sinukoff, E. (2018). Radvel: The radial velocity modeling toolkit. *Publications of the Astronomical Society of the Pacific*, 130(986), 044504.

Gaia Collaboration, Brown, A. G. A., Vallenari, A., Prusti, T., de Bruijne, J. H. J., Babusiaux, C., Bailer-Jones, C. A. L., Biermann, M., Evans, D. W., Eyer, L., Jansen, F., Jordi, C., Klioner, S. A., Lammers, U., Lindegren, L., Luri, X., Mignard, F., Panem, C., Pourbaix, D., Randich, S., Sartoretti, P., Siddiqui, H. I., Soubiran, C., van Leeuwen, F., Walton, N. A., Arenou, F., Bastian, U., Cropper, M., Drimmel, R., Katz, D., Lattanzi, M. G., Bakker, J., Cacciari, C., Castañeda, J., Chaoul, L., Cheek, N., De Angeli, F., Fabricius, C., Guerra, R., Holl, B., Masana, E., Messineo, R., Mowlavi, N., Nienartowicz, K., Panuzzo, P., Portell, J., Riello, M., Seabroke, G. M., Tanga, P., Thévenin, F., Gracia-Abril, G., Comoretto, G., Garcia-Reinaldos, M., Teyssier, D., Altmann, M., Andrae, R., Audard, M., Bellas-Velidis, I., Benson, K., Berthier, J., Blomme, R., Burgess, P., Busso, G., Carry, B., Cellino, A., Clementini, G., Clotet, M., Creevey, O., Davidson, M., De Ridder, J., Delchambre, L., Dell'Oro, A., Ducourant, C., Fernández-Hernández, J., Fouesneau, M., Frémat, Y., Galluccio, L., García-Torres, M., González-Núñez, J., González-Vidal, J. J., Gosset, E., Guy, L. P., Halbwachs, J. L., Hambly, N. C., Harrison, D. L., Hernández, J., Hestroffer, D., Hodgkin, S. T., Hutton, A., Jasniewicz, G., Jean-Antoine-Piccolo, A., Jordan, S., Korn, A. J., Krone-Martins, A., Lanzafame, A. C., Lebzelter, T., Löffler, W., Manteiga, M., Marrese, P. M., Martín-Fleitas, J. M., Moitinho, A., Mora, A., Muinonen, K., Osinde, J., Pancino, E., Pauwels, T., Petit, J. M., Recio-Blanco, A., Richards, P. J., Rimoldini, L., Robin, A. C., Sarro, L. M., Siopis, C., Smith, M., Sozzetti, A., Süveges, M., Torra, J., van Reeven, W., Abbas, U., Abreu Aramburu, A., Accart, S., Aerts, C., Altavilla, G., Álvarez, M. A., Alvarez, R., Alves, J., Anderson, R. I., Andrei, A. H., Anglada Varela, E., Antiche, E., Antoja, T., Arcay, B., Astraatmadja, T. L., Bach, N., Baker, S. G., Balaguer-Núñez, L., Balm, P., Barache, C., Barata, C., Barbato, D., Barblan, F., Barklem, P. S., Barrado, D., Barros, M.,

Barstow, M. A., Bartholomé Muñoz, S., Bassilana, J. L., Becciani, U., Bellazzini, M., Berihuete, A., Bertone, S., Bianchi, L., Bienaymé, O., Blanco-Cuaresma, S., Boch, T., Boeche, C., Bombrun, A., Borrachero, R., Bossini, D., Bouquillon, S., Bourda, G., Bragaglia, A., Bramante, L., Breddels, M. A., Bressan, A., Brouillet, N., Brüsemeister, T., Brugaletta, E., Bucciarelli, B., Burlacu, A., Busonero, D., Butkevich, A. G., Buzzi, R., Caffau, E., Cancelliere, R., Cannizzaro, G., Cantat-Gaudin, T., Carballo, R., Carlucci, T., Carrasco, J. M., Casamiquela, L., Castellani, M., Castro-Ginard, A., Charlot, P., Chemin, L., Chiavassa, A., Cocozza, G., Costigan, G., Cowell, S., Crifo, F., Crosta, M., Crowley, C., Cuypers, J., Dafonte, C., Damerdji, Y., Dapergolas, A., David, P., David, M., de Laverny, P., De Luise, F., De March, R., de Martino, D., de Souza, R., de Torres, A., Debosscher, J., del Pozo, E., Delbo, M., Delgado, A., Delgado, H. E., Di Matteo, P., Diakite, S., Diener, C., Distefano, E., Dolding, C., Drazinos, P., Durán, J., Edvardsson, B., Enke, H., Eriksson, K., Esquej, P., Eynard Bontemps, G., Fabre, C., Fabrizio, M., Faigler, S., Falcão, A. J., Farràs Casas, M., Federici, L., Fedorets, G., Fernique, P., Figueras, F., Filippi, F., Findeisen, K., Fonti, A., Fraile, E., Fraser, M., Frézouls, B., Gai, M., Galleti, S., Garabato, D., García-Sedano, F., Garofalo, A., Garralda, N., Gavel, A., Gavras, P., Gerssen, J., Geyer, R., Giacobbe, P., Gilmore, G., Girona, S., Giuffrida, G., Glass, F., Gomes, M., Granvik, M., Gueguen, A., Guerrier, A., Guiraud, J., Gutiérrez-Sánchez, R., Haigron, R., Hatzidimitriou, D., Hauser, M., Haywood, M., Heiter, U., Helmi, A., Heu, J., Hilger, T., Hobbs, D., Hofmann, W., Holland, G., Huckle, H. E., Hypki, A., Icardi, V., Janßen, K., Jevardat de Fombelle, G., Jonker, P. G., Juhász, Á. L., Julbe, F., Karampelas, A., Kewley, A., Klar, J., Kochoska, A., Kohley, R., Kolenberg, K., Kontizas, M., Kontizas, E., Koposov, S. E., Kordopatis, G., Kostrzewa-Rutkowska, Z., Koubsky, P., Lambert, S., Lanza, A. F., Lasne, Y., Lavigne, J. B., Le Fustec, Y., Le Poncin-Lafitte, C., Lebreton, Y., Leccia, S., Leclerc, N., Lecoeur-Taibi, I., Lenhardt, H., Leroux, F., Liao, S., Licata, E., Lindstrøm, H. E. P., Lister, T. A., Livanou, E., Lobel, A., López, M., Managau, S., Mann, R. G., Mantelet, G., Marchal, O., Marchant, J. M., Marconi, M., Marinoni, S., Marschalkó, G., Marshall, D. J., Martino, M., Marton, G., Mary, N., Massari, D., Matijevič, G., Mazeh, T., McMillan, P. J., Messina, S., Michalik, D., Millar, N. R., Molina, D., Molinaro, R., Molnár, L., Montegriffo, P., Mor, R., Morbidelli, R., Morel, T., Morris, D., Mulone, A. F., Muraveva, T., Musella, I., Nelemans, G., Nicastro, L., Noval, L., O'Mullane, W., Ordénovic, C., Ordóñez-Blanco, D., Osborne, P., Pagani, C., Pagano, I., Pailler, F., Palacin, H., Palaversa, L., Panahi, A., Pawlak, M., Piersimoni, A. M., Pineau, F. X., Plachy, E., Plum, G., Poggio, E., Poujoulet, E., Prša, A., Pulone,

L., Racero, E., Ragaini, S., Rambaux, N., Ramos-Lerate, M., Regibo, S., Reylé, C., Riclet, F., Ripepi, V., Riva, A., Rivard, A., Rixon, G., Roegiers, T., Roelens, M., Romero-Gómez, M., Rowell, N., Royer, F., Ruiz-Dern, L., Sadowski, G., Sagristà Sellés, T., Sahlmann, J., Salgado, J., Salguero, E., Sanna, N., Santana-Ros, T., Sarasso, M., Savietto, H., Schultheis, M., Sciacca, E., Segol, M., Segovia, J. C., Ségransan, D., Shih, I. C., Siltala, L., Silva, A. F., Smart, R. L., Smith, K. W., Solano, E., Solitro, F., Sordo, R., Soria Nieto, S., Souchay, J., Spagna, A., Spoto, F., Stampa, U., Steele, I. A., Steidelmüller, H., Stephenson, C. A., Stoev, H., Suess, F. F., Surdej, J., Szabados, L., Szegedi-Elek, E., Tapiador, D., Taris, F., Tauran, G., Taylor, M. B., Teixeira, R., Terrett, D., Teyssand ier, P., Thuillot, W., Titarenko, A., Torra Clotet, F., Turon, C., Ulla, A., Utrilla, E., Uzzi, S., Vaillant, M., Valentini, G., Valette, V., van Elteren, A., Van Hemelryck, E., van Leeuwen, M., Vaschetto, M., Vecchiato, A., Veljanoski, J., Viala, Y., Vicente, D., Vogt, S., von Essen, C., Voss, H., Votruba, V., Voutsinas, S., Walmsley, G., Weiler, M., Wertz, O., Wevers, T., Wyrzykowski, Ł., Yoldas, A., Žerjal, M., Ziaeepour, H., Zorec, J., Zschocke, S., Zucker, S., Zurbach, C., & Zwitter, T. (2018). Gaia Data Release 2. Summary of the contents and survey properties. *A&A*, 616, A1.

Gaia Collaboration, Brown, A. G. A., Vallenari, A., Prusti, T., de Bruijne, J. H. J., Babusiaux, C., Biermann, M., Creevey, O. L., Evans, D. W., Eyer, L., Hutton, A., Jansen, F., Jordi, C., Klioner, S. A., Lammers, U., Lindegren, L., Luri, X., Mignard, F., Panem, C., Pourbaix, D., Randich, S., Sartoretti, P., Soubiran, C., Walton, N. A., Arenou, F., Bailer-Jones, C. A. L., Bastian, U., Cropper, M., Drimmel, R., Katz, D., Lattanzi, M. G., van Leeuwen, F., Bakker, J., Cacciari, C., Castañeda, J., De Angeli, F., Ducourant, C., Fabricius, C., Fouesneau, M., Frémat, Y., Guerra, R., Guerrier, A., Guiraud, J., Jean-Antoine Piccolo, A., Masana, E., Messineo, R., Mowlavi, N., Nicolas, C., Nienartowicz, K., Pailler, F., Panuzzo, P., Riclet, F., Roux, W., Seabroke, G. M., Sordo, R., Tanga, P., Thévenin, F., Gracia-Abril, G., Portell, J., Teyssier, D., Altmann, M., Andrae, R., Bellas-Velidis, I., Benson, K., Berthier, J., Blomme, R., Brugaletta, E., Burgess, P. W., Busso, G., Carry, B., Cellino, A., Cheek, N., Clementini, G., Damerdji, Y., Davidson, M., Delchambre, L., Dell'Oro, A., Fernández-Hernández, J., Galluccio, L., García-Lario, P., Garcia-Reinaldos, M., González-Núñez, J., Gosset, E., Haigron, R., Halbwachs, J. L., Hambly, N. C., Harrison, D. L., Hatzidimitriou, D., Heiter, U., Hernández, J., Hestroffer, D., Hodgkin, S. T., Holl, B., Janßen, K., Jevardat de Fombelle, G., Jordan, S., Krone-Martins, A., Lanzafame, A. C., Löffler, W., Lorca, A., Manteiga, M., Marchal, O., Marrese, P. M., Moitinho, A.,

Mora, A., Muinonen, K., Osborne, P., Pancino, E., Pauwels, T., Petit, J. M., Recio-Blanco, A., Richards, P. J., Riello, M., Rimoldini, L., Robin, A. C., Roegiers, T., Rybizki, J., Sarro, L. M., Siopis, C., Smith, M., Sozzetti, A., Ulla, A., Utrilla, E., van Leeuwen, M., van Reeven, W., Abbas, U., Abreu Aramburu, A., Accart, S., Aerts, C., Aguado, J. J., Ajaj, M., Altavilla, G., Álvarez, M. A., Álvarez Cid-Fuentes, J., Alves, J., Anderson, R. I., Anglada Varela, E., Antoja, T., Audard, M., Baines, D., Baker, S. G., Balaguer-Núñez, L., Balbinot, E., Balog, Z., Barache, C., Barbato, D., Barros, M., Barstow, M. A., Bartolomé, S., Bassilana, J. L., Bauchet, N., Baudesson-Stella, A., Becciani, U., Bellazzini, M., Bernet, M., Bertone, S., Bianchi, L., Blanco-Cuaresma, S., Boch, T., Bombrun, A., Bossini, D., Bouquillon, S., Bragaglia, A., Bramante, L., Breedt, E., Bressan, A., Brouillet, N., Bucciarelli, B., Burlacu, A., Busonero, D., Butkevich, A. G., Buzzi, R., Caffau, E., Cancelliere, R., Cánovas, H., Cantat-Gaudin, T., Carballo, R., Carlucci, T., Carnerero, M. I., Carrasco, J. M., Casamiquela, L., Castellani, M., Castro-Ginard, A., Castro Sampol, P., Chaoul, L., Charlot, P., Chemin, L., Chiavassa, A., Cioni, M. R. L., Comoretto, G., Cooper, W. J., Cornez, T., Cowell, S., Crifo, F., Crosta, M., Crowley, C., Dafonte, C., Dapergolas, A., David, M., David, P., de Laverny, P., De Luise, F., De March, R., De Ridder, J., de Souza, R., de Teodoro, P., de Torres, A., del Peloso, E. F., del Pozo, E., Delbo, M., Delgado, A., Delgado, H. E., Delisle, J. B., Di Matteo, P., Diakite, S., Diener, C., Distefano, E., Dolding, C., Eappachen, D., Edvardsson, B., Enke, H., Esquej, P., Fabre, C., Fabrizio, M., Faigler, S., Fedorets, G., Fernique, P., Fienga, A., Figueras, F., Fouron, C., Fragkoudi, F., Fraile, E., Franke, F., Gai, M., Garabato, D., Garcia-Gutierrez, A., García-Torres, M., Garofalo, A., Gavras, P., Gerlach, E., Geyer, R., Giacobbe, P., Gilmore, G., Girona, S., Giuffrida, G., Gomel, R., Gomez, A., Gonzalez-Santamaria, I., González-Vidal, J. J., Granvik, M., Gutiérrez-Sánchez, R., Guy, L. P., Hauser, M., Haywood, M., Helmi, A., Hidalgo, S. L., Hilger, T., Hładczuk, N., Hobbs, D., Holland, G., Huckle, H. E., Jasniewicz, G., Jonker, P. G., Juaristi Campillo, J., Julbe, F., Karbevska, L., Kervella, P., Khanna, S., Kochoska, A., Kontizas, M., Kordopatis, G., Korn, A. J., Kostrzewa-Rutkowska, Z., Kruszyńska, K., Lambert, S., Lanza, A. F., Lasne, Y., Le Campion, J. F., Le Fustec, Y., Lebreton, Y., Lebzelter, T., Leccia, S., Leclerc, N., Lecoeur-Taibi, I., Liao, S., Licata, E., Lindstrøm, E. P., Lister, T. A., Livanou, E., Lobel, A., Madrero Pardo, P., Managau, S., Mann, R. G., Marchant, J. M., Marconi, M., Marcos Santos, M. M. S., Marinoni, S., Marocco, F., Marshall, D. J., Martin Polo, L., Martín-Fleitas, J. M., Masip, A., Massari, D., Mastrobuono-Battisti, A., Mazeh, T., McMillan, P. J., Messina, S., Michalik, D., Millar, N. R., Mints, A., Molina, D., Molinaro, R.,

Molnár, L., Montegriffo, P., Mor, R., Morbidelli, R., Morel, T., Morris, D., Mulone, A. F., Munoz, D., Muraveva, T., Murphy, C. P., Musella, I., Noval, L., Ordénovic, C., Orrù, G., Osinde, J., Pagani, C., Pagano, I., Palaversa, L., Palicio, P. A., Panahi, A., Pawlak, M., Peñalosa Esteller, X., Penttilä, A., Piersimoni, A. M., Pineau, F. X., Plachy, E., Plum, G., Poggio, E., Poretti, E., Poujoulet, E., Prša, A., Pulone, L., Racero, E., Ragaini, S., Rainer, M., Raiteri, C. M., Rambaux, N., Ramos, P., Ramos-Lerate, M., Re Fiorentin, P., Regibo, S., Reylé, C., Ripepi, V., Riva, A., Rixon, G., Robichon, N., Robin, C., Roelens, M., Rohrbasser, L., Romero-Gómez, M., Rowell, N., Royer, F., Rybicki, K. A., Sadowski, G., Sagristà Sellés, A., Sahlmann, J., Salgado, J., Salguero, E., Samaras, N., Sanchez Gimenez, V., Sanna, N., Santoveña, R., Sarasso, M., Schultheis, M., Sciacca, E., Segol, M., Segovia, J. C., Ségransan, D., Semeux, D., Shahaf, S., Siddiqui, H. I., Siebert, A., Siltala, L., Slezak, E., Smart, R. L., Solano, E., Solitro, F., Souami, D., Souchay, J., Spagna, A., Spoto, F., Steele, I. A., Steidelmüller, H., Stephenson, C. A., Süveges, M., Szabados, L., Szegedi-Elek, E., Taris, F., Tauran, G., Taylor, M. B., Teixeira, R., Thuillot, W., Tonello, N., Torra, F., Torra, J., Turon, C., Unger, N., Vaillant, M., van Dillen, E., Vanel, O., Vecchiato, A., Viala, Y., Vicente, D., Voutsinas, S., Weiler, M., Wevers, T., Wyrzykowski, Ł., Yoldas, A., Yvard, P., Zhao, H., Zorec, J., Zucker, S., Zurbach, C., & Zwitter, T. (2021). Gaia Early Data Release 3. Summary of the contents and survey properties. *A&A*, 649, A1.

Gillon, M., Triaud, A. H. M. J., Demory, B.-O., Jehin, E., Agol, E., Deck, K. M., Lederer, S. M., de Wit, J., Burdanov, A., Ingalls, J. G., Bolmont, E., Leconte, J., Raymond, S. N., Selsis, F., Turbet, M., Barkaoui, K., Burgasser, A., Burleigh, M. R., Carey, S. J., Chaushev, A., Copperwheat, C. M., Delrez, L., Fernandes, C. S., Holdsworth, D. L., Kotze, E. J., Van Grootel, V., Almleaky, Y., Benkhaldoun, Z., Magain, P., & Queloz, D. (2017). Seven temperate terrestrial planets around the nearby ultracool dwarf star TRAPPIST-1. *Nature*, 542, 456.

Gonzalez, G. (1997). The stellar metallicity-giant planet connection. *Monthly Notices of the Royal Astronomical Society*, 285(2), 403–412.

Grasset, O., Schneider, J., & Sotin, C. (2009). A Study of the Accuracy of Mass-Radius Relationships for Silicate-Rich and Ice-Rich Planets up to 100 Earth Masses. *The Astrophysical Journal*, 693, 722–733.

Greaves, J. S., Richards, A. M. S., Bains, W., Rimmer, P. B., Sagawa, H., Clements, D. L., Seager, S., Petkowski, J. J., Sousa-Silva, C., Ranjan, S., Drabek-Maunder, E., Fraser, H. J., Cartwright, A., Mueller-Wodarg, I., Zhan, Z., Friberg, P., Coulson, I., Lee, E., & Hoge, J. (2021). Phosphine gas in the cloud decks of Venus. *Nature Astronomy*, 5, 655–664.

Günther, M. N. & Daylan, T. (2019). Allesfitter: Flexible Star and Exoplanet Inference From Photometry and Radial Velocity. Astrophysics Source Code Library.

Günther, M. N. & Daylan, T. (2021). Allesfitter: Flexible Star and Exoplanet Inference from Photometry and Radial Velocity. *ApJS*, 254(1), 13.

Hands, T. O. & Helled, R. (2022). Super stellar abundances of alkali metals suggest significant migration for hot Jupiters. *Monthly Notices of the Royal Astronomical Society*, 509(1), 894–902.

Hebb, L., Collier-Cameron, A., Loeillet, B., Pollacco, D., Hébrard, G., Street, R. A., Bouchy, F., Stempels, H. C., Moutou, C., Simpson, E., Udry, S., Joshi, Y. C., West, R. G., Skillen, I., Wilson, D. M., McDonald, I., Gibson, N. P., Aigrain, S., Anderson, D. R., Benn, C. R., Christian, D. J., Enoch, B., Haswell, C. A., Hellier, C., Horne, K., Irwin, J., Lister, T. A., Maxted, P., Mayor, M., Norton, A. J., Parley, N., Pont, F., Queloz, D., Smalley, B., & Wheatley, P. J. (2009). WASP-12b: The Hottest Transiting Extrasolar Planet Yet Discovered. *The Astrophysical Journal*, 693, 1920–1928.

Helled, R., Anderson, J. D., Podolak, M., & Schubert, G. (2011). Interior models of Uranus and Neptune. *Astrophysical Journal*, 726(1).

Helled, R. & Guillot, T. (2018). *Internal Structure of Giant and Icy Planets: Importance of Heavy Elements and Mixing*, (pp.44). Springer International Publishing: Cham.

Horner, J. & Jones, B. W. (2010). Determining habitability: which exoEarths should we search for life? *International Journal of Astrobiology*, 9, 273–291.

Huang, C. X., Vanderburg, A., Pál, A., Sha, L., Yu, L., Fong, W., Fausnaugh, M., Shporer, A., Guerrero, N., Vanderspek, R., & Ricker, G. (2020). Photometry of 10 Million Stars from the First Two Years of TESS Full Frame Images: Part I. *Research Notes of the American Astronomical Society*, 4(11), 204.

Jenkins, J. M., Twicken, J. D., McCauliff, S., Campbell, J., Sanderfer, D., Lung, D., Mansouri-Samani, M., Girouard, F., Tenenbaum, P., Klaus, T., Smith, J. C., Caldwell, D. A., Chacon, A. D., Henze, C., Heiges, C., Latham, D. W., Morgan, E., Swade, D., Rinehart, S., & Vanderspek, R. (2016). The TESS science processing operations center. In G. Chiozzi & J. C. Guzman (Eds.), *Software and Cyberinfrastructure for Astronomy IV*, volume 9913 of *Society of Photo-Optical Instrumentation Engineers (SPIE) Conference Series* (pp. 99133E).

Kellermann, C., Becker, A., & R., R. (2018). Interior structure models and fluid Love numbers of exoplanets in the super-Earth regime. *Astronomy & Astrophysics*.

Kiefer, F. (2019). Determining the mass of the planetary candidate HD 114762 b using Gaia. *A&A*, 632, L9.

Kislyakova, K. G., Noack, L., Johnstone, C. P., Zaitsev, V. V., Fossati, L., Lammer, H., Khodachenko, M. L., Odert, P., & Güdel, M. (2017). Magma oceans and enhanced volcanism on TRAPPIST-1 planets due to induction heating. *Nature Astronomy*, 1(12), 878–885.

Koch, D. G., Borucki, W. J., Basri, G., Batalha, N. M., Brown, T. M., Caldwell, D., Christensen-Dalsgaard, J., Cochran, W. D., DeVore, E., Dunham, E. W., Gautier, Thomas N., I., Geary, J. C., Gilliland, R. L., Gould, A., Jenkins, J., Kondo, Y., Latham, D. W., Lissauer, J. J., Marcy, G., Monet, D., Sasselov, D., Boss, A., Brownlee, D., Caldwell, J., Dupree, A. K., Howell, S. B., Kjeldsen, H., Meibom, S., Morrison, D., Owen, T., Reitsema, H., Tarter, J., Bryson, S. T., Dotson, J. L., Gazis, P., Haas, M. R., Kolodziejczak, J., Rowe, J. F., Van Cleve, J. E., Allen, C., Chandrasekaran, H., Clarke, B. D., Li, J., Quintana, E. V., Tenenbaum, P., Twicken, J. D., & Wu, H. (2010). Kepler Mission Design, Realized Photometric Performance, and Early Science. *The Astrophysical Journal Letters*, 713(2), L79–L86.

Latham, D. W., Mazeh, T., Stefanik, R. P., Mayor, M., & Burki, G. (1989). The unseen companion of HD114762: a probable brown dwarf. *Nature*, 339(6219), 38–40.

Lawton, A. T. & Wright, P. (1989). A planetary system for Gamma Cephei? *Journal of the British Interplanetary Society*, 42, 335.

Léger, A., Selsis, F., Sotin, C., Guillot, T., Despois, D., Mawet, D., Ollivier, M., Labèque, A., Valette, C., Brachet, F., Chazelas, B., & Lammer, H. (2004). A new family of planets? "Ocean-Planets". *Icarus*, 169, 499–504.

Lodders, K., Palme, H., & Gail, H. P. (2009). Abundances of the Elements in the Solar System. *Landolt-Börnstein*, 4B, 712.

Lopez, E. D. & Fortney, J. J. (2014). Understanding the mass-radius relation for sub-neptunes: Radius as a proxy for composition. *The Astrophysical Journal*, 792(1), 1.

Lovis, C., Ségransan, D., Mayor, M., Udry, S., Benz, W., Bertaux, J. L., Bouchy, F., Correia, A. C. M., Laskar, J., Lo Curto, G., Mordasini, C., Pepe, F., Queloz, D., & Santos, N. C. (2011). The HARPS search for southern extra-solar planets. XXVIII. Up to seven planets orbiting HD 10180: probing the architecture of low-mass planetary systems. *A&A*, 528, A112.

Madhusudhan, N., Lee, K. K. M., & Mousis, O. (2012). A possible carbon-rich interior in super-earth 55 cancri e. *The Astrophysical Journal Letters*, 759(2), L40.

Majewski, S. R., Schiavon, R. P., Frinchaboy, P. M., Allende Prieto, C., Barkhouser, R., Bizyaev, D., Blank, B., Brunner, S., Burton, A., Carrera, R., Chojnowski, S. D., Cunha, K., Epstein, C., Fitzgerald, G., García Pérez, A. E., Hearty, F. R., Henderson, C., Holtzman, J. A., Johnson, J. A., Lam, C. R., Lawler, J. E., Maseman, P., Mészáros, S., Nelson, M., Nguyen, D. C., Nidever, D. L., Pinsonneault, M., Shetrone, M., Smee, S., Smith, V. V., Stolberg, T., Skrutskie, M. F., Walker, E., Wilson, J. C., Zasowski, G., Anders, F., Basu, S., Beland, S., Blanton, M. R., Bovy, J., Brownstein, J. R., Carlberg, J., Chaplin, W., Chiappini, C., Eisenstein, D. J., Elsworth, Y., Feuillet, D., Fleming, S. W., Galbraith-Frew, J., García, R. A., García-Hernández, D. A., Gillespie, B. A., Girardi, L., Gunn, J. E., Hasselquist, S., Hayden, M. R., Hekker, S., Ivans, I., Kinemuchi, K., Klaene, M., Mahadevan, S., Mathur, S., Mosser, B., Muna, D., Munn, J. A., Nichol, R. C., O'Connell, R. W., Parejko, J. K., Robin, A. C., Rocha-Pinto, H., Schultheis, M., Serenelli, A. M., Shane, N., Silva Aguirre, V., Sobeck, J. S., Thompson, B., Troup, N. W., Weinberg, D. H., & Zamora, O. (2017). The Apache Point Observatory Galactic Evolution Experiment (APOGEE). *Astronomical Journal*, 154(3), 94.

Martell, S. L., Tinney, C. G., Marshall, J. P., Wittenmyer, R., Zwitter, T., Carollo, D., Kafle, P. R., Huber, D., Stello, D., Lewis, G. F., Bland-Hawthorn, J., Kos, J., Sharma, S., De Silva, G., Ness, M., Buder, S., Lind, K., Nataf, D., Da Costa, G. S., Lin, J., Freeman, K. C., Schlesinger, K. J., Casagrande, L., Duong, L., Asplund, M., Watson, F. G., Simpson, J., Hyde, E. A., Zucker, D. B., Horner, J., Casey, A. R., Anguiano, B., Bacigalupo, C., & Navin, C. A. (2016). The GALAH survey: observational overview and Gaia DR1 companion. *Monthly Notices of the Royal Astronomical Society*, 465(3), 3203–3219.

Mayor, M. & Queloz, D. (1995). A Jupiter-mass companion to a solar-type star. *Nature*, 378, 355.

McArthur, B. E., Endl, M., Cochran, W. D., Benedict, G. F., Fischer, D. A., Marcy, G. W., Butler, R. P., Naef, D., Mayor, M., Queloz, D., Udry, S., & Harrison, T. E. (2004). Detection of a neptune-mass planet in the rho1 cancri system using the hobby-eberly telescope. *The Astrophysical Journal Letters*, 614(1), L81.

Mocquet, A., Grasset, O., & Sotin, C. (2014). Very high-density planets: a possible remnant of gas giants. *Philosophical Transactions of the Royal Society of London A: Mathematical, Physical and Engineering Sciences*, 372(2014).

Morton, T. D. (2015). isochrones: Stellar model grid package.

Morton, T. D., Bryson, S. T., Coughlin, J. L., Rowe, J. F., Ravichandran, G., Petigura, E. A., Haas, M. R., & Batalha, N. M. (2016). False positive probabilities for all kepler objects of interest: 1284 newly validated planets and 428 likely false positives. *The Astrophysical Journal*, 822(2), 86.

Naef, D., Latham, D. W., Mayor, M., Mazeh, T., Beuzit, J. L., Drukier, G. A., Perrier-Bellet, C., Queloz, D., Sivan, J. P., Torres, G., Udry, S., & Zucker, S. (2001). Hd 80606 b, a planet on an extremely elongated orbit*. *Astronomy & Astrophysics*, 375(2), L27–L30.

Noack, L., Godolt, M., von Paris, P., Plesa, A.-C., Stracke, B., Breuer, D., & Rauer, H. (2014). Can the interior structure influence the habitability of a rocky planet? *P&SS*, 98, 14–29.

Osborn, A. & Bayliss, D. (2020). Investigating the planet-metallicity correlation for hot Jupiters. *Monthly Notices of the Royal Astronomical Society*, 491(3), 4481–4487.

Perryman, M. (2018). *The Exoplanet Handbook*. Cambridge University Press.

Perryman, M., Hartman, J., Bakos, G. Á., & Lindegren, L. (2014). Astrometric Exoplanet Detection with Gaia. *The Astrophysical Journal*, 797(1), 14.

Petigura, E. A., Marcy, G. W., Winn, J. N., Weiss, L. M., Fulton, B. J., Howard, A. W., Sinukoff, E., Isaacson, H., Morton, T. D., & Johnson, J. A. (2018). The California-Kepler Survey. IV. Metal-rich Stars Host a Greater Diversity of Planets. *Astronomical Journal*, 155(2), 89.

Recio-Blanco, A., de Laverny, P., Allende Prieto, C., Fustes, D., Manteiga, M., Arcay, B., Bijaoui, A., Dafonte, C., Ordenovic, C., & Ordoñez Blanco, D. (2016). Stellar parametrization from Gaia RVS spectra. *A&A*, 585, A93.

Ricker, G. R., Winn, J. N., Vanderspek, R., Latham, D. W., Bakos, G. A., Bean, J. L., Berta-Thompson, Z. K., Brown, T. M., Buchhave, L., Butler, N. R., Butler, R. P., Chaplin, W. J., Charbonneau, D. B., Christensen-Dalsgaard, J., Clampin, M., Deming, D., Doty, J. P., Lee, N. D., Dressing, C., Dunham, E. W., Endl, M., Fressin, F., Ge, J., Henning, T., Holman, M. J., Howard, A. W., Ida, S., Jenkins, J. M., Jernigan, G., Johnson, J. A., Kaltenegger, L., Kawai, N., Kjeldsen, H., Laughlin, G., Levine, A. M., Lin, D., Lissauer, J. J., MacQueen, P., Marcy, G., McCullough, P. R., Morton, T. D., Narita, N., Paegert, M., Palle, E., Pepe, F., Pepper, J., Quirrenbach, A., Rinehart, S. A., Sasselov, D., Sato, B., Seager, S., Sozzetti, A., Stassun, K. G., Sullivan, P., Szentgyorgyi, A., Torres, G., Udry, S., & Villasenor, J. (2014). Transiting exoplanet survey satellite. *Journal of Astronomical Telescopes, Instruments, and Systems*, 1, 1 – 1 – 10.

Rogers, L. A. (2015). Most 1.6 earth-radius planets are not rocky. *The Astrophysical Journal*, 801(1), 41.

Rogers, L. A. & Seager, S. (2010). A framework for quantifying the degeneracies of exoplanet interior compositions. *The Astrophysical Journal*, 712(2), 974.

Santos, N. C., Israelian, G., & Mayor, M. (2001). The metal-rich nature of stars with planets. *A&A*, 373, 1019–1031.

Schaefer, L. & Fegley, B. (2009). Chemistry of Silicate Atmospheres of Evaporating Super-Earths. *The Astrophysical Journal Letters*, 703, L113–L117.

Seager, S. (2013). Exoplanet habitability. *Science*, 340(6132), 577–581.

Shallue, C. J. & Vanderburg, A. (2018). Identifying exoplanets with deep learning: A five-planet resonant chain around kepler-80 and an eighth planet around kepler-90. *The Astronomical Journal*, 155(2), 94.

Shapiro, R. & Schulze-Makuch, D. (2009). The Search for Alien Life in Our Solar System: Strategies and Priorities. *Astrobiology*, 9(4), 335–343.

Smalley, B. (2005). T_{eff} and log g determinations. *Memorie della Societa Astronomica Italiana Supplementi*, 8, 130.

Sotin, C., Grasset, O., & Mocquet, A. (2007). Mass radius curve for extrasolar Earth-like planets and ocean planets. *Icarus*, 191, 337–351.

Spiegel, D. S., Fortney, J. J., & Sotin, C. (2014). Structure of exoplanets. *Proceedings of the National Academy of Sciences*, 111(35), 12622–12627.

Stassun, K. G., Oelkers, R. J., Pepper, J., Paegert, M., De Lee, N., Torres, G., Latham, D. W., Charpinet, S., Dressing, C. D., Huber, D., Kane, S. R., Lépine, S., Mann, A., Muirhead, P. S., Rojas-Ayala, B., Silvotti, R., Fleming, S. W., Levine, A., & Plavchan, P. (2018). The TESS Input Catalog and Candidate Target List. *Astronomical Journal*, 156(3), 102.

Steinmetz, M., Zwitter, T., Siebert, A., Watson, F. G., Freeman, K. C., Munari, U., Campbell, R., Williams, M., Seabroke, G. M., Wyse, R. F. G., Parker, Q. A., Bienaymé, O., Roeser, S., Gibson, B. K., Gilmore, G., Grebel, E. K., Helmi, A., Navarro, J. F., Burton, D., Cass, C. J. P., Dawe, J. A., Fiegert, K., Hartley, M., Russell, K. S., Saunders, W., Enke, H., Bailin, J., Binney, J., Bland -Hawthorn, J., Boeche, C., Dehnen, W., Eisenstein, D. J., Evans, N. W., Fiorucci, M., Fulbright, J. P., Gerhard, O., Jauregi, U., Kelz, A., Mijović, L., Minchev, I., Parmentier, G., Peñarrubia, J., Quillen, A. C., Read, M. A., Ruchti, G., Scholz, R. D., Siviero, A., Smith, M. C., Sordo, R., Veltz, L., Vidrih, S., von Berlepsch, R., Boyle, B. J., & Schilbach, E. (2006). The Radial Velocity Experiment (RAVE): First Data Release. *Astronomical Journal*, 132(4), 1645–1668.

Suissa, G., Chen, J., & Kipping, D. (2018). A hardcore model for constraining an exoplanet's core size. *Monthly Notices of the Royal Astronomical Society*, 476(2), 2613–2620.

Sullivan, P. W., Winn, J. N., Berta-Thompson, Z. K., Charbonneau, D., Deming, D., Dressing, C. D., Latham, D. W., Levine, A. M., McCullough, P. R., Morton, T., Ricker, G. R., Vanderspek, R., & Woods, D. (2015). The transiting exoplanet survey satellite: Simulations of planet detections and astrophysical false positives. *The Astrophysical Journal*, 809(1), 77.

Swift, J. J., Bottom, M., Johnson, J. A., Wright, J. T., McCrady, N., Wittenmeyer, R., Plavchan, P. P., Riddle, R. L., Muirhead, P. S., Herzig, E., Myles, J., Blake, C. H., Eastman, J. D., Beatty, T. G., Barnes, S. I., Gibson, S. R., Lin, B., Zhao, M., Gardner, P., Falco, E. E., Criswell, S., Nava, C., Robinson, C., Sliski, D. H., Hedrick, R., Ivarsen, K., Hjelstrom, A., de Vera, J., & Szentgyorgyi, A. (2015). Miniature exoplanet radial velocity array i: design, commissioning, and early photometric results. *Journal of Astronomical Telescopes, Instruments, and Systems*, 1, 1 – 1 – 19.

Tasker, E., Tan, J., Heng, K., Kane, S., Spiegel, D., Brasser, R., Casey, A., Desch, S., Dorn, C., Hernlund, J., Houser, C., Laneuville, M., Lasbleis, M., Libert, A.-S., Noack, L., Unterborn, C., & Wicks, J. (2017). The language of exoplanet ranking metrics needs to change. *Nature Astronomy*, 1(2), 0042.

Teske, J. K., Thorngren, D., Fortney, J. J., Hinkel, N., & Brewer, J. M. (2019). Do Metal-rich Stars Make Metal-rich Planets? New Insights on Giant Planet Formation from Host Star Abundances. *Astronomical Journal*, 158(6), 239.

Thiabaud, A., Marboeuf, U., Alibert, Y., Leya, I., & Mezger, K. (2015). Elemental ratios in stars vs planets. *Astronomy & Astrophysics*, 580, A30.

Tsapras, Y. (2018). Microlensing Searches for Exoplanets. *Geosciences*, 8(10), 365.

Unterborn, C. T., Desch, S. J., Hinkel, N. R., & Lorenzo, A. (2018). Inward migration of the TRAPPIST-1 planets as inferred from their water-rich compositions. *Nature Astronomy*, 2, 297–302.

Valencia, D., O'Connell, R. J., & Sasselov, D. (2006). Internal structure of massive terrestrial planets. *Icarus*, 181(2), 545 – 554.

Valencia, D., Sasselov, D. D., & O'Connell, R. J. (2007). Detailed Models of Super-Earths: How Well Can We Infer Bulk Properties? *The Astrophysical Journal*, 665, 1413–1420.

Vanderburg, A., Huang, C. X., Rodriguez, J. E., Becker, J. C., Ricker, G. R., Vanderspek, R. K., Latham, D. W., Seager, S., Winn, J. N., Jenkins, J. M., Addison, B., Bieryla, A., Briceño, C., Bowler, B. P., Brown, T. M., Burke, C. J., Burt, J. A., Caldwell, D. A., Clark, J. T., Crossfield, I., Dittmann, J. A., Dynes, S., Fulton, B. J., Guerrero, N., Harbeck, D., Horner, J., Kane, S. R., Kielkopf, J., Kraus, A. L., Kreidberg, L., Law, N., Mann, A. W., Mengel, M. W., Morton, T. D., Okumura, J., Pearce, L. A., Plavchan, P., Quinn, S. N., Rabus, M., Rose, M. E., Rowden, P., Shporer, A., Siverd, R. J., Smith, J. C., Stassun, K., Tinney, C. G., Wittenmyer, R., Wright, D. J., Zhang, H., Zhou, G., & Ziegler, C. A. (2019). TESS Spots a Compact System of Super-Earths around the Naked-eye Star HR 858. *The Astrophysical Journal Letters*, 881(1), L19.

Venturini, J. & Helled, R. (2017). The formation of mini-neptunes. *The Astrophysical Journal*, 848(2), 95.

Vogt, S. S., Wittenmyer, R. A., Butler, R. P., O'Toole, S., Henry, G. W., Rivera, E. J., Meschiari, S., Laughlin, G., Tinney, C. G., Jones, H. R. A., Bailey, J., Carter, B. D., & Batygin, K. (2010). A Super-Earth and Two Neptunes Orbiting the Nearby Sun-like Star 61 Virginis. *The Astrophysical Journal*, 708(2), 1366–1375.

Wagner, F. W., Tosi, N., Sohl, F., Rauer, H., & Spohn, T. (2012). Rocky super-Earth interiors. Structure and internal dynamics of CoRoT-7b and Kepler-10b. *A&A*, 541, A103.

Weiss, L. M. & Marcy, G. W. (2014). The mass-radius relation for 65 exoplanets smaller than 4 earth radii. *The Astrophysical Journal Letters*, 783(1), L6.

Winn, J. N., Sanchis-Ojeda, R., Rogers, L., Petigura, E. A., Howard, A. W., Isaacson, H., Marcy, G. W., Schlaufman, K. C., Cargile, P., & Hebb, L. (2017). Absence of a Metallicity Effect for Ultra-short-period Planets. *Astronomical Journal*, 154(2), 60.

Wittenmyer, R. A., Clark, J. T., Sharma, S., Stello, D., Horner, J., Kane, S. R., Stevens, C. P., Wright, D. J., Spina, L., Čotar, K., Asplund, M., Bland-Hawthorn, J., Buder, S., Casey, A. R., De Silva, G. M., D'Orazi, V., Freeman, K., Kos, J., Lewis, G., Lin, J., Lind, K., Martell, S. L., Simpson, J. D., Zucker, D. B., & Zwitter, T. (2020). K2-HERMES II. Planet-candidate properties from K2 Campaigns 1-13. *Monthly Notices of the Royal Astronomical Society*, 496(1), 851–863.

Wittenmyer, R. A., Horner, J., Tinney, C. G., Butler, R. P., Jones, H. R. A., Tuomi, M., Salter, G. S., Carter, B. D., Koch, F. E., O'Toole, S. J., Bailey, J., & Wright, D. (2014). The Anglo-Australian Planet Search. XXIII. Two New Jupiter Analogs. *The Astrophysical Journal*, 783(2), 103.

Wittenmyer, R. A., Jones, M. I., Horner, J., Kane, S. R., Marshall, J. P., Mustill, A. J., Jenkins, J. S., Rojas, P. A. P., Zhao, J., Villaver, E., Butler, R. P., & Clark, J. (2017). The pan-pacific planet search. vii. the most eccentric planet orbiting a giant star. *The Astronomical Journal*, 154(6), 274.

Wolszczan, A. (1994). Confirmation of Earth-Mass Planets Orbiting the Millisecond Pulsar PSR B1257+12. *Science*, 264(5158), 538–542.

Zeng, L. & Jacobsen, S. B. (2017). A simple analytical model for rocky planet interiors. *The Astrophysical Journal*, 837(2), 164.

Zeng, L. & Sasselov, D. (2013). A Detailed Model Grid for Solid Planets from 0.1 through 100 Earth Masses. *PASP*, 125(925), 227.

Zeng, L., Sasselov, D. D., & Jacobsen, S. B. (2016). Mass-Radius Relation for Rocky Planets Based on PREM. *The Astrophysical Journal*, 819(2), 127.

A

K2-HERMES II. Planet-candidate properties from K2 Campaigns 1-13

A significant contribution was made to the following paper which includes adjacent work to this thesis. This includes using the same methodology as in (Clark et al., 2021) to refine the planetary parameters of candidate and confirmed planetary systems observed by the K2 mission. My contribution includes determining the physical stellar parameters of the host stars, and recomputing their planetary companion radii. I also calculated the stellar luminosities, equilibrium temperatures and habitable zones for all planetary systems. The majority of plots within this text were also created by me. The published paper Wittenmyer et al. (2020), "K2-HERMES II. Planet-candidate properties from K2 Campaign" follows.

Monthly Notices of the ROYAL ASTRONOMICAL SOCIETY

MNRAS **496,** 851–863 (2020) doi:10.1093/mnras/staa1528
Advance Access publication 2020 June 3

K2-HERMES II. Planet-candidate properties from K2 Campaigns 1-13

Robert A. Wittenmyer [1]★ Jake T. Clark,[1] Sanjib Sharma [2] Dennis Stello,[3] Jonathan Horner,[1] Stephen R. Kane,[4] Catherine P. Stevens,[5] Duncan J. Wright,[1] Lorenzo Spina,[6] Klemen Čotar [7] Martin Asplund,[8] Joss Bland-Hawthorn [2] Sven Buder [8,9,10] Andrew R. Casey [6] Gayandhi M. De Silva,[2] Valentina D'Orazi [11] Ken Freeman,[8] Janez Kos,[2] Geraint Lewis [2] Jane Lin,[2] Karin Lind,[10,12] Sarah L. Martell [3,9] Jeffrey D. Simpson [3] Daniel B. Zucker[13,14] and Tomaz Zwitter [7]

[1]*University of Southern Queensland, Centre for Astrophysics, USQ Toowoomba, Toowoomba, QLD 4350, Australia*
[2]*Sydney Institute for Astronomy, School of Physics, University of Sydney, Sydney, NSW 2006, Australia*
[3]*School of Physics, University of New South Wales, Sydney, NSW 2052, Australia*
[4]*Department of Earth and Planetary Sciences, University of California, Riverside, CA 92521, USA*
[5]*Department of Physics, Westminster College, New Wilmington, PA 16172, USA*
[6]*Monash Centre for Astrophysics, School of Physics and Astronomy, Monash University, Monash, VIC 3800, Australia*
[7]*Faculty of Mathematics and Physics, University of Ljubljana, Jadranska 19, 1000 Ljubljana, Slovenia*
[8]*Research School of Astronomy and Astrophysics, Australian National University, Canberra, ACT 2611, Australia*
[9]*ARC Centre of Excellence for All Sky Astrophysics in 3 Dimensions (ASTRO 3D), Canberra, ACT 2611, Australia*
[10]*Max Planck Institute for Astronomy (MPIA), Koenigstuhl 17, D-69117 Heidelberg, Germany*
[11]*INAF Osservatorio Astronomico di Padova, vicolo dell'Osservatorio 5, I-35122 Padova, Italy*
[12]*Department of Physics and Astronomy, Uppsala University, Box 516, SE-751 20 Uppsala, Sweden*
[13]*Department of Physics and Astronomy, Macquarie University, Sydney, NSW 2109, Australia*
[14]*Research Centre in Astronomy, Astrophysics and Astrophotonics, Macquarie University, Sydney, NSW 2109, Australia*

Accepted 2020 May 21. Received 2020 May 20; in original form 2020 March 10

ABSTRACT

Accurate and precise radius estimates of transiting exoplanets are critical for understanding their compositions and formation mechanisms. To know the planet, we must know the host star in as much detail as possible. We present complete results for planet-candidate hosts from the K2-HERMES survey, which uses the HERMES multi-object spectrograph on the Anglo-Australian Telescope to obtain $R \sim 28\,000$ spectra for more than 30 000 K2 stars. We present complete host-star parameters and planet-candidate radii for 224 K2 candidate planets from C1–C13. Our results cast severe doubt on 30 K2 candidates, as we derive unphysically large radii, larger than $2R_{\rm Jup}$. This work highlights the importance of obtaining accurate, precise, and self-consistent stellar parameters for ongoing large planet search programs – something that will only become more important in the coming years, as *TESS* begins to deliver its own harvest of exoplanets.

Key words: techniques: spectroscopic – planets and satellites: fundamental parameters – stars: fundamental parameters.

1 INTRODUCTION

With the discovery of the first planets orbiting other stars (Campbell, Walker & Yang 1988; Latham et al. 1989; Wolszczan & Frail 1992; Mayor & Queloz 1995), humanity entered the 'Exoplanet Era'. For the first time, we had confirmation that the Solar system was not unique, and began to realize that planets are ubiquitous in the cosmos (e.g. Fressin et al. 2013; Winn & Fabrycky 2015; Hardegree-Ullman et al. 2019). At the same time, we learned that planetary systems are far more diverse than we had previously imagined. We discovered planets denser than lead and more insubstantial than candy floss (Burgasser et al. 2010; Masuda 2014; Johns et al. 2018; Raetz et al. 2019), found a myriad of systems containing giant planets orbiting perilously close to their host stars (e.g. Mayor & Queloz 1995; Masset & Papaloizou 2003; Bouchy et al. 2005; Hellier et al.

★ E-mail: rob.w@usq.edu.au

2011; Albrecht et al. 2012; Wright et al. 2012), and discovered others with planets moving on highly elongated, eccentric orbits, similar to those of comets in the Solar system (e.g. Wittenmyer et al. 2007; Tamuz et al. 2008; Harakawa et al. 2015; Wittenmyer et al. 2017). We even uncovered two types of planets that have no direct analogue in the Solar system – the super-Earths and sub-Neptunes (e.g. Charbonneau et al. 2009; Vogt et al. 2010; Winn et al. 2011; Howard et al. 2012; Sinukoff et al. 2016).

The rate at which we found new exoplanets was boosted dramatically by the launch of the *Kepler* spacecraft in 2009. In the years that followed, *Kepler* performed the first great census of the Exoplanet Era. In doing so, it revolutionized exoplanetary science, discovering some 2347 validated planets,[1] and finding hundreds of multiply-transiting systems (e.g. Borucki et al. 2010; Batalha et al. 2013; Mullally et al. 2015). After the failure of its second reaction wheel in 2013, the spacecraft was repurposed to carry out the 'K2' mission (Howell et al. 2014). *Kepler's* golden years were spent in ∼80-d observations of fields along the ecliptic plane, with targets selected by the broader astronomical community for a wide range of astrophysical studies beyond planet search. A total of 20 pointings ('campaigns') were performed until the spacecraft station-keeping fuel was exhausted in 2018 October. Altogether, the K2 mission observed more than 150 000 stars across 20 campaigns, resulting in 397 confirmed and 891 candidate planets to date.[2]

With the exception of the small number of directly imaged exoplanets (e.g. Kalas et al. 2008; Marois et al. 2008, 2010; Lagrange et al. 2009), our knowledge of the new worlds we discover has been gleaned indirectly. We observe a star doing something unexpected, and infer the presence of a planet. Our knowledge of the planets we find in this manner is directly coupled to our understanding of their host stars. For example, consider the case of a planet discovered using the transit technique. By measuring the degree to which the light of the planet's host star is attenuated during the transit, it is possible to infer the planet's size. The larger the planet, the more light it will block, and the greater the dimming of its host star. As a result, it is relatively straightforward to determine the size of the planet *relative to its host star*. When converting those measurements to a true diameter for the newly discovered world, however, one must base that diameter on the calculated/assumed size of the host star. Any uncertainty in the size of the host carries through to the determination of the size of the planet.

For that reason, it is critically important for us to be able to accurately characterize the stars that host planets. The more information we have about those stars, and the more precise those data, the more accurately we can determine the nature of their orbiting planets.

Over the past few years, the Galactic Archaeology with HERMES survey (GALAH) has been gathering highly detailed spectra of a vast number of stars in the local Solar neighbourhood (e.g. De Silva et al. 2015; Martell et al. 2017; Buder et al. 2018). The survey uses the High Efficiency and Resolution Multi-Element Spectrograph (HERMES) on the Anglo-Australian Telescope (Freeman 2012; Simpson et al. 2016) to simultaneously obtain approximately 400 spectra in a given exposure. Analysis of those high-resolution spectra allows the determination of a variety of the properties of those stars, along with the calculation of accurate abundances for up to thirty different elements in their outer atmospheres. GALAH aims to survey a million stars, facilitating an in-depth study of our Galaxy's star formation history – and has already yielded impressive results (e.g. Duong et al. 2018; Gao et al. 2018; Quillen et al. 2018; Zwitter et al. 2018; Kos et al. 2018a,b; Čotar et al. 2019a,b; Žerjal et al. 2019). Whilst the data obtained by the GALAH survey is clearly of great interest to stellar and Galactic astronomers, it can also provide information of critical importance to the exoplanet community. For that reason, in this work we describe the results of the K2-HERMES survey, whose design follows that of the main GALAH program, but is designed specifically to maximize the scientific value of the plethora of exoplanets and oscillating stars discovered during *Kepler's* K2 mission (Wittenmyer et al. 2018; Sharma et al. 2019).

K2-HERMES is a survey born out of the urgent need for accurate, precise, and self-consistent physical parameters for stars including those hosting candidate planets. Using the same instrumental setup and data processing pipelines as GALAH, the K2-HERMES survey aims to collect a spectrum for as many K2 target stars as possible in a given colour–magnitude limited sample. For each target so observed, we compute spectroscopic stellar parameters ($T_{\rm eff}$, log g, [Fe/H]), as well as the derived physical parameters such as mass, radius, luminosity, and age. The HERMES instrument was specifically designed to measure the chemical abundances of up to thirty elements for the GALAH survey, and so those abundances are also delivered by the standard GALAH data processing pipeline. A forthcoming paper, Clark et al. (in preparation), will present a detailed analysis of the chemical abundance results in the context of the *Transiting Exoplanet Survey Satellite* mission, *TESS*.

In this paper, we present the complete results of planet-candidate properties from the K2-HERMES survey for K2 campaigns 1-13. In Section 2, we briefly describe the observing strategy and data analysis procedures, and we detail how the stellar physical parameters have been derived. Section 3 gives the physical properties of the K2 planet candidates and their host stars. Finally, in Section 4, we place our results in context and present our conclusions.

2 OBSERVATIONS AND DATA ANALYSIS

Target selection for the K2-HERMES program is described fully in our previous work (Wittenmyer et al. 2018; Sharma et al. 2019). Fig. 1 shows the HERMES field of view overlaid on the *Kepler* field. For this study, we selected all K2 planet candidate host stars which had been observed in the K2-HERMES program.

2.1 Determination of stellar parameters

We find 199 stars hosting 224 K2 planet candidates for which K2-HERMES spectra are available. The reduction and analysis procedures are identical to those of the GALAH and TESS-HERMES surveys, as described fully in Kos et al. (2017), Buder et al. (2018), and Sharma et al. (2018).

With a self-consistent set of spectroscopic parameters in hand ($T_{\rm eff}$, log g, [Fe/H]), we derived the stellar physical parameters using the `isochrones` Python package (Morton 2015). `isochrones` is a Bayesian isochronic modeller that determines the mass, radius, and age of stars given various photometric and spectroscopic inputs using MESA Isochrones & Stellar Tracks (MIST) (Dotter 2016) grids. For our analysis, we used the effective temperature ($T_{\rm eff}$), surface gravity (log g), 2MASS (H, J, K_s) (Skrutskie et al. 2006), and *Gaia* (G, G_{RP}, G_{BP}) photometric magnitudes along with parallax

[1] as of 2020 February 26, from the NASA Exoplanet Archive, https://exoplanetarchive.ipac.caltech.edu/. A further 2420 candidate planets were found during the *Kepler* main mission, and still await confirmation.
[2] Planet data obtained from the NASA Exoplanet Archive, accessed 2020 February 26, at https://exoplanetarchive.ipac.caltech.edu/

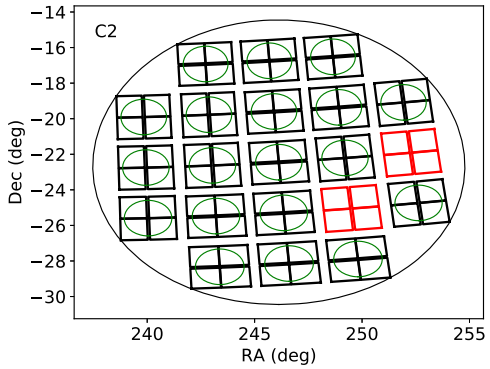

Figure 1. The *Kepler* field of view and the layout of its CCD modules, overlaid with the HERMES field of view (green circles). The red modules are inoperative.

values obtained by *Gaia* DR2 (Gaia Collaboration 2018) where available.

Accurate isochrone models rely upon a star's global metallicity, commonly referred as [M/H]. The assumption that the iron abundance [Fe/H] can be a proxy (or even equal) to [M/H] breaks down for metal-poor stars. In these metal-poor stars, the radiative opacity can be heavily affected by alpha-elements, in our case Mg, Si, Ca, and Ti. Including alpha-elements into our global metallicity thus better predicts the physical parameters derived with `isochrones`. We calculate our [α/Fe] values through equation (1), which is the exact procedure taken by GALAH DR2:

$$[\alpha/Fe] = \frac{\sum \frac{[X/Fe]}{(e\_[X/Fe])^2}}{\sum (e\_[X/Fe])^{-2}}, \quad (1)$$

where X = Mg, Si, Ca, Ti, and e_[X/Fe] is the abundance's associated error. [α/Fe] is calculated even if one or more of these elements are missing. From [Fe/H] and [α/Fe], we can then calculate [M/H] through a relationship between these quantities laid out in Salaris, Chieffi & Straniero (1993):

$$[M/H] = [Fe/H] + \log_{10}\left(0.638 * f_\alpha + 0.362\right), \quad (2)$$

where f_α is the α-element enhancement factor given by $f_\alpha = 10^{[\frac{\alpha}{Fe}]}$. Our calculated [M/H] value is then used for our isochrone star model on top of the discussed parameters above. After the model reaches convergence, median output values of the stellar mass, radius, density, age, bolometric luminosity and equivalent evolution phase and their corresponding 1-σ errors are calculated from the posterior distributions. We calculate the stellar luminosity by:

$$\left(\frac{L}{L_\odot}\right) = \left(\frac{R}{R_\odot}\right)^2 \left(\frac{T}{T_\odot}\right)^4. \quad (3)$$

A Hertzsprung–Russell diagram of our results is shown in Fig. 2, based on our $T_{\rm eff}$, log g, and `isochrones`-derived stellar luminosity. This sanity check confirms that none of our 199 K2 stars fall in unphysical regions of parameter space. Three stars (EPIC 201516974, 211351816, 211390903) show asteroseismic detections of the large frequency separation, $\Delta\nu$, and the frequency at maximum power, $\nu_{\rm max}$. For these detections we used EVEREST K2 light curves (Luger et al. 2016) that we analysed following the approach by Stello et al. (2017), which uses the method by Huber et al. (2009) with the improvements described in Huber et al. (2011) and in Yu et al. (2018). Then, using the seismic $\Delta\nu$ and $\nu_{\rm max}$ and

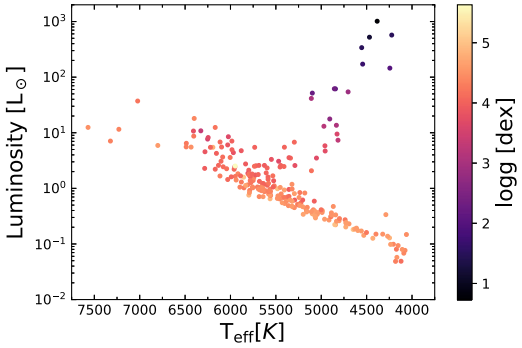

Figure 2. H–R diagram of our K2-HERMES and `isochrones`-derived results for 199 K2 stars.

the methods of Hon, Stello & Yu (2018) and Sharma et al. (2016), we derived physical parameters for these three stars and give them in Table 1 alongside our spectroscopic results from `isochrones`.

The resulting stellar parameters are given in Table 2. Our K2-HERMES results have the following median uncertainties: $T_{\rm eff}$: 74 K, log g: 0.19 dex, [Fe/H]: 0.08 dex, M_*: 0.036 $M_\odot$, R_*: 0.019 $R_\odot$. Figs 3–5 compare our K2-HERMES spectroscopic parameters with those presented by Huber et al. (2016) (based largely on multicolour photometry), and recent results from Hardegree-Ullman et al. (2020) based on LAMOST spectra. Fig. 6 shows the comparison between our derived stellar radii and masses and those of Huber et al. (2016) and Hardegree-Ullman et al. (2020), as well as the radii inferred from *Gaia*.

A primary motivation for refining stellar parameters is to determine which planets would be best suited for follow-up activities (Chandler, McDonald & Kane 2016; Kempton et al. 2018; Ostberg & Kane 2019). This is particularly true of studies related to potentially habitable planets and the effect of stellar properties on the extent of the Habitable Zone (HZ) (Kane 2014, 2018). The stellar parameters derived above were used to estimate several key properties of the known planets and their systems, shown in Table 3. We calculated the incident flux received by the planet in units of the solar constant ($F_\oplus$) using the semimajor axis and stellar luminosity. We further calculated the equilibrium temperature for each planet ($T_{\rm eq}$) using both 'hot dayside' and well-mixed models, which assume that the planet re-radiates as a blackbody over 2π and 4π steradians, respectively (Kane & Gelino 2011). Finally, we calculated the HZ boundaries for each of the stars, using the formalism described by Kopparapu et al. (2013, 2014). We calculated the 'runaway greenhouse' and 'maximum greenhouse' boundaries (referred to as the 'conservative' HZ) and the empirically derived 'recent Venus' and 'early Mars' boundaries (referred to as the 'optimistic' HZ). A thorough description of these boundaries and how they are used is provided by Kane et al. (2016). Although all of the planets whose insolation properties are shown in Table 3 are interior to the HZ, some of the planets do lie in the Venus Zone (VZ) (Kane, Kopparapu & Domagal-Goldman 2014). Terrestrial planets that lie within the VZ are also valued targets for follow-up activities as they can provide insight into the boundaries of habitability and the divergence of the Venus/Earth atmospheric evolution (Kane et al. 2019). Further investigations of these systems may yet reveal additional planets within the HZ of the stars, increasing the value of those systems through comparative planetology studies of planets throughout the system.

Table 1. Stellar parameters derived from seismology, and comparison with the spectroscopic results from K2-HERMES.

EPIC	log g Seismology	Radius ($R_\odot$)	Mass ($M_\odot$)	log g K2-HERMES	Radius ($R_\odot$)	Mass ($M_\odot$)
201516974	2.934 ± 0.010	5.26 ± 0.16	0.87 ± 0.07	2.69 ± 0.16	5.84 ± 0.25	1.30 ± 0.14
211351816	3.245 ± 0.007	4.11 ± 0.07	1.08 ± 0.05	4.16 ± 0.17	4.42 ± 0.24	1.56 ± 0.15
211390903	2.626 ± 0.022	8.8 ± 0.5	1.19 ± 0.20	2.89 ± 0.19	11.10 ± 0.56	1.73 ± 0.28

Table 2. Spectroscopic and derived stellar parameters. The full version of this table is available online.

EPIC	$T_{\rm eff}$ (K)	log g	[Fe/H]	Mass ($M_\odot$)	Radius ($R_\odot$)
201110617	4247.7 ± 465.7	4.83 ± 0.23	−0.17 ± 0.10	0.695 ± 0.020	0.663 ± 0.009
201127519	4737.0 ± 58.1	4.23 ± 0.17	0.15 ± 0.07	0.832 ± 0.026	0.777 ± 0.008
201128338	4205.2 ± 81.0	4.37 ± 0.18	−0.47 ± 0.07	0.610 ± 0.012	0.594 ± 0.007
201132684	5407.0 ± 54.8	4.37 ± 0.17	0.10 ± 0.07	0.915 ± 0.029	0.947 ± 0.013
201155177	4694.2 ± 98.1	4.56 ± 0.21	−0.20 ± 0.09	0.760 ± 0.025	0.727 ± 0.014
201160662	6486.5 ± 68.9	4.25 ± 0.19	−0.81 ± 0.08	1.240 ± 0.072	2.020 ± 0.067
201264302	4181.5 ± 207.5	4.33 ± 0.21	−0.48 ± 0.09	0.446 ± 0.025	0.421 ± 0.006
201390927	4288.2 ± 71.9	4.57 ± 0.19	−0.30 ± 0.08	0.884 ± 0.053	1.050 ± 0.091
201393098	5625.9 ± 73.6	3.94 ± 0.19	−0.34 ± 0.08	1.070 ± 0.039	1.700 ± 0.040
201403446	6132.3 ± 59.9	4.05 ± 0.18	−0.47 ± 0.07	1.060 ± 0.040	1.430 ± 0.034

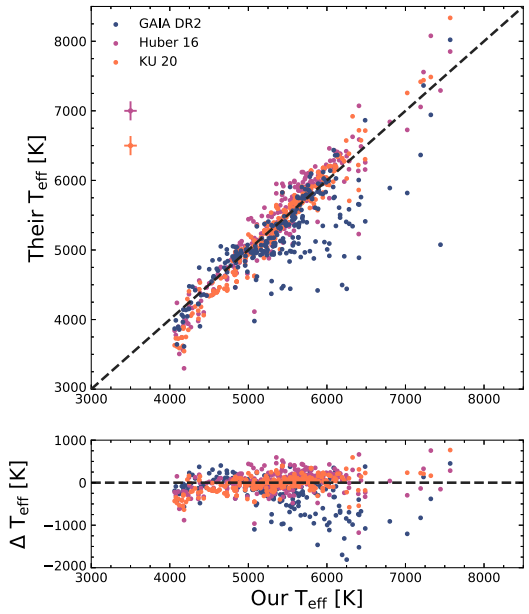

Figure 3. Comparison of our revised $T_{\rm eff}$ with published values. The RMS differences are: *Gaia* – 29 K, H16–16 K, KU20–11 K. Median error bars are also shown.

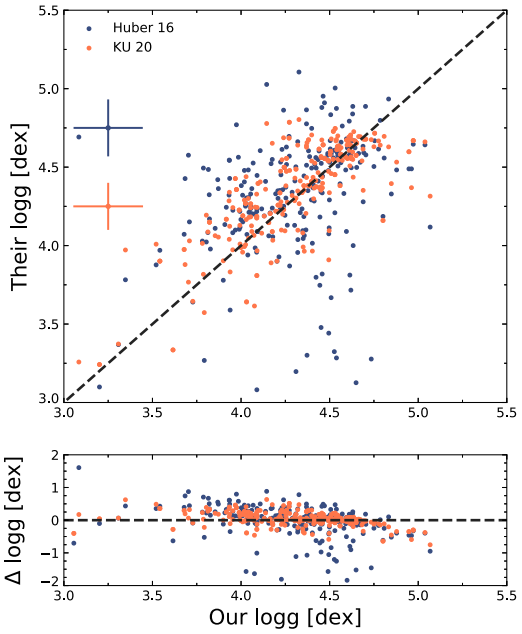

Figure 4. Comparison of our revised log g with published values. The RMS differences are: H16–0.03 dex, KU20–0.01 dex. Median error bars are also shown.

3 PLANET CANDIDATE PARAMETERS

Table 4 gives the properties of the 224 planet candidates from C1-C13 for which the K2-HERMES program has obtained spectra of their host stars. The orbital period and relative radius R_p/R_* are obtained from the NASA Exoplanet Archive, with the relevant references cited in Table 4. Where multiple published values exist, the most recent reference was chosen for our analysis. The semimajor axis values have been recalculated based on the orbital period and the revised stellar masses given in Table 2. We derived the planet-candidate radii by multiplying R_p/R_* by the stellar radii obtained by `isochrones` as described above. Uncertainties in the planetary radii result from the propagated uncertainties in R_* and R_p/R_*. As in our previous work (Wittenmyer et al. 2018), for those planet candidates without published uncertainties in R_p/R_*, we adopted the median fractional uncertainty of 0.0025 derived from the catalogue of Crossfield et al. (2016).

Using our self-consistent stellar radii, we find the derived planet-candidate radii to lie in a reasonable range for approximately

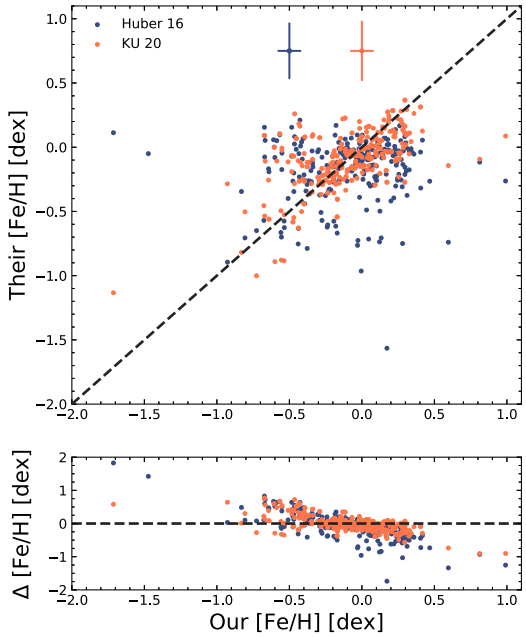

Figure 5. Comparison of our revised [Fe/H] with published values. The RMS differences are: H16–0.02 dex, KU20–0.01 dex. Median error bars are also shown.

90 per cent of the planet candidates examined here. We set an upper limit of $2R_{\rm Jup}$ ($22\,R_\oplus$), a radius larger than which no planet has been confirmed. By this criterion, we find 30 candidates with unphysically large radii, and we strongly suspect them to be false positives. All have a disposition status of 'candidate' (i.e. not 'confirmed') on the NASA Exoplanet Archive, and they are enumerated in Table 5.

We checked the *Gaia* DR2 results for evidence of hidden binarity in these 30 targets. One star (EPIC 203929178) had highly significant excess astrometric noise (hundreds of sigma). A further seven stars had uncertainties in their absolute radial velocities more than 3σ larger than the expected RV precision for stars of their temperature (Katz et al. 2019). We also flag eleven stars as giants with $\log g \lesssim 3.0$ from our spectroscopic determination. Those giant-star hosts are more likely to be false positives, e.g. wherein a grazing eclipse by an M dwarf can produce the *K*2 transit-like signal, or where the transiting object orbits a different star, as postulated by the analysis of *Kepler* giants in Sliski & Kipping (2014). Two stars have a weak secondary set of spectral lines, and are marked as binaries here. None of the 30 stars in Table 5 have K2-HERMES-derived stellar parameters that are unusually imprecise (Table 2), and so we are confident in our disposition of these planetary candidates as false positives due to their unrealistically large inferred radii. Furthermore, two stars in Table 5 have seismic detections confirming their evolved nature. EPIC 211351816, hosting the confirmed planet K2-97b (Grunblatt et al. 2018), also has a seismic detection. We derive its radius to be $4.11 \pm 0.07\,{\rm R}_\odot$ (Table 1), in turn yielding a planetary radius of $11.22 \pm 1.43\,R_\oplus$ which agrees with our K2-HERMES radius determination ($12.07 \pm 1.66\,R_\oplus$),

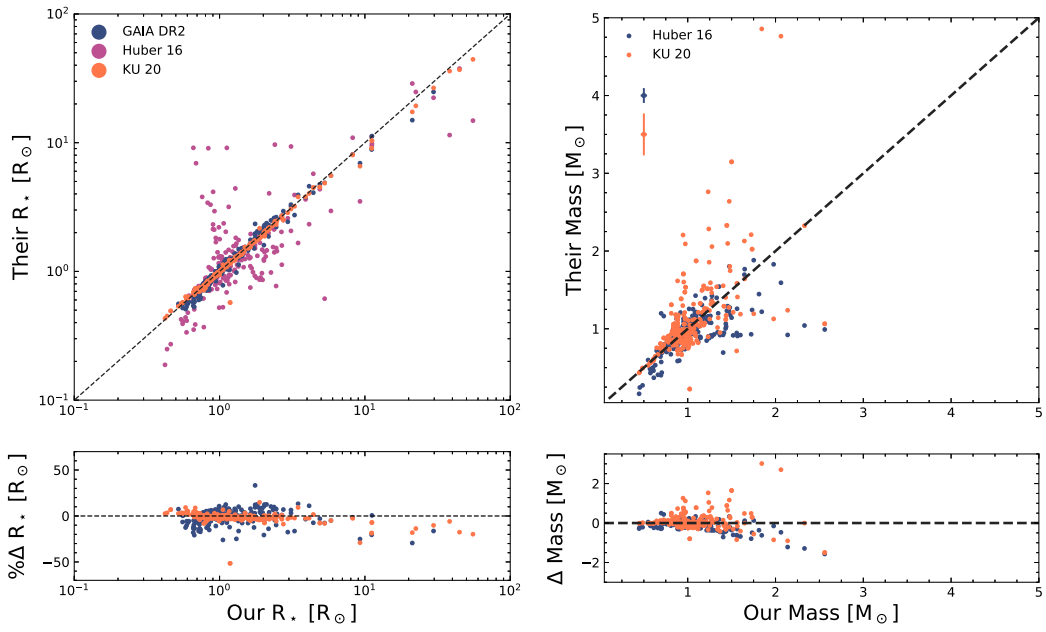

Figure 6. Comparison of our derived stellar physical parameters with published values.

Table 3. Planetary insolation and Habitable Zone boundaries. The full version of this table is available online.

EPIC	Incident Flux $F_\oplus$	T_{eq} (K) hot dayside	T_{eq} (K) well-mixed	HZ (au) inner, opt	HZ (au) inner, conserv	HZ (au) outer, conserv	HZ (au) outer opt
201110617.01	566.1	1616.0	1358.9	0.29	0.37	0.69	0.72
201127519.01	70.9	961.2	808.3	0.41	0.52	0.96	1.01
201128338.01	3.4	451.2	379.4	0.25	0.32	0.60	0.64
201132684.01	178.6	1211.0	1018.3	0.64	0.81	1.44	1.51
201132684.02	87.7	1013.8	852.5	0.64	0.81	1.44	1.51
201155177.01	57.3	911.4	766.4	0.38	0.48	0.88	0.93
201160662.01	8243.2	3156.7	2654.4	1.83	2.31	4.02	4.24
201264302.01	1722.6	2134.3	1794.7	0.18	0.23	0.42	0.45
201390927.01	262.3	1333.2	1121.1	0.47	0.59	1.11	1.17
201393098.01	73.7	970.7	816.3	1.22	1.54	2.73	2.88

Table 4. Planet-candidate properties. References – 1: Mayo et al. (2018), 2: Livingston et al. (2018b), 3: Crossfield et al. (2016), 4: Adams, Jackson & Endl (2016), 5: Vanderburg et al. (2016), 6: Schmitt et al. (2016), 7: Zink et al. (2019), 8: Pope, Parviainen & Aigrain (2016), 9: Dressing et al. (2017), 10: Nardiello et al. (2016), 11: Petigura et al. (2017), 12: Mann et al. (2017), 13: Kruse et al. (2019).

EPIC	K2 ID	Reference	P (d)	a (au)	R_p/R_*	R_p ($R_\oplus$)
201110617	K2-156	1	0.813149 ± 0.000050	0.01510 ± 0.00014	0.017041 ± 0.0014	1.23 ± 0.10
201127519	–	1	6.178369 ± 0.000195	0.06197 ± 0.0006	0.115111 ± 0.0049	9.77 ± 0.43
201128338	K2-152	2	32.6479 ± 0.01483	0.16952 ± 0.00119	0.0344 ± 0.0037	2.23 ± 0.24
201132684.01	K2-158b	2	5.90279 ± 0.00233	0.06205 ± 0.00068	0.0123 ± 0.0012	1.27 ± 0.13
201132684.02	K2-158c	2	10.06049 ± 0.00148	0.08853 ± 0.00095	0.0255 ± 0.0016	2.64 ± 0.17
201155177	K2-42	3	6.68796 ± 0.00093	0.06339 ± 0.00070	0.0304 ± 0.0028	2.41 ± 0.23
201160662	–	13	1.5374115 ± 0.0000062	0.02800 ± 0.00054	0.259 ± 0.071	57.13 ± 15.77
201264302	–	4	0.212194 ± 0.000026	0.00532 ± 0.00010	0.0271 ± 0.004	1.25 ± 0.18
201390927	–	2	2.638 ± 0.0003	0.03585 ± 0.00072	0.0265 ± 0.0025	3.04 ± 0.39
201393098	K2-7	3	28.6777 ± 0.0086	0.18752 ± 0.00232	0.0177 ± 0.0018	3.29 ± 0.34
201403446	K2-46	1	19.15454 ± 0.002849	0.14283 ± 0.00182	0.01705 ± 0.00127	2.66 ± 0.21
201407812	–	5	2.8268121	0.04192 ± 0.00060	0.4560	119.51 ± 4.02
201445732	–	13	11.20381 ± 0.00055	0.09748 ± 0.00122	0.0182 ± 0.0027	2.37 ± 0.35
201516974	–	6	36.7099 ± 0.0125	0.23590 ± 0.00833	0.0489 ± 0.0033	31.18 ± 2.50
201546283	K2-27	1	6.771389 ± 0.000062	0.06831 ± 0.00071	0.049112 ± 0.001573	4.70 ± 0.16
201561956	–	13	13.2359 ± 0.0031	0.10587 ± 0.00162	0.0208 ± 0.0046	2.17 ± 0.49
201606542	–	4	0.444372 ± 0.000042	0.01119 ± 0.00011	0.0136 ± 0.002	1.63 ± 0.24
201649426	–	5	27.770388	0.16741 ± 0.00090	0.3722	33.45 ± 0.44
201754305.02	K2-16b	3	7.61856 ± 0.00096	0.06675 ± 0.00071	0.0268 ± 0.0022	1.93 ± 0.16
201754305.01	K2-16c	3	19.077 ± 0.0033	0.12310 ± 0.00131	0.0299 ± 0.003	2.15 ± 0.22
201779067	–	5	27.242912	0.19034 ± 0.00326	0.2367	64.10 ± 1.94
201841433	–	5	12.339133	0.09614 ± 0.00097	0.02881	2.33 ± 0.21
201855371	K2-17	1	17.969079 ± 0.0014	0.11508 ± 0.00085	0.029715 ± 0.003	1.96 ± 0.20
201856786.01	–	13	3.83794 ± 0.00041	0.04178 ± 0.00090	0.0172 ± 0.003	1.46 ± 0.26
201856786.02	–	13	5.24086 ± 0.00094	0.05143 ± 0.00111	0.0166 ± 0.0027	1.41 ± 0.24
201912552	K2-18	3	32.9418 ± 0.0021	0.15444 ± 0.01138	0.0517 ± 0.0021	2.46 ± 0.14
201923289	–	5	0.78214992	0.01616 ± 0.00021	0.01346	1.34 ± 0.25
202634963	–	5	28.707623	0.20176 ± 0.00356	0.2136	44.32 ± 1.25
202675839	–	1	15.466674 ± 0.0016	0.13015 ± 0.00205	$0.12002^{+0.3}_{-0.062}$	21.36 ± 53.40
202821899	–	1	4.474513 ± 0.0003	0.05944 ± 0.00115	0.033719 ± 0.0056	8.32 ± 1.43
203070421	–	5	1.7359447	0.03340 ± 0.00062	0.02551	7.66 ± 0.81
203518244	–	5	0.8411257	0.01893 ± 0.00019	0.01098	2.84 ± 0.65
203533312	–	4	0.17566 ± 0.000183	0.00698 ± 0.00013	0.0248 ± 0.001	7.23 ± 0.35
203616858	–	13	1.68027 ± 0.00011	0.02775 ± 0.00051	0.0207 ± 0.0238	2.85 ± 3.28
203633064	–	13	0.7099504 ± 0.0000013	0.01775 ± 0.00020	0.357 ± 0.079	82.26 ± 18.41
203753577	–	5	3.4007758	0.04702 ± 0.00077	0.06863	9.74 ± 1.53
203771098.02	K2-24b	1	20.885016 ± 0.000438	0.15273 ± 0.00097	0.045111 ± 0.00227	5.71 ± 0.30
203771098.01	K2-24c	1	42.363982 ± 0.000795	0.24473 ± 0.00155	0.061091 ± 0.00174	7.74 ± 0.24
203826436.03	K2-37b	1	4.443774 ± 0.0005	0.05084 ± 0.00056	0.017091 ± 0.01883	1.56 ± 1.72
203826436.01	K2-37c	1	6.429582 ± 0.0003	0.06503 ± 0.00072	0.029105 ± 0.00353	2.66 ± 0.32
203826436.02	K2-37d	1	14.090996 ± 0.001078	0.10973 ± 0.00121	0.027017 ± 0.003572	2.47 ± 0.33
203925865	–	13	8.796890 ± 0.00059	0.08910 ± 0.00084	0.0217 ± 0.003	4.69 ± 0.66
203929178	–	3	1.153886 ± 0.000028	0.02385 ± 0.00044	0.53 ± 0.23	101.86 ± 45.55
204197636	–	13	46.1373 ± 0.00760	0.23732 ± 0.00238	0.033 ± 0.0024	3.06 ± 0.2
204221263.02	K2-38b	3	4.01628 ± 0.00044	0.05009 ± 0.00036	0.01329 ± 0.00099	1.67 ± 0.13

Table 4 *– continued*

EPIC	K2 ID	Reference	P (d)	a (au)	R_p/R_*	R_p ($R_\oplus$)
204221263.01	K2-38c	3	10.56098 ± 0.00081	0.09543 ± 0.00068	0.0195 ± 0.014	2.45 ± 1.76
204914585	–	5	18.357773	0.14669 ± 0.00221	0.01924	2.58 ± 0.34
204991696	–	13	49.8558 ± 0.0035	0.28089 ± 0.00270	0.02222 ± 0.0023	3.11 ± 0.33
205071984.01	K2-32b	1	8.991942 ± 0.000158	0.08206 ± 0.00084	0.056494 ± 0.0013	5.19 ± 0.14
205071984.03	K2-32c	1	20.661623 ± 0.001762	0.14289 ± 0.00148	0.034033 ± 0.001598	3.13 ± 0.15
205071984.02	K2-32d	1	31.715061 ± 0.002567	0.19013 ± 0.0019	0.037299 ± 0.002528	3.43 ± 0.24
205111664	–	5	15.937378	0.11803 ± 0.00112	0.02135	2.24 ± 0.27
205146011	–	13	1.057171 ± 0.000061	0.01985 ± 0.00023	0.0137 ± 0.002	1.41 ± 0.21
205170731	–	13	14.2005 ± 0.0027	0.11034 ± 0.00109	0.0276 ± 0.0053	2.81 ± 0.54
205470347	–	13	1.86732 ± 0.00016	0.02727 ± 0.00016	0.00857 ± 0.00146	0.66 ± 0.11
205503762	–	13	6.4349 ± 0.0012	0.06815 ± 0.00085	0.0152 ± 0.0052	2.24 ± 0.77
205570849	–	3	16.8580 ± 0.0011	0.12831 ± 0.00168	0.047 ± 0.057	6.21 ± 7.53
205618538	–	13	2.167697 ± 0.000022	0.03735 ± 0.00081	0.04472 ± 0.00154	11.38 ± 0.57
205924614	K2-55	3	2.849258 ± 00.000033	0.03536 ± 0.00031	0.0552 ± 0.0013	4.17 ± 0.11
205938820	–	13	4.20773 ± 0.00075	0.04966 ± 0.00052	0.0161 ± 0.0023	1.53 ± 0.22
205944181	–	1	2.475641 ± 0.000057	0.03479 ± 0.00042	$0.055833^{+0.19}_{-0.03}$	5.28 ± 17.97
205950854	K2-168	1	15.853989 ± 0.001415	0.11803 ± 0.00161	0.022489 ± 0.001272	2.21 ± 0.13
205951125	–	13	6.79143 ± 0.0008	0.06487 ± 0.00061	0.0259 ± 0.0064	2.08 ± 0.52
205957328	–	1	14.353438 ± 0.001491	0.11117 ± 0.00077	0.023912 ± 0.004385	2.11 ± 0.39
205998649	–	13	8.3958 ± 0.0028	0.08268 ± 0.00102	0.0181 ± 0.007	3.87 ± 1.50
206024342	–	3	14.637 ± 0.0021	0.11259 ± 0.00194	0.0249 ± 0.0015	2.34 ± 0.15
206026136	K2-57	3	9.0063 ± 0.0013	0.07525 ± 0.00068	0.0308 ± 0.0028	2.24 ± 0.21
206036749	–	3	1.131316 ± 0.00003	0.02226 ± 0.00034	0.047 ± 0.057	3.76 ± 0.23
206038483	K2-60	3	3.002627 ± 0.000018	0.04178 ± 0.00063	0.06191 ± 0.00035	9.87 ± 0.25
206047055	–	13	4.10290 ± 0.00180	0.05208 ± 0.00062	0.0106 ± 0.0022	2.22 ± 0.47
206055981	–	5	20.643928	0.12730 ± 0.00099	0.03129	2.10 ± 0.17
206082454.02	K2-172b	1	14.316941 ± 0.001445	0.11326 ± 0.00110	0.017579 ± 0.001495	1.67 ± 0.14
206082454.01	K2-172c	1	29.62682 ± 0.001607	0.18392 ± 0.00178	0.033824 ± 0.001324	3.21 ± 0.13
206103150.01	WASP-47b	3	4.159221 ± 0.000015	0.05047 ± 0.00058	0.10214 ± 0.0003	12.71 ± 0.27
206103150.02	WASP-47d	3	9.03164 ± 0.00064	0.08464 ± 0.00098	0.026 ± 0.0015	3.24 ± 0.20
206103150.03	WASP-47e	3	0.789518 ± 0.00006	0.01667 ± 0.00019	0.01344 ± 0.00088	1.67 ± 0.12
206114630	–	1	7.445026 ± 0.0003	0.07031 ± 0.00044	0.025337 ± 0.033876	2.29 ± 3.06
206125618	K2-64	3	6.53044 ± 0.00067	0.06671 ± 0.00089	0.0259 ± 0.0017	2.49 ± 0.18
206135682	–	5	5.025831	0.05165 ± 0.00037	0.01961	1.43 ± 0.18
206208956	–	13	5.01038 ± 0.00019	0.05878 ± 0.00120	0.0257 ± 0.0047	4.49 ± 0.85
206245553	K2-73	1	7.495692 ± 0.000283	0.07520 ± 0.00074	0.022901 ± 0.001345	2.65 ± 0.16
206260577	–	13	1.982116 ± 0.000012	0.03254 ± 0.00068	0.157 ± 0.048	31.20 ± 9.59
206369173	–	13	2.018725 ± 0.000066	0.03656 ± 0.00369	0.056 ± 0.018	129.64 ± 46.49
206414361	–	13	3.47722 ± 0.00038	0.03675 ± 0.00023	0.0253 ± 0.0086	1.44 ± 0.49
206417197	–	4	0.442094 ± 0.000086	0.01071 ± 0.00011	0.0138 ± 0.001	1.18 ± 0.09
206476150	–	13	12.19649 ± 0.00082	0.10263 ± 0.00120	0.0192 ± 0.0019	2.10 ± 0.21
210394706.02	–	13	3.16363 ± 0.00029	0.03565 ± 0.00025	0.0222 ± 0.00380	1.41 ± 0.24
210394706.01	–	13	15.0818 ± 0.0025	0.10097 ± 0.00070	0.0326 ± 0.0045	2.08 ± 0.29
210402237	K2-79	1	10.993948 ± 0.000627	0.09707 ± 0.00101	0.027782 ± 0.001543	3.85 ± 0.22
210414957	–	3	0.969967 ± 0.000012	0.02049 ± 0.00020	0.35 ± 0.15	80.64 ± 34.62
210508766.01	K2-83b	3	2.74697 ± 0.00018	0.03182 ± 0.00018	0.0268 ± 0.0019	1.59 ± 0.11
210508766.02	K2-83c	3	9.99767 ± 0.00081	0.07530 ± 0.00043	0.0319 ± 0.0018	1.89 ± 0.11
210559259	–	7	14.2683 ± 0.0012	0.10583 ± 0.00105	$0.02854^{+0.0011}_{-0.00082}$	2.24 ± 0.09
210609658	–	1	14.145239 ± 0.000468	0.12894 ± 0.00310	0.06327 ± 0.00188	22.66 ± 0.91
210629082	–	1	27.353103 ± 0.007472	0.19187 ± 0.00358	0.019308 ± 0.0029	4.13 ± 0.63
210664763	–	13	3.72007 ± 0.00047	0.04714 ± 0.00064	0.01450 ± 0.003	1.56 ± 0.32
210678858.03	–	13	10.0696 ± 0.0013	0.08767 ± 0.00066	0.0190 ± 0.0033	1.66 ± 0.29
210678858.02	–	13	14.8484 ± 0.0011	0.11358 ± 0.00085	0.0302 ± 0.003	2.64 ± 0.26
210678858.01	–	13	31.3537 ± 0.0019	0.18695 ± 0.00140	0.0432 ± 0.003	3.78 ± 0.27
210707130	K2-85	1	0.684553 ± 0.000013	0.01348 ± 0.00011	0.018081 ± 0.001436	1.32 ± 0.11
210718708	K2-86	1	8.775864 ± 0.0009	0.07978 ± 0.00093	0.025082 ± 0.003131	2.27 ± 0.28
210731500	K2-87	3	9.72739 ± 0.00087	0.08914 ± 0.00124	0.0441 ± 0.0032	6.79 ± 0.51
210775710	–	1	59.848566 ± 0.000184	0.29810 ± 0.00401	0.100817 ± 0.001863	11.45 ± 0.27
210857328	K2-177	1	14.155185 ± 0.00315	0.12655 ± 0.00223	0.015987 ± 0.0018	3.07 ± 0.36
210961508	–	4	0.349935 ± 0.000042	0.01050 ± 0.00036	0.0263 ± 0.003	8.47 ± 1.01
211087003.02	–	13	28.29213 ± 0.00126	0.18102 ± 0.00229	0.0338 ± 0.0023	3.84 ± 0.27
211327855	–	13	1.72397 ± 0.00027	0.02727 ± 0.00028	0.0137 ± 0.0038	1.26 ± 0.35
211335816	–	8	4.99	0.06106 ± 0.00103	0.043667 ± 0.0025	8.25 ± 0.53

Table 4 *– continued*

EPIC	K2 ID	Reference	P (d)	a (au)	R_p/R_*	R_p ($R_\oplus$)
211336616	–	8	44.13	0.26941 ± 0.02413	0.020655 ± 0.0025	25.26 ± 3.81
211351816	K2-97	1	8.405276 ± 0.001166	0.09382 ± 0.00307	0.025002 ± 0.003158	12.07 ± 1.66
211355342	K2-181	1	6.894252 ± 0.00043	0.07088 ± 0.00085	0.024829 ± 0.002084	2.87 ± 0.25
211357309	–	9	0.46395 ± 0.00002	0.00921 ± 0.00005	0.017 ± 0.001	0.86 ± 0.05
211359660	K2-182	1	4.736884 ± 0.000075	0.05257 ± 0.00046	0.032108 ± 0.001498	2.77 ± 0.13
211365543	–	8	5.264	0.06275 ± 0.00082	0.009804	1.68 ± 0.43
211390903	–	10	7.757595 ± 0.000822	0.09205 ± 0.00502	0.0251 ± 0.0007	30.42 ± 1.76
211491383	K2-269	1	4.145398 ± 0.001032	0.05213 ± 0.00100	0.008372 ± 0.001162	1.34 ± 0.20
211535327	–	13	20.2244 ± 0.0021	0.13749 ± 0.00166	0.0323 ± 0.0043	3.03 ± 0.41
211562654.03	K2-183b	1	0.469269 ± 0.000026	0.01139 ± 0.00014	$0.027288^{+0.27}_{-0.015}$	2.88 ± 28.54
211562654.01	K2-183c	1	10.793471 ± 0.000803	0.09213 ± 0.00117	0.026365 ± 0.002542	2.79 ± 0.27
211562654.02	K2-183d	1	22.629496 ± 0.001949	0.15093 ± 0.00192	0.026677 ± 0.002712	2.82 ± 0.29
211586387	–	8	35.383	0.22064 ± 0.00402	0.18841 ± 0.00165	2.25 ± 0.19
211611158.02	–	1	52.714072 ± 0.003819	0.27437 ± 0.00257	0.02803 ± 0.00436	2.79 ± 0.44
211611158	K2-185b	1	10.616646 ± 0.0018	0.09427 ± 0.00089	0.013164 ± 0.002118	1.31 ± 0.21
211733267	–	1	8.658168 ± 0.00003	0.07925 ± 0.00083	$0.1921^{+0.114}_{-0.059}$	18.94 ± 11.25
211736305	–	13	14.5616 ± 0.0026	0.11075 ± 0.00138	0.0305 ± 0.0149	2.71 ± 1.33
211736671	K2-108	1	4.73379 ± 0.000153	0.05695 ± 0.00065	0.030069 ± 0.002987	5.75 ± 0.59
211763214	–	1	21.191788 ± 0.003275	0.14294 ± 0.00129	0.015441 ± 0.00162	1.35 ± 0.14
211770696	–	1	16.27284 ± 0.002441	0.12608 ± 0.00175	0.018155 ± 0.00156	2.66 ± 0.24
211800191	–	1	1.106175 ± 0.000009	0.02092 ± 0.00040	0.089351 ± 0.06	11.42 ± 7.67
211816003	K2-272	11	14.453513 ± 0.001783	0.10872 ± 0.00145	0.0336 ± 0.0041	2.98 ± 0.37
211818569	K2-121	1	5.185759 ± 0.000014	0.05269 ± 0.00037	0.10208 ± 0.003964	7.49 ± 0.30
211923431	–	8	29.729	0.18570 ± 0.00199	0.025878 ± 0.0025	3.28 ± 0.33
211945201	–	1	19.491795 ± 0.000516	0.14891 ± 0.00228	0.038014 ± 0.002554	5.81 ± 0.40
211970147	K2-102	12	9.915651 ± 0.001194	0.08342 ± 0.00073	0.0169 ± 0.001	1.35 ± 0.08
211978988	–	1	36.556251 ± 0.004239	0.21767 ± 0.00283	0.026283 ± 0.001964	3.24 ± 0.25
211990866	K2-100	12	1.673915 ± 0.000011	0.02882 ± 0.00028	0.0267 ± 0.0011	3.64 ± 0.16
212006344	K2-122	9	2.21940 ± 0.00007	0.02828 ± 0.00020	0.020 ± 0.001	1.29 ± 0.07
212099230	–	11	7.112273 ± 0.000284	0.07139 ± 0.00131	0.0302 ± 0.0011	3.19 ± 0.12
212110888	K2-34	1	2.995646 ± 0.000006	0.04285 ± 0.00076	0.088002 ± 0.001666	13.93 ± 0.39
212136123	–	8	2.226	0.03192 ± 0.00033	0.026003 ± 0.0025	2.27 ± 0.22
212141021	–	8	2.918	0.03729 ± 0.00041	0.015674 ± 0.0025	1.33 ± 0.21
212159623	–	13	4.70751 ± 0.00065	0.05533 ± 0.00078	0.0139 ± 0.002	1.51 ± 0.22
212164470.01	K2-188b	1	1.742983 ± 0.00026	0.02881 ± 0.00041	0.010407 ± 0.0009	1.36 ± 0.12
212164470.02	K2-188c	1	7.807595 ± 0.000597	0.07827 ± 0.00112	0.021697 ± 0.001430	2.84 ± 0.20
212300977	WASP-55	11	4.465635 ± 0.000023	0.05359 ± 0.00058	0.1223 ± 0.0004	15.09 ± 0.26
212301649	–	8	1.225	0.02145 ± 0.00031	0.014962 ± 0.0025	1.40 ± 0.25
212362217	–	13	0.6962935 ± 0.0000087	0.01514 ± 0.00027	0.0319 ± 0.0369	3.94 ± 4.56
212393193.01	–	8	14.452	0.11948 ± 0.00141	0.0182 ± 0.0025	2.29 ± 0.32
212393193.02	–	8	36.152	0.22018 ± 0.00259	0.0183 ± 0.0025	2.30 ± 0.32
212425103	–	8	0.946	0.01782 ± 0.00024	0.017346 ± 0.0025	1.54 ± 0.23
212432685	–	11	0.531704 ± 0.000035	0.01293 ± 0.00021	0.0169 ± 0.0018	2.18 ± 0.43
212440430	–	8	19.991	0.14224 ± 0.00187	0.023276 ± 0.0025	2.54 ± 0.28
212464382	–	13	4.07337 ± 0.00051	0.04757 ± 0.00046	0.01071 ± 0.00184	0.94 ± 0.16
212495601	–	8	21.677	0.14710 ± 0.00177	0.024596 ± 0.0025	2.71 ± 0.28
212521166	K2-110	1	13.863910 ± 0.000229	0.10373 ± 0.00085	0.033432 ± 0.001766	2.61 ± 0.14
212560683	–	13	13.7043 ± 0.0037	0.11317 ± 0.00114	0.0118 ± 0.0033	1.31 ± 0.37
212585579	–	11	3.021795 ± 0.000094	0.04170 ± 0.00056	0.3876 ± 0.3569	46.56 ± 42.88
212587672	–	1	23.226001 ± 0.003092	0.15929 ± 0.00198	0.021599 ± 0.003624	2.33 ± 0.39
212624936	–	13	11.81387 ± 0.00093	0.09971 ± 0.00128	0.0258 ± 0.0036	2.63 ± 0.37
212639319	–	1	13.843725 ± 0.000948	0.12740 ± 0.00167	$0.037754^{+0.297}_{-0.0096}$	11.05 ± 86.92
212645891	–	1	0.328152 ± 0.000001	0.00934 ± 0.00018	$0.136972^{+0.113}_{-0.06}$	17.05 ± 14.07
212646483	–	8	8.253	0.08348 ± 0.00122	0.029071 ± 0.0025	6.98 ± 0.66
212652418	–	13	19.1324 ± 0.0031	0.14091 ± 0.00202	0.0186 ± 0.0022	2.78 ± 0.34
212672300	K2-194	1	39.721386 ± 0.0057	0.24073 ± 0.00258	0.026065 ± 0.002509	3.90 ± 0.39
212686205	K2-128	1	5.675814 ± 0.000427	0.05520 ± 0.00050	0.016952 ± 0.00133	1.22 ± 0.10
212688920	–	8	62.841	0.30670 ± 0.00604	0.231222 ± 0.0025	27.02 ± 0.62
212689874.01	K2-195b	1	15.853543 ± 0.00079	0.12127 ± 0.00172	0.029741 ± 0.001265	3.20 ± 0.15
212689874.02	K2-195c	1	28.482786 ± 0.00731	0.17922 ± 0.00257	0.026054 ± 0.0024	2.81 ± 0.26
212779596.01	K2-199b	1	3.225423 ± 0.000071	0.03811 ± 0.00035	0.025852 ± 0.002447	1.89 ± 0.18
212779596.02	K2-199c	1	7.374497 ± 0.000118	0.06614 ± 0.00060	0.038968 ± 0.002060	2.86 ± 0.15

Table 4 – *continued*

EPIC	K2 ID	Reference	P (d)	a (au)	R_p/R_*	R_p ($R_\oplus$)
212803289	K2-99	1	18.248708 ± 0.000634	0.15352 ± 0.00168	0.042431 ± 0.001169	12.42 ± 0.48
212828909	K2-200	1	2.849883 ± 0.000188	0.03724 ± 0.00027	0.015799 ± 0.001590	1.33 ± 0.13
213408445	–	13	2.49686 ± 0.00022	0.04315 ± 0.00386	0.072 ± 0.022	301.12 ± 94.83
213546283	–	1	9.770186 ± 0.000325	0.08877 ± 0.00103	0.029436 ± 0.0015	3.73 ± 0.20
213703832	–	11	0.515513 ± 0.000024	0.01397 ± 0.00157	0.0409 ± 0.0096	50.02 ± 13.08
213840781	–	11	12.364531 ± 0.000375	0.10365 ± 0.00208	0.4363 ± 0.2602	60.98 ± 36.40
214419545	–	13	9.40172 ± 0.00048	0.08572 ± 0.00096	0.016 ± 0.0021	2.36 ± 0.31
214630761	–	13	1.236438 ± 0.000022	0.02620 ± 0.00050	0.143 ± 0.04	48.41 ± 13.94
214741009	–	11	7.269622 ± 0.000521	0.09463 ± 0.00400	0.4156 ± 0.3808	419.79 ± 386.31
214888033	–	13	7.457597 ± 0.000096	0.07353 ± 0.00086	0.077 ± 0.015	9.42 ± 1.84
214984368	–	13	0.2633809 ± 0.000003	0.01066 ± 0.00119	0.090 ± 0.021	440.29 ± 137.57
215125108	–	13	0.738067 ± 0.000026	0.01837 ± 0.00149	0.095 ± 0.027	232.37 ± 73.82
215175768	–	13	1.726115 ± 0.000098	0.02788 ± 0.00040	0.0610 ± 0.021	6.28 ± 2.17
215364084	–	13	2.74324 ± 0.00017	0.04290 ± 0.00192	0.0526 ± 0.0265	30.33 ± 15.39
215381481	–	13	0.533393 ± 0.000027	0.01352 ± 0.00096	0.01206 ± 0.00232	72.96 ± 15.99
216111905	–	13	3.02030 ± 0.00032	0.04040 ± 0.00045	0.0410 ± 0.020	5.73 ± 2.80
216363472	–	13	8.69290 ± 0.00085	0.08138 ± 0.00108	0.0154 ± 0.0170	1.68 ± 1.86
216405287	K2-202	1	3.405164 ± 0.000126	0.04334 ± 0.00061	0.023171 ± 0.001335	2.28 ± 0.14
216494238	K2-280	1	19.894641 ± 0.002898	0.14649 ± 0.00183	0.047857 ± 0.002267	6.74 ± 0.35
218195416	–	13	0.4951253 ± 0.0000031	0.01447 ± 0.00023	0.1410 ± 0.0130	33.41 ± 3.54
218300572	–	13	1.589843 ± 0.000013	0.03266 ± 0.00094	0.114 ± 0.033	43.20 ± 12.86
219388192	–	1	5.292605 ± 0.000031	0.05860 ± 0.00076	0.094335 ± 0.000852	10.92 ± 0.22
219480273	–	13	26.48370 ± 0.0051	0.17671 ± 0.00195	0.0132 ± 0.0033	2.03 ± 0.51
219800881	K2-231	13	13.84457 ± 0.00154	0.11357 ± 0.00156	0.0248 ± 0.0018	2.74 ± 0.20
220170303	K2-203	1	9.695101 ± 0.001334	0.08375 ± 0.00062	0.01647 ± 0.003246	1.37 ± 0.27
220186645	K2-204	1	7.055784 ± 0.000650	0.07246 ± 0.00090	0.023711 ± 0.00094	3.50 ± 0.18
220198551	–	13	0.7988453 ± 0.0000083	0.01593 ± 0.00011	0.079 ± 0.035	7.26 ± 3.22
220209578	–	11	8.904519 ± 0.000205	0.08322 ± 0.00115	0.3805 ± 0.3287	44.04 ± 38.07
220245303	–	1	3.680340 ± 0.000359	0.04394 ± 0.00032	0.012565 ± 0.0022	1.05 ± 0.18
220282718	–	13	0.5551606 ± 0.0000058	0.01364 ± 0.00019	0.0630 ± 0.034	11.21 ± 6.06
220322327	–	13	3.313470 ± 0.00024	0.04074 ± 0.00047	0.042 ± 0.033	3.62 ± 2.85
220341183	K2-213	1	8.130870 ± 0.001799	0.08241 ± 0.00088	0.011526 ± 0.001564	1.66 ± 0.23
220400100	–	7	10.7946 ± 0.0019	0.08817 ± 0.00080	$0.0314^{+0.0039}_{-0.0019}$	2.49 ± 0.31
220431824	–	13	9.073266 ± 0.000037	0.08652 ± 0.00102	0.1213 ± 0.0026	23.71 ± 0.71
220436189	–	13	13.60940 ± 0.00330	0.09313 ± 0.00064	0.0396 ± 0.0045	2.42 ± 0.28
220436208	–	11	5.235714 ± 0.000316	0.05920 ± 0.00071	0.0337 ± 0.0034	4.38 ± 0.46
220459477	–	13	2.38098 ± 0.00018	0.03250 ± 0.00039	0.0215 ± 0.0038	1.82 ± 0.32
220470563	–	13	7.30383 ± 0.00043	0.06855 ± 0.00049	0.02790 ± 0.0036	2.23 ± 0.29
220481411	K2-216	1	2.174789 ± 0.000039	0.02953 ± 0.00029	0.023117 ± 0.001166	1.74 ± 0.09
220621788	K2-220	1	13.682511 ± 0.000721	0.10864 ± 0.00103	0.021843 ± 0.001610	2.43 ± 0.18
220629489	K2-283	11	1.921076 ± 0.000050	0.02890 ± 0.00028	0.0404 ± 0.0048	3.59 ± 0.43
220639177	–	13	7.14238 ± 0.00069	0.06660 ± 0.00067	0.0236 ± 0.0057	1.86 ± 0.45
220643470	–	1	2.653230 ± 0.000089	0.04349 ± 0.00461	0.041582 ± 0.002685	134.86 ± 21.21
220674823.01	–	1	0.571299 ± 0.000015	0.01329 ± 0.00017	0.016876 ± 0.00137	1.82 ± 0.15
220674823.02	–	1	13.339746 ± 0.001089	0.10854 ± 0.00138	0.027358 ± 0.003262	2.95 ± 0.35
228725791.01	K2-247b	2	2.25021 ± 0.00036	0.02989 ± 0.00027	0.0283 ± 0.0025	2.10 ± 0.19
228725791.02	K2-247c	2	6.49424 ± 0.00260	0.06059 ± 0.00056	0.0292 ± 0.0032	2.17 ± 0.24
228734889	–	1	48.249552 ± 0.000173	0.25637 ± 0.00368	0.172572 ± 0.00245	19.60 ± 0.53
228735255	K2-140	1	6.569213 ± 0.000020	0.06909 ± 0.00089	0.114173 ± 0.000560	12.72 ± 0.32
228736155	K2-226	1	3.271106 ± 0.000369	0.04227 ± 0.00071	0.016535 ± 0.001862	1.66 ± 0.19
228754001	K2-132	1	9.173866 ± 0.001534	0.09237 ± 0.00294	0.029103 ± 0.001475	12.43 ± 0.73
229017395	K2-258	2	19.09210 ± 0.00633	0.13931 ± 0.00174	0.0210 ± 0.0014	3.12 ± 0.22
247047370	–	7	4.20566 ± 0.00018	0.04910 ± 0.00064	0.0267 ± 0.0029	2.50 ± 0.27
247063356	–	7	9.7051 ± 0.0016	0.09163 ± 0.00119	0.0197 ± 0.0020	2.37 ± 0.24

and is about 3σ smaller than the radius given by Grunblatt et al. (2018).

Fig. 7 shows the comparison between planet-candidate radii derived in this work and the values from the literature sources (as per the references given in Table 4). The right-hand panel details planets smaller than $4\,R_\oplus$ and differentiates those having previously published radius estimates derived from spectroscopy versus photometry. We also show results from Kruse et al. (2019), who used stellar radii determined from *Gaia* DR2. No systematic trend is evident in our revised planet radii. Of the 125 candidates with published spectroscopically derived radii, for which we obtain $R_p < 22\,R_\oplus$, our results are 4σ different for five of them. Four

Table 5. Candidates larger than 22 $R_\oplus$. These candidates are highly likely to be false positives.

EPIC	R_p ($R_\oplus$)	Comments
201160662	57.13 ± 15.77	*Gaia* RV error 4.5σ too large
201407812	119.51 ± 4.02	Double-lined binary. *Gaia* RV error 3.0σ too large
201516974	31.18 ± 2.50	*Gaia* RV error 4.0σ too large. Seismic log $g = 2.934 \pm 0.010$
201649426	33.45 ± 0.44	*Gaia* RV error 4.6σ too large
201779067	64.10 ± 1.94	*Gaia* RV error 8.2σ too large
202634963	44.32 ± 1.25	Double-lined binary
203633064	82.26 ± 18.41	–
203929178	101.86 ± 74.42	*Gaia* astrometric noise 419σ
206260577	31.20 ± 9.59	–
206369173	129.64 ± 46.49	$\log g = 1.69 \pm 0.15$
210414957	80.64 ± 34.62	Large uncertainty from R_p/R_*
210609658	22.66 ± 0.91	*Gaia* RV error 3.1σ too large
211336616	25.26 ± 3.81	$\log g = 2.06 \pm 0.18$
211390903	30.42 ± 1.76	$\log g = 2.89 \pm 0.19$. Seismic $\log g = 2.626 \pm 0.022$
212585579	46.56 ± 42.88	*Gaia* RV error 3.1σ too large
212688920	27.02 ± 0.62	–
213408445	301.12 ± 94.83	$\log g = 1.21 \pm 0.19$
213703832	50.02 ± 13.08	$\log g = 2.34 \pm 0.21$.
213840781	60.98 ± 36.40	Large uncertainty from R_p/R_*.
214630761	48.41 ± 13.94	–
214741009	419.79 ± 386.31	$\log g = 2.25 \pm 0.21$.
214984368	440.29 ± 137.57	$\log g = 1.50 \pm 0.18$
215125108	232.37 ± 73.82	$\log g = 2.01 \pm 0.21$
215364084	30.33 ± 15.39	$\log g = 3.08 \pm 0.22$
215381481	72.96 ± 15.99	$\log g = 0.73 \pm 0.19$
218195416	33.41 ± 3.54	–
218300572	43.20 ± 12.86	–
220209578	122.05 ± 105.52	Large uncertainty from R_p/R_*.
220431824	23.71 ± 0.71	–
220643470	134.86 ± 21.21	$\log g = 1.51 \pm 0.13$

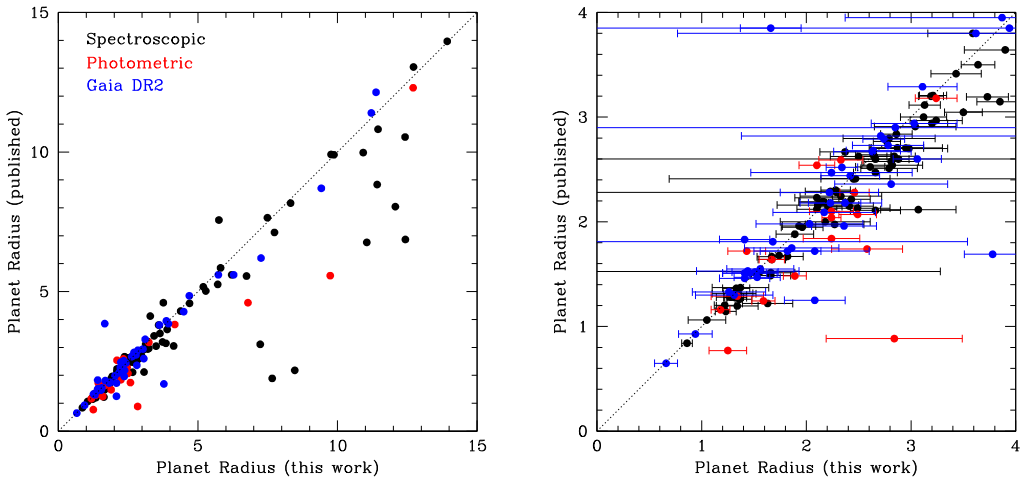

Figure 7. Left-hand panel: Comparison of our derived planetary radii with those from the literature. Error bars have been omitted for clarity. Right-hand panel: Same, but for planet candidates smaller than 4$R_\oplus$. The red points denote published radii derived from photometry, whilst black points are those published values derived from spectroscopy and blue points are from *Gaia* DR2. Large error bars arise from uncertainties in the radius ratio R_p/R_* rather than the stellar radii.

of those (EPIC 203070421, 203533312, 210961508, 228754001) orbit evolved stars with log g ranging from 3.31 to 3.78 and radii from 2.67 to 3.91 $R_\odot$. This results in larger inferred planetary radii, turning some potentially rocky worlds into gas giants. Our revised radii for these planet candidates lie in the realm of Saturn and Jupiter, and so remain eminently plausible.

A large-scale analysis of spectroscopic parameters for stars hosting *Kepler* planet candidates revealed a 'radius gap' (Fulton

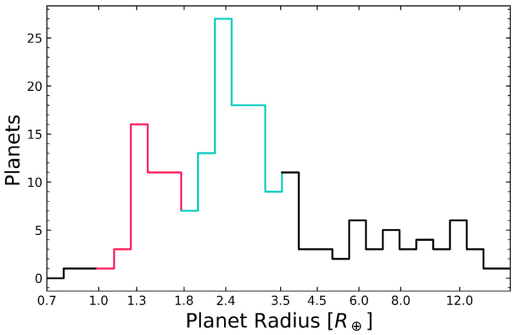

Figure 8. Histogram of our revised planet radii. Red: Rocky planets. Cyan: Gaseous 'mini-Neptune' planets. The radius gap noted by Fulton et al. (2017) and Hardegree-Ullman et al. (2020) is evident.

et al. 2017), with planets of 1.5–2.0$R_\oplus$ apparently depleted by more than a factor of two. Subsequent studies have confirmed that result; Van Eylen et al. (2018) used 117 planets with median radius uncertainties of 3.3 per cent as derived from asteroseismology to further characterize the radius gap. In Fig. 8, we show the distribution of planet-candidate radii from our K2-HERMES sample. Our sample, although smaller than the surveys conducted by Fulton et al. (2017) and Hardegree-Ullman et al. (2020), also sees a drop off in exoplanetary candidates and confirmed exoplanets centred around 1.8$R_\oplus$. Hardegree-Ullman et al. (2020) in particular showed that K2 planet candidates were depleted within a radius gap centred at 1.9 $R_\oplus$.

In Fig. 9, we explore the radius gap in more detail, showing the planet radii as a function of both orbital period and semimajor axis. The radius gap was shown by Van Eylen et al. (2018) to have a slope dependent on orbital period, with a slope of $\frac{\mathrm{d}\log R}{\mathrm{d}\log P}$ of approximately $-1/9$, a value corroborated by Gupta & Schlichting (2019) and illustrated in Fig. 9. In this Figure, we show as filled circles those

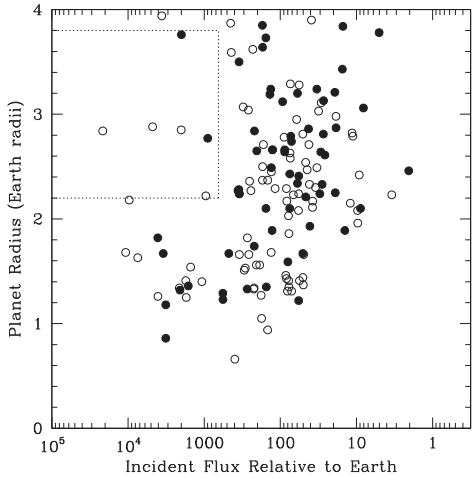

Figure 10. Planet radius versus incident flux, in Earth units. The filled circles indicate planets for which we obtain radius estimates at better than 10 per cent precision. The dashed lines enclose the hot Super-Earth desert (Lundkvist et al. 2016).

95 planets for which we derive radii with precision of 10 per cent or better. The K2 sample investigated here gave consistent results for the shape and slope of this evaporation valley, with the exception of four candidates. These planets (EPIC 206082454, 201754305.02, 210508766.02, 228725791.01) appear as filled circles falling on the dashed line in the right-hand panel of Fig. 9. These candidates have radii with precisions of better than 10 per cent. Interestingly, three of these four are members of multiple systems. Fig. 10 gives the planet radius as a function of incident stellar flux (Table 3). The hot super-Earth desert postulated by Lundkvist et al. (2016) is shown as a box enclosing the region between 2.2–3.8 $R_\oplus$ and $S_{\rm inc}$ >650 $F_\oplus$. Near

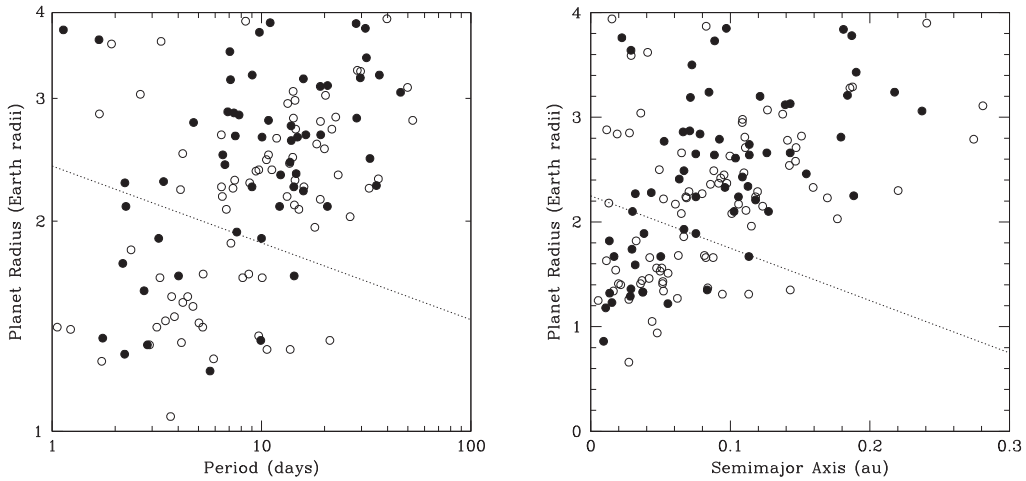

Figure 9. Left-hand panel: Planet radius versus orbital period; the filled circles indicate planets for which we obtain radius estimates at better than 10 per cent precision. The dashed line indicates the slope in the radius valley as noted by Van Eylen et al. (2018) and Gupta & Schlichting (2019). Right-hand panel: Planet radius versus semimajor axis, as computed from the *K*2 period and our derived host-star masses. The symbols have the same meaning as in the left-hand panel.

the edges of this region lie only two planet candidates with radius estimates better than 10 per cent precision, EPIC 206036749.01 and EPIC 211359660.01.

4 SUMMARY AND CONCLUSION

In this work, we have presented a self-consistent catalogue of spectroscopic host-star parameters for 199 *K*2 planet hosts, and the derived physical parameters of 224 planets. We use the revised radii for these planet candidates to cast doubt on 30 as-yet-unconfirmed planets, and we strongly suspect those to be false positives. We also examine the distribution of planet radii as a function of period, showing that the radius gap of the main *Kepler* sample is indeed also evident in this *K*2 sample. The slope of the radius valley is also consistent with that obtained for the *Kepler* planets by Van Eylen et al. (2018) and Gupta & Schlichting (2019), with a handful of interesting exceptions.

In addition to the 30 planet candidates which are rendered implausible based on their revised host-star parameters, our results confirm the small radii of a handful of nearly Earth-sized planets. They are EPIC 205470347 ($0.66 \pm 0.11\,R_\oplus$), EPIC 211357309 ($0.86 \pm 0.05\,R_\oplus$), EPIC 212464382 ($0.94 \pm 0.16\,R_\oplus$), and EPIC 220245303 ($1.05 \pm 0.18\,R_\oplus$). However, as shown in Table 3, these Earth-sized planets are far from Earth-like, receiving stellar flux hundreds of times greater than the Earth.

Our results highlight the importance of accurate stellar parametrization in the characterization of newly discovered exoplanets. Fortunately, with surveys like GALAH and instruments like HERMES it is possible to rapidly characterize large numbers of potential exoplanet host stars. In the coming decade, as the exoplanet discovery rate continues to climb, such surveys will prove pivotal in ensuring the fidelity of the exoplanet catalogue.

ACKNOWLEDGEMENTS

DS is supported by Australian Research Council Future Fellowship FT1400147. SS is funded by University of Sydney Senior Fellowship made possible by the office of the Deputy Vice Chancellor of Research, and partial funding from Bland-Hawthorn's Laureate Fellowship from the Australian Research Council. SLM acknowledges support from the Australian Research Council through Discovery Project grant DP180101791. SB acknowledges funds from the Alexander von Humboldt Foundation in the framework of the Sofja Kovalevskaja Award endowed by the Federal Ministry of Education and Research. This research has been supported by the Australian Research Council (grants DP150100250 and DP160103747). Parts of this research were supported by the Australian Research Council (ARC) Centre of Excellence for All Sky Astrophysics in 3 Dimensions (ASTRO 3D), through project number CE170100013. LC is supported by Australian Research Council Future Fellowship FT160100402. This research has made use of NASA's Astrophysics Data System (ADS), and the SIMBAD data base, operated at CDS, Strasbourg, France. This research has made use of the NASA Exoplanet Archive, which is operated by the California Institute of Technology, under contract with the National Aeronautics and Space Administration under the Exoplanet Exploration Program. We thank the Australian Time Allocation Committee for their generous allocation of AAT time, which made this work possible. We acknowledge the traditional owners of the land on which the AAT stands, the Gamilaraay people, and pay our respects to elders past, present, and emerging.

REFERENCES

Adams E. R., Jackson B., Endl M., 2016, AJ, 152, 47
Albrecht S. et al., 2012, ApJ, 757, 18
Batalha N. M. et al., 2013, ApJS, 204, 24
Borucki W. J. et al., 2010, Science, 327, 977
Bouchy F. et al., 2005, A&A, 444, L15
Buder S. et al., 2018, MNRAS, 478, 4513
Burgasser A. J. et al., 2010, ApJ, 725, 1405
Campbell B., Walker G. A. H., Yang S., 1988, ApJ, 331, 902
Chandler C. O., McDonald I., Kane S. R., 2016, AJ, 151, 59
Charbonneau D. et al., 2009, Nature, 462, 891
Čotar K. et al., 2019, MNRAS, 483, 3196
Čotar K. et al., 2019, MNRAS, 487, 2474
Crossfield I. J. M. et al., 2016, ApJS, 226, 7
De Silva G. M. et al., 2015, MNRAS, 449, 2604
Dotter A., 2016, ApJS, 222, 8
Dressing C. D. et al., 2017, AJ, 154, 207
Duong L. et al., 2018, MNRAS, 476, 5216
Freeman K. C., 2012, in Aoki W., ed., ASP Conf. Ser. Vol. 458, Galactic Archaeology: Near-field Cosmology and the Formation of the Milky Way. Astron. Soc. Pac., San Francisco, p. 393
Fressin F. et al., 2013, ApJ, 766, 81
Fulton B. J. et al., 2017, AJ, 154, 109
Gaia Collaboration 2018, A&A, 616, A1
Gao X. et al., 2018, MNRAS, 481, 2666
Grunblatt S. K. et al., 2018, ApJ, 861, L5
Gupta A., Schlichting H. E., 2019, MNRAS, 487, 24
Harakawa H. et al., 2015, ApJ, 806, 5
Hardegree-Ullman K. K. et al., 2019, AJ, 158, 75
Hardegree-Ullman K. K. et al., 2020, ApJS, 247, 28
Hellier C., Anderson D. R., Collier-Cameron A., Miller G. R. M., Queloz D., Smalley B., Southworth J., Triaud A. H. M. J., 2011, ApJ, 730, L31
Hon M., Stello D., Yu J., 2018, MNRAS, 476, 3233
Howard A. W. et al., 2012, ApJS, 201, 15
Howell S. B. et al., 2014, PASP, 126, 398
Huber D., Stello D., Bedding T. R., Chaplin W. J., Arentoft T., Quirion P.-O., Kjeldsen H., 2009, Commun. Asteroseismol., 160, 74
Huber D. et al., 2011, ApJ, 743, 143
Huber D. et al., 2016, ApJS, 224, 2
Johns D. et al., 2018, ApJS, 239, 14
Kalas P. et al., 2008, Science, 322, 1345
Kane S. R., 2014, ApJ, 782, 111
Kane S. R., 2018, ApJ, 861, L21
Kane S. R., Gelino D. M., 2011, ApJ, 741, 52
Kane S. R., Kopparapu R. K., Domagal-Goldman S. D., 2014, ApJ, 794, L5
Kane S. R. et al., 2016, ApJ, 830, 1
Kane S. R. et al., 2019, J. Geophys. Res., 124, 2015
Katz D. et al., 2019, A&A, 622, A205
Kempton E. M.-R. et al., 2018, PASP, 130, 114401
Kopparapu R. K. et al., 2013, ApJ, 765, 131
Kopparapu R. K., Ramirez R. M., SchottelKotte J., Kasting J. F., Domagal-Goldman S., Eymet V., 2014, ApJ, 787, L29
Kos J. et al., 2017, MNRAS, 464, 1259
Kos J. et al., 2018, MNRAS, 473, 4612
Kos J. et al., 2018, MNRAS, 480, 5242
Kruse E., Agol E., Luger R., Foreman-Mackey D., 2019, ApJS, 244, 11
Lagrange A.-M. et al., 2009, A&A, 493, L21
Latham D. W., Mazeh T., Stefanik R. P., Mayor M., Burki G., 1989, Nature, 339, 38
Livingston J. H. et al., 2018b, AJ, 156, 78
Luger R., Agol E., Kruse E., Barnes R., Becker A., Foreman-Mackey D., Deming D., 2016, AJ, 152, 100
Lundkvist M. S. et al., 2016, Nat. Commun., 7, 11201
Mann A. W. et al., 2017, AJ, 153, 64
Marois C., Macintosh B., Barman T., Zuckerman B., Song I., Patience J., Lafrenière D., Doyon R., 2008, Science, 322, 1348

Marois C., Zuckerman B., Konopacky Q. M., Macintosh B., Barman T., 2010, Nature, 468, 1080
Martell S. L. et al., 2017, MNRAS, 465, 3203
Masset F. S., Papaloizou J. C. B., 2003, ApJ, 588, 494
Masuda K., 2014, ApJ, 783, 53
Mayo A. W. et al., 2018, AJ, 155, 136
Mayor M., Queloz D., 1995, Nature, 378, 355
Morton T. D., 2015, Isochrones: Stellar model grid package, record ascl:1503.010
Mullally F. et al., 2015, ApJS, 217, 31
Nardiello D., Libralato M., Bedin L. R., Piotto G., Borsato L., Granata V., Malavolta L., Nascimbeni V., 2016, MNRAS, 463, 1831
Ostberg C., Kane S. R., 2019, AJ, 158, 195
Petigura E. A. et al., 2017, AJ, 153, 142
Pope B. J. S., Parviainen H., Aigrain S., 2016, MNRAS, 461, 3399
Quillen A. C. et al., 2018, MNRAS, 478, 228
Raetz S., Heras A. M., Fernández M., Casanova V., Marka C., 2019, MNRAS, 483, 824
Salaris M., Chieffi A., Straniero O., 1993, ApJ, 414, 580
Schmitt J. R. et al., 2016, AJ, 151, 159
Sharma S., Stello D., Bland-Hawthorn J., Huber D., Bedding T. R., 2016, ApJ, 822, 15
Sharma S. et al., 2018, MNRAS, 473, 2004
Sharma S. et al., 2019, MNRAS, 490, 5335
Simpson J. D. et al., 2016, MNRAS, 459, 1069
Sinukoff E. et al., 2016, ApJ, 827, 78
Skrutskie M. F. et al., 2006, AJ, 131, 1163
Sliski D. H., Kipping D. M., 2014, ApJ, 788, 148
Stello D. et al., 2017, ApJ, 835, 83
Tamuz O. et al., 2008, A&A, 480, L33
Van Eylen V., Agentoft C., Lundkvist M. S., Kjeldsen H., Owen J. E., Fulton B. J., Petigura E., Snellen I., 2018, MNRAS, 479, 4786
Vanderburg A. et al., 2016, ApJS, 222, 14
Vogt S. S. et al., 2010, ApJ, 708, 1366
Winn J. N., Fabrycky D. C., 2015, ARA&A, 53, 409
Winn J. N. et al., 2011, ApJ, 737, L18
Wittenmyer R. A., Endl M., Cochran W. D., Levison H. F., 2007, AJ, 134, 1276
Wittenmyer R. A. et al., 2017, AJ, 154, 274
Wittenmyer R. A. et al., 2018, AJ, 155, 84
Wolszczan A., Frail D. A., 1992, Nature, 355, 145
Wright J. T., Marcy G. W., Howard A. W., Johnson J. A., Morton T. D., Fischer D. A., 2012, ApJ, 753, 160
Yu J., Huber D., Bedding T. R., Stello D., Hon M., Murphy S. J., Khanna S., 2018, ApJS, 236, 42
Zink J. K. et al., 2019, Res. Notes Am. Astron. Soc., 3, 43
Zwitter T. et al., 2018, MNRAS, 481, 645
Žerjal M. et al., 2019, MNRAS, 484, 4591

SUPPORTING INFORMATION

Supplementary data are available at *MNRAS* online.

Table 2. Spectroscopic and derived stellar parameters.
Table 3. Planetary insolation and habitable zone boundaries.

Please note: Oxford University Press is not responsible for the content or functionality of any supporting materials supplied by the authors. Any queries (other than missing material) should be directed to the corresponding author for the article.

This paper has been typeset from a TEX/LATEX file prepared by the author.

B

Other Published Works

During my PhD, I have also researched and worked in many areas of exoplanetary science. Below is a list of publications I have worked on throughout my PhD, including the abstract for each paper.

B.1 The Youngest Planet to Have a Spin-Orbit Alignment Measurement AU Mic b

B. C. Addison, J. Horner, R. A. Wittenmyer, A. Heitzmann, P. Plavchan, D. J. Wright, B. A. Nicholson, J. P. Marshall, J. T. Clark, M. N. Günther, S. R. Kane, T. Hirano, S. Wang, J. Kielkopf, A. Shporer, C. G. Tinney, H. Zhang, S. Ballard, T. Bedding, B. P. Bowler, M. W. Mengel, J. Okumura, E. Gaidos, & X.-Y. Wang 2021. **The Youngest Planet to Have a Spin-Orbit Alignment Measurement AU Mic b**. Astronomical Journal 162(4), *We report measurements of the sky-projected spin-orbit angle for AU Mic b, a Neptune-size planet orbiting a very young (20 Myr) nearby pre-main-sequence M-dwarf star, which also hosts a bright, edge-on, debris disk. The planet was recently discovered from preliminary analysis of radial-velocity*

observations and confirmed to be transiting its host star from photometric data from the NASA's TESS mission. We obtained radial-velocity measurements of AU Mic over the course of two partially observable transits and one full transit of planet b from high-resolution spectroscopic observations made with the MINERVA-Australis telescope array. Only a marginal detection of the Rossiter-McLaughlin effect signal was obtained from the radial velocities, in part due to AU Mic being an extremely active star and the lack of full transit coverage plus sufficient out-of-transit baseline. As such, a precise determination of the obliquity for AU Mic b is not possible in this study and we find a sky-projected spin-orbit angle of $\lambda = 47^{+26^{\circ}}_{-54}$ *. This result is consistent with both the planet's orbit being aligned or highly misaligned with the spin axis of its host star. Our measurement independently agrees with, but is far less precise than observations carried out on other instruments around the same time that measure a low-obliquity orbit for the planet. AU Mic is the youngest exoplanetary system for which the projected spin-orbit angle has been measured, making it a key data point in the study of the formation and migration of exoplanets-particularly given that the system is also host to a bright debris disk.*

B.2 The GALAH+ survey: Third data release

S. Buder, S. Sharma, J. Kos, A. M. Amarsi, T. Nordlander, K. Lind, S. L. Martell, M. Asplund, J. Bland-Hawthorn, A. R. Casey, G. M. de Silva, V. D'Orazi, K. C. Freeman, M. R. Hayden, G. F. Lewis, J. Lin, K. J. Schlesinger, J. D. Simpson, D. Stello, D. B. Zucker, T. Zwitter, K. L. Beeson, T. Buck, L. Casagrande, J. T. Clark, K. Čotar, G. S. da Costa, R. de Grijs, D. Feuillet, J. Horner, P. R. Kafle, S. Khanna, C. Kobayashi, F. Liu, B. T. Montet, G. Nandakumar, D. M. Nataf, M. K. Ness, L. Spina, T. Tepper-García, Y.-S. Ting, G. Traven, R. Vogrinčič, R. A. Wittenmyer, R. F. G. Wyse, M. Žerjal, & GALAH Collaboration 2021. **The GALAH+ survey: Third data release**. Monthly Notices of the Royal Astronomical Society 506(1), 201-150

The ensemble of chemical element abundance measurements for stars, along with precision distances and orbit properties, provides high-dimensional data to study the evolution of the Milky Way. With this third data release of the Galactic Archaeology with HERMES (GALAH) survey, we publish 678 423 spectra for 588 571 mostly nearby stars (81.2 per cent of stars are within <2 kpc), observed with the HERMES spectrograph at the Anglo-Australian Telescope. This release (hereafter GALAH+ DR3) includes all observations from GALAH Phase 1 (bright, main, and faint survey, 70 per cent), K2-HERMES (17 per cent), TESS-HERMES (5 per cent), and a

subset of ancillary observations (8 per cent) including the bulge and >75 stellar clusters. We derive stellar parameters T_{eff}, log g, [Fe/H], v_{mic}, v_{broad}, and v_{rad} using our modified version of the spectrum synthesis code Spectroscopy Made Easy (SME) and 1D MARCS model atmospheres. We break spectroscopic degeneracies in our spectrum analysis with astrometry from Gaia DR2 and photometry from 2MASS. We report abundance ratios [X/Fe] for 30 different elements (11 of which are based on non-LTE computations) covering five nucleosynthetic pathways. We describe validations for accuracy and precision, flagging of peculiar stars/measurements and recommendations for using our results. Our catalogue comprises 65 per cent dwarfs, 34 per cent giants, and 1 per cent other/unclassified stars. Based on unflagged chemical composition and age, we find 62 per cent young low-α, 9 per cent young high-α, 27 per cent old high-α, and 2 per cent stars with [Fe/H]≤-1. Based on kinematics, 4 per cent are halo stars. Several Value-Added-Catalogues, including stellar ages and dynamics, updated after Gaia eDR3, accompany this release and allow chrono-chemodynamic analyses, as we showcase.

B.3 TOI-1431b/MASCARA-5b: A Highly Irradiated Ultra-Hot Jupiter Orbiting One of the Hottest & Brightest Known Exoplanet Host Stars

B. C. Addison, E. Knudstrup, I. Wong, G. Hebrard, P. Dorval, I. Snellen, S. Albrecht, A. Bello-Arufe, J.-M. Almenara, I. Boisse, X. Bonfils, S. Dalal, O. Demangeon, S. Hoyer, F. Kiefer, N. C. Santos, G. Nowak, R. Luque, M. Stangret, E. Palle, R. Tronsgaard, V. Antoci, L. A. Buchhave, M. N. Gunther, T. Daylan, F. Murgas, H. Parviainen, E. Esparza-Borges, N. Crouzet, N. Narita, A. Fukui, K. Kawauchi, N. Watanabe, M. Rabus, M. C. Johnson, G. P. P. L. Otten, G. J. Talens, S. H. C. Cabot, D. A. Fischer, F. Grundahl, M. Fredslund Andersen, J. Jessen-Hanse, P. Palle, A. Shporer, D. R. Ciardi, J. T. Clark, R. A. Wittenmyer, D. J. Wright, J. Horner, K. A. Collins, E. L. N. Jensen, J. F. Kielkopf, R. P. Schwarz, G. Srdoc, M. Yilmaz, H. V. Senavci, B. Diamond, D. Harbeck, T. D. Komacek, J. C. Smith, S. Wang, J. D. Eastman, K. G. Stassun, D. W. Latham, R. Vanderspek, S. Seager, J. N. Winn, J. M. Jenkins, D. R. Louie, L. G. Bouma, J. D. Twicken, A. M. Levine, & B. McLean 2021. **TOI-1431b/MASCARA-5b: A Highly Irradiated Ultra-Hot Jupiter Orbiting One of the Hottest & Brightest Known Exoplanet Host Stars**. arXiv e-prints *We present the discovery of a highly irradiated and moderately inflated ultra-hot Jupiter, TOI-1431b/MASCARA-5b (HD 201033b), first detected by NASA's Transiting Exoplanet Survey Satellite mission (TESS) and the Multi-site All-Sky CAmeRA (MASCARA). The signal*

was established to be of planetary origin through radial velocity measurements obtained using SONG, SOPHIE, FIES, NRES, and EXPRES, which show a reflex motion of $K = 294.1 \pm 1.1$ $m\,s^{-1}$. *A joint analysis of the TESS and ground-based photometry and radial velocity measurements reveals that TOI-1431b has a mass of* $M_p = 3.12 \pm 0.18$ M_J *(*990 ± 60 $M_\oplus$*), an inflated radius of* $R_p = 1.49 \pm 0.05$ R_J *(*16.7 ± 0.6 $R_\oplus$*), and an orbital period of* $P = 2.650237 \pm 0.000003$ *d. Analysis of the spectral energy distribution of the host star reveals that the planet orbits a bright (*$V = 8.049$ *mag) and young (*$0.29^{+0.32}_{-0.19}$ *Gyr) Am type star with* $T_{\rm eff} = 7690^{+400}_{-250}$ K*, resulting in a highly irradiated planet with an incident flux of* $\langle F \rangle = 7.24^{+0.68}_{-0.64} \times 10^9$ *erg* s^{-1} cm^{-2} *(*5300^{+500}_{-470} $S_\oplus$*) and an equilibrium temperature of* $T_{eq} = 2370 \pm 70$ *K. TESS photometry also reveals a secondary eclipse with a depth of* 127^{+4}_{-5} *ppm as well as the full phase curve of the planet's thermal emission in the red-optical. This has allowed us to measure the dayside and nightside temperature of its atmosphere as* $T_{\rm day} = 3004 \pm 64$ *K and* $T_{\rm night} = 2583 \pm 63$ *K, the second hottest measured nightside temperature. The planet's low day/night temperature contrast (~420 K) suggests very efficient heat transport between the dayside and nightside hemispheres.*

B.4 TOI-257b (HD 19916b): a warm sub-saturn orbiting an evolved F-type star

B. C. Addison, D. J. Wright, B. A. Nicholson, B. Cale, T. Mocnik, D. Huber, P. Plavchan, R. A. Wittenmyer, A. Vanderburg, W. J. Chaplin, A. Chontos, J. T. Clark, J. D. Eastman, C. Ziegler, R. Brahm, B. D. Carter, M. Clerte, N. Espinoza, J. Horner, J. Bentley, A. Jordán, S. R. Kane, J. F. Kielkopf, E. Laychock, M. W. Mengel, J. Okumura, K. G. Stassun, T. R. Bedding, B. P. Bowler, A. Burnelis, S. Blanco-Cuaresma, M. Collins, I. Crossfield, A. B. Davis, D. Evensberget, A. Heitzmann, S. B. Howell, N. Law, A. W. Mann, S. C. Marsden, R. A. Matson, J. H. O'Connor, A. Shporer, C. Stevens, C. G. Tinney, C. Tylor, S. Wang, H. Zhang, T. Henning, D. Kossakowski, G. Ricker, P. Sarkis, M. Schlecker, P. Torres, R. Vanderspek, D. W. Latham, S. Seager, J. N. Winn, J. M. Jenkins, I. Mireles, P. Rowden, J. Pepper, T. Daylan, J. E. Schlieder, K. A. Collins, K. I. Collins, T.-G. Tan, W. H. Ball, S. Basu, D. L. Buzasi, T. L. Campante, E. Corsaro, L. González-Cuesta, G. R. Davies, L. de Almeida, J.-D. do Nascimento, R. A. García, Z. Guo, R. Handberg, S. Hekker, D. R. Hey, T. Kallinger, S. D. Kawaler, C. Kayhan, J. S. Kuszlewicz, M. N. Lund, A. Lyttle, S. Mathur, A. Miglio, B. Mosser, M. B. Nielsen, A. M. Serenelli, V. S. Aguirre, & N. Themeßl 2021. **TOI-257b (HD 19916b): a warm sub-saturn orbiting an evolved F-type star**. Monthly Notices of the

Royal Astronomical Society 502(3), 3722-3704

We report the discovery of a warm sub-Saturn, TOI-257b (HD 19916b), based on data from NASA's Transiting Exoplanet Survey Satellite (TESS). The transit signal was detected by TESS and confirmed to be of planetary origin based on radial velocity observations. An analysis of the TESS photometry, the MINERVA-Australis, FEROS, and HARPS radial velocities, and the asteroseismic data of the stellar oscillations reveals that TOI-257b has a mass of $M_P = 0.138 \pm 0.023$ M_J *(*43.9 ± 7.3 $M_\oplus$*), a radius of* $R_P = 0.639 \pm 0.013$ R_J *(*7.16 ± 0.15 $R_\oplus$*), bulk density of* $0.65^{+0.12}_{-0.11}$ *(cgs), and period* $18.38818^{+0.00085}_{-0.00084}$ days*. TOI-257b orbits a bright (*$V = 7.612$ *mag) somewhat evolved late F-type star with* $M_* = 1.390 \pm 0.046$ M_{sun}, $R_* = 1.888 \pm 0.033$ R_{sun}, $T_{eff} = 6075 \pm 90$ K, *and* $v \sin i = 11.3 \pm 0.5$ km s^{-1}*. Additionally, we find hints for a second non-transiting sub-Saturn mass planet on a ~71 day orbit using the radial velocity data. This system joins the ranks of a small number of exoplanet host stars (~100) that have been characterized with asteroseismology. Warm sub-Saturns are rare in the known sample of exoplanets, and thus the discovery of TOI-257b is important in the context of future work studying the formation and migration history of similar planetary systems.*

B.5 Recreating the OSIRIS-REx slingshot manoeuvre from a network of ground-based sensors

T. Jansen-Sturgeon, B. A. D. Hartig, G. J. Madsen, P. A. Bland, E. K. Sansom, H. A. R. Devillepoix, R. M. Howie, M. Cupák, M. C. Towner, M. A. Cox, N. D. Nevill, Z. N. P. Hoskins, G. P. Bonning, J. Calcino, J. T. Clark, B. M. Henson, A. Langendam, S. J. Matthews, T. P. McClafferty, J. T. Mitchell, C. J. O'Neill, L. T. Smith, & A. W. Tait 2020. **Recreating the OSIRIS-REx slingshot manoeuvre from a network of ground-based sensors**. PASA 37

Optical tracking systems typically trade off between astrometric precision and field of view. In this work, we showcase a networked approach to optical tracking using very wide field-of-view imagers that have relatively low astrometric precision on the scheduled OSIRIS-REx slingshot manoeuvre around Earth on 22 Sep 2017. As part of a trajectory designed to get OSIRIS-REx to NEO 101955 Bennu, this flyby event was viewed from 13 remote sensors spread across Australia and New Zealand to promote triangulatable observations. Each observatory in this portable network was constructed to be as lightweight and portable as possible, with hardware based off the successful design of the Desert Fireball Network. Over a 4-h collection window, we gathered 15 439 images of the night sky in the predicted direction of the OSIRIS-REx spacecraft. Using

a specially developed streak detection and orbit determination data pipeline, we detected 2 090 line-of-sight observations. Our fitted orbit was determined to be within about 10 km of orbital telemetry along the observed 109 262 km length of OSIRIS-REx trajectory, and thus demonstrating the impressive capability of a networked approach to Space Surveillance and Tracking.

B.6 A planet within the debris disk around the pre-main-sequence star AU Microscopii

P. Plavchan, T. Barclay, J. Gagné, P. Gao, B. Cale, W. Matzko, D. Dragomir, S. Quinn, D. Feliz, K. Stassun, I. J. M. Crossfield, D. A. Berardo, D. W. Latham, B. Tieu, G. Anglada-Escudé, G. Ricker, R. Vanderspek, S. Seager, J. N. Winn, J. M. Jenkins, S. Rinehart, A. Krishnamurthy, S. Dynes, J. Doty, F. Adams, D. A. Afanasev, C. Beichman, M. Bottom, B. P. Bowler, C. Brinkworth, C. J. Brown, A. Cancino, D. R. Ciardi, M. Clampin, J. T. Clark, K. Collins, C. Davison, D. Foreman-Mackey, E. Furlan, E. J. Gaidos, C. Geneser, F. Giddens, E. Gilbert, R. Hall, C. Hellier, T. Henry, J. Horner, A. W. Howard, C. Huang, J. Huber, S. R. Kane, M. Kenworthy, J. Kielkopf, D. Kipping, C. Klenke, E. Kruse, N. Latouf, P. Lowrance, B. Mennesson, M. Mengel, S. M. Mills, T. Morton, N. Narita, E. Newton, A. Nishimoto, J. Okumura, E. Palle, J. Pepper, E. V. Quintana, A. Roberge, V. Roccatagliata, J. E. Schlieder, A. Tanner, J. Teske, C. G. Tinney, A. Vanderburg, K. von Braun, B. Walp, J. Wang, S. X. Wang, D. Weigand, R. White, R. A. Wittenmyer, D. J. Wright, A. Youngblood, H. Zhang, & P. Zilberman 2020. **A planet within the debris disk around the pre-main-sequence star AU Microscopii**. Nature582(7813), 500-497

AU Microscopii (AU Mic) is the second closest pre-main-sequence star, at a distance of 9.79 parsecs and with an age of 22 million years. AU Mic possesses a relatively rare and spatially resolved edge-on debris disk extending from about 35 to 210 astronomical units from the star, and with clumps exhibiting non-Keplerian motion. Detection of newly formed planets around such a star is challenged by the presence of spots, plage, flares and other manifestations of magnetic 'activity' on the star. Here we report observations of a planet transiting AU Mic. The transiting planet, AU Mic b, has an orbital period of 8.46 days, an orbital distance of 0.07 astronomical units, a radius of 0.4 Jupiter radii, and a mass of less than 0.18 Jupiter masses at 3σ confidence. Our observations of a planet co-existing with a debris disk offer the opportunity to test the predictions of current models of planet formation and evolution.

B.7 Stability analysis of three exoplanet systems

J. P. Marshall, J. Horner, R. A. Wittenmyer, J. T. Clark, & M. W. Mengel 2020. **Stability analysis of three exoplanet systems**. Monthly Notices of the Royal Astronomical Society 494(2), 2288-2280

The orbital solutions of published multiplanet systems are not necessarily dynamically stable on time-scales comparable to the lifetime of the system as a whole. For this reason, dynamical tests of the architectures of proposed exoplanetary systems are a critical tool to probe the stability and feasibility of the candidate planetary systems, with the potential to point the way towards refined orbital parameters of those planets. Such studies can even help in the identification of additional companions in such systems. Here, we examine the dynamical stability of three planetary systems, orbiting HD 67087, HD 110014, and HD 133131A. We use the published radial velocity measurements of the target stars to determine the best-fitting orbital solutions for these planetary systems using the systemic console. We then employ the N-body integrator mercury to test the stability of a range of orbital solutions lying within 3σ of the nominal best fit for a duration of 100 Myr. From the results of the N-body integrations, we infer the best-fitting orbital parameters using the Bayesian package astroemperor. We find that both HD 110014 and HD 133131A have long-term stable architectures that lie within the 1σ uncertainties of the nominal best fit to their previously determined orbital solutions. However, the HD 67087 system exhibits a strong tendency towards instability on short time-scales. We compare these results to the predictions made from consideration of the angular momentum deficit criterion, and find that its predictions are consistent with our findings.

B.8 The Pan-Pacific Planet Search - VIII. Complete results and the occurrence rate of planets around low-luminosity giants

R. A. Wittenmyer, R. P. Butler, J. Horner, J. Clark, C. G. Tinney, B. D. Carter, L. Wang, J. A. Johnson, & M. Collins 2020. **The Pan-Pacific Planet Search - VIII. Complete results and the occurrence rate of planets around low-luminosity giants**. Monthly Notices of the Royal Astronomical Society 491(4), 5257-5248

Our knowledge of the populations and occurrence rates of planets orbiting evolved intermediate-mass stars lags behind that for solar-type stars by at least a decade. Some radial velocity surveys have targeted these low-luminosity giant stars, providing some insights into the properties of

their planetary systems. Here, we present the final data release of the Pan-Pacific Planet Search (PPPS), a 5 yr radial velocity survey using the 3.9 m Anglo-Australian Telescope. We present 1293 precise radial velocity measurements for 129 stars, and highlight 6 potential substellar-mass companions, which require additional observations to confirm. Correcting for the substantial incompleteness in the sample, we estimate the occurrence rate of giant planets orbiting low-luminosity giant stars to be approximately $7.8^{+9.1}_{-3.3}$ *per cent. This result is consistent with the frequency of such planets found to orbit main-sequence A-type stars, from which the PPPS stars have evolved.*

B.9 Minerva-Australis. I. Design, Commissioning, and First Photometric Results

B. Addison, D. J. Wright, R. A. Wittenmyer, J. Horner, M. W. Mengel, D. Johns, C. Marti, B. Nicholson, J. Soutter, B. Bowler, I. Crossfield, S. R. Kane, J. Kielkopf, P. Plavchan, C. G. Tinney, H. Zhang, J. T. Clark, M. Clerte, J. D. Eastman, J. Swift, M. Bottom, P. Muirhead, N. McCrady, E. Herzig, K. Hogstrom, M. Wilson, D. Sliski, S. A. Johnson, J. T. Wright, J. A. Johnson, C. Blake, R. Riddle, B. Lin, M. Cornachione, T. R. Bedding, D. Stello, D. Huber, S. Marsden, & B. D. Carter 2019. **Minerva-Australis. I. Design, Commissioning, and First Photometric Results**. PASP131(1005),-115003

The MINERVA-Australis telescope array is a facility dedicated to the follow-up, confirmation, characterization, and mass measurement of planets orbiting bright stars discovered by the Transiting Exoplanet Survey Satellite (TESS)—a category in which it is almost unique in the Southern Hemisphere. It is located at the University of Southern Queensland' s Mount Kent Observatory near Toowoomba, Australia. Its flexible design enables multiple 0.7 m robotic telescopes to be used both in combination, and independently, for high-resolution spectroscopy and precision photometry of TESS transit planet candidates. MINERVA-Australis also enables complementary studies of exoplanet spin-orbit alignments via Doppler observations of the Rossiter-McLaughlin effect, radial velocity searches for nontransiting planets, planet searches using transit timing variations, and ephemeris refinement for TESS planets. In this first paper, we describe the design, photometric instrumentation, software, and science goals of MINERVA-Australis, and note key differences from its Northern Hemisphere counterpart, the MINERVA array. We use recent transit observations of four planets, WASP-2b, WASP-44b, WASP-45b, and HD 189733b, to demonstrate the photometric capabilities of MINERVA-Australis.

B.10 The HD 181433 Planetary System: Dynamics and a New Orbital Solution

J. Horner, R. A. Wittenmyer, D. J. Wright, T. C. Hinse, J. P. Marshall, S. R. Kane, J. T. Clark, M. Mengel, M. T. Agnew, & D. Johns 2019. **The HD 181433 Planetary System: Dynamics and a New Orbital Solution**. Astronomical Journal 158(3), *We present a detailed analysis of the orbital stability of the HD 181433 planetary system, finding it to exhibit strong dynamical instability across a wide range of orbital eccentricities, semimajor axes, and mutual inclinations. We also analyze the behavior of an alternative system architecture, proposed by Campanella, and find that it offers greater stability than the original solution, as a result of the planets being trapped in strong mutual resonance. We take advantage of more recent observations to perform a full refit of the system, producing a new planetary solution. The best-fit orbit for HD 181433 d now places the planet at a semimajor axis of 6.60 ± 0.22 au, with an eccentricity of 0.469 ± 0.013. Extensive simulations of this new system architecture reveal it to be dynamically stable across a broad range of potential orbital parameter space, increasing our confidence that the new solution represents the ground truth of the system. Our work highlights the advantage of performing dynamical simulations of candidate planetary systems in concert with the orbital fitting process, as well as supporting the continuing monitoring of radial velocity planet search targets.*

B.11 TESS Spots a Compact System of Super-Earths around the Naked-eye Star HR 858

A. Vanderburg, C. X. Huang, J. E. Rodriguez, J. C. Becker, G. R. Ricker, R. K. Vanderspek, D. W. Latham, S. Seager, J. N. Winn, J. M. Jenkins, B. Addison, A. Bieryla, C. Briceño, B. P. Bowler, T. M. Brown, C. J. Burke, J. A. Burt, D. A. Caldwell, J. T. Clark, I. Crossfield, J. A. Dittmann, S. Dynes, B. J. Fulton, N. Guerrero, D. Harbeck, J. Horner, S. R. Kane, J. Kielkopf, A. L. Kraus, L. Kreidberg, N. Law, A. W. Mann, M. W. Mengel, T. D. Morton, J. Okumura, L. A. Pearce, P. Plavchan, S. N. Quinn, M. Rabus, M. E. Rose, P. Rowden, A. Shporer, R. J. Siverd, J. C. Smith, K. Stassun, C. G. Tinney, R. Wittenmyer, D. J. Wright, H. Zhang, G. Zhou, & C. A. Ziegler 2019. **TESS Spots a Compact System of Super-Earths around the Naked-eye Star HR 858**. The Astrophysical Journal Letters881(1), *Transiting Exoplanet Survey Satellite (TESS) observations have revealed a compact multiplanet system*

around the sixth-magnitude star HR 858 (TIC 178155732, TOI 396), located 32 pc away. Three planets, each about twice the size of Earth, transit this slightly evolved, late F-type star, which is also a member of a visual binary. Two of the planets may be in mean motion resonance. We analyze the TESS observations, using novel methods to model and remove instrumental systematic errors, and combine these data with follow-up observations taken from a suite of ground-based telescopes to characterize the planetary system. The HR 858 planets are enticing targets for precise radial velocity observations, secondary eclipse spectroscopy, and measurements of the Rossiter-McLaughlin effect.

B.12 Truly eccentric - I. Revisiting eight single-eccentric planetary systems

R. A. Wittenmyer, J. T. Clark, J. Zhao, J. Horner, S. Wang, & D. Johns 2019. **Truly eccentric - I. Revisiting eight single-eccentric planetary systems**. Monthly Notices of the Royal Astronomical Society 484(4), 5867-5859

We examine eight known single-eccentric planetary systems in light of recently released large data archives and new analysis techniques. For four of these systems (HD 7449, HD 65216, HD 89744, HD 92788) we find evidence for additional long-period companions. HD 65216c is a Jupiter analogue, with a period of 14.7 yr, e = 0.18, and m sin i of 2M_{Jup}, while the remaining candidate companions move on as-yet-incomplete orbits. Our results highlight the importance of revisiting the analysis of known exoplanetary systems when new data become available, particularly given the possibility that poorly sampled data might previously have led to the detection of a 'false-positive' single-eccentric planet, when the system in question actually contains two (or more) planets on near-circular orbits.

B.13 Truly eccentric - II. When can two circular planets mimic a single eccentric orbit?

R. A. Wittenmyer, C. Bergmann, J. Horner, J. Clark, & S. R. Kane 2019. **Truly eccentric - II. When can two circular planets mimic a single eccentric orbit?**. Monthly Notices of the Royal Astronomical Society 484(3), 4238-4230

When, in the course of searching for exoplanets, sparse sampling and noisy data make it necessary to disentangle possible solutions to the observations, one must consider the possibility that

what appears to be a single eccentric Keplerian signal may in reality be attributed to two planets in near-circular orbits. There is precedent in the literature for such outcomes, whereby further data or new analysis techniques reveal hitherto occulted signals. Here, we perform suites of simulations to explore the range of possible two-planet configurations that can result in such confusion. We find that a single Keplerian orbit with e □ 0.5 can virtually never be mimicked by such deceptive system architectures. This result adds credibility to the most eccentric planets that have been found to date, and suggests that it could well be worth revisiting the catalogue of moderately eccentric 'confirmed' exoplanets in the coming years, as more data become available, to determine whether any such deceptive couplets are hidden in the observational data.

B.14 A Jovian planet in an eccentric 11.5 day orbit around HD 1397 discovered by TESS

L. D. Nielsen, F. Bouchy, O. Turner, H. Giles, A. S. Mascareño, C. Lovis, M. Marmier, F. Pepe, D. Ségransan, S. Udry, J. F. Otegi, G. Ottoni, M. Stalport, G. Ricker, R. Vanderspek, D. W. Latham, S. Seager, J. N. Winn, J. M. Jenkins, S. R. Kane, R. A. Wittenmyer, B. Bowler, I. Crossfield, J. Horner, J. Kielkopf, T. Morton, P. Plavchan, C. G. Tinney, H. Zhang, D. J. Wright, M. W. Mengel, J. T. Clark, J. Okumura, B. Addison, D. A. Caldwell, S. M. Cartwright, K. A. Collins, J. Francis, N. Guerrero, C. X. Huang, E. C. Matthews, J. Pepper, M. Rose, J. Villaseñor, B. Wohler, K. Stassun, S. Howell, D. Ciardi, E. Gonzales, R. Matson, C. Beichman, & J. Schlieder 2019. **A Jovian planet in an eccentric 11.5 day orbit around HD 1397 discovered by TESS**. A&A 623 *The Transiting Exoplanet Survey Satellite TESS has begun a new age of exoplanet discoveries around bright host stars. We present the discovery of HD 1397b (TOI-120.01), a giant planet in an 11.54-day eccentric orbit around a bright (V = 7.9) G-type subgiant. We estimate both host star and planetary parameters consistently using EXOFASTv2 based on TESS time-series photometry of transits and radial velocity measurements with CORALIE and MINERVA-Australis. We also present high angular resolution imaging with NaCo to rule out any nearby eclipsing binaries. We find that HD 1397b is a Jovian planet, with a mass of 0.415 ± 0.020 M_J and a radius of 1.026 ± 0.026 R_J. Characterising giant planets in short-period eccentric orbits, such as HD 1397b, is important for understanding and testing theories for the formation and migration of giant planets as well as planet-star interactions.*

B.15 Re-analyzing the Dynamical Stability of the HD 47366 Planetary System

J. P. Marshall, R. A. Wittenmyer, J. Horner, J. Clark, M. W. Mengel, T. C. Hinse, M. T. Agnew, & S. R. Kane 2019. **Re-analyzing the Dynamical Stability of the HD 47366 Planetary System**. Astronomical Journal 157(1), *Multi-planet systems around evolved stars are of interest to trace the evolution of planetary systems into the post-main-sequence phase. HD 47366, an evolved intermediate-mass star, hosts two giant planets on moderately eccentric orbits. Previous analysis of the planetary system has revealed that it is dynamically unstable on timescales much shorter than the stellar age unless the planets are trapped in mutual 2:1 mean-motion resonance, inconsistent with the orbital solution presented in Sato et al., or are moving on mutually retrograde orbits. Here we examine the orbital stability of the system presented in S16 using the n-body code MERCURY over a broad range of a-e parameter space consistent with the observed radial velocities, assuming they are on co-planar orbits. Our analysis confirms that the system as proposed in S16 is not dynamically stable. We therefore undertake a thorough reanalysis of the available observational data for the HD 47366 system, through the Levenberg-Marquardt technique and confirmed by MCMC Bayesian methodology. Our reanalysis reveals an alternative, lower-eccentricity fit that is vastly preferred over the highly eccentric orbital solution obtained from the nominal best-fit presented in S16. The new, improved dynamical simulation solution reveals the reduced eccentricity of the planetary orbits, shifting the HD 47366 system into the edge of a broad stability region, increasing our confidence that the planets are all that they seem to be. Our rigorous examination of the dynamical stability of HD 47366 stands as a cautionary tale in finding the global best-fit model.*

B.16 The K2-HERMES Survey. I. Planet-candidate Properties from K2 Campaigns 1-3

R. A. Wittenmyer, S. Sharma, D. Stello, S. Buder, J. Kos, M. Asplund, L. Duong, J. Lin, K. Lind, M. Ness, T. Zwitter, J. Horner, J. Clark, S. R. Kane, D. Huber, J. Bland-Hawthorn, A. R. Casey, G. M. De Silva, V. D'Orazi, K. Freeman, S. Martell, J. D. Simpson, D. B. Zucker, B. Anguiano, L. Casagrande, J. Esdaile, M. Hon, M. Ireland, P. R. Kafle, S. Khanna, J. P. Marshall, M. H. M. Saddon, G. Traven, & D. Wright 2018. **The K2-HERMES Survey. I. Planet-candidate Properties from K2 Campaigns 1-3**. Astronomical Journal 155(2),

Accurate and precise radius estimates of transiting exoplanets are critical for understanding their compositions and formation mechanisms. To know the planet, we must know the host star in as much detail as possible. We present first results from the K2-HERMES project, which uses the HERMES multi-object spectrograph on the Anglo-Australian Telescope to obtain R ~ 28000 spectra of up to 360 stars in one exposure. This ongoing project aims to derive self-consistent spectroscopic parameters for about half of K2 target stars. We present complete stellar parameters and isochrone-derived masses and radii for 46 stars hosting 57 K2 candidate planets in Campaigns 1-3. Our revised host-star radii cast severe doubt on three candidate planets: EPIC 201407812.01, EPIC 203070421.01, and EPIC 202843107.01, all of which now have inferred radii well in excess of the largest known inflated Jovian planets.

B.17 The Pan-Pacific Planet Search. VII. The Most Eccentric Planet Orbiting a Giant Star

R. A. Wittenmyer, M. I. Jones, J. Horner, S. R. Kane, J. P. Marshall, A. J. Mustill, J. S. Jenkins, P. A. P. Rojas, J. Zhao, E. Villaver, R. P. Butler, & J. Clark 2017. **The Pan-Pacific Planet Search. VII. The Most Eccentric Planet Orbiting a Giant Star**. Astronomical Journal 154(6), *Radial velocity observations from three instruments reveal the presence of a 4 M_{Jup} planet candidate orbiting the K giant HD 76920. HD 76920b has an orbital eccentricity of 0.856 ± 0.009, making it the most eccentric planet known to orbit an evolved star. There is no indication that HD 76920 has an unseen binary companion, suggesting a scattering event rather than Kozai oscillations as a probable culprit for the observed eccentricity. The candidate planet currently approaches to about four stellar radii from its host star, and is predicted to be engulfed on a ~100 Myr timescale due to the combined effects of stellar evolution and tidal interactions.*

This page intentionally left blank.